DECEMBER 1957

A.I.Ch.E. JOURNAL

Published by the American Institute of Chemical Engineers

CONTENTS

Practical, Efficient, and Economical

SOLVENT EXTRACTION

with

YORK-SCHEIBEL LIQUID-LIQUID EXTRACTORS

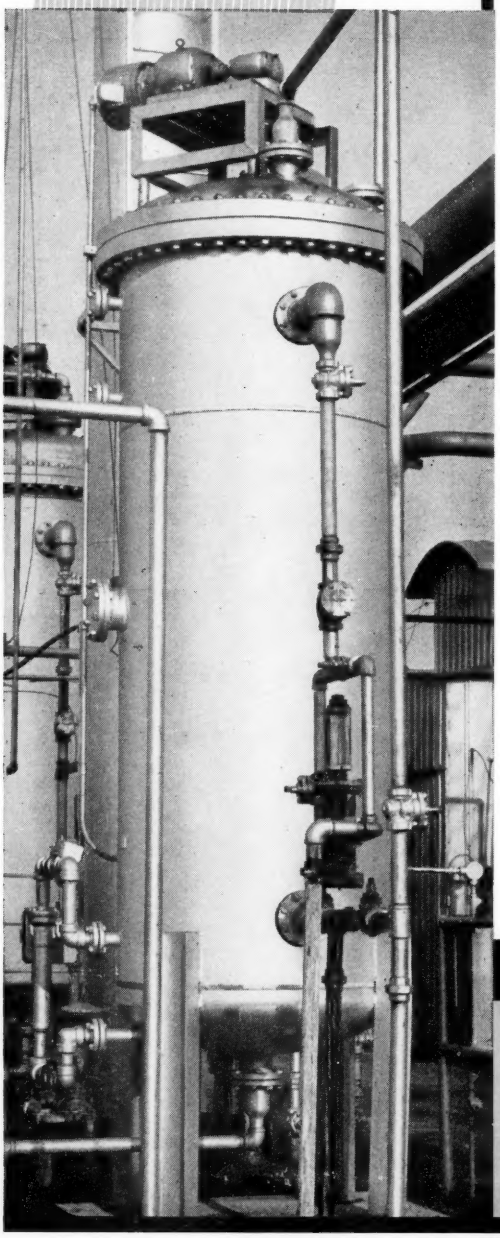

The YORK-SCHEIBEL patented multi-stage extraction column:

- Is ideal for the common multi-stage, countercurrent extractions in which the feed material is contacted with a single solvent.
- Is effective and efficient for fractional liquid extraction in which the feed material is contacted with two selective and immiscible solvents flowing countercurrent through the column.
- May be designed for liquid streams carrying solids in suspension.

The columns employ agitators in each stage to insure complete liquid-liquid contacting. The phase separating sections between the mixing zones consist of wire mesh packing, a new arrangement of baffles, or both baffles and packing.

High stage efficiencies are obtained even with difficult-to-separate materials. Here are a few of the extractions for which York-Scheibel columns have no equal:

- *close boiling mixtures*
- *non-volatile mixtures*
- *structural isomers*
- *materials from dilute solutions*
- *azeotropic mixtures*
- *impurities and color bodies*
- *heat sensitive materials*

Check these outstanding features:

- √ *Single, compact column*
- √ *High throughput capacity*
- √ *Efficient laboratory, pilot plant and large scale performance*
- √ *High efficiency*
- √ *Low cost per stage*
- √ *Low stage height*

SEND INFORMATION on your requirements and let York engineers recommend the best design for your conditions.

YORK

YORK PROCESS EQUIPMENT CORP.
4 Central Avenue, West Orange, N.J.
Send for latest literature giving complete details

A.I.Ch.E. JOURNAL

DECEMBER 1957 · VOL. 3, NO. 4

The A.I.Ch.E. Journal, an official publication of the American Institute of Chemical Engineers, is devoted in the main to theoretical developments and research in chemical engineering and allied branches of engineering and science. Manuscripts should be submitted to the New York office.

Publication Office, Richmond, Virginia. Published quarterly in March, June, September, and December by the American Institute of Chemical Engineers, 25 West 45 Street, New York 36 New York. Manuscripts and other communications should be sent to the New York office. Correspondence with the editor may be addressed to him at Yale University, 225 Prospect Street, New Haven 11, Connecticut. Statements and opinions in the *A.I.Ch.E. Journal* are those of the contributors, and the American Institute of Chemical Engineers assumes no responsibility for them. Subscriptions: one year, member $4.50, nonmember $9.00; two years, member $7.50, nonmember $15.00; additional yearly postage, Canada 50 cents, Pan American Union $1.50, other foreign $2.00 (foreign subscriptions payable in advance). Single copies: $3.00. Second-class mail privileges authorized at Richmond, Virginia.

National headquarters of A.I.Ch.E. is concerned about nondelivery of copies of the *A.I.Ch.E. Journal* and urgently requests subscribers to give prompt notification of any change of address. Sixty days must be allowed for changes to be made in the records.

A.I.Ch.E. JOURNAL

George Granger Brown

1896-1957

For many of us August twenty-sixth will be remembered as a black day. On that day we lost a loved and respected leader. For well over 30 years George Granger Brown guided engineering students, and the mark he left on all of us will be for many years a living tribute to him.

As a man, he set a pattern which we might all emulate. He was warm and human. If in his early days he was a few minutes late to class because of some household chores, he briefly and unhestitatingly bragged, because he took pride in doing things for his children. In later years, as their accomplishments made him proud, he could not keep from mentioning them, though never beyond a justifiable expression of his devotion to his family. Another reflection of this side of his character was his interest in his community. He enthusiastically participated in many of the cultural and civic activities in Ann Arbor.

As a professional engineer and consultant, he was strictly honest. He was a man of strong convictions and always was ready to back his convictions aggressively. His philosophy included the belief that the best defense was frequently a good offense. The strength of his opinions drew him into vigorous arguments and sometimes lost for him the friendship, but never the respect, of those with whom he disagreed.

It was as a teacher, however, that he sparkled at his very best. His enthusiastic interest in all his classes irresistibly generated a reciprocal enthusiasm on the part of the students. He was always ready to be challenged by a student, and many were the lively discussions in his class. He was never caught short for a response and inevitably handled these exchanges to the enrichment of the student, regardless of whether he was a beginner or graduate.

George Granger Brown foresaw many years in advance the swing toward the teaching of more scientific material to undergraduate engineers and took as his personal project the development of a course in chemical engineering thermodynamics which was calculated to stimulate independent and effective thinking. He shunned elaborate and extensive mathematical gymnastics and insisted on direct reasoning from a few basic scientific facts.

As a researcher, he employed his boundless energy and enthusiasm to carry him and his coworkers easily to their goals. The stimulating manner in which he handled these programs is reflected in the large number of his students who chose to follow him into the teaching profession. If he was demanding of his students, it was not distasteful to them because all realized that he demanded more of himself. The only difficulties encountered here stemmed from the fact that he always worked himself to his limit. Sometimes he was available only as he moved rapidly from one assignment to the next, but he never refused a request for help.

As a leader of his department, he was always looking toward the betterment of the staff, the facilities, and the students. The effectiveness of his leadership is clearly reflected in the many advances made by his department while he was chairman.

His devotion to the Institute was most clearly demonstrated in his acceptance of the Treasurer's office. To a man who had served on the Council, who had been a leader of some of the most important committees, and who had been honored with the Presidency and the William H. Walker Award, the work of the Treasurer's office surely must have looked more like a chore which needed to be done than an honor, but he performed the task with characteristic energy and ability.

It was possible over the years to experience many different relationships with him: sharing with him a successful venture, slaving for him when he was driving hard, disagreeing with him violently on occasion. Working with him called up the whole gamut of emotions, but through it all there remained outstanding and unshaken a feeling of complete respect. He was a leader.

A.S.F.

Prediction of Cake-washing Results with Continuous Filtration Equipment

A. P. R. CHOUDHURY and D. A. DAHLSTROM

The Eimco Corporation, Palatine, Illinois

This paper proposes a theory of filter-cake washing on continuous filtration equipment based upon the assumption that mixing of the strong liquor and wash fluid is controlling. The theory can be conveniently applied to experimental filtration leaf tests for determining wash efficiency and is easily extrapolated to full-scale results with the normally experienced uneven cake thickness and wash-fluid distribution taken into account.

To obtain the necessary wash-fluid volume for proper soluble removal, a correlation method of wash time as a function of wash ratio with parameters of cake-formation time has been derived from commonly accepted filtration theory. Experimental and plant data indicate a close agreement with the theory, and the method can be employed to predict filtration rate as a function of wash ratio. A typical illustration has been given to determine filtration requirements for recovering soluble uranium after leaching of the ore by continuous filtration. Washing rate was proved to be controlling, and this design based only on cake-formation rate would yield insufficient wash ratios and excessive soluble uranium loss. Final filter and flow-sheet design must be based on uranium recovery which can be predicted by the proposed methods.

In any continuous filtration application, at least two distinct rates must always be considered and in many cases even three or four. These may be briefly summarized as (1) cake-formation rate, (2) cake-"dewatering" rate, (3) cake-washing rate to remove soluble values or contaminations, (4) thermal drying rate of the filter cake. The first two rates are always encountered, but the third and fourth depend on the application. Generally speaking, one of the four rates will be controlling in the determination of filtration requirements, as it will exhibit the most critical influence. Careful investigation of each rate encountered in a filter application must be made prior to the full-scale application. It is also emphasized that each rate is controlled by diverse factors or influenced to a different degree by similar variables; therefore, analysis methods must be developed for each phase of filtration which allow determination of individual requirements that can later be incorporated into prediction of the following important results or specifications over the desired range of operating conditions: (1) filtration rates, (2) final cake moisture or liquor content, (3) filtrate clarity, (4) final cake soluble concentration or recovery of soluble values, (5) wash-fluid requirements, (6) thermal requirements when cake drying is practiced, (7) power and capacity requirements for all auxiliaries such as filtrate and vacuum pumps, and (8) required filter design to achieve all objectives.

The following discussion will be limited to determination of cake-washing results and requirements. However, this can never be dissociated from the other phenomena and the methods to be developed will also illustrate how cake-washing requirements can be designed to predict all the necessary results and specifications. Other papers have dealt with the other three phenomena and can be referred to for greater detail (*2, 5, 6, 7*).

THEORY OF CAKE WASHING

The theory of filter cake washing must be considered from two standpoints: (1) removal or displacement of cake liquor by the washing fluid and (2) wash-fluid rate through the filter cake. The former is naturally important in determining total strong liquor or soluble value recovery from the feed slurry; however, wash rate must also be known in order that the proper amount of wash fluid may be administered.

Removal of Cake Liquor By Washing

The effectiveness of removal of liquor or soluble salts by cake washing has been the subject of different and extensive theories. However, they have either been concerned largely with batch filtration utilizing relatively thick cakes and single-phase flow or the migration of fluids within porous media found in oil field reservoirs. This is in contrast to washing of cakes in continuous filtration, where two-phase flow may occur and thin cakes with relatively large wash-fluid rates are involved.

Taylor (*9*) analyzed capillary flow and von Rosenberg (*10*) extended the qualitative concept of displacement in a single pore to more complex porous media with numerous pores. The penetration of resident fluid by invading fluid establishes a radial concentration gradient, and consequently the fluid interdiffuses. Ruth, on the other hand, proposed displacement of one fluid by another in both laminar and nonlaminar flow (*4*). Presumably it was felt that the rapidity of washing precluded any significant amount of interdiffusion between the two fluids.

From the available experimental data, it was felt by the authors that mixing within the cake would probably be the controlling factor in removal of strong liquor by washing on a continuous filter. This would be analogous to the so-called "diffusion" washing equation postulated by Rhodes as follows (*3*):

$$\frac{c}{c_0} = e^{-kFt/L} \tag{1}$$

In order to apply this type of equation to continuous-filtration cake washing, it is convenient to develop the expression on the basis of percentage of solute remaining in the filter cake, with 100% being that remaining if no washing were performed. Accordingly, Equation (1) was revised as follows:

By material balance,

$$S_w = (1 - R)S_0 \tag{2}$$

Thus,

$$\frac{dS_w}{dV_w} = c = -S_0 \frac{dR}{dV_w} \tag{3}$$

Also,

$$c_0 = \frac{S_0}{V_l} \tag{4}$$

Therefore,

$$\frac{c}{c_0} = -\frac{S_0\, dR/dV_w}{S_0/V_l} = e^{-kFt/L} = e^{-kV_w/L} \tag{5}$$

Before integrating Equation (5), one can substitute an equivalent for cake thickness L,

$$V_l = \frac{L\rho_c X}{\rho_l} \quad \text{or} \quad L = \frac{\rho_l V_l}{\rho_c X} \tag{6}$$

It should be noted that a unit filtration area is assumed for Equation (6). Substituting for L in Equation (5) gives

$$\frac{dR}{dV_w} = -\frac{1}{V_l} \exp\left[\frac{-k\rho_c X V_w}{\rho_l V_l}\right] \tag{7}$$

Equation (7) may now be integrated for a constant V_l condition (i.e., constant cake thickness, which also stipulates constant V_l, ρ_c, ρ_l, X, and k). In addition, the term $k\rho_c X/\rho_l$ can be combined into a single constant k'.

Thus,

$$R = \frac{1}{k'} e^{-k' V_w / V_l}$$

$$+ \text{integration constant} \qquad (8)$$

Boundary conditions implied by Rhodes's original equation are $R = 0$ at $v_w =$ infinity. If these are employed, the integration constant becomes zero. Thus, taking the log of both sides of Equation (8) gives

$$\log R = -k' \frac{V_w}{V_l} + \log (1/k') \qquad (9)$$

Equation (9) indicates that a semilog plot of log R vs. V_w/V_l should yield a straight-line relationship. The term V_w/V_l is the number of displacements of wash (i.e., wash volume divided by original liquor volume in the cake prior to wash) and is termed the "wash ratio n."

To prove the relationship between R and wash ratio n, extensive data on several different applications were compiled. Figure 1 is a typical plot for the washing of aluminum trihydrate with water. It is crystalized from a caustic and carbonate liquor, and the filter cake must be washed to recover practically all Na_2O values.

Observation of Figure 1 indicates a good straight-line agreement with the data below wash ratios of 2.1. Results on other materials yielded straight-line relationships. Deviations beyond a wash ratio of 2.0 have generally been well below the extrapolated straight line. However, care should be exercised in employment of Equation (10) above n values of 2.0 without proper experimental work. It should also be noted that where cake-washing rate and removal of solubles are controlling, it will usually be more economical to install two stages of filtration with n values below 2.0 to obtain desired results rather than to employ a single state with a high wash ratio.

The equation of the average straight line of plots similar to Figure 1 is

$$\frac{R'}{100} = \left(1 - \frac{E}{100}\right)^n \qquad (10)$$

Thus, if the wash efficiency E is established, Equation (10) may be employed to determine the recovery of soluble values as a function of applied wash ratio. If filtration leaf-testing techniques are employed to obtain a plot similar to Figure 1 and thus determine E, the wash efficiency should be lowered to take into account full-scale deviations, which are caused by uneven cake thicknesses across the filtration area and uneven wash-water distribution across the cake. Normally, experimental wash efficiency E will be lowered by 10% but the actual value will depend on the type of filter and the method of applying the wash fluid.

In order to calculate the recovery of soluble values from the original feed liquor per filter station, the following data are necessary: (1) feed solids concentration, (2) filter cake liquor content prior to washing, (3) liquid content of cake at discharge from the filter, and (4) wash efficiency E determined by experiment and properly corrected for full-scale application. It is readily apparent that all these four points can be determined by proper filtration leaf testing. The first recovery is obtained by simple material balance around the cake-formation and initial "dewatering" phase of the filter cycle prior to cake washing. The remaining recovery is calculated by use of Equation (10).

Wash efficiency E values have been

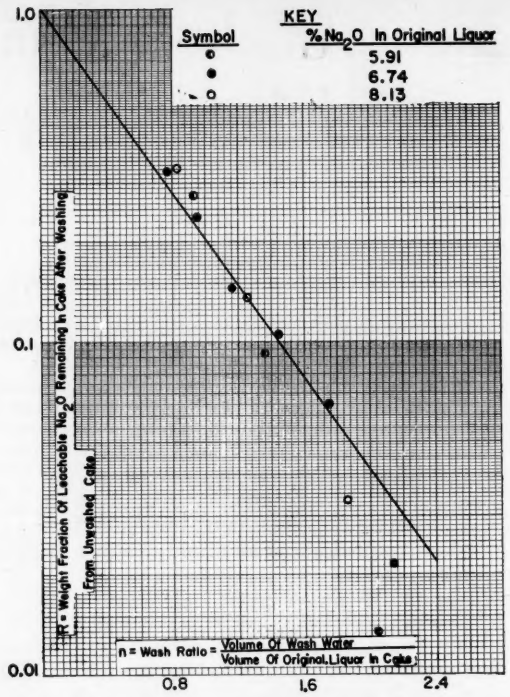

Fig. 1. Weight fraction leachable Na_2O remaining in filter cake after washing from original unwashed cake, R, vs. wash ratio, n.

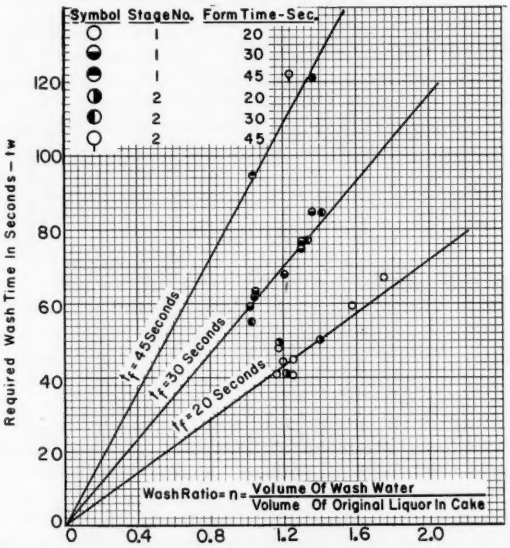

Fig. 2. Wash time as a function of wash ratio parameters of form time. First- and second-stage acid-leached uranium-ore filters. Cotton ST-19 filter media, 23 in. Hg vacuum; 0.1 sq. ft. leaf, pH–1.975 to 1.99; average percentage of −200 mesh in filter cake, 55.1 wt. %; feed percentage of solids, stage 1—58.4%, stage 2—60.0%.

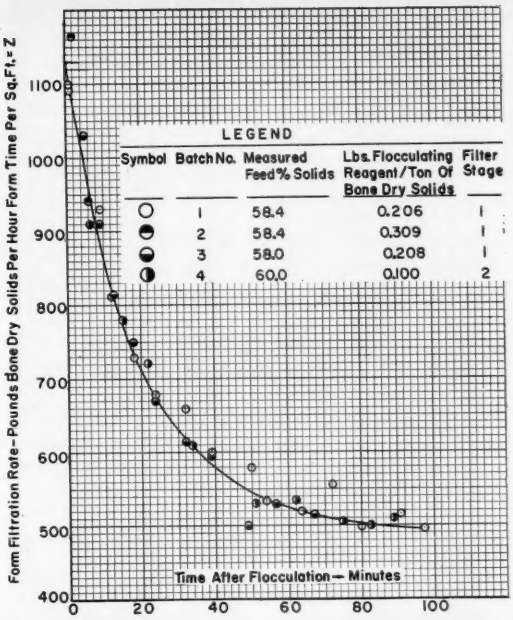

Fig. 3. Leaf-test form filtration rate vs. time after flocculation. Leached uranium ore slurries. Cotton ST-19 filter media; 23 in. Hg vacuum; average %-200 mesh in filter cakes-55.1 wt. %; pH — 1.975 to 1.99—filtration stages 1 and 2 included; form filtration rates corrected to 30 sec. form time.

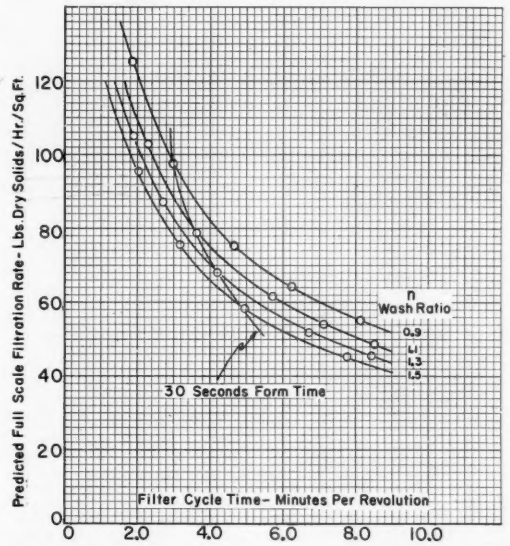

Fig. 4. Predicted full-scale filtration vs. cycle time. Parameters of wash ratio—leached uranium slurry. Basis: 20-min. retention time after flocculation; drum filters—cotton St.-19F; filter media—23 in. Hg vacuum; 60% feed solid concentration, 80% design factor on leaf-test data.

found to vary from a minimum of 35% to a maximum of 86%. Generally speaking, the lower values are found with cakes that wash very rapidly such as some long fibers employed in paper making. This is probably due to chaneling and insufficient time for more complete mixing. It should also be noted that cake moisture content after washing and final "dewatering" is usually lower than before washing. This phenomenon has been found to be more pronounced as the viscosity difference between original liquor and wash fluid increases. This naturally increases the efficiency of washing due to improved drainage.

RATE OF CAKE WASHING

From the preceding, it has been proposed that recovery of soluble values from a filter cake by cake washing will be a function of wash ratio n. Once this function has been determined, it becomes possible to calculate both the final product purity and total recovery of soluble material per filter stage for any value of applied wash. However, time required for washing must also be related to wash ratio and other filtration factors in order to predict full-scale filtration rates which permit the realization of desired soluble recoveries. The modified Hagen-Poiseuille equation for flow of liquor through capillaries generally applied to filtrate rate studies is (*1*)

$$\frac{dV}{Adt} = \frac{(-\Delta P)}{\mu\left(\alpha w \frac{V}{A} + r\right)} \qquad (11)$$

As continuous filtration is a cyclic process, the actual filtration rate experienced from each square foot of area per unit time must be obtained from the integrated form of Equation (11). Before this integration is performed however, it is convenient to discuss the term r, which is the resistance of the filter media; drainage decking; and internal piping of the filter. It is apparent that correct filter design can result in a negligible resistance for the drainage decking and internal piping and will be assumed so in this paper. This may not necessarily be true for filter media if selection is improper or an extremely "tight" medium is employed. However, as cake-formation time in continuous filtration with cake washing is usually achieved in a range from a few seconds to a maximum of two minutes, it would be expected that filter-media resistance would be small to negligible. While the resistance r will be assumed negligible, correlation methods will be given to prove this assumption in the course of the theoretical development.

With r assumed negligible, Equation (11) can be integrated between the limits of $V = 0$ and V_f with $t = 0$ and t_f. The integration assumes parameters of constant pressure drop, feed-solids concentration, temperature, and specific cake resistance. Thus

$$\frac{V_f}{A} = \left[\frac{2(-\Delta P)t_f}{\mu\alpha w}\right]^{1/2} \qquad (12)$$

With t_f expressed in minutes, multiplying both sides of Equation (12) by $60/t_f$ would yield filtration rate as volume of filtrate per unit area per hour of cake-formation time. Thus no consideration at this point is given to time required for cake washing, dewatering, or discharge. However, this can be easily achieved once the fraction of the total filter-cycle time available for cake formation is known; therefore

$$\frac{60}{t_f}\cdot\frac{V}{A} = Z = \left[\frac{7{,}200(-\Delta P)}{\mu\alpha w t_f}\right]^{1/2} \qquad (13)$$

Z is termed the "form filtration rate" and can be expressed in terms of weight of dry cake solids per unit area per hour

of cake-formation time by multiplying both sides of Equation (13) by w.

From Equation (13), a log-log plot of Z as a function of cake-formation time t_f should yield a straight line of slope -0.50 for constant-feed-solids concentration, size distribution, and pressure drop. If a straight-line relationship is not experienced, this would indicate that the filter-media resistance r could not be neglected. For most continuous-filtration problems, the straight-line correlation has resulted with proper filter-media selection. In several cases slopes will be more negative than -0.50 but this can be traced to migration of fines within the filter cake with time causing a change in permeability.

While Equation (13) is convenient for determining cake-formation filtration rates, it cannot serve to predict cake-washing times. If the wash fluid is assumed equal to the viscosity of the feed liquor, the wash rate per unit area from Equation (11) with $r = 0$ should be equal to

$$\text{wash rate} = \left(\frac{dV}{Adt}\right)_w = \frac{(-\Delta P)}{\mu\alpha w \dfrac{V_f}{A}} \quad (14)$$

As no solids are being deposited during washing, the wash rate should remain constant. Furthermore, if viscosities for both the wash and feed liquor are known, reasonable estimation of wash rate could be obtained by multiplication of Equation (14) by the ratio of the reciprocal of viscosities. From Equation (14) total wash volume after substituting for V_f/A from Equation (12) is

$$\frac{V_w}{A} = t_w\left(\frac{dV}{Adt}\right)_w = \frac{(-\Delta P)t_w}{\mu\alpha w \dfrac{V_f}{A}}$$

$$= \left[\frac{(-\Delta P)}{2\mu\alpha w t_f}\right]^{1/2} t_w \quad (15)$$

Equation (15) can be converted to a wash-ratio expression by dividing by the volume of liquor in the cake prior to washing. Volume of cake liquor prior to washing can be expressed by revising Equation (12) to the following:

$$\frac{V_l}{A} = K\left[\frac{2(-\Delta P)t_f}{\mu\alpha w}\right]^{1/2} \quad (16)$$

Dividing Equation (15) by V_l/A or its equivalent and rearranging gives

$$t_w = 2Kt_f \frac{V_w}{V_l} = 2Kt_f n \quad (17)$$

From Equation (17) a plot of required wash time t_w as a function of wash ratio n should yield straight lines going through the origin with parameters of cake formation times t_f. Furthermore, at the same wash ratio, required wash times should be theoretically directly proportional to cake-formation times. It is stressed that such plots assume constant filter feed-solids concentration and size distribution, pressure drop and cake-liquor content prior to washing for any particular filtration problem. If these values are varied appreciably, additional parameters would be nesessary.

A typical plot of required wash time as a function of wash ratio is illustrated by Figure 2. The tests were performed on filtration and washing of acid-leached uranium ore slurries of constant feed solids concentration, size distribution, and pressure drop. It will be noted that a reasonable straight-line agreement is

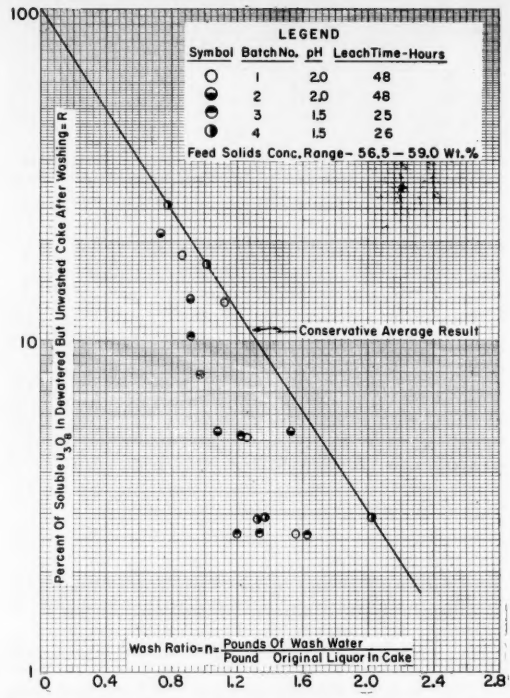

Fig. 5. Percentage of soluble uranium in dewatered but unwashed cake after washing vs. wash ratio.

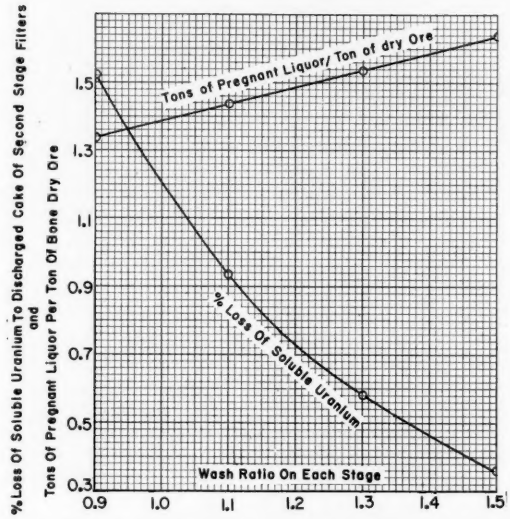

Fig. 6. Predicted % loss of soluble uranium to discharged second-stage filter cake and tons of pregnant liquor per ton of dry ore vs. wash ratio per filter stage. Bases: feed solids concentration to stages I and II = 60.0 wt. %; cake moisture content prior to washing, stage I—19.7%; cake moisture content prior to washing, stage II—19.35%; cake washing efficiency E = 70%; cake moisture content at discharge, stage I—18.0%; cake moisture content at discharge, stage II—17.5%; two-stage drum filtration and cake washing.

obtained for all parameters. Furthermore, the ratio between parameters at the same wash ratio is only slightly greater than the ratio of cake-formation times. This small increase over the theoretical ratio is due to the slightly greater cake-liquor contents prior to washing that were experienced in this case as cake-formation time was increased.

By use of graphs similar to Figure 2 in conjunction with log-log plots of form-filtration rates as a function of cake-formation time, it is possible to predict full-scale filtration rates as a function of wash ratio. Thus, filter design can be matched to obtain desirable soluble recovery or elimination as determined by the required wash ratio on the filter.

PREDICTION OF FULL-SCALE RESULTS AND FILTER-STATION REQUIREMENTS

In order to illustrate the application of the preceding development, a typical case will be analyzed. Although continuous drum filters will be employed in the example, the method may be applied to other types of continuous filters as long as appropriate consideration is given to the allowable time for cake washing for the particular filter construction.

Uranium ore is processed by leaching the finely ground solids in an acid (normally sulfuric acid) or carbonate liquor for 8 to 72 hr. Continuous leach agitators in series are generally used and solids concentrations of 55 to 65 wt. % are employed in order to reduce reagent consumption and holdup volume. After leaching, the "pregnant liquor" containing the uranium in solution must be separated from the very large amount of gangue solids before further processing can be done to finally obtain a dried uranium precipitate of sufficient purity to meet rigid specifications. In addition, the U_3O_8 content in the dry ore may be as low as 0.08 wt. %, which necessitates a soluble uranium recovery of 99.5% in separating the gangue solids from the "pregnant liquor." Finally, liquor volumes after separation normally must be maintained within certain limits in order to minimize capital investment and operating costs in the remainder of the flow sheet.

General practice where filtration is used for recovery of "pregnant liquor" is to employ two-stage continuous-drum filtration with cake washing on each stage and intermediate repulping. By this method, initial investment and operating costs are minimized and the flow sheet is simplified. However, care must be exercised in original design to ensure that a sufficient wash ratio will be experienced on each filter stage. Accordingly, filtration rates are based upon a design wash ratio that will limit soluble uranium losses to a maximum of 0.5%.

In the particular application to be illustrated, design solids concentration was 60.0 wt. % with 55 to 57% −200 mesh in the dry solids. Several filtration leaf tests were performed at 58 to 60% solids concentration on many slurries in order to determine form-filtration rates. Because of the nature of the slimes created in both the grind and leach circuits together with the acid content of the liquor, flocculating reagents must be employed to agglomerate these fractions. Jaguar (a refined endosperm of the Guar seed) was found to be optimum for this slurry on the filter application. However, owing to the acid nature of the pregnant liquor, a partial degradation of the flocculi with time was apparent which also affected filtration rate. Accordingly, extensive tests were made to observe the magnitude of the breakdown.

Figure 3 is the resultant plot of form-filtration rate as a function of time after flocculation. Three batches of first-stage feed slurry ranging from 58.0 to 58.4 wt. % solids concentration were tested and one second-stage batch at 60 wt. % solids concentration. Average −200 mesh content of the solids was 55.1 wt. %. It will be noted that all form-filtration rates have been corrected by means of Equation (13), to 30 sec. form time as form times ranging from 20 to 60 sec. were investigated. It was stated earlier that the square-root relationship was appropriate if filter-media resistance was negligible and there was no migration of fines within the cake. The close agreement of the data with the average curve drawn in Figure 3 indicates that these assumptions are correct for the slurries tested.

The average curve of Figure 3 is typical of many leached uranium slurries tested in that flocculi degradation is quite rapid initially but asymptotically approaches a minimum form-filtration rate. It should be emphasized that the minimum value still represents an operable condition but naturally it is desirable to take advantage of higher filterability by designing the filter stations for minimum holdup time. The design basis for this application was 20-min. retention time, which yields a sufficient engineering safety factor. Thus, from Figure 3, form-filtration rate Z at any form time t_f would be

$$Z = 715\left(\frac{0.5}{t_f}\right)^{1/2} \qquad (18)$$

During the leaf tests various aliquots of wash fluid were applied to the filter cakes formed at three different cake-formation and wash times measured. Filter-cake moisture contents after 30 sec. dewatering time both before and after washing were determined so that wash fluid applied in terms of wash ratio might be calculated. Wash ratio was measured as pounds of wash fluid per pound of cake moisture owing to the insignificant difference in specific gravity between the two liquids. Thus a plot of wash time as a function of wash ratio with parameters of cake-formation time was developed and was given earlier in Figure 2. It will be noted that both filtration stages are included in this plot and results were similar.

Employing Equation (18) and Figure 2 makes it possible to determine full-scale filtration rates as a function of wash ratio. In this application 105° of the periphery of the drum filter is employed for cake washing. This design permits proper dewatering prior to and after washing, which is essential to high recoveries. In addition, a design factor of 80% on leaf-test form-filtration rates is utilized in predicting full-scale rates. To illustrate the calculation of full-scale results, the following example is given

To find: Full-scale filtration rates at 0.75 min. form time and 1.5 wash ratio

Wash time at 1.5 wash ratio
= 135.7 sec. = 2.26 min. (from Figure 2)

Cycle time = $2.26 \times 360°/105°$
= 7.75 min./rev.

Form filtration rate = $715\ (0.5/0.75)^{1/2}$
= 584 lb. dry solids/(sq. ft.)(hr.) form time

Predicted full-scale rate
$$= 584 \times \frac{0.75 \text{ form time}}{7.75 \text{ total time}} \times \frac{0.8 \text{ design}}{\text{factor}}$$
= 45.1 lb. dry solids/(sq. ft.)(hr.)

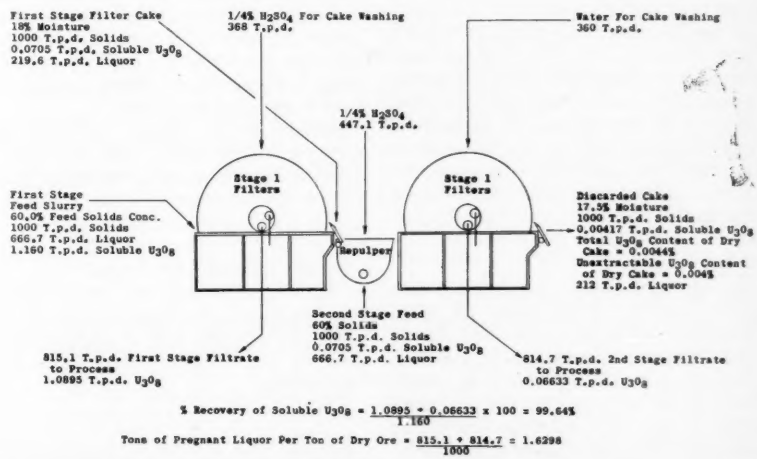

Fig. 7. Flow sheet for uranium recovery of a leached uranium ore with two-stage filtration. Basis: 0.120 wt. % of total U_3O_8 in raw dry ore; 0.004 wt. % of unextractable U_3O_8 in raw dry ore; 1.5 wash ratio on stages I and II—70% washing efficiency = E; 1,000 tons/day of dry ore to plant.

Figure 4 is the resultant plot of predicted full-scale filtration rate as a function of filter-cycle time with parameters of wash ratio (0.9, 1.1, 1.3 and 1.5 lb. of wash fluid/lb. of moisture in the unwashed cake). The curves obtained are typical in that filtration rate increases rapidly as filter-cycle time is reduced. It is apparent that wash ratio is a very important criterion in that an appreciable displacement of the parameter occurs as wash ratio is decreased. Also included on the graph is a parameter of 30 sec. form time. This form time was employed as a design basis as reasonable cake thicknesses of 0.5 in. were obtained. This basis would permit approximately 30% excess capacity to handle peak-tonnage loadings merely by reducing filter-cycle time through the variable-speed drive on the filter. This excess capacity is also obtained without appreciable loss in soluble uranium, as design-wash ratio can be maintained.

To illustrate further the importance of cake-washing rates in determining full-scale filtration rates, it is interesting to note the percentage of cycle time devoted to cake formation. In the sample calculation given above, cake-formation time was 0.75 min. and filter-cycle time equaled 7.75 min./rev. Thus cake-formation time was only 9.7% of total cycle time. If washing was not performed, maximum cake-formation time would be about 35% of the total cycle time for a standard low-submergence filter. It is apparent that the necessary wash ratio for proper uranium recovery could not be experienced if design was based solely on cake-formation time.

To calculate soluble uranium recovery, wash efficiency E for cake washing must be determined. Figure 5 is a semilog plot of percentage of soluble U_3O_8 remaining in the cake after washing, on the basis of 100% remaining if no washing were performed (R'), as a function of wash ratio n. It will be noted that a straight line has been drawn for the data through $R' = 100$ at $n = 0$. This line has been termed a "conservative average" as the majority of data lie to the left of the line. Because of the critical importance of maintaining a very low soluble-uranium loss, the line is not drawn through the average of the data points but instead through the poorest results. Thus average results should be improved over predicted values

From Figure 5, at a wash ratio $n = 1.0$, $R' = 17.5\%$. Thus wash efficiency $E = 100 - R' = 82.5\%$. In determining wash efficiencies of many different leached uranium ores, wash efficiency E values have varied between the narrow range of 80 to 86%. For full-scale predictions wash efficiency E was assumed as 70%. This yields a safety factor of 12.5% to account for uneven cake thickness and wash-water distribution. Thus Equation (10) becomes

$$R' = 100(0.3)^n \qquad (19)$$

It is now possible to calculate full-scale soluble-uranium recovery as a function of wash ratio. The following assumptions, all determined from experimental data, are necessary:

1. Feed-solids concentration to both filter stages = 60.0 wt. %.
2. Moisture content prior to washing

   Stage I = 19.7 wt. %
   Stage II = 19.35 wt. %

3. Moisture content in cake at discharge

   Stage I = 18.0 wt. %
   Stage II = 17.5 wt. %

4. Equation (19) is employed for calculation of soluble-uranium recovery by cake washing.

Figure 6 is a plot of percentage loss of soluble uranium to the discharged cake of the second-stage filters as function of wash ratio. The same wash ratio is applied to both filter stages, which is normal in uranium-ore processing. It will be noted that a wash ratio of at least 1.363 would have to be employed to minimize soluble uranium loss to 0.5%.

Also included in Figure 6 is a plot of tons of pregnant liquor per ton of dry solids. Plant limitations require a maximum design value of 1.65 tons of pregnant liquor per ton of dry solids. Because of the importance of minimum soluble uranium loss, a wash ratio of 1.5 was selected for final design. Thus, from Figure 6, soluble-uranium loss is 0.36% and pregnant liquor rate is 1.63 tons/ton of dry ore.

Figure 7 is the resultant material-balance flow sheet for the two-stage operation. A design rate of 1,000 tons of dry ore/day has been assumed with 0.120 wt. % total U_3O_8 in the raw dry ore and 0.004 wt. % being unextracted by leaching. One-quarter percent sulfuric acid is employed for first-stage cake washing and repulping to maintain proper pH level. Fresh water is used for second-stage cake washing. All other assumptions have been given previously.

Because of the selected design wash ratio of 1.5 to ensure proper soluble-uranium recovery, design filtration rate can also be determined. From Figure 4, at the design cake-formation time of 30 sec. with a 1.5 wash ratio per filter stage, full-scale filtration rate equals 58.5 lb. of dry solids/(hr.)(sq. ft.). Design cycle time would be 4.90 min./rev. Thus, for a plant rate of 1,000 tons of dry ore/day, 1,426 sq. ft. of filtration area/stage would be required.

NOTATION

A = area
c = concentration of the solute in the filtrate at any time after washing begins, weight per unit volume
c_0 = concentration of the solute in original liquor
E = wash efficiency, % = 100 − R' at $n = 1.0$
F = wash flow rate, volume per unit time
k, k', K = constants
L = cake thickness, length
n = wash ratio = volume of wash fluid per unit volume of original liquor in unwashed cake
R = weight fraction of solute remaining in cake after washing on the basis of $R = 1.0$ prior to washing
R' = % solute remaining in the cake after washing on the basis of $R' = 100$ prior to washing
r = resistance of filter media, lines, etc.
S_0 = weight of solute originally present in the cake prior to washing
S_w = cumulative weight of solute in the wash filtrate
t = time
t_f = cake-formation time
t_w = cake-washing time
V = volume of filtrate at any time t
V_f = volume of filtrate at time t_f
V_l = volume of liquor in cake prior to washing
V_w = volume of wash filtrate
w = weight of dry cake solids per unit volume of filtrate
X = weight fraction of liquor in cake prior to washing
Z = form-filtration rate expressed as volume of filtrate or weight of dry-cake solids per unit area per hour of cake-formation time
α = specific cake resistance
$-\Delta P$ = pressure drop across filter
μ = liquid viscosity
ρ_c = density of wet cake prior to washing
ρ_l = density of liquor in cake

LITERATURE CITED

1. Carman, *Trans. Inst. Chem. Engrs.*, **16**, 174 (1938).
2. Henderson, A. S., C. F. Cornell, A. F. Dunyon, and D. A. Dahlstrom, *Mining Engineer*, **9**, 349 (1957).
3. Rhodes, F. H., *Ind. Eng. Chem.*, **26**, 1331 (1934).
4. Ruth, B. F., paper presented at annual meeting, A.I.Ch.E. (Dec. 7–10, 1952).
5. Schepman, B. A., B. Martin, and D. A. Dahlstrom, *Chem. Eng. Progr.*, **52**, 423 (1956).
6. Silverblatt, C. E., and D. A. Dahlstrom, paper presented at Second International Conference on Coal Preparation, Essen, Germany, (September, 1954).
7. ———, *Ind. Eng. Chem.*, **46**, 1201 (1954).
8. Swearingen, J. S., *Oil & Gas J.*, **52**, No. 7, 283 (1953).
9. Taylor, G. I., *Proc. Roy. Soc. (London)*, **A219**, 186 (1953).
10. Von Rosenberg, D. U., *A.I.Ch.E. Journal*, **2**, 55 (1956).

Axial Mixing in Pipes

L. J. TICHACEK, C. H. BARKELEW, and THOMAS BARON

Shell Development Company, Emeryville, California

The problem of axial mixing in straight pipes is analyzed by a modification of G. I. Taylor's analysis. The treatment presented here includes the effect of both Schmidt and Reynolds numbers throughout the turbulent-flow range. All applicable data on flow of gases and liquids are found to confirm the validity of the method.

The analysis indicates that axial mixing increases rapidly as the flow approaches the laminar region, especially for liquids, and that pipe roughness causes a relatively small increase in axial mixing. Turbulent eddy diffusion in the axial direction has a negligible effect.

The results of the analysis are applicable to those systems wherein the kinematic viscosity of the flowing mixture does not vary greatly from one region to another and in which the concentration region of interest is spread out along a sufficient length of pipe. These limitations are broad enough to permit most practical problems to be treated by the method.

The passage of fluid through a pipe is accompanied by mixing in the axial direction. This effect, which can be observed, for instance, by noting the dispersion of tracers, results in intermixing of products in pipe lines, in decreasing the driving force in tubular reactors, and in diminishing the sharpness of signals in tracer experiments.

In unbroken straight pipes axial mixing is due to diffusion in the axial direction because of molecular or turbulent motions and to the relative axial motion of fluid elements at different radial positions. However, the effects of axial molecular and turbulent diffusion are negligible compared with the interpenetration due to relative motion. The latter depends greatly on the shape of the velocity profile and the rate of radial diffusion. The more nearly the velocity profile approaches that for plug flow, the smaller is the amount of axial mixing. A high rate of radial diffusion tends to keep the concentration radially uniform; the different radial fluid elements then have more nearly the same composition and in moving with respect to one another, cause less severe mixing. Thus axial mixing is pronounced in the case of laminar flow, where the flow is least pluglike and where radial diffusion is small (molecular instead of turbulent).

The first analysis of axial mixing based on radial variation of the velocity was made by G. I. Taylor (*17* to *19*), who treated first the case of laminar flow in capillary tubes and later the case of turbulent flow in pipes. His treatment of turbulent flow is valid only for high Reynolds numbers because he used a velocity profile valid only when the laminar sublayer and transition layers are negligibly small. Experimental results support this treatment for Reynolds numbers greater than 20,000.

In the calculations presented here, Taylor's method is refined and extended to cover the whole range of turbulent flows. The chief differences introduced here are the inclusion of the effect of molecular diffusion and the use of experimental velocity profiles rather than a generalized profile. It was necessary to rearrange the mathematical expressions so as to increase the accuracy of calculations based on measured profiles. Also an error analysis is presented which shows that the calculations are valid for most practical purposes.

Mixing because of bends, elbows, valves pumps, etc., must be considered as an effect additional to that discussed here.

THEORETICAL ANALYSIS

In Taylor's analysis the differential equation for transport of material from a radial element of a disk moving with average stream velocity V was written as

$$\frac{1}{r}\frac{\partial}{\partial r}\left(\alpha r \frac{\partial c}{\partial r}\right) = (u - V)\frac{\partial c}{\partial x} + \frac{\partial c}{\partial t}, \quad (1)$$

where

r = distance from center of pipe
α = diffusivity in radial direction
u = axial velocity at r
x = axial distance from reference plane of velocity V

This equation applies to a point moving along with the mean velocity V and neglects molecular and eddy diffusion in the axial direction. To obtain a first approximation to the solution of the mixing problem it is assumed that $\partial c/\partial x$ is constant in the pipe. It follows that $\partial c/\partial t = 0$, and

$$\alpha r \frac{\partial c}{\partial r} = \frac{\partial c}{\partial x}\int_0^r (u - V)r'\,dr' \quad (2)$$

Further integration gives c_r, the concentration at position r:

$$c_r - c_a = \frac{\partial c}{\partial x}\int_a^r \frac{1}{\alpha r'}\,dr' \cdot \int_0^{r'} (u - V)r''\,dr'' \quad (3)$$

The net transport past any reference plane moving with the fluid with the mean velocity V is

$$Q = 2\pi\int_0^a (c_r - c_a)(u - V)r\,dr \quad (4)$$

where a is the pipe radius. Inspection of Equations (3) and (4) shows that the net transport is proportional to the axial concentration gradient; therefore an effective coefficient of axial diffusion E can be defined in the usual way:

$$Q = -\pi a^2 E\frac{\partial c_m}{\partial x} \quad (5)$$

Thus one obtains from Equations (3), (4) and (5),

$$E = -\frac{2}{a^2}\int_0^a (u - V)r\,dr\int_a^r \frac{1}{\alpha r'}\,dr' \cdot \int_0^{r'} (u - V)r''\,dr'' \quad (6)$$

Taylor used the equivalent of this expression to find the apparent axial diffusivity E, evaluating u and α as functions of r

from a universal velocity profile. The analysis may be extended by using measured velocity profiles, and accounting for molecular transport in α.

$$\alpha = \epsilon_D + \mathbf{D} \tag{7}$$

A similar expression can be applied for the transport of momentum:

$$\tau = -(\epsilon_m + \nu)\rho \frac{\partial u}{\partial r} \tag{8}$$

If it is assumed that $\epsilon_D = \epsilon_m$, then from Equations (7) and (8)

$$\alpha = -\frac{\tau}{\rho}\frac{\partial r}{\partial u} - \nu\left(1 - \frac{1}{N_{Sc}}\right) \tag{9}$$

where N_{Sc} is the Schmidt number. τ can be expressed in terms of τ_0, the shear stress at the wall, or λ, the Moody friction factor ($\lambda/4 = f$, the Fanning friction factor), as follows:

$$\tau = \frac{r}{a}\tau_0 = \frac{r}{a}\cdot\frac{1}{8}\lambda\rho V^2 \tag{10}$$

Equations (6), (9), and (10) then reduce to

$$E = \frac{2}{a^2}\int_0^a \frac{dr}{-\frac{\lambda}{8}\frac{r^2}{a}V^2\frac{\partial r}{\partial u} - r\nu\left(1 - \frac{1}{N_{Sc}}\right)} \cdot \int_0^r (u - V)r'\,dr' \int_0^r (u - V)r''\,dr'' \tag{11}$$

where order of integration has also been changed. The substitution $z = (r/a)^2$ yields the final expression

$$\frac{E}{DV} = \frac{2}{\lambda}\int_0^1 \left\{\frac{1}{-\frac{\partial z}{\partial(u/V)} - \frac{32}{\lambda N_{Re}}\left[1 - \frac{1}{N_{Sc}}\right]}\right\} \frac{dz}{z}\left\{\int_0^z \left(\frac{u}{V} - 1\right)dz'\right\}^2 \tag{12}$$

The variation of u/V with z (i.e., the velocity profile) is dependent only on the Reynolds number and pipe roughness. Thus E/DV depends on the Reynolds number, friction factor (or the roughness), and Schmidt number. It should be understood that this analysis cannot be applied to the mixing of two fluids flowing one behind the other unless the kinematic viscosity is approximately the same in each fluid; i.e., the fluids should not have Reynolds numbers so dissimilar as to cause substantial differences between their velocity profiles.

Evaluation can be done numerically as follows. For a chosen Reynolds number the velocity profile is plotted in the form u vs. z (i.e., vs. r^2/a^2). The values of $\partial u/\partial z$ and $A(z)$ are then calculated for various values of z:

$$A(z) = \int_0^z u\,dz'$$

which also yields $V = A(1)$. After tabulation of values of $[(1/V)A(z) - z]$ and $[(1/V)A(z) - z]^2$, the final integrand

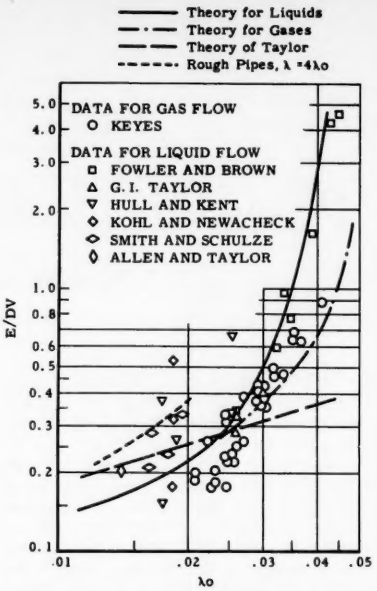

Fig. 1. Axial mixing coefficient vs. smooth-tube friction factor.

$$\frac{\frac{1}{z}\left[\frac{1}{V}A(z) - z\right]^2}{-V\frac{\partial z}{\partial u} - \frac{2}{\lambda N_{Re}}\left[1 - \frac{1}{N_{Sc}}\right]}$$

is found to be a reasonably smooth function of z and thus can be integrated according to Simpson's method. These calculations were made for flow in smooth pipes over a range of Reynolds numbers by use of the velocity profile data of several investigators (*2, 7* to *11, 13, 15*).

Equation (12) shows that as long as the Schmidt number is larger than 100 it does not appreciably affect the value of E/DV. For low Schmidt numbers around $N_{Sc} = 1$ the value of E/DV is more sensitive to variations in N_{Sc}. Calculations indicate, however, that differences in N_{Sc} normally encountered in gases will cause variations in E/DV no greater than those due to experimental error in determining E/DV. Accordingly, two cases were considered: one in which the Schmidt number was taken as 1.0, which is typical of gases, the other in which the Schmidt number was taken larger than 100, which is typical of liquids. For both of these cases the values of E/DV calculated from Equation (12) are shown in Figure 1 as a smooth curve with λ_0 as abscissa where λ_0 is the (Moody) friction factor in a smooth tube.

DATA ON AXIAL MIXING

The results of observations of axial mixing in liquids as reported by a number of investigators (*1, 3, 4, 6, 14, 18*) are plotted on Figure 1. The data scatter somewhat, but there is substantial agreement with the theory. The data of several observers (*12, 14*) were discarded completely or in part because of the inapplicability of this theory under the conditions of certain experiments, i.e., one liquid much more viscous than the other, turbulence not fully developed, or coils in the pipe which cause secondary flow and distortion of the velocity profile.

Observations of axial mixing in gases have been reported by Keyes (*5*), who attempted to measure the thickness of the hypothetical "film" in terms of which mass transfer resistance is usually expressed. Unfortunately the thickness of a "holdup film" calculated from his data demonstrably bears no unique relation to the thickness of the "mass transfer film." Furthermore, the agreement of his data with theory as shown in Figure 1 indicates that there is no need to introduce

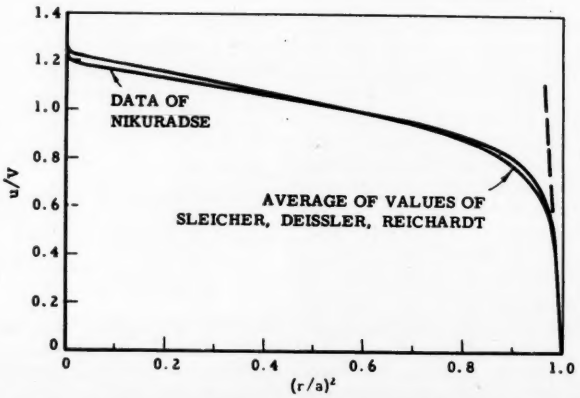

Fig. 2. Comparison of several sets of velocity profile data at $N_{Re} = 42{,}000$.

hypothetical films to describe axial dispersion.

EFFECT OF PIPE ROUGHNESS

An attempt was made to evaluate the effect of pipe roughness on axial mixing. Available velocity profile data (*9*) are not accurate enough, especially near and in the layer of roughening, to show more than a qualitative effect of roughness on axial dispersion.

Pipe roughness produces two effects which partially compensate each other: (1) the velocity profile is less pluglike, and (2) turbulence near the walls, and thus radial diffusion, is greater. Usually the first effect dominates, with the result that roughness tends to increase the axial mixing. An approximate curve is partially drawn in Figure 1 for the case of pipe roughnesses such that $\lambda = 4\lambda_0$. (λ is the actual friction factor; λ_0 is the friction factor in a smooth tube for flow at the same Reynolds number.)

LIMITATIONS OF THE THEORY AND OF ITS APPLICATION

Accuracy of Evaluation

It should be pointed out that the accuracy with which E/DV can be evaluated depends sensitively on the accuracy of the velocity profile. This is illustrated by Figure 2, in which two slightly different sets of velocity profile data are given for Reynolds numbers of about 42,000. Although the magnitudes of the velocities u/V at various radial positions are seldom in disagreement by more than 3% between one set of data and the other, E/DV nevertheless depends on more than the second power of the difference $(u/V - 1)$, and as a consequence there is a 50% disagreement between values of E/DV obtained from the two profiles. Since the value of E/DV does depend very markedly on the profile used, the values of u/V employed for calculations in this paper are presented in Table 1. These values are the result of smoothing and averaging velocity profiles taken by many investigators (*2, 7* to *11, 13, 15*).

It should also be pointed out that the calculation for liquids at Reynolds numbers below 10,000 is very difficult. In this region the nearly laminar film at the pipe walls becomes increasingly important and radial diffusion there is difficult to evaluate. Even though velocity profiles may indicate a laminar region, nevertheless the flow may be intermittently turbulent and the effective radial diffusivity may be much larger than for purely molecular diffusion. [Such an effect is clearly exposed by the work of Stirba and Hurt (*16*).] It is in this region that axial mixing data are most important. Fortunately, and perhaps fortuitously, the data available for this region ($\lambda_0 > 0.03$) confirm the calculations.

TABLE 1 VELOCITY PROFILES USED IN CALCULATIONS

$N_{Re} \times 10^{-3}$	2.56	3.04	4.0	6.0	10.0	40.0	43.4	91.	205.	500.	2790.
u/V at $(r/a)^2$											
0	1.463	1.367	1.320	1.308	1.276	1.241	1.213	1.213	1.190	1.166	1.140
.1	1.411	1.320	1.268	1.244	1.222	1.195	1.167	1.165	1.146	1.135	1.113
.2	1.347	1.280	1.235	1.201	1.182	1.156	1.134	1.130	1.116	1.109	1.093
.3	1.283	1.239	1.197	1.164	1.147	1.117	1.105	1.094	1.088	1.081	1.072
.4	1.215	1.193	1.156	1.128	1.109	1.078	1.070	1.058	1.060	1.053	1.050
.5	1.138	1.140	1.111	1.086	1.069	1.039	1.033	1.023	1.031	1.025	1.026
.6	1.028	1.062	1.054	1.033	1.024	.996	.994	.983	.997	.994	1.000
.7	.866	.936	.976	.968	.967	.946	.952	.939	.954	.959	.970
.8	.633	.731	.841	.860	.880	.880	.897	.888	.899	.913	.922
.85	.486	.581	.710	.762	.804	.836	.861	.853	.862	.883	.891
.9	.324	.390	.485	.611	.677	.776	.808	.807	.814	.839	.847
.95	.162	.195	.248	.348	.441	.670	.709	.738	.740	.765	.784
1.0	0	0	0	0	0	0	0	0	0	0	0
$(E/DV)_{gases}$	1.64	.98	.64	.49	.40	.282	.185	.188	.175	.153	.135
$(E/DV)_{liquids}$			2.82		.53		.185	.188	.175	.153	.135
λ_0	.048	.044	.040	.035	.0305	.0215	.021	.018	.0155	.013	.010

Assumptions in the Theory

Equation (2) is based on the assumption that $\partial c/\partial x$ is constant throughout the pipe. For some systems, therefore, this first-order approximation limits the accuracy with which E/DV can be calculated accordingly to Equation (12). Greater accuracy in evaluating E/DV can be attained by making a first-order approximation to the variation of $\partial c/\partial x$ in the pipe. This refinement is here used to indicate the validity of Equation (12) under various conditions.

The differential equation for variation of the axial concentration gradient is obtained by differentiating Equation (1) with respect to x:

$$\frac{\partial^2 c}{\partial t \partial x} = \frac{1}{r}\frac{\partial}{\partial r}\left(\alpha r \frac{\partial^2 c}{\partial r \partial x}\right) - (u - V)\frac{\partial^2 c}{\partial x^2} \qquad (13)$$

The difference between the value of the axial gradient at any radial position and the value at the center of this pipe is then found by integrating Equation (13):

$$\left.\frac{\partial c}{\partial x}\right|_r - \left.\frac{\partial c}{\partial x}\right|_0 = \int_0^r \frac{1}{\alpha r'}\,dr' \cdot \int_0^{r'} (u - V)\frac{\partial^2 c}{\partial x^2}\, r''\, dr'' + \int_0^r \frac{1}{\alpha r'}\,dr' \int_0^{r'} \frac{\partial^2 c}{\partial t \partial x}\, r''\, dr'' \qquad (14)$$

Since a first-order approximation of $\partial c/\partial x\,|_r$ is desired, the quantities $\partial^2 c/\partial x^2$ and $\partial^2 c/\partial t\,\partial x$ are replaced by their mean values, $\partial^2 c_m/\partial x^2$ and $\partial^2 c_m/\partial t \partial x$, respectively. Substitution for the latter term is made according to the relation

$$\frac{\partial}{\partial x}\frac{\partial c_m}{\partial t} = \frac{\partial}{\partial x}\left(E\frac{\partial^2 c_m}{\partial x^2}\right) \qquad (15)$$

With these substitutions Equation (14) is reduced to

$$\left.\frac{\partial c}{\partial x}\right|_r - \left.\frac{\partial c}{\partial x}\right|_0 = \frac{\partial^2 c_m}{\partial x^2}\int_0^r \frac{1}{\alpha r'}\,dr' \cdot \int_0^{r'} (u - V) r''\, dr'' + E\frac{\partial^3 c_m}{\partial x^3}\int_0^r \frac{r'}{2\alpha}\,dr' \qquad (16)$$

For convenience the term $\partial c/\partial x\,|_0$ is related to $\partial c_m/\partial x$ by the calculation of

$$\frac{\partial c_m}{\partial x} - \left.\frac{\partial c}{\partial x}\right|_0 = \frac{1}{a^2}\int_0^a \left\{\left.\frac{\partial c}{\partial x}\right|_r - \left.\frac{\partial c}{\partial x}\right|_0\right\} 2r\, dr \qquad (17)$$

The equivalent of $\partial c/\partial x$ from Equation (16) is substituted for $\partial c/\partial x$ in Equation (1). The term $\partial c/\partial t$ in Equation (1) is approximated by $\partial c_m/\partial t$, which can be replaced by $E(\partial^2 c_m/\partial x^2)$. Modified in this way Equation (1) is the basis of a development paralleling that in Equations (2) to (12). The result is a second-order approximation to the value of the

axial mixing coefficient (designated E'). For Schmidt numbers near 1.0 or Reynolds numbers greater than 10,000 the error in the first-order approximation for E is estimated from

$$\frac{E'}{DV} - \frac{E}{DV} = -\frac{2}{\lambda}\int_0^1 \left(\frac{u}{V} - 1\right) dz \cdot \int_1^z - \frac{\partial u/V\, dz'}{\partial z' z'} \cdot \int_0^{z'} \left\{\left(\frac{u}{V} - 1\right)\frac{c_m''}{c_m'}\frac{4a}{\lambda}\left[\Theta(z'') - \bar{\Theta}\right] - \frac{c_m'''}{c_m'}\frac{8a^2}{\lambda}\frac{E}{DV}\left(\frac{u}{V} - 1\right)^2 + \frac{E}{DV}\,2a\,\frac{c_m''}{c_m'}\right\} dz'' \qquad (18)$$

where c_m', c_m'', and c_m''' are used for the first, second, and third derivatives, respectively, with regard to x, and where

$$\Theta(z) = \int_0^z \frac{-\partial(uV)}{\partial z'}\frac{dz'}{z'} \cdot \int_0^{z'} \left(\frac{u}{V} - 1\right) dz'' \qquad (19)$$

and

$$\bar{\Theta} = \int_0^1 \Theta(z)\, dz \qquad (20)$$

For a given Reynolds number and friction factor, Equation (18) relates the approximate error in the plotted values of E/DV to the various axial derivatives of c_m, these derivatives being expressed in terms of pipe diameters. This error has been evaluated at two Reynolds numbers, as follows:

$$\left.\begin{aligned} &\text{For } N_{Re} = 10{,}000 \\ &\frac{E' - E}{E} = 2.8a\,\frac{c_m''}{c_m'} - 30a^2\,\frac{c_m'''}{c_m'} \\ &\text{For } N_{Re} = 205{,}000 \\ &\frac{E' - E}{E} = 3.7a\,\frac{c_m''}{c_m'} - 16a^2\,\frac{c_m'''}{c_m'} \end{aligned}\right\} \qquad (21)$$

It is seen that the accuracy of the first-order approximation depends on the shape and scale of the concentration wave along the pipe axis as characterized by the ratios a^2c_m''/ac_m' and a^3c_m'''/ac_m'. The term c_m''/c_m' in Equations (21) indicates that E' is greater on the back (upstream) side of a concentration pulse than on the front side; the experiments of Taylor (*18*) reveal such a "tailing off" behind a short concentration pulse.

The term c_m'''/c_m' does not change sign from the front to the back of the concentration pulse or contaminated region; i.e., c_m'''/c_m' is roughly symmetrical in x. This term therefore describes an over-all discrepancy between predicted values of E/DV and those obtained by experiments on gross spreading of material in pipes. Evaluation of this effect for the case of flow at a Reynolds number of 10,000 was made for three types of axial concentration profiles: error function (one liquid following another), sinusoidal (Keyes experiments), and error-function derivative (Taylor's pulse-injection experiments). It was found that Equation (12) could be applied with less than 25% error (less than the usual scatter of data in such work) to those cases of mixing in which the characteristic concentration length was greater than 50 to 100 pipe diameters. For smaller characteristic lengths, E/DV can be substantially larger than predicted by Equation (12).

Table 2. Effect of Axial Eddy Diffusivity

$N_{Re} \times 10^{-3}$	ϵ_{max}/DV	E/DV	ϵ_{max}/E
2.56	0.0079	1.64	0.005
4.0	0.0135	0.65	0.021
10.0	0.0105	0.38	0.028
205	0.0066	0.18	0.037
2800	0.0055	0.14	0.039

(The characteristic length is taken as the wave length for the case with sinusoidal variation of concentration, or as the "contaminated length" for the other two cases. *Contaminated length* is here defined as the length of the region in which the concentration is between 1 and 99% of the maximum concentration of either fluid.) It can therefore be concluded that the system studied by Keyes and likewise any practical pipe-line mixing problem will have axial concentration gradients of a size and variation that will allow treatment by this theory.

EFFECT OF AXIAL EDDY DIFFUSION

It is assumed in this development that the effects of axial turbulent diffusion are negligible when compared with the mixing caused by radial differences in the velocity. An estimate of the magnitude of axial turbulent diffusion can be obtained from the values of the radial turbulent diffusivity. In Table 2 the coefficients of axial mixing are compared with the values of the eddy diffusivity at the radial position where eddy diffusivity is greatest. In all cases the eddy diffusivity, ϵ, is seen to be negligible.

NOTATION

a = pipe radius
c = concentration
c_m = mean concentration across pipe cross section
c_m', c_m'', c_m''' = first, second, and third derivatives of c_m with respect to x
D = pipe diameter
$\mathbf{D}$ = molecular diffusion coefficient
E = effective axial mixing coefficient
E' = effective axial mixing coefficient calculated without neglect of radial variation of $\partial c/\partial x$
N_{Re} = Reynolds number, DV/ν
N_{Sc} = Schmidt number, $\nu/\mathbf{D}$
Q = net transport of solute past reference plane with velocity V
r = radial coordinate
t = time
u = time-averaged velocity at a point in the pipe
V = mean velocity across pipe
x = axial coordinate, reckoned from a reference plane moving with velocity V
z = transformed radial coordinate, $(r/a)^2$

Greek Letters

α = total effective radial diffusion coefficient, Equation (7)
ϵ_D = coefficient of eddy transport of mass
ϵ_m = coefficient of eddy transport of momentum
λ = friction factor (Moody)
λ_0 = friction factor in a smooth tube
ν = kinematic viscosity
ρ = density
τ = shear stress
τ_0 = shear stress at the wall

LITERATURE CITED

1. Allen, C. M., and E. A. Taylor, *Trans. Am. Soc. Mech. Engrs.*, **45**, 285 (1923).
2. Deissler, R. G., *Natl. Advisory Comm. Aeronaut. Technical Note* 2138 (1950).
3. Fowler, F. C., and G. G. Brown, *Trans. Am. Inst. Chem. Engrs.*, **39**, 491 (1943).
4. Hull, D. E., and J. W. Kent, *Ind. Eng. Chem.*, **44**, 2745 (1952).
5. Keyes, J. J., *A.I.Ch.E. Journal*, **1**, 305 (1955).
6. Kohl, J., and R. L. Newacheck, paper presented at the fall 1953 meeting of the Am. Soc. Mech. Engrs. Petroleum Division.
7. Laufer, John, *Natl. Advisory Comm. Aeronaut. Technical Note* 2954 (1953).
8. Nikuradse, J., *Forschungsheft* 356 (1932).
9. *Ibid.*, 361 (1933).
10. Reichardt, H., *Z. Ang. Math. u. Mech.*, **31**, 208 (1951).
11. Senecal, V. E., and R. R. Rothfus, *Chem. Eng. Progr.*, **49**, 533 (1953).
12. Shipley, J. R., *Pipe Line News*, p. 31 (December, 1951).
13. Sleicher, C. A., Ph.D. thesis, Univ. Michigan, Ann Arbor (1955).
14. Smith, S. S., and R. K. Schulze, *Petroleum Eng.*, p. 330 (October, 1948).
15. Stanton, T. E., *Proc. Roy. Soc.* (*London*), **A85**, 366 (1911).
16. Stirba, Clifford, and D. M. Hurt, *A.I.Ch.E. Journal*, **1**, 178 (1955).
17. Taylor, G. I., *Proc. Roy. Soc.* (*London*), **A219**, 186 (1953).
18. *Ibid.*, **A223**, 446 (1954).
19. *Ibid.*, **A225**, 473.

Reaction of Porous Solids

E. E. PETERSEN

University of California, Berkeley, California

A method is presented for the analysis of a reaction between a porous solid and a gaseous reactant where the kinetic expression is linear in the concentration and where appreciable concentration gradients are established in the pore system as a result of diffusive transport rate. Two cases are treated mathematically: a single cylindrical pore initially of uniform diameter and a porous solid initially containing uniform cylindrical pores with random intersections. The mathematical solutions to the latter case are used to interpret the experimental results reported in the literature on the gasification of graphite rods with carbon dioxide. Values of the computed effective diffusivity are an order of magnitude smaller than the bulk diffusivity at the same temperature and pressure.

Numerous heterogeneous reactions between a solid and a fluid phase have been studied, many of which are industrially important. In most instances it is desirable to increase the "reactivity" of the solid phase by dispersing it in a finely divided state or by developing a porous structure within the solid phase or by combinations of both in order to obtain a high specific surface area. In order to utilize the large surface area developed within solids, the reactant must be transported into the interior of the solid, where the major part of the reaction occurs, and the resultant products must be transported out. The important mechanism for transport is generally diffusion. However, solids with high specific surface areas are characterized by small pores, and appreciable concentration gradients are obtained in the pore system when the diffusive transport rates are large. These concentration gradients decrease the effectiveness for chemical reaction of each unit surface progressively more deeply within the interior of the solid. This paper is concerned with the quantitative description of the reaction between a porous solid and a fluid phase when concentration gradients occur within the pore system. Two cases will be considered: a single uniform pore and a porous cylindrical sample containing uniform cylindrical pores with random intersections.

Thiele (*7*) solved the analogous problem of heterogeneous reactions between porous catalysts and fluids in which the pore geometry of the solid phase was assumed to be independent of time. He solved the cases of uniform cylindrical pores for zero first and second order reactions and spheres with first order kinetics. The current literature on these systems is well summarized by Wheeler (*10*) and Weisz and Prator (*9*).

The unsteady state equation describing the simultaneous reaction and mass transport in a porous solid is

$$\frac{\partial C}{\partial t} = -\text{div}\,(-D\ \text{grad}\ C) - \text{div}\,(uC) - aR' \qquad (1)$$

where the terms on the right side of the equation refer to the diffusive transport, the convective transport, and a source or sink corresponding to chemical reaction The corresponding energy equation is not considered in this paper, as constant temperature is assumed throughout the solid phase. The radius of the pore is a function of position and time and appears in the divergence terms of Equation (1). Therefore, Equation (2) must be solved simultaneously with Equation (1).

$$\frac{\partial r}{\partial t} = \frac{M}{\rho_s} R' \qquad (2)$$

With the aid of Equations (1) and (2) the single-pore and cylindrical-rod cases will be considered individually. Each case will be subject to the following restrictions:

1. The convective term is dropped because the reaction yields no net change in number of moles or because the pore radii are so small that convective transport is small compared with diffusive transport.
2. The reaction is first order.
3. The pore walls are smooth. If the walls have a surface roughness σ, which is constant, the second term on the right becomes $(2\sigma kC)/r$.
4. The diffusivity is constant; therefore the equation does not apply in the Knudsen region for large changes in r.

All these restrictions can be removed, but the results tabulated in this paper are subject to the assumptions listed above.

SINGLE-PORE MODEL

A sketch of the single-pore model is shown in Figure 1. The initial pore is a long cylindrical pore of radius r_0 and length $2L$ where $L \gg r_0$. The concentration at either pore mouth is C_0 and constant. For this model Equation (1) becomes

$$\frac{\partial C}{\partial t} = \frac{D}{r^2}\frac{\partial}{\partial x}\left(r^2\frac{\partial C}{\partial x}\right) - \frac{2}{r}kC \qquad (3)$$

Equations (2) and (3) can be put in dimensionless form:

$$\frac{\partial \psi}{\partial \tau} = \frac{1}{\xi^2}\frac{\partial}{\partial \eta}\left(\xi^2\frac{\partial \psi}{\partial \eta}\right) - \alpha^2\frac{\psi}{\xi} \qquad (4)$$

where

$$\xi = \frac{r}{r_0},\ \eta = \frac{x}{L},\ \psi = \frac{C}{C_0},\ \tau = \frac{Dt}{L^2},$$

and

$$\alpha = L\sqrt{\frac{2k}{r_0 D}}.$$

$$\frac{\partial \xi}{\partial \tau} = \frac{M}{2\rho_s}\alpha^2 C_0 \psi \qquad (5)$$

Equations (4) and (5) can be solved numerically, but in order to keep the solution stable an unreasonably large number of iterations would be required. However, it is apparent from the physical picture and can be justified mathematically* that, although an unsteady state solution to Equations (4) and (5) is required, the concentrations within the pore very rapidly approach a steady state profile; that is, before any significant amount of material is reacted from the pore wall the concentration profile has approached the steady state solution for a uniform pore of radius r_0. Then as material is removed from the pore walls, the concentration profile within the pore is almost exactly identical with the steady state profile. This simplification greatly reduces the time required to obtain solutions because Equation (4) is now an ordinary nonlinear differential equation and is solved numerically by computing the steady state concentration profile in the initial pore by Equation (6) below:

$$\frac{1}{\xi^2}\frac{d}{d\eta}\left(\xi^2\frac{d\psi}{d\eta}\right) - \alpha^2\frac{\psi}{\xi} = 0 \qquad (6)$$

The new pore-radius profile is computed from the concentration profile by use of Equation (5). The steady state concentration profile is then computed for the new pore-radius profile, and so on.

The problem now is to solve Equation (6) with boundary conditions:

$$\psi(0) = 1;\quad \left.\frac{d\psi}{d\eta}\right|_{\eta=1} = 0 \qquad (7)$$

This can be numerically handled very conveniently by matrix algebra. If the η coordinate is arbitrarily divided into m intervals where $m = 0$ is at the pore mouth, in finite-difference form Equation (6) can be expressed as

$$a_m\psi_{m+1} + b_m\psi_m + d_m\psi_{m-1} = 0 \qquad (8)$$

where m takes values of $1, 2, 3, \cdots m$ and

$$a_m = 1 + \frac{\xi_{m+1} - \xi_{m-1}}{2\xi_m}$$

*See Appendix I.

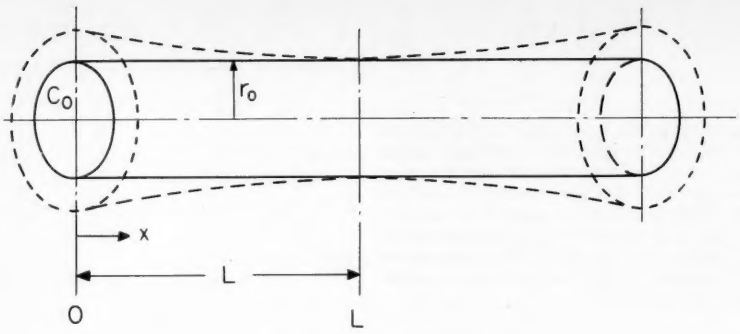

Fig. 1. Single-pore model.

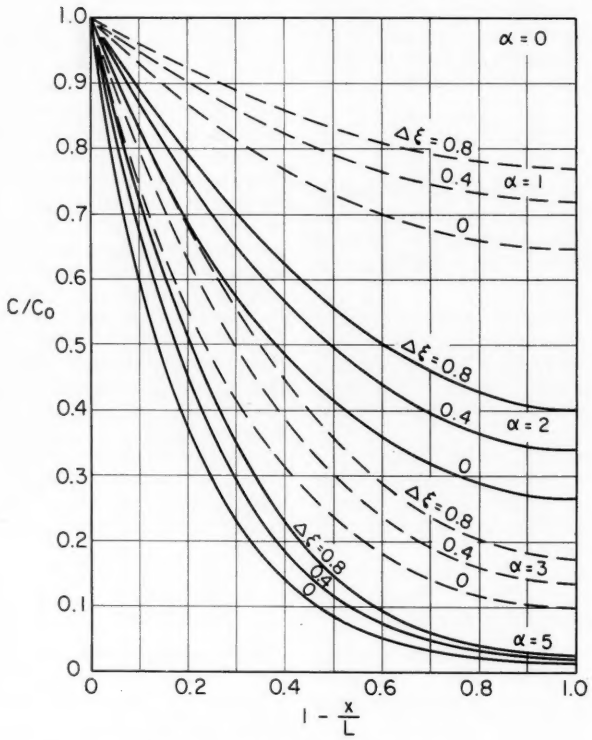

Fig. 2. Concentration profiles within single pore.

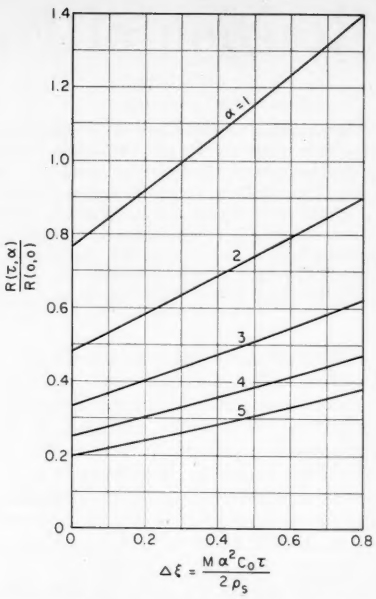

Fig. 3. Relative reaction rates as a function of time for various values of the parameter α for single-pore model.

$$(\psi) \equiv \begin{bmatrix} \psi_1 \\ \psi_2 \\ \psi_3 \\ \cdot \\ \cdot \\ \cdot \\ \psi_m \end{bmatrix} \quad \text{and} \quad (B) \equiv \begin{bmatrix} -d_1 \\ 0 \\ 0 \\ 0 \\ \cdot \\ \cdot \\ \cdot \end{bmatrix}$$

The solution to the equations above can be represented by Equation (10):

$$(\psi) = (A^{-1})(B) \qquad (10)$$

where (A^{-1}) is the inverse matrix of (A). The inversion for this particular case can be accomplished by the method of cofactors (3).

A finite-difference form of Equation (5) is given below:

$$\xi_{m,\tau+\Delta\tau} - \xi_{m,\tau} = \frac{M}{2\rho_s}\alpha^2 C_0 \psi \Delta\tau$$

$$= \Delta\xi_m$$

$$b_m = -\left[2 + \frac{\alpha^2 \Delta\eta^2}{\xi_m}\right]$$

$$d_m = 1 - \frac{\xi_{m+1} - \xi_{m-1}}{2\xi_m}$$

One has m equations given by Equation (8) and two boundary conditions of Equation (7) which can be written compactly in the matric equation below:

$$(A)(\psi) = (B) \qquad (9)$$

where

$$(A) \equiv \begin{bmatrix} b_1 & a_1 & 0 & 0 & 0 \cdots & & & \\ d_2 & b_2 & a_2 & 0 & 0 & 0 \cdots & & \\ 0 & d_3 & b_3 & a_3 & 0 & 0 \cdots & & \\ 0 & 0 & d_4 & b_4 & a_4 & 0 \cdots & & \\ \cdots & \cdots & \cdots & \cdots & \cdots & \cdots & \cdots & \cdots \\ & & \cdots 0 & 0 & d_{m-2} & b_{m-2} & a_{m-2} & 0 \\ & & \cdots 0 & 0 & 0 & d_{m-1} & b_{m-1} & a_{m-1} \\ & & \cdots 0 & 0 & 0 & 0 & a_m + d_m & b_m \end{bmatrix}$$

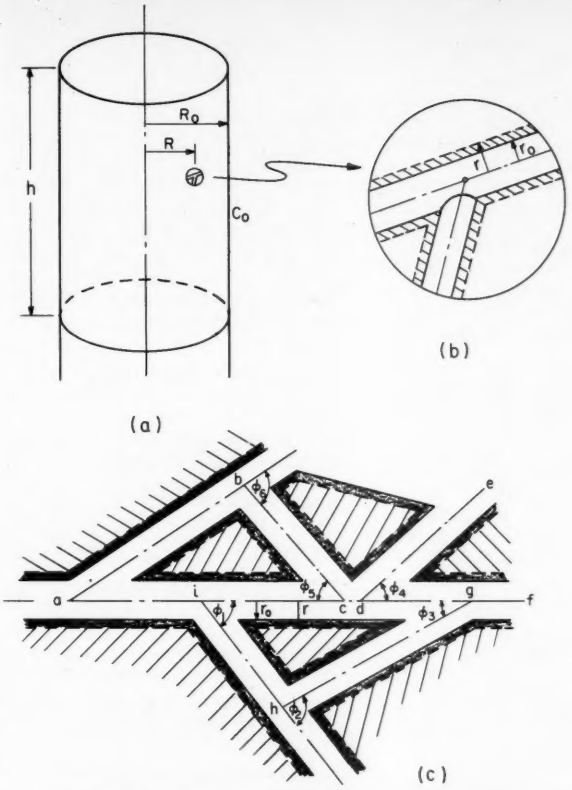

Fig. 4. Model of porous solid with random intersections.

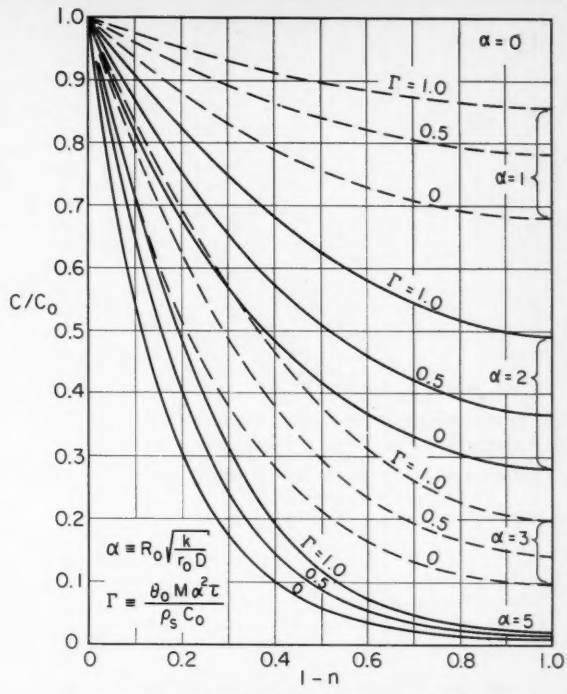

Fig. 5. Concentration profiles within porous-solid model.

If $\Delta\xi_0$ = the change in radius at the pore mouth in time τ, then

$$\frac{\Delta\xi_m}{\Delta\xi_0} = \frac{\psi_m}{\psi_0}$$

$$\Delta\xi_m = \left(\frac{\psi_m}{\psi_0}\right)\Delta\xi_m. \qquad (11)$$

The numerical computations were made on the IBM type 650 magnetic drum computer. The computer program made provision for changing the number of space and time intervals, the values of which were chosen so that the absolute error of the computed concentration profiles is within about 1%.

The results of these computations are shown in Figures 2 and 3. In Figure 2 the concentrations at various depths within the pore are shown. The concentration profiles for $\tau = 0$ are the same as given by Thiele (7). As the pore enlarges owing to reaction, the concentration progressively increases at points within the interior. The rates at which single pores react are shown in Figure 3. The ordinate is the ratio of the rate at which the pore reacts to that which would be obtained in the initial pore if the area of the pores was completely accessible at unit concentration. The abscissa is a dimensionless time obtained from Equation (5) and corresponds to the fractional change in pore radius at time τ. Again, the values at $\tau = 0$ correspond to the solutions obtained by Thiele (7).

The results of the single-pore model are useful in predicting general behavior; however, they do not possess certain characteristics of porous materials. For example, the rates in Figure 3 would continue to increase with time, whereas the rate of reaction of a porous solid would go through a maximum owing to the eventual decrease in the sample area as the sample disappears. To get this observed behavior a model must be used which considers every pore in the system and its spatial relation to other pores.

CYLINDRICAL PELLET MODEL

In a long cylindrical rod of radius R_0 and of length h, containing cylindrical pores initially of uniform radius r_0, intersecting each other randomly as shown in Figure 4, the dimensions of the solid are such that $h \gg R_0 \gg r_0$. If the structure of the solid is initially of uniform porosity θ_0 and the pores are distributed randomly throughout the solid, an arbitrary plane passed through the sample will have a fraction θ_0 corresponding to pores and the remainder $1 - \theta_0$ corresponding to solid, provided that the arbitrary plane is large enough to intersect a statistical number of pores. In order to solve Equation (1), a relationship between the pore radius r and the porosity θ must be obtained.

The required relationship between θ and r can be obtained by assuming that the differential volume used to develop Equation (1) can be represented by the idealized network of pores shown in Figure 4c. Since the concentration is constant, the pores increase from r_0 to r uniformly throughout the differential volume. The length of the pore system per unit volume L is defined as the sum of the center-line distances of the pores; i.e.,

$$L = ab + bc + cd + gh + \cdots$$

and N = the number of pore intersections per unit volume. If the pores enlarge uniformly, then the surface area of the smooth pores of radius r is given by

$$S = 2\pi r\left[L - r\sum_{i=1}^{N}\left(\frac{1}{\sin\phi_i}\right)\right] - r^2\sum_{i=1}^{N}\beta(\phi_i) \qquad (12)$$

where the second term on the right accounts for the area of the openings in the pore walls and $\beta(\phi_i)$ is a shape factor of the ith intersection based on the angle ϕ_i. The term

$$\sum_{i=1}^{N}\left(\frac{1}{\sin\phi_i}\right)$$

accounts for the shortening of the actual length of the pore as the intersection enlarges. If no new pore intersections are

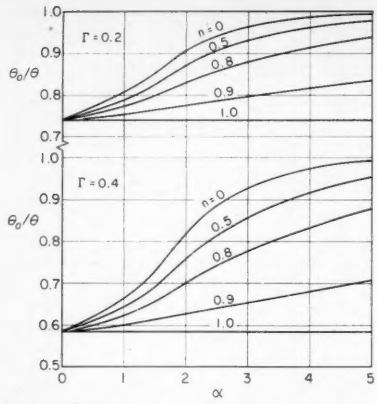

Fig. 6. Dependence of the reduced porosity on the parameter α at various reduced radii.

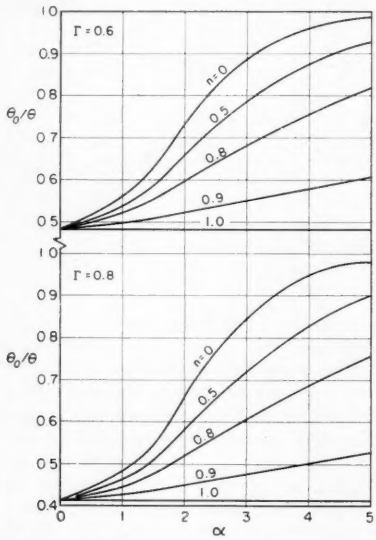

Fig. 7. Dependence of the reduced porosity on the parameter α at various reduced radii.

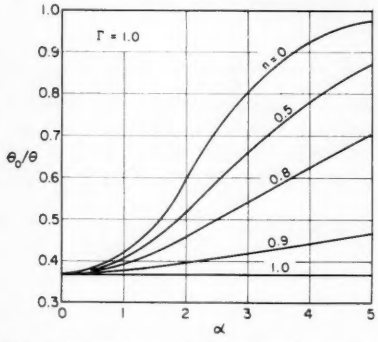

Fig. 8. Dependence of the reduced porosity on the parameter α at various reduced radii.

produced, the terms

$$\sum_{i=1}^{N}\left(\frac{1}{\sin\phi_i}\right) \quad \text{and} \quad \sum_{i=1}^{N}\beta(\phi_i)$$

are constant for a given solid and are abbreviated by A and B, respectively.

$$\therefore\ S = 2\pi r(L - Ar) - Br^2 \qquad (13)$$

$$\therefore \int_0^{\theta} d(\theta')$$

$$= \int_0^{r} [2\pi y(L - Ay) - By^2]\, dy \qquad (14)$$

$$\theta = L\pi r^2 - \left(\frac{2\pi A + B}{3}\right) r^3 \qquad (15)$$

$$\frac{\theta}{\theta_0} = \frac{\pi L r^2 - \left(\frac{2\pi a + B}{3}\right) r^3}{\pi L r_0^{\,2} - \left(\frac{2\pi A + B}{3}\right) r_0^{\,3}} \qquad (16)$$

which reduces to

$$\frac{\theta}{\theta_0} = \xi^2\left(\frac{G - \xi}{G - 1}\right) \qquad (17)$$

where

$$G \equiv \frac{3\pi L}{r_0(2\pi A + B)}$$

To evaluate G, Equation (17) is assumed valid from $\theta = 0$ to $\theta = 1$. As $\theta \to 1$, $S \to 0$. Therefore

$$\frac{d\theta}{d\xi} = 2\xi\left(\frac{G - \xi}{G - 1}\right) - \xi^2\left(\frac{1}{G - 1}\right) \qquad (18)$$

$$\therefore \qquad 2(G - \xi) - \xi = 0$$

$$\xi = \frac{2G}{3} \qquad (19)$$

Substituting Equation (19) into Equation (17) and solving for G gives

$$G^3 - \frac{27}{4\theta_0} G + \frac{27}{4\theta_0} = 0 \qquad (20)$$

Many solids have porosities between 0.30 and 0.40. The particular samples for which data were available had an initial porosity θ_0 of 0.303. Using the value of $\theta_0 = 0.303$ in Equation (20) gives a value of $G = 4.105$. This value of G in Equation (17) gives the required relationship between θ and ξ.

In cylindrical coordinates Equations (1) and (2) become

$$\frac{\partial C}{\partial t} = \frac{D}{\theta R}\frac{\partial}{\partial R}\left(\theta R \frac{\partial C}{\partial R}\right) - akC \qquad (21)$$

$$\frac{\rho_s}{M\theta}\frac{d\theta}{dt} = kaC \qquad (22)$$

where a = the area per unit volume of pores. From Equations (17) and (18),

$$a = \frac{d\theta}{\theta r_0\, d\xi}$$

$$= \frac{(2G - 3\xi)}{r_0\xi(G - \xi)} \qquad (23)$$

In dimensionless form Equations (21) and (22) are

$$\frac{\partial \psi}{\partial \tau} = \frac{1}{\theta\eta}\frac{\partial}{\partial \eta}\left(\theta\eta \frac{\partial \psi}{\partial \eta}\right)$$

$$- \alpha^2\left(\frac{2G - 3\xi}{\xi(G - \xi)}\right)\psi \qquad (24)$$

and

$$\frac{d\xi}{d\tau} = \frac{\theta_0 M}{\rho_s}\alpha^2 C \qquad (25)$$

where

$$\alpha^2 = \frac{R_0^{\,2}k}{r_0 D}, \quad \tau = \frac{Dt}{R_0^{\,2}}, \quad \xi = \frac{r}{r_0},$$

$$\eta = \frac{R}{R_0}, \quad \text{and} \quad \psi = \frac{C}{C_0}$$

The rate of reaction per unit length of sample at any time τ is

$$\Re(\tau) = -2\pi R_0 \theta D\left(\frac{\partial C}{\partial R}\right)_{R_0}$$

$$= -2\pi\theta C_0 D\left(\frac{\partial \psi}{\partial \eta}\right)_{R_0 = 1} \qquad (26)$$

If the entire surface of the sample is available, the initial rate of reaction per unit length of sample is

$$\Re(0) = \frac{\pi R_0^{\,2} k\theta_0(2G - 3)C_0}{r_0(G - 1)} \qquad (27)$$

Therefore

$$\frac{\Re(\tau, \alpha)}{\Re(0, 0)} = -\frac{2}{\alpha^2}\frac{\xi^2(G - \xi)}{2(G - 3)}\left(\frac{\partial \psi}{\partial \eta}\right)_{R_0 = 1} \qquad (28)$$

Numerical solutions to Equations (17), (24), (25), and (28) were obtained by the numerical method outlined earlier. The numerical results are shown in Figures 5 through 9 in terms α, τ, ξ, η and a new parameter Γ defined by

$$\Gamma \equiv \frac{\theta_0 M\alpha^2 C_0 \tau}{\rho_s}$$

or

$$= \frac{\theta_0 M k C_0 t}{\rho_s r_0} \qquad (29)$$

From Equation (25) it is clear that Γ corresponds to the change in reduced pore radius at the pore mouth; i.e., at $\Gamma = 1.0$, the value of the pore radius at the pore mouth has doubled.

Figure 5 shows the concentration profiles as functions of α and Γ. The concentration profiles for $\Gamma = 0$ can be checked by an analytical solution, as this corresponds to cases where the pores are uniform and $\xi = 1$. The initial steady state concentration profiles are given by the solution to Equation (30) below.

$$\frac{d^2\psi}{d\eta^2} + \frac{1}{\eta}\frac{d\psi}{d\eta} - \beta^2\psi = 0 \qquad (30)$$

where

$$\beta^2 = \frac{\alpha^2(2G - 3)}{(G - 1)}$$

The solution to Equation (24) for the boundary conditions

$$\left.\frac{\partial \psi}{\partial \eta}\right|_{\eta = 0} = 0$$

and $\psi(1) = 1$ is

$$\psi = \frac{J_0(i\beta\eta)}{J_0(i\beta)} \qquad (31)$$

Values of the center-line concentration obtained numerically and from Equation (31) agree to within 1% for the values of α reported.

The extent of reaction at various depths within cylindrical samples, represented by the porosity ratio θ_0/θ, is shown in Figures 6, 7, and 8 as a function of Γ and α. The integral rates of reaction $\Re(\tau)$, i.e., the summation of the point values of reaction over the solid, are given in Figure 9 in terms of Γ, α, and $\Re(0)$. In the range of Γ from 0 to 1, the integral reaction rate goes through a maximum for values of α up to 4. Values of the relative reaction can be computed analytically for the case of $\Gamma = 0$ by differentiating Equation (31) in placing the value of the gradient at $\eta = 1$ in Equation (28). The relative rate becomes

$$\frac{\Re(0, \alpha)}{\Re(0, 0)} = \frac{2}{\beta}\frac{iJ_1(i\beta)}{J_0(i\beta)} \qquad (32)$$

The relative rates obtained numerically and from Equation (32) agree to within 0.6% for the values of α reported.

The equations and method of solution presented herein can be used to interpret the reaction between a porous solid and a gaseous reactant where the kinetic expression is or can be reduced to a linear function of concentration. The particular set of numerical results presented in Figures 5 through 9 is limited to solids having initial porosity of 0.3.

ILLUSTRATIVE EXAMPLE

The computed results based on the pellet model can be used to interpret the experiments of Petersen and Wright (*5*) on the gasification of graphite at 1,100°C. with carbon dioxide at 1 atm. pressure. Rao (*6*) further studied the graphite–carbon dioxide reaction under conditions similar to those used by these workers. According to his results the reaction appeared to follow closely first-order kinetics with respect to carbon dioxide concentration and showed no poisoning effects by carbon monoxide under these conditions. Figure 10 summarizes the bulk-density-profile measurements made on 2- by ½-in.-diameter rod samples (*5*) reacted to weight losses of 0.63, 1, 2 and 3.26 g. in 29, 47, 86 and 129 min. of reaction time, respectively. The curves of Figure 10 are extrapolated to θ_0/θ at $\eta = 1$ and converted to values of ξ at the pore mouths by use of Equation (17). Figure 11 shows values of ξ vs. t. It will be observed that the relationship is nonlinear and in this respect does not correspond to the model assumed. If Equation (25) is rearranged, the slope of this plot can be related to the intrinsic reactivity and several constants:

$$\frac{d\xi}{dt} = \frac{\theta_0 M}{\rho_s}\frac{k}{r_0}C_0 \qquad (33)$$

where $\psi = 1$ at the pore mouth. Accordingly, the intrinsic reactivity k at the pore mouth can be computed from the slope of ξ vs. t curve in Figure 11. The variation of k can be independently estimated by selecting the value of α which most satisfactorily correlates the measured bulk-density curves and assuming that the diffusivity is constant. The latter method is only approximate because the numerical solutions to the differential equations are based upon α remaining constant during the integration. The value of α should be selected by matching curves near $\eta = 1$ and should give a predicted bulk-density profile lying slightly below the experimental line. Relative values of k were computed by the two methods given above at four values of the reaction time, and the methods agreed to within about 10%.

The magnitude of the effective diffusivity D_{eff} can be estimated from the α and k/r_0. After 47 min. of reaction time

$$\left(\frac{d\xi}{dt}\right)_{n=1} = 0.0054 \text{ min}^{-1}$$

and

$$\frac{k}{r_0} = \frac{\rho_s}{M\theta_0 C_0}\left(\frac{d\xi}{dt}\right)_{n=1}$$

$$= \frac{(2.22)(22{,}414)(1373)(0.0054)}{(12.01)(0.303)(273)(60)}$$

$$= 6.20 \text{ sec}^{-1}$$

The corresponding value of α is about 4.3; therefore

$$D_{eff} = \frac{R_0^2 k}{\alpha^2 r_0}$$

$$= \frac{(2.54)^2(6.2)}{(4)(4.3)^2}$$

$$= 0.135 \text{ sq. cm./sec.}$$

The magnitude of D_{eff} computed by this method does not compare favorably with bulk diffusivity D_B of 2.13 sq. cm./sec. calculated by the method given by Hirschfelder, Curtiss and Bird (*1*) for the CO_2–CO system at 1,373°K. Small values of the ratio D_{eff}/D_B have been reported in the literature. Hoogschagen (*2*) discusses values of this ratio obtained from his own experiments as well as those from other investigators. Walker and coworkers (*8*) reported an experimental value of D_{eff} equal to 0.046 sq. cm./sec. (at standard temperature and pressure) for similar graphite material in a system containing an H_2–N_2 mixture. From this experimental value one can estimate the D_{eff} for the CO_2–CO system at 1,373°K. by the ratio of D_B for the CO_2–CO system at 1,373°K. to D_B of the H_2–N_2 system at standard temperature and pressure. The estimated D_{eff} is therefore 0.145 sq. cm./sec., which is very close to the value obtained in this work.

A somewhat higher value of D_{eff} can be obtained if a "tortuosity factor" is included in the definition of α to allow for the fact that the axes of pores are not perpendicular to cylinder axis. The latter is assumed when R is used as an independent variable in Equation (21). The inclusion of a tortuosity factor ζ would change this variable to ζR. Values of ζ greater than 2 are difficult to justify on theoretical grounds. If a tortuosity factor had been used in this analysis, the D_{eff} calculated would be increased by a factor of ζ^2.

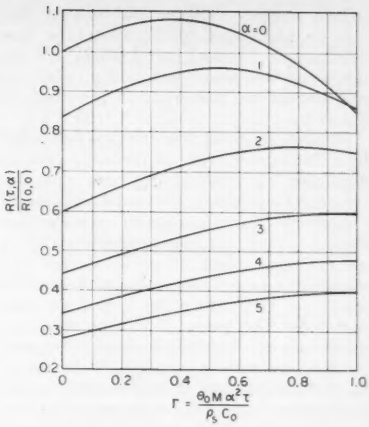

Fig. 9. Relative reaction rates as a function of time for various values of the parameter α for porous-solid model.

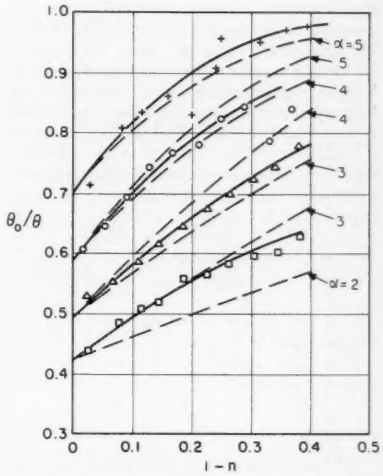

Fig. 10. Comparison of reduced porosity profiles computed from porous-solid model with those experimentally measured for the reaction of graphite rods with carbon dioxide at 1,100°C.

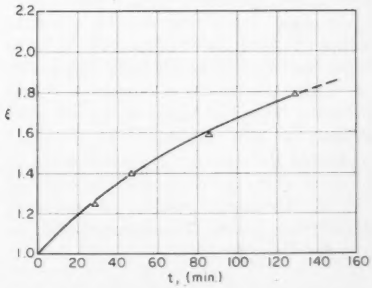

Fig. 11. Reduced radius at pore mouth as a function of time for reaction between graphite rods and carbon dioxide at 1,100°C.

It is unlikely that the low value of D_{eff} can be attributed to Knudsen-type flow because the mean pore radius in the unreacted samples is about 2 μ, with the majority of the pore radii in the range of 0.5 to 4 μ (*4*).

The low magnitude of the D_{eff} computed from the α and k/r_0 can probably best be explained by reexamining how well the structural features of the model and sample correspond. The graphite rods are made from ground petroleum coke particles with a rather large range of particle sizes (*4*), which are bound together with coal-tar pitch and heat treated at very high temperatures. The pores of this material are made up of interstitial spaces between particles and vary in "diameter" and shape. In the replacement of this system by an "equivalent" system of uniform cylindrical pores characterized by an average diameter, it is not surprising that the diffusivity necessary to give the correct rate of mass transport is much smaller than the bulk diffusion coefficient normally calculated at the temperature and pressure at which the experiment is carried out.

The integral reaction rates can be calculated from Figure 9 and compared with the experimental value. After 47 min. of reaction time the integral reaction rate of the graphite samples was 1.53 g./hr. According to Equation (27), if the entire sample surface had been available the rate of reaction would have been 7.75 g./hr. From Figure 9 $\Re(\tau)/\Re(0) = 0.4$ at values of $\Gamma = 0.4$ and $\alpha = 4.3$. If a correction is made to allow for the variation of k with reaction, the predicted rate for this sample is

$$\Re(\tau) = \frac{(7.75)(0.0054)(0.4)}{(0.01)} = 1.66\,\text{g./hr.}$$

where the values of 0.0054 and 0.01 are proportional to k at 47 and 0 min., respectively. The agreement between the estimated and observed rates is satisfactory.

SUMMARY

The method used in this paper to solve the differential equation for simultaneous diffusion and chemical reaction can be applied to systems where the kinetic term is linear in concentration. The numerical results presented herein are valid for materials with an initial uniform porosity of 0.3. The interpretation of the experimental gasification results between graphite and carbon dioxide making use of the pore model described in this paper indicates that the value of the effective diffusivity is an order of magnitude lower than the corresponding bulk diffusivity calculated at the same temperature and pressure. This low value of the effective diffusivity will probably be obtained whenever the real pore system containing pores of varying "diameters" is replaced by an idealized system of uniform, cylindrical pores characterized by an average diameter.

ACKNOWLEDGMENT

The author wishes to express his appreciation to Dr. Theodore Vermeulen and Dr. Andreas Acrivos for their helpful discussions concerning this work.

APPENDIX I

For very short reaction times, Equation (4) reduces to

$$\frac{\partial \psi}{\partial \tau} = \frac{\partial^2 \psi}{\partial \eta^2} - \alpha^2 \psi \qquad (34)$$

where $\xi \approx 1$. The solution to Equation (34) can be compared to the corresponding steady state solution, and if the concentration at a depth L within the pore approaches the steady state value before appreciable increase in ξ occurs at the pore mouth, then the solution based upon a series of secular steady state concentration profiles is a close approximation of the solution to unsteady state partial-differential equations.

The solution to Equation (34) at $\eta = 1$, for the boundary conditions given in Equation (7) and the initial condition that $\psi = 0$ for all η at $\tau = 0$ is given by

$$\psi(\tau, \eta) = \frac{\cosh\{\alpha(1-\eta)\}}{\cosh\alpha} - \frac{4}{\pi}\sum_{n=0}^{\infty} \frac{(-1)^n \exp\left\{-\left[\frac{\alpha^2 - (2n+1)^2\pi^2}{4}\right]\tau\right\} \cos\left\{\frac{(2n+1)(1-\eta)\pi}{2}\right\}}{(2n+1)\left[1 + \frac{4}{(2n+1)^2\pi^2}\right]} \qquad (35)$$

The corresponding steady state equation is

$$\psi(\infty, \eta) = \frac{\cosh\{\alpha(1-\eta)\}}{\cosh\alpha} \qquad (36)$$

The fractional approach to steady state at some time τ is given by the quotient of Equations (35) and (36), which for the case of $\alpha = 1$, $\eta = 1$, and $\tau = 10$, reduces to

$$\frac{\psi(10, 1)}{\psi(\infty, 1)} = 0.99999$$

However, during the interval $\tau = 10$, the fractional change in $\Delta\xi$ at the pore mouth as given by Equation (5) is

$$\frac{\Delta\xi}{\xi} = \frac{M}{2\rho_s}(\alpha^2)C_0\psi(\Delta\tau) = \frac{(12.01)(1)(273)(10)}{(2)(2.22)(22{,}414)(1{,}373)} = 2.4 \times 10^{-4}$$

for the conditions of the graphite–carbon dioxide reaction used as an example in this paper. For $\alpha = 5$, $\psi(10, 1)/\psi(\infty, 1) = 0.999994$ and $\Delta\xi/\xi = 6 \times 10^{-3}$. Therefore, the secular steady state solutions presented in this paper are valid except for extremely high values of C_0 and M/ρ_s.

NOTATION

a = specific surface area, area per unit volume of pores
C = concentration of reactant
C_0 = concentration of reactant at pore mouth
D = diffusion coefficient
G = constant
k = intrinsic reactivity
L = half pore length
M = molecular weight
N = number of pore intersections per unit volume of solid
r_0 = initial pore radius
r = pore radius
R' = reaction rate per unit surface area
$\Re$ = integral reaction rate
s = surface area of sample per unit volume of solid
t = time
u = average bulk gas velocity in pores
x = distance from pore mouth

Greek Letters

α = dimensionless parameter, $L\sqrt{\frac{k}{r_0 D}}$ or $R_0\sqrt{\frac{k}{r_0 D}}$
β = constant
$\beta(\phi_i)$ = shape factor
Γ = dimensionless parameter, $\theta_0 M k C_0 t/\rho_s r_0$
ξ = reduced pore radius, r/r_0
η = reduced radius, R/R_0
ϕ_i = angle of intersection of ith pore
ψ = reduced concentration, C/C_0
θ = porosity
θ_0 = initial porosity
ρ_s = density of solid phase
ζ = "tortuosity factor"
σ = surface roughness
τ = reduced time, Dt/L^2 or Dt/R_0^2
J_0 = Bessels function of 1st kind, zero order
J_1 = Bessels function of 1st kind, first order
div = divergence operator
grad = gradient operator

LITERATURE CITED

1. Hirschfelder, J. O., C. F. Curtiss, and R. B. Bird, "Molecular Theory of Gases and Liquids," John Wiley and Sons, New York (1954).
2. Hoogschagen, Jan, *Ind. Eng. Chem.*, **47**, 906 (1955).
3. Michael, A. D., "Matrix and Tensor Calculus," John Wiley and Sons, New York (1947).
4. Petersen, E. E., *Ind. Eng. Chem.*, **47**, 1630 (1955).
5. ———, and C. C. Wright, *ibid.*, p. 1,624.
6. Rao, P. V. N. Ramachandra, M.S. thesis, Univ. Calif., Berkeley (1954).
7. Thiele, E. W., *Ind. Eng. Chem.*, **31**, 916 (1939).
8. Walker, P. L., Jr., Frank Rusinko, Jr., and Emile Raats, *J. Phys. Chem.*, **59**, 245 (1955).
9. Weisz, P. B., and C. D. Prator, "Advances in Catalysis," vol. VI, Academic Press, Inc., New York (1954).
10. Wheeler, A., *ibid.*, vol. III (1951).

Diffusion Coefficients in Hydrocarbon Systems: Methane in the Liquid Phase of the Methane–*n*-Heptane System

H. H. REAMER and B. H. SAGE

California Institute of Technology, Pasadena, California

The production and refining of petroleum involve many processes in which conditions deviate markedly from equilibrium. For prediction of the behavior of such nonequilibrium systems, information concerning the molecular-transport characteristics of the paraffin hydrocarbons is of practical interest.

Fick diffusion coefficients for methane were measured in the liquid phase of the methane–*n*-heptane system at temperatures between 40° and 340°F. at pressures up to 3,500 lb./sq. in., but the pressure range was limited at the higher temperatures by approach to the critical state of this binary system.

The measurements obtained confirmed the fact that the Fick diffusion coefficients for methane decrease with an increase in the concentration of this component and increase rapidly with an increase in temperature for a constant composition. These data together with similar information for other binary paraffin hydrocarbon systems indicate that the Fick diffusion coefficients for methane decrease with an increase in the molecular weight of the less volatile component.

A knowledge of the molecular transport in hydrocarbon liquids is useful in predicting behavior under nonequilibrium conditions, but the experimental background regarding diffusion in hydrocarbon liquids is limited. Pomeroy (*10*), Hill (*5, 6*) and Bertram (*2*) investigated the diffusion of methane and propane into a number of hydrocarbon liquids at pressures below 500 lb./sq. in., Kirkwood (*7*) reviewed the relationship of molecular transport, and Drickamer (*21, 22*) reported numerous investigations of molecular transport in and between liquid and gas phases and found a resistance to material transport at the interface.

Measurements were made of the Fick diffusion coefficients for methane in the liquid phase of the methane–*n*-decane (*13*) and the methane–*n*-pentane systems (*11*) for pressures up to within 500 lb./sq. in. of the critical pressures at temperatures from 40° to 280°F. Similar measurements were reported for methane in the liquid phase of the methane–*n*-butane system (*14*) at pressures up to nearly 2,000 lb./sq. in. in the temperature interval between 10° and 220°F. The current study presents measurements of the Fick diffusion coefficient for methane in the liquid phase of the methane–*n*-heptane system. In this instance data were obtained at temperatures from 40° to 340°F. and at pressures up to 3,500 lb./sq. in. At the higher temperatures it was not possible to reach this pressure because of approach to the critical pressure (*16*) of the system.

METHODS AND APPARATUS

The method employed was similar to that used by Pomeroy (*10*) and involved the measurement of the rate of introduction of methane into a quiescent, heterogeneous, isochoric mixture of methane and *n*-heptane. The heterogeneous system was brought to equilibrium at a chosen state and the pressure of the quiescent system was then increased rapidly to a predetermined level. The quantity of methane required to maintain the variable-weight system under isobaric-isothermal conditions was determined as a function of time. A description of the equipment and the method of interpretation of the results is available in reference *13*.

The quantity of methane introduced was determined by means of a volumetric injector (*13*) operated at a known rate by a motor, the speed of which was controlled by a quartz oscillator (*15*). Experience indicated that uncertainty in the introduction of methane was less than 0.1% of the total quantity added during the period of measurement. The quantity of *n*-heptane employed was determined gravimetrically by weighing-bomb techniques (*19*). The uncertainty in the quantity of *n*-heptane introduced was less than 0.05%.

Pressure in the isochoric diffusion vessel was determined by means of a balance (*19*) with a probable error of 0.1 lb./sq. in. or 0.05%, whichever was the larger measure of uncertainty. Variations in pressure during the diffusion process were less than 0.2 lb./sq. in. Temperatures were measured with platinum resistance thermometers of the strain-free type (*8*), which were compared with reference resistance thermometers calibrated by the National Bureau of Standards. The temperature of the bath within which the diffusion vessel was located was controlled with a variation of less than 0.005°F. The calibration of the resistance thermometers was made with sufficient care and frequency so that the temperature of the system was related to the international platinum scale within 0.02°F. Somewhat larger uncertainties in temperature may have existed during the short period required to raise the pressure from the initial to the final value. Time intervals during the sequence of measurements were established with an uncertainty of 3 sec.

Experimental measurements yielded values of the weight of methane introduced into the isochoric vessel as a function of time. The Fick diffusion coefficient was related to the average conditions obtaining during such measurements in the following way (*13*):

$$D^*_{F,k} = \left[\frac{(1+\bar{V}^*_{i,l}c_{i,l}+\bar{V}^*_{k,l}c_{k,l})}{(1+\bar{V}^*_{i,l}c_{i,l})^*\left(1+\frac{c_k}{c_i}\right)^*}\right] \cdot \left[\frac{\pi m_k^{\,2}}{4\theta(c_{k,i,e}-c_{k,0})^2}\right] \cdot \left[\frac{\bar{V}^*_{k,g}}{\bar{V}^*_{k,g}-\bar{V}^*_{k,l}}\right]^2 \qquad (1)$$

Local equilibrium was assumed (*7*) and the first and third brackets of Equation (1) could be evaluated from available equilibrium data (*9, 16*). The first bracket is a correction for the hydrodynamic velocity (*13*) in the liquid phase. This velocity cor-

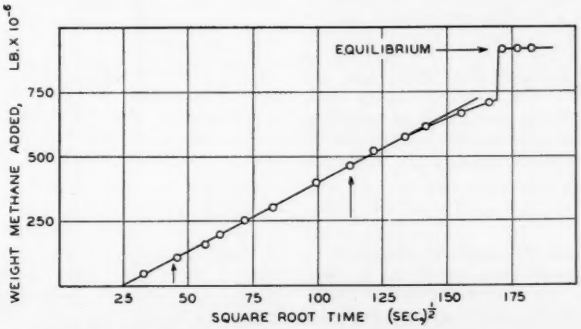

Fig. 1. Typical experimental measurements at 160°F.

Table 1. Sample of Detailed Experimental Measurements

Pressure, lb./sq. in. abs.	Weight fraction methane	Time, sec.	Weight of methane added, lb.
		160°F.	
411.0*	0.020	0	
766.2†	0.039	510	—
		1050	49.871×10^{-6}
		2070	110.662
		3190	160.532
		3880	201.303
		5100	251.902
		6860	307.232
		9880	400.421
		12690	466.309
		14860	521.276
		17940	575.879
		20410	614.464
		24090	668.339
		27600	708.018
		29480	911.868
		31420	911.868
		33380	911.868

*Initial equilibrium pressure.
†Pressure remained constant throughout the measurements.

responds to the momentum of the fluid during diffusion. The second bracket involves the measurements of the weight of methane as a function of time and is obtained from the diffusion data. The third bracket represents a correction to the weight of material introduced into the isochoric vessel to establish that crossing the liquid-gas interface. Detailed discussion of the derivation of Equation (1) is available (*13*).

More complicated expressions taking the resistance at the interface into account are also available (*13*). Experience with measurements of this type indicates that the resistance at the interface for similar systems (*20*) is so small that it can safely be neglected in these studies. The deviation from the linear relationship between the weight of methane transported across the interface and the square root of time was sufficiently small to confirm this point of view. The resistance of the gas phase may be disregarded, since, if local equilibrium (*7*) exists, the composition on the liquid-phase side of the interface is solely a function of the prevailing temperature and pressure.

A typical record of the experimental data obtained in a particular situation is depicted in Figure 1 for a temperature of 160°F. The standard deviation of the experimental points from a straight line was 5.2×10^{-6} lb. for the time period indicated between the two vertical arrows. This measure of deviation assumed that there was no uncertainty in the measurement of time. The quantity of methane entering the liquid phase to obtain equilibrium is indicated by the location of the horizontal arrow.

MATERIALS

The sample of *n*-heptane employed in this investigation was purchased as pure grade from the Phillips Petroleum Company and was reported to contain less than 0.01 mole fraction of material other than *n*-heptane. The *n*-heptane was dried with sodium and subjected to two fractionations at a reflux ratio of 20 in a column containing sixteen glass plates, the central 80% portion of the overhead being retained from each fractionation. The product from the second fractionation was passed as a liquid over activated alumina and deaerated by refluxing at reduced pressure. The sample had a specific weight of 42.429 lb./cu. ft. as compared with a value of 42.419 lb./cu. ft. reported by Rossini (*18*) for an air-saturated sample at 77°F. The index of refraction relative to the *D* lines of sodium at this same temperature was 1.3852. This value is in close agreement with a value for air-saturated *n*-heptane at 77°F. of 1.38511, selected by Rossini (*18*). The close agreement of the measured specific weight and index of refraction for this sample with critically chosen values for the pure hydrocarbon and the statements of the supplier leads the authors to believe that the sample of *n*-heptane contained less than 0.001 mole fraction of impurities.

Methane was obtained from a well in the San Joaquin Valley of California. The sample received at the laboratory contained approximately 0.001 mole fraction of carbon dioxide with traces of heavier paraffin hydrocarbons and was in equilibrium in an aqueous phase at a pressure of approximately 1,400 lb./sq. in. The nearly pure methane was passed over calcium chloride, activated charcoal, potassium hydroxide, Ascarite, and anhydrous calcium sulfate. Spectroscopic analysis indicates that methane obtained from this well after being subjected to the treatment

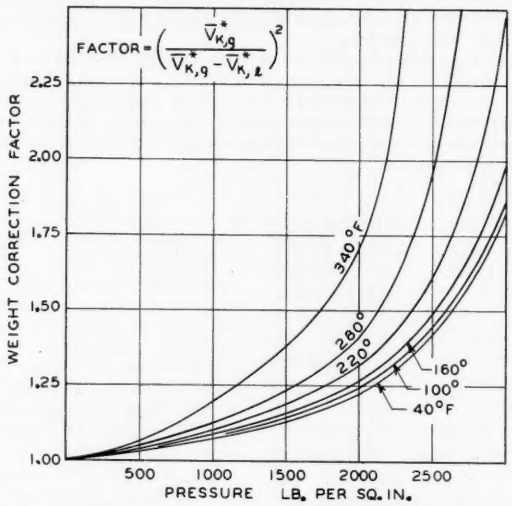

Fig. 2. Weight-correction factor for methane–*n*-heptane system.

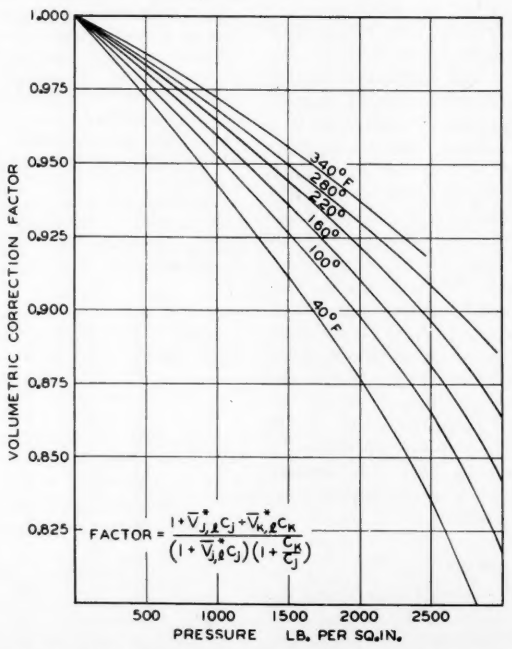

Fig. 3. Volumetric correction factor for methane–*n*-heptane system.

Table 2. Summary of Experimental Results

Pressure, lb./sq. in. abs.		Composition methane weight fraction		Concentration methane lb./cu. ft.		$(\Delta m_k)^{2*}$ / θ lb.²/sec.	Standard error of estimate, lb.	Volumetric correction factor	Fick diffusion coefficient, sq. ft./sec.	
Initial	Final	Initial	Final	Initial	Final				Uncorrected	Corrected
						40° F.				
59.4	410.6	0.004	0.027	0.167	1.139	29.160×10^{-12}	2.6×10^{-6}	0.9785	6.651×10^{-3}	6.508×10^{-3}
410.6	761.8	0.027	0.052	1.139	2.147	28.409	9.3	0.9578	6.210	5.948
762.8	1114.0	0.052	0.079	2.148	3.180	27.668	3.7	0.9362	5.993	5.611
1114.1	1465.3	0.079	0.109	3.180	4.219	27.773	13.2	0.9138	6.188	5.654
1465.3	1816.6	0.109	0.140	4.219	5.240	25.705	5.1	0.8903	6.203	5.522
1818.9	2170.1	0.140	0.178	5.250	6.325	18.404	12.2	0.8645	4.299	3.717
2849.2	3049.9	0.278	0.326	8.768	9.695	12.250	6.6	0.7669	5.670	4.349
						100°F.				
34.6	335.7	0.003	0.014	0.076	0.751	22.090×10^{-12}	3.4×10^{-6}	0.9863	10.468×10^{-3}	10.325×10^{-3}
724.8	1062.4	0.042	0.064	1.654	2.459	24.502	3.4	0.9503	8.732	8.298
1075.0	1426.3	0.065	0.089	2.489	3.347	25.705	3.1	0.9310	8.426	7.845
1426.3	1777.6	0.089	0.117	3.347	4.222	23.912	8.3	0.9110	7.915	7.210
1791.0	2142.2	0.118	0.149	4.259	5.179	28.090	23.2	0.8886	9.051	8.042
2152.4	2503.6	0.150	0.188	5.208	6.225	25.100	17.0	0.8622	7.397	6.378
						160°F.				
59.8	411.0	0.003	0.020	0.110	0.786	27.668×10^{-12}	9.0×10^{-6}	0.9848	13.330×10^{-3}	13.128×10^{-3}
411.0	766.2	0.020	0.039	0.786	1.489	27.458	5.2	0.9696	12.537	12.156
766.2	1117.5	0.039	0.059	1.489	2.163	28.196	5.3	0.9585	14.479	13.878
1470.8	1822.1	0.081	0.106	2.971	3.682	18.062	11.1	0.9203	9.242	8.506
1823.6	2184.2	0.107	0.136	3.686	4.518	26.522	8.9	0.9010	10.802	9.733
2184.1	2535.3	0.136	0.172	4.518	5.381	25.908	39.7	0.8791	11.120	9.775
2535.9	2877.1	0.172	0.217	5.382	6.311	16.728	26.2	0.8530	7.459	6.362
						220°F.				
753.7	1104.9	0.035	0.054	1.259	1.890	26.214×10^{-12}	5.9×10^{-6}	0.9604	15.582×10^{-3}	14.965×10^{-3}
1119.4	1470.6	0.055	0.076	1.918	2.581	30.581	10.5	0.9463	17.422	16.486
1454.0	1805.2	0.075	0.099	2.554	3.249	26.522	7.1	0.9314	14.717	13.708
1806.0	2157.3	0.099	0.127	3.250	3.996	27.878	13.9	0.9147	14.633	13.385
2164.2	2515.4	0.128	0.163	4.010	4.803	23.620	9.5	0.8960	12.833	11.498
2310.7	2511.4	0.141	0.162	4.323	4.797	7.453	12.4	0.8963	11.329	10.154
						280°F.				
418.7	759.9	0.027	0.033	0.582	1.120	30.140×10^{-12}	2.7×10^{-6}	0.9775	23.919×10^{-3}	23.381×10^{-3}
758.7	1109.9	0.033	0.050	1.118	1.677	31.136	1.7	0.9691	24.258	23.508
1110.5	1461.8	0.050	0.071	1.677	2.250	28.516	7.7	0.9527	22.505	21.440
1461.7	1812.9	0.071	0.094	2.250	2.867	29.052	6.5	0.9385	21.374	20.059
1814.0	2165.3	0.094	0.124	2.869	3.549	25.604	6.6	0.9245	17.877	16.527
2198.4	2399.1	0.127	0.148	3.622	4.039	6.502	5.1	0.9144	14.161	12.949
2598.2	2799.0	0.175	0.216	4.500	5.046	4.928	2.9	0.8948	12.242	10.953
						340°F.				
717.0	1018.1	0.029	0.045	0.925	1.377	21.068×10^{-12}	6.9×10^{-6}	0.9715	26.219×10^{-3}	25.472×10^{-3}
1323.4	1624.4	0.063	0.082	1.840	2.308	15.524	3.5	0.9510	21.577	20.520
1624.2	1925.2	0.082	0.105	2.308	2.809	19.272	7.4	0.9403	26.493	24.912

*Effective cross-sectional area = 0.019262 sq. ft.

described above contains less than 0.002 mole fraction of material other than methane.

EQUILIBRIUM DATA

As indicated in Equation (1), a rather detailed knowledge of the equilibrium volumetric and phase behavior of this system is required in order to interpret the diffusion measurements. Initially an effort was made to employ the measurements of Boomer and coworkers (*3*) upon the methane-nitrogen-heptane system to evaluate these quantities. However it was found that the data of Boomer, because of limited composition and temperature range, did not permit the evaluation of the partial volumes of the components in the liquid and gas phases with an accuracy comparable to the rate measurement obtained. For this reason the volumetric and phase behavior of the methane–*n*-heptane system was investigated (*9*, *16*). These data are in good agreement with the measurement of Beattie (*1*) upon pure *n*-heptane and in fair agreement with the earlier measurements of Boomer. The recent data (*16*) were employed to evaluate the partial volumes required to obtain the Fick diffusion coefficients from Equation (1). In this instance the graphical method of Roozeboom (*17*) was employed to determine the partial volume in the liquid phase as a function of pressure, temperature, and composition. Figure 2 depicts the weight-correction factor which is made necessary by the increase in volume in the liquid phase and the consequent decrease in the volume of the gas phase. It is apparent that at the higher pressures this correction becomes of importance and its accurate evaluation is a necessary part of the determination of the Fick diffusion coefficient from the experimental measurements. Figure 3 shows the volumetric correction factor which accounts for the hydrodynamic velocity (*13*). This effect is much smaller than the weight-correction factor shown in Figure 2 but is of sufficient magnitude to justify its inclusion in the evaluation of the Fick diffusion coefficient. The data of Figures 2 and 3 were employed in connection with the present experimental measurements to determine the Fick diffusion coefficient.

EXPERIMENTAL RESULTS

Measurements of the rate of solution of methane in the liquid phase of the

TABLE 3. FICK DIFFUSION COEFFICIENT FOR METHANE

Pressure, lb./sq.in. abs.	Composition methane weight fraction	Concentration methane, lb./cu. ft.	Fick diffusion coefficient, sq. ft./sec.
	40°F.		
500	0.036	1.373	6.4
1,000	0.070	2.835	5.8
1,500	0.112	4.312	5.2
2,000	0.160	5.799	4.5
2,500	0.220	7.437	3.9
3,000	0.313	9.465	3.2*
	100°F.		
500	0.028	1.110	9.7
1,000	0.060	2.313	8.8
1,500	0.095	3.527	7.8
2,000	0.136	4.788	6.8
2,500	0.188	6.212	5.9*
3,000	0.264	7.916	4.8*
3,500	0.395	9.818	3.9*
	160°F.		
500	0.025	0.950	13.9
1,000	0.052	1.945	12.3
1,500	0.083	2.974	10.7
2,000	0.121	4.098	9.2
2,500	0.168	5.301	7.8
3,000	0.238	6.686	6.4*
3,500	0.372	8.411	5.1*
	220°F.		
500	0.022	0.811	19.6
1,000	0.048	1.706	17.2
1,500	0.078	2.636	14.7
2,000	0.114	3.661	12.3
2,500	0.161	4.767	10.0*
3,000	0.238	6.078	8.0*
	280°F.		
500	0.020	0.696	26.2
1,000	0.045	1.503	22.7
1,500	0.073	2.320	19.3
2,000	0.109	3.224	16.0
2,500	0.161	4.266	12.8
	340°F.		
500	0.019	0.610	33.0
1,000	0.044	1.346	28.4
1,500	0.074	2.104	23.9
2,000	0.113	2.962	19.6*

*Values were obtained by extrapolation of experimental data at lower pressures.

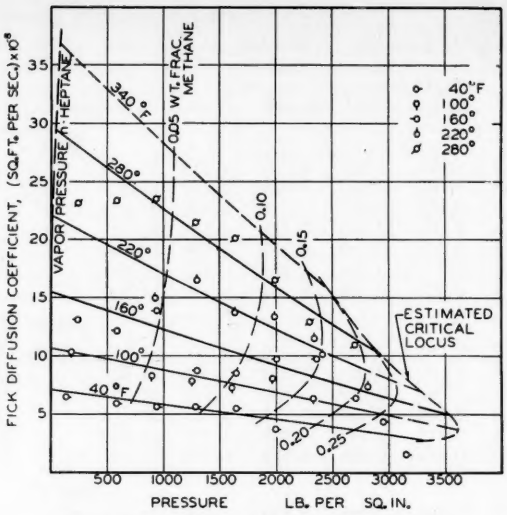

Fig. 4. Fick diffusion coefficients for methane.

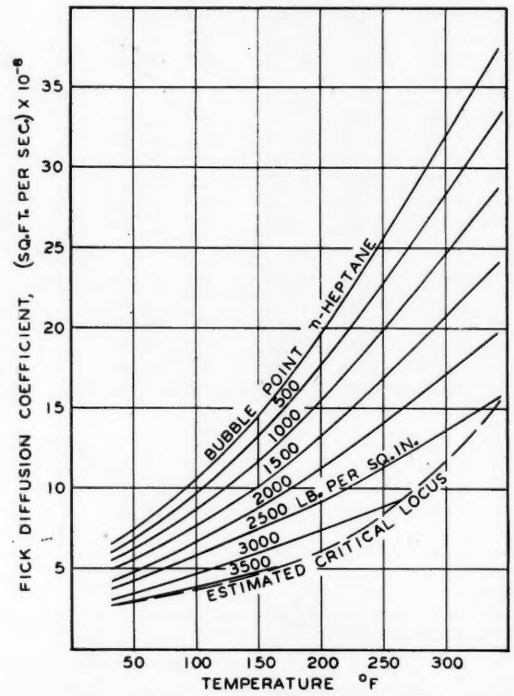

Fig. 5. Influence of temperature upon Fick diffusion coefficient for methane.

methane–*n*-heptane system were carried out at six temperatures between 40° and 340°F. in accordance with procedures already described (*13*). A sample of these experimental data constitutes Table 1 and the entire set of experimental measurements is available (*4*). The experimental results are recorded in terms of the weight of methane added per unit area of gas-liquid interface as a function of time. Table 2 records for each set of measurements the information necessary for the solution of Equation (1). In this table values of the Fick diffusion coefficient determined with and without the correction for the hydrodynamic velocity were included. Values of the standard error of estimate, also included in Table 2, were determined from the deviations of the experimentally measured weight of methane added from the straight line drawn through the data, as is shown in the example of Figure 1. The standard error of estimate was evaluated upon the assumption that all the uncertainty was associated with the weight of methane added and none with the time. The average relative percentage of deviation was 1.3.

The experimental results for the Fick diffusion coefficient with the hydrodynamic velocity taken into account are shown in Figure 4. Lines of constant composition have been included on this diagram along with the estimated locus of critical states. The latter data were obtained from available equilibrium measurements (*16*). In Figure 4 the experimental points were located at the linear average of the initial and final pressures used in each measurement. The deviation of the experimental points from the simple curves is due in a large measure to the severe requirements for accuracy

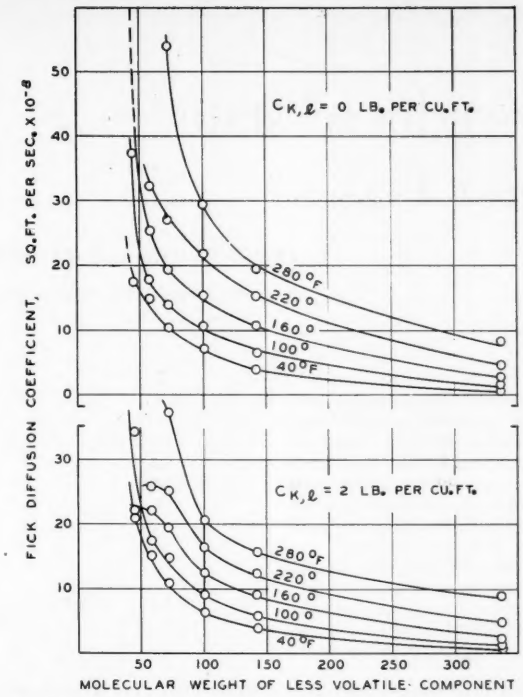

Fig. 6. Effect of molecular weight of less volatile component upon Fick diffusion coefficient for methane.

that are placed on the equilibrium data (*16*). The uncertainties in evaluating the concentrations and the partial volumes required in the solution of Equation (1) contribute a large part of the variation shown in Figure 4. The effect of temperature upon the Fick diffusion coefficient is presented in Figure 5. At the low temperatures there is only a small decrease in the coefficient with an increase in pressure. At the higher temperatures the coefficient decreases rapidly with an increase in pressure.

Smoothed values of the Fick diffusion coefficient for methane in the liquid phase of the methane–*n*-heptane system are recorded in Table 3. The concentration of methane and its weight fraction as determined for equilibrium conditions (*16*) at the indicated pressure and temperature have been included. Standard deviation of the experimental measurements shown in Figure 4 from smoothed data of Table 3 was 0.97×10^{-8} sq. ft./sec. This evaluation was made on the assumption that all the uncertainty existed in the Fick diffusion coefficient and none in the determination of the temperature, pressure, or concentration.

The experimental data presented in this discussion followed the same trend as was found for the Fick diffusion coefficients for methane in the liquid phase of the methane–*n*-decane (*13*) and the methane–*n*-pentane (*11*) systems. The behavior in the vicinity of the critical state is only an estimate, as it was not possible to determine experimentally the transport characteristics near this state by the methods exmployed here.

The effect of the molecular weight of the less volatile component upon the Fick diffusion coefficient of methane at a pressure of 2,000 lb./sq. in. is shown in Figure 6. The data include information for the methane–*n*-pentane (*11*), methane–*n*-decane (*13*), and methane–white-oil (*12*) systems. It is seen that there is a marked change in the Fick diffusion coefficient with the molecular weight of the less volatile component.

ACKNOWLEDGMENT

This work is a contribution from Project 37 of the American Petroleum Institute at the California Institute of Technology. The methane was supplied through the courtesy of The Texas Company. C. H. Duffy and M. O. Abdullah assisted with the experimental work, Virginia Berry with the calculations, and B. Lawson Miller with the preparation of the manuscript. W. N. Lacey reviewed the manuscript.

NOTATION

c_k = concentration of component k, lb./cu. ft.
$D_{F,k}$ = Fick diffusion coefficient of component k, sq. ft./sec.
m_k = weight of component k added per unit area of interface, lb./sq. ft.
$\bar{V}_k$ = partial specific volume of component k, cu. ft./lb.
Δ = difference in
θ = time, sec.

Superscript

* = average condition

Subscripts

e = conditions at equilibrium
g = gas phase
i = conditions at interface
j = component j, the stagnant component
k = component k, the diffusing component
l = liquid phase
0 = initial conditions

LITERATURE CITED

1. Beattie, J. A., and W. C. Kay, *J. Am. Chem. Soc.*, **59**, 1586 (1937).
2. Bertram, E. A., and W. N. Lacey, *Ind. Eng. Chem.*, **28**, 316 (1936).
3. Boomer, E. H., C. A. Johnson, and A. G. A. Piercey, *Can. J. Research*, **B16**, 396 (1938).
4. Duffy, C. H., H. H. Reamer, and B. H. Sage, Doc. 5439, obtainable from the American Documentation Institute, Photoduplication Service, Library of Congress, Washington 25, D. C., for $2.50 for photoprints or $1.75 for 35-mm. microfilm.
5. Hill, E. S., and W. N. Lacey, *Ind. Eng. Chem.*, **26**, 1324 (1934).
6. *Ibid.*, p. 1327.
7. Kirkwood, J. G., and Bryce Crawford, Jr., *J. Phys. Chem.*, **56**, 1048 (1952).
8. Meyers, C. H., *Bur. Standards J. Research*, **9**, 807 (1932).
9. Nichols, W. B., H. H. Reamer, and B. H. Sage, *Ind. Eng. Chem.*, **47**, 2219 (1955).
10. Pomeroy, R. D., W. N. Lacey, N. F. Scudder, and F. P. Stapp, *ibid.*, **25**, 1014 (1933).
11. Reamer, H. H., C. H. Duffy, and B. H. Sage, *ibid.*, **48**, 282 (1956).
12. *Ibid.*, p. 285.
13. Reamer, H. H., J. B. Opfell, and B. H. Sage, *ibid.*, **48**, 275 (1956).
14. Reamer, H. H., and B. H. Sage, *Chem. Eng. Data Series*, **1**, 71 (1956).
15. ———, *Rev. Sci. Instr.*, **24**, 362 (1953).
16. Reamer, H. H., B. H. Sage and W. N. Lacey, *Chem. Eng. Data Series*, **1**, 29 (1956).
17. Roozeboom, H. W. Bakhuis, "Die Heterogenen Gleichgewichte vom Standpunkte der Phasenlehre," vol. II, part 1, p. 288, F. Vieweg und Sohn, Braunschweig, (1904).
18. Rossini, F. D., et al., "Selected Values of Physical and Thermodynamic Properties of Hydrocarbons and Related Compounds," Carnegie Press, Pittsburgh (1953).
19. Sage, B. H., and W. N. Lacey, *Trans. Am. Inst. Mining Met. Engrs.*, **174**, 102 (1948).
20. Schlinger, W. G., H. H. Reamer, B. H. Sage, and W. N. Lacey, "Report of Progress-Fundamental Research on Occurrence and Recovery of Petroleum, 1952–1953," pp. 70–106, Am. Petroleum Inst.
21. Tung, L. H., and H. G. Drickamer, *J. Chem. Phys.*, **20**, 6 (1952).
22. *Ibid.*, p. 10.

Thermal-conductivity–reduced-state Correlation for the Inert Gases

E. JAMES OWENS and GEORGE THODOS

Northwestern Technological Institute, Evanston, Illinois

The fragmentary thermal-conductivity data for argon available in the literature have been correlated by use of a residual thermal conductivity $k - k^*$ vs. density ρ relationship. This correlation produced a unique continuous curve which was found to be singularly independent of temperature and pressure for both gaseous- and liquid-state data. From low-pressure thermal-conductivity values k^* and the relationship given above, it is possible to determine thermal conductivities at any condition of temperature and pressure for which a corresponding density is available. This procedure was used to calculate reliable thermal conductivities k for high-pressure regions where experimental data were lacking.

In a similar manner the critical thermal conductivity k_c for argon was established directly from the critical density and the quantity $k_{T_c}{}^*$. The k_c value permitted the calculation of reduced thermal conductivities k_R and made possible the construction of an extensive reduced-state chart. Although this correlation was developed mainly from data for argon, it was found to apply equally as well to the other inert gases as postulated from the theory of corresponding states.

A comparison of thermal conductivities calculated from the reduced-state plot with over 200 experimental points produced an average deviation of 1.8% for all the inert gases. This chart was also found applicable to the diatomic gases and their mixtures but produced significant deviations for substances having more than two atoms per molecule.

Present-day heat transfer studies require an exacting definition of the thermal properties of fluids over wide ranges of temperature and pressure. In general, the thermal properties of fluids can be obtained from reliable correlations already available in the literature (*5, 18, 43*); however, present methods do not permit the calculation of accurate thermal conductivities for both gases and liquids except over limited ranges of temperature and pressure. Thermal-conductivity values available in the literature are generally presented only for the more common substances and in most cases are restricted to the low-pressure region where P_R is essentially equal to zero. Relatively few experimental data are available for high pressures and for conditions approaching the critical point.

Existing theoretical methods (*8, 14, 34*) for estimating thermal conductivities are generally limited to the low-pressure region and cannot be used to predict accurate values for the liquid state. Similarly, theoretical equations (*15, 42*) are available for predicting the thermal conductivity of certain types of liquids, but these relationships cannot be applied to the gaseous state. Specific correlations are available for calculating the thermal conductivity of gases at high pressures (*7, 11, 32*); however, these methods require a considerable amount of experimental data or are restricted in application owing to questionable accuracy. In the present investigation (*39*) an attempt was made to overcome these limitations and to produce a method for calculating the thermal conductivity of both gases and liquids over wide ranges of temperature and pressure.

PREVIOUS DEVELOPMENTS

Early attempts to predict the thermal conductivity of gases have been based primarily upon kinetic theory. Most of these developments have been limited to the low-pressure region, where the mean free path of gas molecules is small in comparison to the dimensions of the system. This region is generally restricted to pressures ranging from 1 atm. to 10 mm. Hg.

Maxwell (*34*), Sutherland (*46*), and Eucken (*8*) have presented theoretical expressions to predict the thermal conductivity of some gases at low pressures with fair accuracy. Although these relationships are of classical interest, they are not applicable to the liquid state and fail to produce reliable thermal conductivities at high pressures and temperatures.

More recently Hirschfelder, Curtiss, and Bird (*14*) developed a relationship for predicting the thermal conductivity of monoatomic gases at low pressures. Using the concepts of statistical mechanics, these investigators derived the following equation for nonpolar gases:

$$k^* = 1.9891 \times 10^{-4} f_k \frac{\sqrt{T/M}}{\sigma^2 \Omega^{(2,2)^*}[T_N]} \qquad (1)$$

Equation (1) can also be applied to polyatomic gases if f_k (*14*) is replaced by the Eucken correction factor (*8*). This equation produces accurate thermal conductivity values at low pressures for many nonpolar gases for which the force constants ϵ and σ are available.

Using concepts of advanced kinetic theory, Enskog (*7*) derived an equation of state and expressions to predict the effect of pressure on the thermal conductivity and viscosity of nonpolar gases:

$$P + \alpha\rho^2 = \frac{RT}{M}\rho[1 + \beta\rho\chi] \qquad (2)$$

$$\frac{\mu}{\mu^*} = \beta\rho\left[\frac{1}{\beta\rho\chi} + 0.7614\beta\rho\chi + 0.8\right] \qquad (3)$$

$$\frac{k}{k^*} = \beta\rho\left[\frac{1}{\beta\rho\chi} + 0.7575\beta\rho\chi + 1.2\right] \qquad (4)$$

in which it is assumed that α and β are constants and χ is a function of density only. In this development Enskog further assumed that multiple collisions between the gas molecules were negligible and that the molecules behaved as rigid elastic spheres which exerted attractive forces only. The basic derivation and use of the Enskog equations are clearly illustrated elsewhere (*16*).

Michels and Botzen (*35*) have found that these relationships are valid up to pressures of approximately 1,000 atm., where the basic assumptions of Enskog begin to break down. Equations (2), (3), and (4) are capable of producing reliable thermal conductivity and viscosity values when sufficient experimental data are available to define the values of α, β, and χ. This requirement limits the application of the Enskog expressions to systems having an extensive experimental background.

Nathan and Comings (*37*) used high-pressure viscosity and P.V.T. data for a number of gases to evaluate α, β, and χ

E. James Owens is at present with the California Research Corporation, Richmond, California.

Large reproductions of Figure 7 in sizes of 8½ by 11 and 11 by 13½ in. are available on request from the Chemical Engineering Department, Northwestern University, Evanston, Illinois.

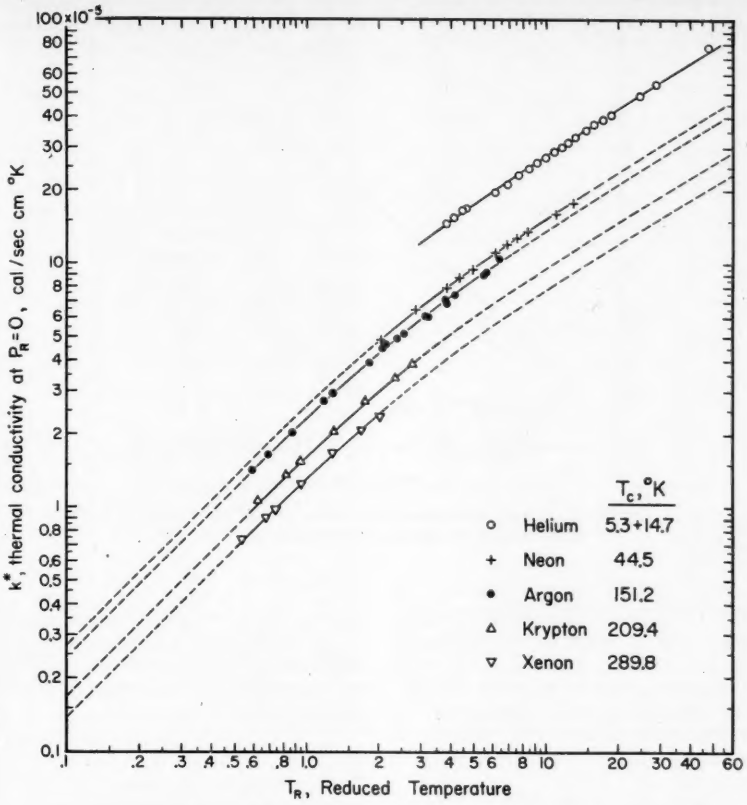

Fig. 1. Thermal-conductivity–reduced-temperature relationships for the inert gases at $P_R = 0$.

in the Enskog equations. Substituting these values into Equation (4) permitted the ratio k/k^* to be calculated directly and plotted as a generalized function of reduced temperature and pressure. This correlation was later revised by Lenoir, Junk, and Comings (*32*) to include data for several additional gases. The revised plot produces satisfactory thermal conductivities for many gases at conditions ranging from reduced temperatures of $T_R = 1$ to $T_R = 3$ and reduced pressures of $P_R = 0.6$ to $P_R = 7.5$. However, its general use is restricted to those substances for which k^* data may be either estimated (*8, 14, 34*) or obtained directly from the literature.

Gamson (*11*) has presented a more flexible correlation in which the reduced thermal conductivity k/k_c, rather than the ratio k/k^*, is plotted as a function of reduced temperature and pressure. Based on the Enskog equations and the work of Nathan and Comings (*37*), Gamson made the fundamental assumption that

$$\frac{k/k^*}{\mu/\mu^*} = f(T_R, P_R) \qquad (5)$$

Equation (5) can be expressed in terms of reduced conditions as

$$\frac{k_R}{\mu_R}\frac{\mu_R^*}{k_R^*} = f(T_R, P_R) \qquad (6)$$

A relationship for the thermal conductivity at the critical point was obtained by evaluating Equation (6) at the critical temperature and pressure where $k_R/\mu_R = 1$. The quantity μ_R^* was calculated from the reduced viscosity plot of Uyehara and Watson (*50*), and $f(T_R, P_R)$ was obtained from the work of Nathan and Comings (*37*) to produce

$$k_c = 2.60 k_{T_c}^* \qquad (7)$$

Using Equation (7), Gamson established a low-pressure reduced-thermal-conductivity curve based on the experimental data for over twenty-five substances. Reduced thermal conductivities at elevated pressures were calculated from Equation (6) by extrapolating the $f(T_R, P_R)$ values determined by Nathan and Comings. In this manner, a generalized reduced-state correlation was constructed to include reduced temperatures in the range from $T_R = 0.3$ to $T_R = 40$ and reduced pressures ranging from $P_R = 0$ to $P_R = 30$.

The accuracy of Gamson's correlation is open to speculation because it was produced from relatively few experimental data obtained in the low-pressure region. Furthermore, the validity of this plot above $T_R = 3.0$ and $P_R = 10.0$ is particularly questionable since an extensive extrapolation of the Nathan and Comings data was used to establish this entire region.

REDUCED-STATE CORRELATIONS

Generalized reduced-state plots are based on the validity of the theory of corresponding states as originally proposed by van der Waals (*51*). It is recognized that the classical form of this theory is only approximately true for all fluids. In order for all substances to conform to the behavior of a corresponding state, it would be necessary for them to have molecules of the same shape with similar intermolecular-force relationships. Since this requirement is not generally met, the classical theory should apply well only to members of a homologous series or to a family of substances which exhibit similar molecular behavior. A universal reduced-thermal-conductivity correlation would of necessity encompass substances of all types, and, therefore, significant errors may be inherent in this type of plot. The application of a reduced-state analysis to a family of similar substances should tend to eliminate such errors and to produce a more accurate correlation. Because of these advantages, the restricted rather than the universal approach was used in the following development.

DEVELOPMENT OF PRESENT METHOD OF CORRELATION

The inert gases have been arbitrarily selected as the basis for the present study. Experimental data for helium, neon, argon, krypton, and xenon have been obtained from the literature sources presented in Table 1.

The low-pressure thermal conductivities* for the inert gases have been plotted against reduced temperature on log-log scales to produce the curves presented in Figure 1. The low-temperature portion of these curves was obtained by extrapolating on rectilinear coordinates the available data to $k^* = 0$ when $T = 0°K$. The relationships of Figure 1 are found to be parallel and should be capable of translation into a single curve when the data are divided by the ordinate at any reduced temperature T_R, such as the thermal conductivity at the critical temperature.

The relationships shown in Figure 1 may be expressed analytically as

$$\log k^* = B \log T_R + \log C \qquad (8)$$

For a set of parallel curves such as that given in Figure 1, B becomes a function of reduced temperature only and is the same for all substances considered in this study. If Equation (8) is evaluated at $T_R = 1.0$, the constant C is defined as

$$C = k_{T_c}^* \qquad (9)$$

*Experimental k values measured at essentially atmospheric pressure, for which P_R is approximately equal to zero.

TABLE 1. SOURCES OF EXPERIMENTAL DATA

Source	Helium	Neon	Argon	Krypton	Xenon
3	X				
12	X				
19	X				
22	X	X	X	X	X
23		X	X		
24	X	X	X		
27		X	X		
28			X	X	X
31	X		X		
32			X		
41	X		X		
45	X		X		
47	X	X			
48	X				
49			X		
54			X		

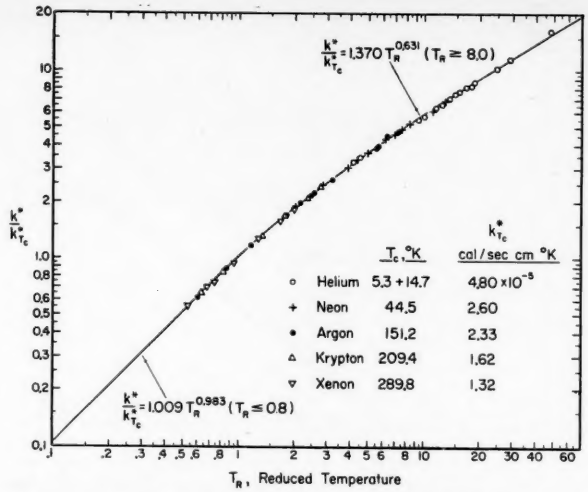

Fig. 2. Correlation of thermal-conductivity ratios for the inert gases at $P_R = 0$ (reference state: critical temperature and $P_R = 0$).

which, when substituted into Equation (8), produces

$$\log \frac{k^*}{k_{T_c}^*} = B \log T_R \qquad (10)$$

Equation (10) suggests that a single curve should result when the thermal conductivity ratio, $k^*/k_{T_c}^*$, is plotted against reduced temperature T_R on log-log coordinates. This behavior should follow for any family of similar substances which produce parallel curves on a plot of the type presented in Figure 1.

Values for the $k_{T_c}^*$ of neon, argon, krypton, and xenon were obtained directly from Figure 1. Thermal conductivity ratios, $k^*/k_{T_c}^*$, calculated from these quantities were plotted against reduced temperature to produce the single curve presented in Figure 2. The straight-line portions of this relationship are defined analytically by the following equations:

$$\frac{k^*}{k_{T_c}^*} = 1.009 T_R^{0.983} \quad \text{for} \quad T_R \leq 0.8 \qquad (11)$$

$$\frac{k^*}{k_{T_c}^*} = 1.370 T_R^{0.631} \quad \text{for} \quad T_R \geq 8.0 \qquad (12)$$

The curve in Figure 2 permitted the low-pressure data for each of the inert gases to be extrapolated over the entire reduced-temperature range covered by the $k^*/k_{T_c}^*$ ratios for all the gases. Accordingly, extrapolated values were calculated for neon, argon, krypton, and xenon and are indicated as the dashed portion of the curves presented in Figure 1.

Initially, the data for helium did not fall in line with the correlation presented in Figure 2. It has been shown (*6*) that this deviation from classical behavior can be explained and accounted for explicitly by the quantum-mechanical principle of corresponding states. However, in this study the helium data were fitted to the relationship of Figure 2 by replacing its true critical temperature of 5.3°K. with an arbitrary pseudocritical value of 20°K. This treatment is similar to that used for correcting the incongruous behavior of helium on other types of reduced-state correlations (*33*, *38*).

An average $k_{T_c}^*$ value for helium was determined from Figure 2 by use of pseudoreduced temperatures T_R' and the available low-pressure data. Thermal-conductivity ratios calculated with this value were plotted on Figure 2 and were found to be consistent with the ratios for the other inert gases only in the reduced temperature range above $T_R = 3.0$.

Figure 3 is presented as an alternative correlation to Figure 2. This plot was prepared by calculating the k^* and $k_{T_c}^*$ values directly from Equation (1). The straight-line portions of the curve are given by the expressions

$$\frac{k^*}{k_{T_c}^*} = T_R \quad \text{for} \quad T_R \leq 1.0 \qquad (13)$$

$$\frac{k^*}{k_{T_c}^*} = 1.276 T_R^{0.645} \quad \text{for} \quad T_R \geq 3.5 \qquad (14)$$

Thermal conductivities obtained from Figure 3 are in good agreement with the experimental values. However, Figure 2 is somewhat more accurate since this was produced directly from experimental data.

Equation (8) can be expressed in the form

$$\log \frac{k^*}{k_c} = B \log T_R + \log \frac{1}{A} \qquad (15)$$

where $A = (k_c/C)$ and is a constant characteristic of a given family of substances. At a reduced temperature of $T_R = 1.0$, Equation (15) simplifies to the following relationship defining the thermal conductivity of a substance at the critical point:

$$k_c = A k_{T_c}^* \qquad (16)$$

The constant A of Equation (16) can be evaluated if a single thermal-conductivity value can be determined at the critical point and if a corresponding $k_{T_c}^*$ value can be established. Ordinarily, low-pressure thermal conductivities can be obtained from the literature; and values at the critical temperature $k_{T_c}^*$ can be determined either directly or by extrapolation. However, if the experimental data for a substance are limited, $k_{T_c}^*$ can be produced directly from a single thermal-conductivity measurement and a relationship of the type presented in Figure 2. With Equation (16) it is then possible to calculate the critical thermal conductivity k_c for each member of a family having an established value of $k_{T_c}^*$.

A reliable value for the critical thermal conductivity of argon was obtained by using an equation of the form originally proposed by Abas-Zade (*1*):

$$k - k^* = a\rho^b \qquad (17)$$

where k and ρ represent the thermal conductivity and density, respectively, at any temperature and pressure and k^* is evaluated at a low pressure* and the same temperature. In Equation (17) the quantity a is a constant, and the exponent b is a function of density only.

The experimental data available for argon were used to calculate the residual thermal conductivities $k - k^*$. These values were correlated with experimental densities ρ (*17*, *20*, *30*, *36*) according to

*A condition where P_R is essentially equal to zero.

Equation (17) to produce the curve presented in Figure 4. It is important to note that the experimental data defined a single, continuous curve for both the gaseous and liquid states and that this function appears to be independent of temperature and pressure as indicated by Equation (17).

The relationship of Figure 4 possesses a number of distinct advantages over previous methods of correlation. For its complete definition, this plot requires only a moderate amount of reliable liquid and high-pressure gaseous-state data. Once established, the correlation defines thermal-conductivity values for all conditions of temperature and pressure corresponding to the entire range of densities plotted on the curve. Consequently, it is also possible to calculate the critical thermal conductivity of a substance k_c directly from the critical density and the corresponding $k_{T_c}{}^*$ value.

Through this approach the critical thermal conductivity of argon was established directly from the density at the critical point and the $k_{T_c}{}^*$ value obtained from Figure 1. Specifically, the critical thermal conductivity for argon was calculated to be $k_c = 7.10 \times 10^{-5}$ cal./(sec.)(cm.)(°K.) from a value of $k_{T_c}{}^* = 2.33 \times 10^{-5}$ and a residual thermal conductivity, $k - k^* = 4.77 \times 10^{-5}$ obtained from Figure 4 at a critical density, $\rho_c = 0.531$ g./cu. cm.

By use of the critical thermal conductivity for argon, the constant of Equation (16) was calculated to be $A = 3.047$. Therefore, for the inert-gas family, Equation (16) becomes

$$k_c = 3.047 k_{T_c}{}^* \qquad (18)$$

Critical thermal conductivities for helium, neon, krypton, and xenon were calculated from Equation (18) with the $k_{T_c}{}^*$ values presented in Figure 2. The resulting critical values for all the inert gases are as follows:

	k_c, cal./(sec.)(cm.)(°K.)
Helium	14.62×10^{-5}
Neon	7.92
Argon	7.10
Krypton	4.92
Xenon	4.02
Radon*	3.12

*Calculated from Equation (20).

The critical-temperature correction necessary to make the correlation of helium consistent with that of the other inert gases has been given previously as 14.7°K., but since high-pressure thermal-conductivity data for helium are limited, a proper correction for the critical pressure is difficult to establish. In order to obtain such a value, an equation of the form (*50*)

$$k_c = dM' T_c' P_c^{\,g} \qquad (19)$$

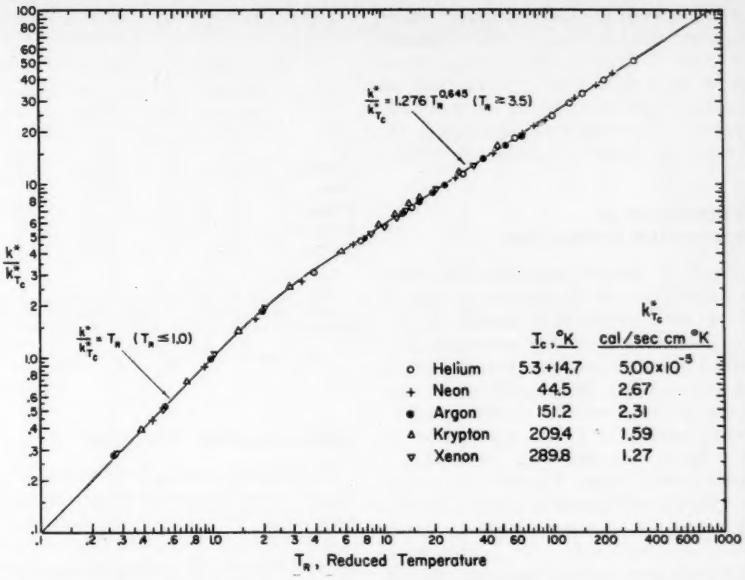

Fig. 3. Thermal-conductivity ratios for the inert gases (reference state: $T_R = 1.0$, $P_R = 0$) (points calculated with the Hirschfelder, Curtiss, and Bird equation).

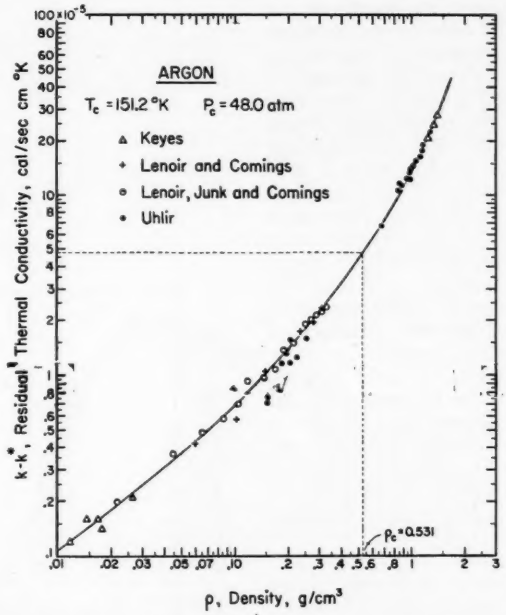

Fig. 4. Relationship of residual thermal conductivity and density for argon in the gaseous and liquid states.

was assumed to apply for all the inert gases. The critical values for neon, argon, krypton, and xenon were used to evaluate the constants of Equation (19), and this equation thereby becomes

$$k_c = 13.39 \times 10^{-5} \frac{P_c^{\,0.223} T_c^{\,0.132}}{M^{0.586}} \qquad (20)$$

From the values $k_c = 14.62 \times 10^{-5}$ cal./(sec.)(cm.)(°K.), $T_c' = 20$°K., and $M = 4.003$, the pseudocritical pressure for helium was calculated from Equation (20) as 9.60 atm. This value requires that a correction of 7.34 atm. be added to the actual critical pressure.

It is logical to assume that Equation

(20) is also applicable to radon, which has the following characteristic constants (*30*): $M = 222$, $T_c = 377.6$°K., $P_c = 62.44$ atm. With these values used in Equation (20), the critical thermal conductivity for radon was calculated to be $k_c = 3.12 \times 10^{-5}$ cal./(sec.)(cm.)(°K.).

CONSTRUCTION OF REDUCED-STATE CORRELATION

Reduced thermal conductivities were calculated for the inert gases by use of all the experimental data available in the literature and the critical constants presented above. These values were plotted against reduced temperature on log-log scales to produce the correlation presented as Figure 5. An examination of this figure indicates that the data for helium, neon, argon, krypton, and xenon all follow a corresponding-states behavior. However, it is apparent that the available data are fragmentary and limited to a few particular regions of temperature and pressure.

In order to extend the range of Figure 5, it was necessary to define the density of argon over the entire region of temperature and pressure required for the final reduced-state correlation. To provide these values, Figure 6 was constructed on the basis of the experimental densities reported in the literature (*17, 20, 30, 36*). For conditions where no experimental data were available, density values were calculated. In the gaseous-state region the compressibility factors of Nelson and Obert (*38*) were used to apply a temperature correction to existing high-pressure data (*36*). To obtain liquid-state values, saturated liquid densities were corrected for pressure effects by means of the ω factors proposed by Watson (*57*). At pressures above $P_R = 5$ it was necessary to extrapolate the gaseous-state isobars into the liquid region.

Figure 7 presents the final reduced-state correlation for the inert gases. In this figure the low-pressure curve $P_R = 0$ was established directly from the corresponding data presented in Figure 5. The construction of the remaining curves was based on the correlations for argon given in Figures 1, 4, and 6.

Each isobar was defined by first selecting a number of density values covering the entire range of desired temperatures for a fixed pressure. A residual thermal conductivity $k - k^*$ corresponding to each density was then obtained from Figure 4. With the proper value of k^* from Figure 1, thermal conductivities were established for the selected temperatures and constant pressure. Reduced thermal conductivities were calculated from these values and then plotted in Figure 7. Isobars constructed in this manner extend up to reduced pressures of 40 and cover a reduced temperature range from 0.1 to 100.

Table 2. Comparison of Thermal Conductivities Calculated From Figure 7 With Experimental Values for the Inert Gases

	Low-pressure region			Liquid and high-pressure gaseous region			Range investigated		Combined average % deviation†
	Experimental Points	% Deviation Maximum	% Deviation Average	Experimental Points	% Deviation Maximum	% Deviation Average	T_R	P_R	
Helium*	34	5.2	1.4	8	1.3	0.8	3.8–48	0–21.4	1.2
Neon	17	2.3	0.6	—	—	—	2 –13	0	0.6
Argon	25	3.7	1.2	96	10.7	2.3	0.57– 6.4	0– 4.5	2.1
Krypton	8	2.9	1.2	9	4.3	2.0	0.59– 2.8	0– 0.2	1.6
Xenon	8	3.0	1.9	7	5.7	4.2	0.5 – 2.0	0– 0.18	3.0

The over-all % deviation for the monoatomic gases is 1.8%.
*The reduced-state plot of Figure 7 applies for helium only in the reduced temperature range above $T_R = 3.0$, therefore for helium no comparisons are included for the liquid region or for the gaseous region below $T_R = 3.0$.
†% Deviation $= \frac{k_{calc.} - k_{exp.}}{k_{exp.}} \times 100$.

NORMALIZED-STATE CORRELATION

The thermal-conductivity values from Figure 7 were replotted with new reference states to produce the normalized plot of Figure 8. This correlation is based on the theorem of corresponding states expressed in terms of molecular properties and intermolecular forces rather than critical constants. The variables in Figure 8 are dimensionless factors defined analytically as follows:

$$T_N = \frac{T}{\epsilon/\kappa} \tag{21}$$

$$P_N = \frac{P}{\epsilon/\sigma^3} \tag{22}$$

$$k_N = \frac{k}{\frac{\kappa}{\sigma^2}\sqrt{\frac{\epsilon N}{M}}} \tag{23}$$

These normalized quantities are derived on the assumption that the intermolecular forces between two molecules of a pure gas follow the Lennard-Jones potential-energy function given by the equation

$$\varphi(r) = 4\epsilon\left[\left(\frac{\sigma}{r}\right)^{12} - \left(\frac{\sigma}{r}\right)^{6}\right] \tag{24}$$

It should be noted that ϵ and σ in Equation (24) are characteristic constants for each specific substance and are combined with the appropriate molecular constants to provide a basis for the dimensionless normalized temperature, pressure, and thermal conductivity defined by Equations (21), (22), and (23). The ϵ and σ values given in Figure 8 were obtained from Hirschfelder, Curtiss, and Bird (*14*).

The normalized plot presented in Figure 8 is convenient because it requires only values of ϵ and σ and the molecular

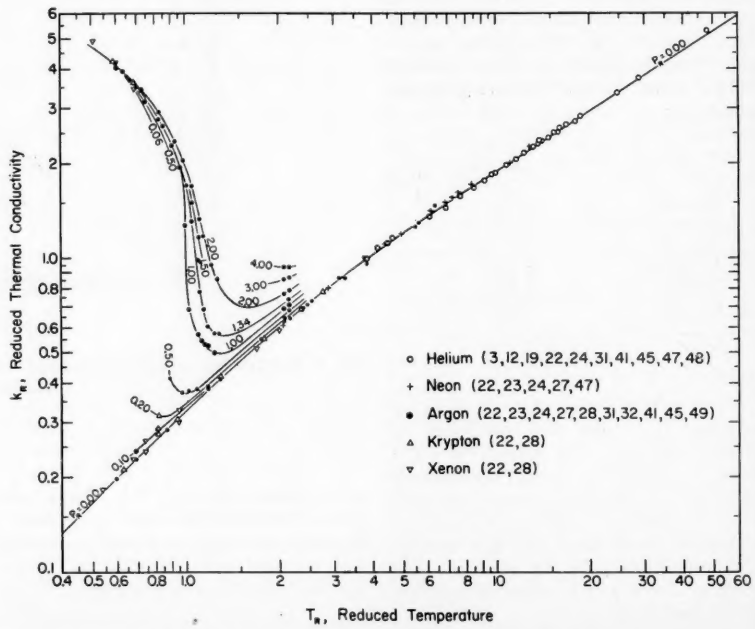

Fig. 5. Reduced-state plot of thermal-conductivity data obtained from the literature.

Table 3. Comparison of Thermal Conductivities Calculated From Figure 7 With Selected Experimental Values for Some Diatomic, Triatomic, and Hydrocarbon Gases

	k_c, cal./(sec.)(cm.)(°K.)	Range investigated T_R	Range investigated P_R	Experimental points	% Deviation Maximum	% Deviation Average	References
Diatomic							
Hydrogen*	50.6×10^{-5}	0.85–7.1	0	13	12.3	4.3	*4, 19, 27, 53*
Nitrogen	8.68	0.54–8.5	0–38.5	126	8.4	2.6	*10, 26, 31, 32, 35, 40, 41, 49*
Oxygen†	10.53	0.55–5.1	0–1.9	19	37.4	7.4	*2, 10, 28*
Carbon monoxide	8.65	0.66–2.8	0	10	7.2	2.4	*19*
Nitric oxide	11.82	0.72–2.1	0	8	3.1	1.0	*19*
Chlorine	9.70	0.48–1.6	0	7	16.0	5.6	*10*
Hydrogen chloride	11.30	0.61–1.78	0	5	6.0	3.4	*10*
Triatomic							
Carbon dioxide	12.2	0.66–2.1	0–2.8	15	29.2	11.6	*19, 26, 31*
Nitrous oxide	13.1	0.61–1.2	0	5	22.0	10.4	*19*
Sulfur dioxide	9.86	0.64–0.68	0	4	2.6	1.3	*9*
Water	33.4	0.58–0.96	0–0.69	9	13.8	5.8	*29*
Hydrocarbons							
Methane	15.8	0.51–2.0	0–4.4	16	16.1	6.5	*19, 28, 32*
Ethane	20.3	1.0 –1.4	0–4.1	13	119	32.0	*32, 55*

*For hydrogen the reduced-state plot of Figure 7 applies only for the isobar $P_R = 0$, for which a corrected critical temperature of 100°K. must be used.
†For oxygen the experimental data include four points in the liquid region which produce large deviations. If these points are not considered, the average deviation for oxygen is 2.7% with a maximum of 6.8%.

weight; all of which can be obtained from the literature or can be evaluated from experimental viscosity data (*14*). No knowledge of the critical temperature, pressure, or thermal conductivity is necessary. However, because of the assumptions made in the theoretical development of this approach, this correlation should be restricted to monoatomic gases. Figure 8 is comparable to Figure 7 and is presented for completeness in view of the novelty of these concepts defining the reference states of transport properties from statistical and quantum mechanic approaches.

DISCUSSION OF RESULTS

The accuracy of the correlation presented in Figure 7 has been checked with the original experimental data taken from the literature sources given in Table 1, and the results of these comparisons are presented in Table 2. It is significant that the over-all deviation of the inert gases is only 1.8% for the 212 experimental points considered. Furthermore, it is observed that the liquid and the high-pressure gaseous regions of Figure 7 are accurate for all the inert gases despite the fact that these general areas were developed only from data for argon. It should be emphasized, however, that this figure is applicable to helium only in the gaseous state for reduced temperatures above $T_R = 3$.

The correlation of Figure 7 has been checked for generality by comparing the results for some diatomic, triatomic, and hydrocarbon gases with experimental values obtained from the literature. Table 3 presents a summary of these comparisons. The calculated deviations indicate that Figure 7 produces reliable thermal conductivities for the diatomic gases; however, it appears that significant errors are encountered for substances having more than two atoms per molecule such as carbon dioxide, nitrous oxide, methane, and ethane.

To make the evaluation of Table 3, it was necessary to calculate an average k_c for each substance by dividing reduced thermal conductivities from Figure 7 into experimental k values and averaging the resulting k_c values. The critical constants obtained in this manner may not necessarily represent the true thermal conductivity at the critical point and therefore should be used only with Figure 7.

Experimental data for a number of mixtures have also been considered from the standpoint of the pseudocritical concept. Critical properties for each mixture were calculated from the following equations:

$$T_c' = \sum_i N_i T_{ci} \qquad (25)$$

$$k_c' = \sum_i N_i k_{ci} \qquad (26)$$

From the comparisons presented in Table 4, it appears that Figure 7 is generally applicable to mixtures of both mono- and diatomic gases including air. However, these comparisons are limited to the low-pressure region, as no high-

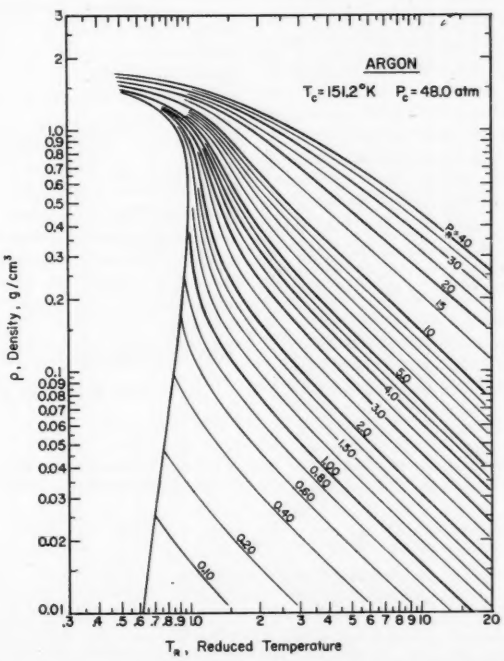

Fig. 6. Density chart for argon in the gaseous and liquid states.

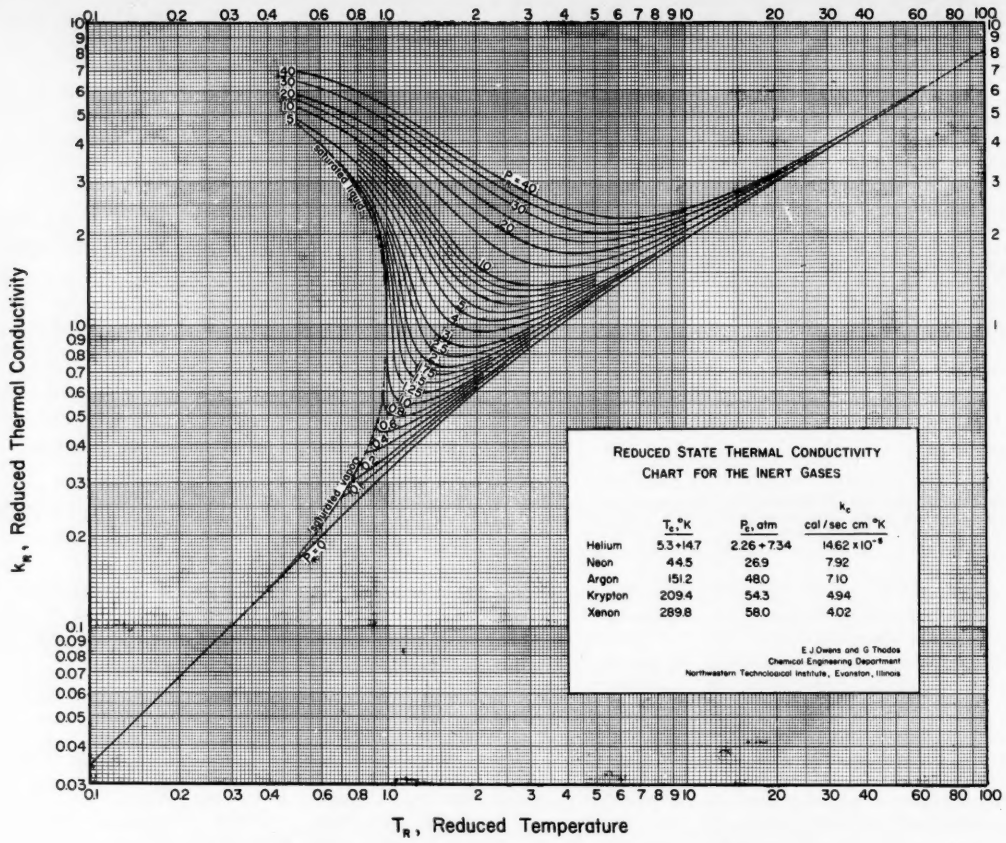

Fig. 7. Reduced-state plot of thermal conductivity for the inert gases.

pressure data for mono- or diatomic gas mixtures are available in the literature.

Since Figure 8 contains the same basic data as given in Figure 7, only a moderate number of comparisons were made to determine the accuracy and limitations of the normalized plot relative to the reduced-state correlation. Based on more than fifty randomly selected experimental values, thermal conductivities calculated from Figure 8 produced an average deviation of about 1% for the inert gases. In these comparisons the data for helium were found to be in excellent agreement with those of the other inert gases for normalized temperatures above $T_N = 2.5$. For helium no correction was required on the original molecular parameters to produce this good agreement.

CONCLUSIONS

The validity of the general correlation method developed in this study is substantiated by the results for the inert gases presented in Table 2. It is important to emphasize that this method requires only a moderate amount of reliable liquid- and high-pressure-gaseous-state data in order to produce an extensive reduced-state correlation of the form given in Figure 7. Also, it is apparent that the proposed procedure should be applicable to any family of similar fluids since it is limited only by the assumption of a corresponding-states behavior.

ACKNOWLEDGMENT

The authors gratefully acknowledge the fellowship grant provided by the Dow Chemical Company which made this study possible.

NOTATION

a = constant
A = constant as defined by Equation (16)
b = function of density
B = function of reduced temperature
C = constant
d, e, f, g = constants for Equation (19)
f_k = thermal-conductivity correction factor to dilute gases for Equation (1)
k = thermal conductivity at any temperature and pressure
k^* = thermal conductivity at low pressures (P_R essentially equal to zero)
$k_{T_c}{}^*$ = thermal conductivity at low pressures and the critical temperature
k_c = thermal conductivity at the critical point
k_c' = pseudocritical thermal conductivity
k_N = normalized thermal conductivity,

$$\frac{k}{\frac{\kappa}{\sigma^2}\sqrt{\frac{\epsilon N}{M}}}$$

Table 4. Comparison of Thermal Conductivities Calculated From Figure 7 With Experimental Values for Some Gaseous Mixtures At Low Pressures

System	Mole Fraction	Temp., °K.	Maximum	Average	References
Helium-argon	He = 0.270, 0.454, 0.847, 0.946	273	14.5	8.7	*56*
Nitrogen-argon	N_2 = 0.204, 0.359, 0.611, 0.780	273	1.9	1.1	*58*
Air*	— — — —	90–873	6.3	1.9	*21, 44, 52*
Carbon monoxide–air	CO = 0.108, 0.321, 0.562, 0.978	291	5.6	5.0	*13*

*The pseudocritical constants for air were calculated to be T_c' = 132.2 °K. and k_c' = 9.08 × 10^{-5} cal./(sec.)(cm.)(°K.). A total of 14 experimental points were used to calculate the % deviation.

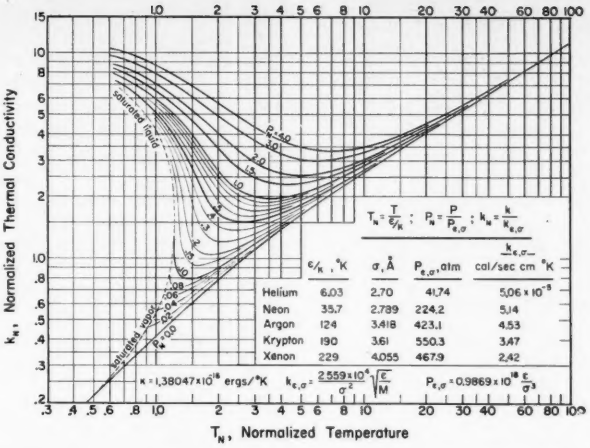

Fig. 8. Normalized thermal-conductivity correlation for the inert gases (after Hirschfelder, Curtiss, and Bird method).

k_R = reduced thermal conductivity, k/k_c

k_R^* = reduced thermal conductivity at low pressures, k^*/k_c

M = molecular weight

N = Avogadro number, 6.0228×10^{23} molecules/gram-mole

N_i = mole fraction of ith component

P = absolute pressure, atm.

P_c = critical pressure, atm.

P_c' = pseudocritical pressure, atm.

P_N = normalized pressure, $P/\epsilon/\sigma^3$

P_R = reduced pressure, P/P_c

r = intermolecular distance, Å.

R = gas constant

T = absolute temperature, °K.

T_c = critical temperature, °K.

T_c' = pseudocritical temperature, °K.

T_N = normalized temperature, $T/\epsilon/\kappa$

T_R = reduced temperature, T/T_c

T_R' = pseudoreduced temperature, T/T_c'

Greek Letters

α = constant for Equation (2)

β = molecular volume

ϵ = maximum energy of attraction between two gas molecules at low pressures, ergs

κ = Boltzmann constant, 1.38047×10^{-16} ergs/°K.

μ = viscosity

μ^* = viscosity at low pressures

μ_c = viscosity at the critical point

μ_R = reduced viscosity, μ/μ_c

μ_R^* = reduced viscosity at low pressures, μ^*/μ_c

ρ = density, g./cc.

ρ_c = critical density, g./cc.

σ = distance between centers of two colliding gas molecules, Å.

$\varphi(r)$ = Lennard-Jones potential-energy function

χ = collision frequency factor

ω = expansion factor for the liquid state

$\Omega^{(2,2)*}[T_N]$ = Lennard-Jones transport-property function

LITERATURE CITED

1. Abas-Zade, A. K., *Zhur. Eksptl. Teort. Fiz.*, **23**, 60 (1952).
2. Borovik, E., *ibid.*, **17**, 328 (1947).
3. Bowers, R., *Proc. Phys. Soc. (London)*, **65A**, 511 (1952).
4. Bromley, L. A., *U. S. Atomic Energy Comm. Tech. Inform. Service UCRL-1852* (1952).
5. Chow, W. M., and J. A. Bright, Jr., *Chem. Eng. Progr.*, **49**, 175 (1953).
6. de Boer, J., and R. J. Lunbeck, *Physica*, **14**, 520 (1948).
7. Enskog, David, *Kgl. Svenska Vetenskapsakad. Handl.*, **63**, No. 4 (1922).
8. Eucken, A., *Forsch. Gebiete Ingenieurw.*, **11B**, 6 (1940).
9. Foz Gazulla, O. R., and S. S. Perez, *Anales fiz. y quim. (Madrid)*, **39**, 399 (1943).
10. Franck, E. U., *Z. Elektrochem.*, **55**, 636 (1951).
11. Gamson, B. W., *Chem. Eng. Progr.*, **45**, 154 (1949).
12. Grenier, C., *Phys. Rev.*, **83**, 598 (1951).
13. Gruss, H., and H. Schmick, *Wiss. Veröffentl. Siemens-Konzern*, **7**, 202 (1928).
14. Hirschfelder, J. O., C. F. Curtiss, and R. B. Bird, "Molecular Theory of Gases and Liquids," pp. 534–578, John Wiley and Sons, New York (1954).
15. *Ibid.*, pp. 633–634.
16. *Ibid.*, pp. 634–652.
17. Holburn, L., H. Schultze, and J. Otto, "*Handbuch der Experimentalphysik*, Vol. VIII, p. 152, Leipzig Akademische Verlagsgesellschaft, M. B. H. (1929).
18. Hougen, O. A., and K. M. Watson, "Chemical Process Principles," pp. 479–535, John Wiley and Sons, New York (1947).
19. Johnston, H. L., and E. R. Grilly, *J. Chem. Phys.*, **14**, 233 (1946).
20. Kamerlingh Onnes, H., and C. A. Crommelin, *Communs. Phys. Lab., Univ. Leiden*, No. 118b (1910).
21. Kannuluik, W. G., and E. H. Carman, *Australian J. Sci. Research*, **A4**, 305 (1951).
22. ———, *Proc. Phys. Soc. (London)*, **65B**, 701 (1952).
23. Kannuluik, W. G., and H. B. Donald, *Australian J. Sci. Research*, **A3**, 417 (1950).
24. Kannuluik, W. G., and L. H. Martin, *Proc. Roy. Soc. (London)*, **A144**, 496 (1934).
25. Keyes, F. G., *Trans. Am. Soc. Mech. Engrs.*, **73**, 589 (1951).
26. *Ibid.*, 597.
27. *Ibid.*, **76**, 809 (1954).
28. *Ibid.*, **77**, 1395 (1955).
29. ———, and D. J. Sandell, Jr., *Ibid.*, **72**, 767 (1950).
30. Lange, N. A., "Handbook of Chemistry," 7 ed., pp. 1458, 1464, Handbook Publishers, Inc., Sandusky, Ohio (1949).
31. Lenoir, J. M., and E. W. Comings, *Chem. Eng. Progr.*, **47**, 223 (1951).
32. Lenoir, J. M., W. A. Junk, and E. W. Comings, *ibid.*, **49**, 539 (1953).
33. Maslan, F. D., and T. M. Littman, *Ind. Eng. Chem.*, **45**, 1566 (1953).
34. Maxwell, J. C., "Collected Works," Vol. II, p. 1, Cambridge University Press, London (1890).
35. Michels, A., and A. Botzen, *Physica*, **19**, 585 (1953).
36. Michels, A., Hub Wijker, and Hk. Wijker, *ibid.*, **15**, 627 (1949).
37. Nathan, M. F., and E. W. Comings, *Ind. Eng. Chem.*, **39**, 964 (1947).
38. Nelson, L. C., and E. F. Obert, *Trans. Am. Soc. Mech. Engrs.*, **76**, 1057 (1954).
39. Owens, E. J., M.S. thesis, Northwestern Univ., Evanston, Ill. (1956).
40. Powers, R. W., R. W. Mattox, and H. L. Johnston, *J. Am. Chem. Soc.*, **76**, 5968 (1954).
41. Rothman, A. J., *U. S. Atomic Energy Comm., Tech. Inform. Service UCRL-2339* (1954).
42. Sakiadis, B. C., and Jesse Coates, *A.I.Ch.E. Journal*, **1**, 275 (1955).
43. *Ibid.*, **2**, 88 (1956).
44. Schmidt, A. F., and B. H. Spurlock, Jr., *Trans. Am. Soc. Mech. Engrs.*, **76**, 823 (1954).
45. Soddy, F., and A. J. Berry, *Proc. Roy. Soc. (London)*, **A84**, 576 (1911).
46. Sutherland, William, *Phil. Mag.*, **40**, 421 (1895).
47. Thomas, L. B., and R. C. Golike, *J. Chem. Phys.*, **22**, 300 (1954).
48. Ubbink, J. B., and W. J. de Haas, *Physica*, **10**, 465 (1943).
49. Uhlir, A., Jr., *J. Chem. Phys.*, **20**, 463 (1952).
50. Uyehara, O. A., and K. M. Watson, *Natl. Petroleum News, Tech. Sec.*, **36**, R764 (Oct. 4, 1944).
51. van der Waals, J. D., *Beibl. Ann. Physik*, **5**, 250 (1881).
52. Vargaftik, N. B., and O. A. Oleshchuk, *Izvest. V.T.I.*, **15**, No. 6, 7 (1946).
53. Vargaftik, N. B., and I. D. Parfenov, *J. Exptl. Theoret. Phys. (U.S.S.R.)*, **8**, 189 (1938).
54. Vines, R. G., *Australian J. Chem.*, **6**, 1 (1953).
55. ———, and L. A. Bennett, *J. Chem. Phys.*, **22**, 360 (1954).
56. Wachsmuth, J., *Physik. Z.*, **9**, 235 (1908).
57. Watson, K. M., *Ind. Eng. Chem.*, **35**, 398 (1943).
58. Weber, S., *Ann. Physik*, **54**, 481 (1917).

Kinetics of Aldehyde Hydrogenation: Vapor-phase Flow System and Supported Nickel Catalyst

C. C. OLDENBURG and HOWARD F. RASE

University of Texas, Austin, Texas

A kinetic study of the catalytic vapor-phase hydrogenation of three aldehydes (acetaldehyde, propionaldehyde, and *n*-butyraldehyde) was made at low conversions with a commercial supported nickel catalyst. A simple initial rate equation was determined and found to agree with a mechanism suggested by the ideal kinetics of Hougen and known experimental evidence. By means of this equation the relative reactivities of the aldehydes were compared and found to agree with the predictions of organic theory. An improved reactor designed to ensure isothermal operation is described.

It would seem that experimentation in applied kinetics should have objectives in addition to the determination of a rate equation or apparent mechanism for a particular reaction. It is well known that an experimentally determined rate equation for a reaction over a given catalyst often has limited usefulness. The kinetic constants are applicable with certainty only for the one catalyst and the range of experimental conditions. It is possible, however, to develop data and concepts of general usefulness from a study of any specific reaction, particularly if certain general objectives are selected during the early stages of a project.

The objectives of the work described in this paper are listed below. The criterion for selection was the extent of their contribution to improved methods for the application of kinetics to process design and development.

C. C. Oldenburg is now with California Research Corporation, Richmond, California.

OBJECTIVES

1. To determine a rate equation and rate constants for the catalytic vapor-phase hydrogenation of aldehydes to the corresponding alcohols by use of a supported nickel catalyst.
2. To determine the relative reactivities of the three aldehydes and the feasibility of correlating kinetic data for members of a family of compounds for engineering purposes.
3. To demonstrate an improved experimental reactor, designed to ensure nearly isothermal operation.
4. To reemphasize the value of theoretical organic chemistry in establishing rate equations useful for design and in comparing reaction rates of members of a family of compounds.

PREVIOUS WORK WITH ALDEHYDES

Although many aldehydes are catalytically hydrogenated to corresponding alcohols on an industrial scale, the kinetics of the reaction has received little attention. The fundamental work done thus far, however, has established that the hydrogenation of aldehydes over nickel at temperatures near 150°C. involves addition across the olefinic bond of the enol form (*2, 3, 7, 10*). Palmer (*7a*), studying the reverse reaction on copper (dehydrogenation of ethyl, *n*-propyl, and *n*-butyl alcohols), found the rates and temperature coefficients to be equal.

EXPERIMENTAL REACTOR—DESIGNED FOR ISOTHERMAL OPERATION

The usual fixed-bed experimental reactor does not have sufficient heat transfer surface for removing the heat of reaction fast enough to prevent a sizable temperature change. This is true in most cases even when the catalyst is mixed at random with inert material. An example is a reactor ½ in. in diameter by 3 in. long in which it is desired to

hydrogenate 0.1 g.-mole of propionaldehyde/hr. If the catalyst bed temperature is 5°F. above the jacket temperature and the over-all heat transfer coefficient is 10 B.t.u./(hr.)(sq. ft./°F.), the heat transfer out of the reactor would be about 1.6 B.t.u./hr., but the heat released by the reaction is about 6 B.t.u./hr., therefore, the heat of reaction could not be removed under these conditions and the bed temperature would probably rise excessively.

A solution to this design problem is to make the catalyst section smaller in diameter but greater in length. This was accomplished by use of a ¼-in., 20 B.W.G. tube, the catalyst pellets being spaced at sufficient distances to permit removal of the heat of reaction.

The jacketed reactor used in this study is shown in Figure 1. It is made of a length of ¼-in. 20 B.W.G. type-304 stainless steel tubing. Heating, vaporizing, and mixing of the reactants takes place in the upper section. Twelve catalyst pellets (⅛- by ⅛-in. cylinders) are spaced by ⅞-in. spacers made from a ⅛-in. rod of type-304 stainless steel. Two thermowells provide catalyst-bed inlet and outlet temperature-measurement points. A temperature-controlled "Ucon" heat transfer fluid was circulated through the jacket at about 3.5 gal./min. The jacket inlet and outlet temperatures were held to within 1°C. Arranging and spacing the catalyst pellets as indicated in Figure 1 results in high linear velocities and good transfer of the exothermic heat of reaction to the jacket thus providing a substantially isothermal reactor if conversions are held to a reasonably low value, i.e., less than 6%. A typical set of temperatures data is as follows:

Location	Temperature, °C.
Reactor inlet (top)	150.2
Reactor outlet (bottom)	150.4
Jacket inlet (bottom)	150.2
Jacket outlet (top)	150.0

Such a small temperature rise, 0.2°C., indicates a substantially isothermal catalyst bed.

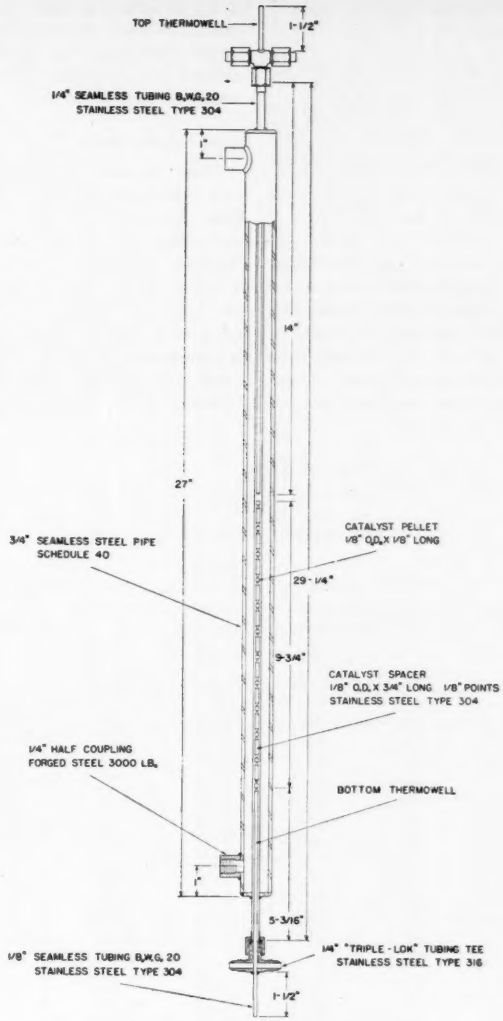

Fig. 1. Reactor drawing.

EXPERIMENTAL DETAILS

Reactants

Aldehydes manufactured by Carbide and Carbon Chemicals Company were employed. Purity limits established by infrared and chemicals methods are listed below together with methods of purification. Acetaldehyde as received was subjected to several types of analysis for purity. Comparison of its infrared spectrum with literature data indicated high purity. Peaks characteristic of water, acid, alcohol, and aldol were not found. The other aldehydes were not of equivalent purity and were distilled as indicated.

Purified propionaldehyde and *n*-butyraldehyde were redistilled 3 hr. prior to a series of runs and stored under nitrogen. Such redistillation was not found necessary for acetaldehyde.

	Maximum purity, %	Maximum water, %	Maximum acid, %	Purification method
Acetaldehyde	98	0.1	0.01	No purification required
Propionaldehyde	99	0.1	0.01	Several distillations followed by treatment with type 4A (Linde Air Products) molecular sieves
n-Butyraldehyde	99	0.1	0.01	Distillation

Analysis

A Beckman IR-2 infrared spectrophotometer was used to measure the alcohol concentration in the condensed reactor effluent. Wave lengths used were for ethanol, 2.88; *n*-propanol, 2.83; and *n*-butanol, 2.91 μ.

Catalyst

A commercial hydrogenation catalyst Ni-0101 T-⅛ in. manufactured by Harshaw Chemical Company was used. It or a similar catalyst has been used by a number of workers for hydrogenation studies (*1, 4, 6, 8, 12, 14*). The catalyst was reduced *in situ* at 250° to 350°C. and 50 lb./sq. in. abs. Hydrogen flow rate was 25 liters/(hr.) (g. of catalyst) for 16 hr. In the reduced state the catalyst is 80% nickel and 20% kieselguhr.

Experimental Procedure

A schematic flow diagram of the system is given in Figure 2. The reactor temperature was maintained by circulating Ucon fluid. Data were taken when the optical density of the reactor effluent became constant after introduction of feed or change in conditions (5 to 30 min.). At regular intervals during a series of runs feed aldehyde was introduced to the infrared cell to establish the blank optical-density reading.

Homogeneous Reaction and Catalytic Effects of Equipment

Runs made in the absence of catalyst showed no conversion of aldehyde. It can thus be concluded that the homogeneous reaction was negligible and that the metal walls of the system had no catalytic effect.

Side Reactions

At high temperatures and low space velocities, conditions would seem to be better for side reactions than under less drastic conditions. Infrared analysis of the hydrogen off gas from such runs however indicated no evidence of expected hydrogenolysis products such as hydrocarbons, carbon monoxide, and carbon dioxide. Infrared analysis of the liquid indicated the presence of only alcohol and aldehyde. Therefore, no side reactions were observed.

Mass Transfer Effects

Mass transfer was indicated to be non rate controlling by the observation that the rate of reaction was definitely dependent on total pressure. A more rigorous method of establishing mass transfer effects is to measure conversion at different combinations of flow and catalyst weight such that the time factor is maintained constant. This method was used and results showed that mass transfer effects were negligible.

TABLE 1
RUN DATA
HYDROGENATION OF PROPIONALDEHYDE

Run	Temp., °C.	Partial Pressures, lb./sq. in. abs. Aldehyde P_u	Hydrogen P_H	Space velocity g. moles/(hr.)(g.) (F_u/W)	Conversion, % x	Initial rate of reaction, g. moles/(hr.)(g.) Measured	Corrected r_0
Unreduced Catalyst Weight = 0.7961 g.							
6B	150.5	10.0	10.0	2.51	2.00	0.0502	0.0502
6C	149.2	15.0	15.0	2.51	2.63	0.0660	0.0660
6D	150.6	20.0	20.0	2.51	3.04	0.0763	0.0763
6E	150.0	22.5	22.5	2.51	3.20	0.0803	0.0803
6F	149.9	25.0	25.0	2.51	3.37	0.0846	0.0846
6G	150.3	27.5	27.5	2.51	3.48	0.0874	0.0874
6H	149.8	30.0	30.0	2.51	3.60	0.0904	0.0904
7A	174.7	14.3	15.7	4.13	2.56	0.106	0.108
7B	174.9	20.0	20.0	3.79	3.05	0.116	0.118
7C	175.0	25.1	24.9	3.79	3.25	0.123	0.125
7D	174.9	30.1	29.9	3.79	3.55	0.135	0.137
7E	175.4	27.6	27.4	3.79	3.43	0.130	0.132
7F	173.8	22.6	22.4	3.79	3.12	0.118	0.120
7G	174.5	17.5	17.5	3.79	2.90	0.110	0.112
7H	175.4	10.0	10.0	3.79	2.28	0.0864	0.0880
7I	174.4	15.0	15.0	3.73	2.80	0.104	0.106
7J	173.8	12.5	12.5	3.73	2.46	0.0932	0.0949
8A	149.4	16.3	13.7	2.95	2.47	0.0729	0.0755
8B	150.4	14.4	15.6	2.95	2.23	0.0657	0.0680
8C	150.1	12.9	17.1	2.95	1.85	0.0545	0.0564
8D	150.4	11.1	18.9	2.95	1.57	0.0463	0.0479
8E	150.1	9.8	20.2	2.95	1.33	0.0392	0.0406
8F	149.2	16.3	13.7	2.95	2.47	0.0729	0.0755
8H	150.7	15.2	14.8	1.29	5.45	0.0703	0.0728
8I	148.5	15.4	14.6	3.98	1.77	0.0703	0.0728
8J	149.1	15.9	14.1	7.05	0.92	0.0648	0.0671
9A	165.5	20.2	19.8	3.83	2.48	0.0950	0.100
9B	164.8	25.2	24.8	3.83	2.79	0.1070	0.113
9C	164.1	27.2	27.5	3.83	2.87	0.1100	0.116
9D	164.2	30.3	29.7	3.83	2.96	0.1130	0.119
9E	163.6	17.7	17.3	3.83	2.34	0.0895	0.0944
9F	164.0	15.0	15.0	3.83	2.13	0.0815	0.0860
9G	164.8	10.1	9.88	3.83	1.70	0.0650	0.0686
9H	164.1	20.2	19.8	3.83	2.49	0.0953	0.1005
16A	149.9	20.4	19.6	2.61	2.64	0.0689	0.0769
16B	150.0	25.5	24.5	2.61	2.90	0.0757	0.0845
16C	150.0	30.6	29.4	2.61	3.12	0.0815	0.0910
16D	149.9	28.0	27.0	2.61	2.98	0.0778	0.0868
16E	149.4	22.9	22.1	2.61	2.78	0.0726	0.0810
16F	150.4	17.8	17.2	2.61	2.45	0.0639	0.0713
16G	149.9	12.2	12.3	2.61	2.04	0.0532	0.0594
16I	150.5	15.3	14.7	2.61	2.38	0.0621	0.0643
16J	151.1	20.4	19.6	2.61	2.65	0.0691	0.0771

Catalyst Activity

Data for the three aldehydes are summarized in Tables 1, 2, and 3*. The range of variables is as follows:

Temperature, °C.	120–180
Pressure, lb./sq. in. abs.	20–60
Mole fraction hydrogen	0.4–0.7
Space velocity, g. moles/(hr.)(g.)	1.5–7
Conversion, %	0.5–3.5

The catalyst activity was checked at regular intervals by use of propionaldehyde hydrogenation as the base reaction. All data are therefore reported as corrected to a single base activity by use of the activity factor described by Hougen and Watson. The decline in activity for propionaldehyde after 64 runs was 10.4%, for *n*-butyraldehyde after 39 runs it was 5%, and for acetaldehyde after 26 runs it was 58%. The high decline in activity for acetaldehyde was probably due to some undetected impurity.

CALCULATION OF INITIAL RATES

The usual method of determining the initial rate of reaction is to measure conversion at various time factors (W/F) and to extrapolate the data to $x = 0$ and $(W/F) = 0$. The slope of the curve at $x = 0$ is the initial rate.

$$r_0 = \left[\frac{dx_u}{d\left(\frac{W}{F_u}\right)}\right]_{x_u=0} \qquad (1)$$

In this work it was found that at conversions up to 5% a plot of x vs. (W/F) was a straight line. Since the maximum conversion encountered was 3.5%, except for the runs that established the linear relationship, initial rates were calculated as follows:

$$r_0 = \frac{x_u}{\left(\frac{W}{F_u}\right)} = (x_u)\left(\frac{F_u}{W}\right) \qquad (2)$$

DETERMINATION OF RATE EQUATION

Because of the complexities associated with catalytic reactions it is imperative that a study of relative rates be approached in the simplest manner possible. Accordingly, only initial rates were considered in this work and a simple kinetic equation was selected to represent the data.

An equation of the form $r_0 = k(P_u)^m(P_H)^n$ was used to correlate the data. The exponents were restricted to integral and half-integral values in order further to simplify the study and subsequent use of the rate equations. By logarithmic correlation of the data the exponents were found to be $m = 1.0$ and $n = -0.5$ for the three aldehydes. Values of k were

*Complete tabular material has been deposited as document 5440 with the American Documentation Institute, Photoduplication Service, Library of Congress, Washington 25, D. C., and may be obtained for $1.25 for photoprints or 35-mm. microfilm.

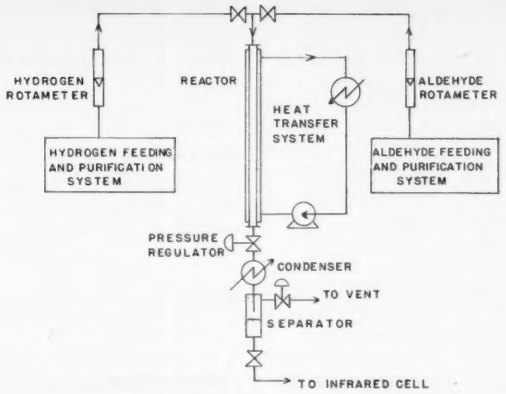

Fig. 2. Flow diagram of experimental unit.

computed by the method of least squares and fitted similarly to the Arrhenius equation. Results are summarized in Table 4.

These values show definite trends. The value of E is substantially constant for all the aldehydes and the value of A increases as the size of the aldehyde increases. This treatment, therefore, gives a quantitative measure of the reactivity of the three aldehydes. Values of k are highest for n-butyraldehydes and lowest for acetaldehyde.

POSSIBLE MECHANISM

Boudart (*5*) has emphasized the value of finding a mechanism based on classical kinetics which after the necessary simplification will give the rate equation selected by the method just described. The mechanism thus selected provides a theoretical framework for subsequent reasoning and speculation.

From plots of initial rate vs. total pressure, as described by Hougen (*15*), it was concluded that the controlling step is the adsorption of the aldehyde. It is further reasonable to assume that hydrogen is atomically adsorbed on the nickel surface. The initial rate equation for expressing these conditions is, according to Hougen and his associates: $r_0 = (k_A P_u)/(1 + K_H P_H)^{1/2}$. This equation may be simplified as suggested by Boudart (*5*) to $r_0 \cong k[P_u/(P_H)]^{1/2}$, which is the equation already shown to fit the data.

COMPARISON OF RELATIVE RATES FOR THE ALDEHYDES

In a comparison of, and an attempt to correlate, applied kinetic data on members of a family of compounds, it is valuable to employ knowledge of the chemistry of the reaction. The results have indicated that the higher the molecular weight of the aldehyde, the greater the initial rate of hydrogenation, in contrast to the behavior observed for the olefins. Ethylene hydrogenates faster than propylene and propylene faster than 1-butene (*6*). The controlling step in the hydrogenation of these two homologous series, however, is different. In olefin hydrogenation the surface reaction is rate controlling (*6*, *11*); whereas with aldehydes the adsorption of aldehyde controls. Thus, when a methyl group is substituted for a hydrogen atom on the ethylene molecule, the rate of surface reaction is decreased. But when a methyl group is substituted for an α-hydrogen atom on the acetaldehyde molecule, the rate of adsorption of the aldehyde is increased. There is no contradiction since different types of reactions are taking place.

Anderson and MacNaughton (*2*) and Badin and Pacsu (*3*) have found that the hydrogenation of an aldehyde involves enolization and addition on the olefinic double bond. On the basis of these findings it might be assumed that the following structure represents the carbonyl compound in a state ready for adsorption:

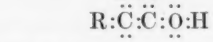

The α-carbon atom is a nucleophilic center. Any structural factor which tends to increase the electron density at a nucleophilic center will enhance its reactivity (*9*). When R is a methyl group the inductive effect is one of electron release, and the electron density at the α carbon of propionaldehyde would be expected to be higher than that of acetaldehyde. Similarly, an ethyl group results in a slightly larger electron release and n-butyraldehyde should have

TABLE 2
RUN DATA
HYDROGENATION OF n-BUTYRALDEHYDE

Run	Temp., °C.	Partial pressures, lb./sq. in. abs. Aldehyde P_u	Hydrogen P_H	Space velocity, g.-moles/(hr.)(g.) (F_u/W)	Conversion, % x	Initial rate of reaction, g.-moles/(hr.)(g.) Measured	Corrected r_0
		Unreduced Catalyst Weight = 0.7961 g.					
19A	160.4	20.4	19.6	1.61	2.63	0.0425	0.106
19B	160.3	25.5	24.5	1.61	2.94	0.0474	0.119
19C	160.1	30.6	29.4	1.61	3.06	0.0494	0.124
19D	159.6	28.1	26.9	1.61	3.14	0.0507	0.127
19E	159.5	23.0	22.0	1.61	2.90	0.0468	0.117
19F	159.5	17.9	17.1	1.61	2.76	0.0446	0.112
19G	159.6	12.7	12.3	1.61	2.37	0.0382	0.0955
24A	179.8	20.1	19.9	3.10	2.26	0.0702	0.181
24B	180.4	25.2	24.8	3.10	2.34	0.0726	0.187
24C	179.0	30.2	29.8	3.10	2.38	0.0740	0.191
24D	178.5	17.6	17.4	3.10	2.05	0.0636	0.164
24E	179.2	12.6	12.4	3.10	1.84	0.0572	0.147
24F	180.0	10.1	9.9	3.10	1.60	0.0497	0.128
24G	181.3	15.1	14.9	3.10	1.90	0.0590	0.152
24H	180.8	20.1	19.9	3.10	2.10	0.0652	0.168
26A	170.5	13.0	27.0	1.64	2.73	0.0450	0.117
26B	169.8	10.4	29.6	1.64	2.63	0.0433	0.113
26C	169.6	8.6	31.4	1.64	2.50	0.0412	0.107
26D	170.0	16.9	23.1	1.64	3.01	0.0496	0.129
26E	170.8	24.0	16.0	1.64	3.01	0.0496	0.129
26F	171.7	13.0	27.0	1.64	2.73	0.0450	0.117
28A	169.1	20.4	19.6	2.39	2.17	0.0517	0.136
28B	171.0	25.5	24.5	2.39	2.30	0.0548	0.145
28C	170.9	30.6	29.4	2.39	2.45	0.0584	0.154
28D	170.7	17.8	17.2	2.39	2.13	0.0507	0.134
28E	170.5	12.7	12.3	2.39	1.90	0.0452	0.119
28F	169.7	10.2	9.8	2.39	1.75	0.0417	0.110

an α-carbon atom of higher electron density than propionaldehyde. The higher the electron density of the α-carbon atom, the greater would be its affinity for centers on the catalyst of opposite charge. (In the presence of the aldehyde such sites as NiH^+ may be postulated as existing.) Therefore, on the basis of the inductive effect the rates of adsorption should increase as the size of R is increased. This prediction was substantiated experimentally.

The effect dies out rapidly as it is transmitted down a saturated chain (*9*); therefore, it would be expected that a bigger difference in rates should occur between acetaldehyde and propionaldehyde than between the latter and *n*-butyraldehyde. Initial rates calculated from the equations of Table 4 for the reaction of equimolar mixtures of hydrogen and aldehyde at 180°C. and 20 lb./sq. in. abs. indicate that relative reactivities are acetaldehyde 1.00, propionaldehyde 1.54, *n*-butyraldehyde 1.91.

Palmer (*7a*) observed constancy of rates and temperature coefficients within his experimental error for the reverse reactions on copper. In the present investigation of the forward reactions on nickel only the temperature coefficients remained constant. Because of the different catalyst and the difficulties experienced by Palmer in regulating flow rates, it is difficult to compare his findings with the initial rate data on the forward reaction of the present investigation.

Extrapolation of the observed trend in reactivity would seem dangerous since the inductive effect may become negligible in relation to steric effects, and it is certainly conceivable that the controlling step could be different in the hydrogenation of another aldehyde. It should be further emphasized that these data were taken at low conversions and that the effect of product composition has not been studied.

Table 3
Run Data
Hydrogenation of Acetaldehyde

Run	Temp., °C.	Partial pressures, lb./sq. in. abs. Aldehyde P_u	Hydrogen P_H	Space velocity, g.-moles/(hr.)(g.) (F_u/W)	Conversion, % x	Initial rate of reaction, g.-moles/(hr.)(g.) Measured	Corrected r_0
		Unreduced Catalyst Weight = 0.7784					
31A	129.5	13.8	27.3	3.12	3.04	0.0948	0.0224
31B	130.4	17.1	33.9	3.12	3.19	0.0995	0.0235
31F	130.6	8.86	17.5	3.12	2.77	0.0865	0.0204
31G	130.8	10.4	20.5	3.12	2.83	0.0884	0.0209
31H	131.6	12.1	23.8	3.12	2.98	0.0930	0.0220
31I	130.9	13.7	27.2	3.12	3.04	0.0948	0.0224
33D	121.1	17.0	33.7	3.12	1.72	0.0536	0.0154
33E	121.3	13.7	27.1	3.12	1.65	0.0514	0.0147
33F	119.2	10.5	20.6	3.12	1.54	0.0480	0.0138
33G	119.8	8.56	17.2	3.12	1.52	0.0473	0.0136
33H	120.9	12.0	23.8	3.12	1.56	0.0486	0.0139
33I	119.9	17.2	23.8	3.92	1.42	0.0556	0.0168
33J	118.9	13.2	27.8	3.92	0.99	0.0388	0.0118
33K	119.5	23.6	17.4	3.92	2.05	0.0803	0.0243
33L	121.5	20.0	21.0	3.92	1.46	0.0572	0.0173
33M	121.3	14.9	26.1	3.92	1.24	0.0486	0.0147
35D	139.9	17.4	17.7	5.90	1.35	0.0796	0.0316
35E	140.1	12.8	13.0	5.90	1.26	0.0743	0.0295
35F	139.7	11.0	11.2	5.90	1.22	0.0719	0.0285
35G	140.3	15.6	15.9	5.90	1.36	0.0802	0.0318

Table 4
Initial Rate Equation for the Hydrogenation of Aldehydes

$$r_0 = k\frac{P_u}{(P_H)^{1/2}}$$

$$\ln k = -\frac{E}{RT} + \ln A$$

	Acetaldehyde	Propionaldehyde	*n*-Butyraldehyde
E*	$+7.8 \pm 0.1 \times 10^3$	$+7.8 \pm 0.1 \times 10^3$	$+7.8 \pm 0.1 \times 10^3$
$\ln A$	+4.94	+5.17	+5.31
Average deviation, %	±13.6	±5.1	±6.9

*Actual values obtained are 7,890, 7,810, and 7,730, respectively.

ACKNOWLEDGMENT

The authors are indebted to Jefferson Chemical Company for providing materials, equipment, and laboratory space.

NOTATION

A = constant of the Arrhenius equation
E = constant of the Arrhenius equation
F = feed rate, g.-moles/hr.
K = adsorption-equilibrium constant
k = reaction-velocity constant
L = total number of molal-adsorption sites per mass of unreduced catalyst
P = partial pressure, lb./sq. in. abs.
r = reaction rate, g.-moles/(hr.)(g. unreduced catalyst)
R = gas constant
T = temperature, °K.
W = unreduced catalyst weight, g.
x = conversion of aldehyde, moles per mole fed
π = total pressure, lb./sq. in. abs.

Subscripts

H = hydrogen
u = aldehyde
o = initial

LITERATURE CITED

1. Akers, W. W., and R. R. White, *Chem. Eng. Progr.*, **44**, 553 (1948).
2. Anderson, L. C., and N. W. MacNaughton, *J. Am. Chem. Soc.*, **64**, 1456 (1942).
3. Badin, E. J., and E. Pacsu, *ibid.*, **66**, 1953 (1944).
4. Binder, G. G., and R. R. White, *Chem. Eng. Progr.*, **46**, 563 (1950).
5. Boudart, Michel, *A.I.Ch.E. Journal*, **2**, 62 (1956).
6. Fair, J. R., Jr., Ph.D. dissertation, Univ. of Texas, Houston (1955).
7. Friedman, Lewis, and J. Turkevich, *J. Am. Chem. Soc.*, **74**, 1669 (1952).

7a. Palmer, W. G., *Proc. Roy. Soc. (London)*, **107A**, 255 (1925).

8. Pursley, J. A., R. R. White, and C. M. Sliepcevich, *Chem. Engr. Prog. Symposium Series* No. 4, **48**, 51 (1952).
9. Royals, E. E., "Advanced Organic Chemistry," Prentice-Hall, New York (1954).
10. Sabatier, Paul, *Compt. rend.*, **136**, 738, 921, 983 (1903).
11. Sussman, M. N., and Charles Potter, *Ind. Eng. Chem.*, **46**, 457 (1954).
12. Tschernitz, J. L., S. Borstein, R. B. Beckmann, and O. A. Hougen, *Trans. Am. Inst. Chem. Engrs.*, **42**, 883 (1946).
13. Weller, Sol, *A.I.Ch.E. Journal*, **2**, 59 (1956).
14. Wilson, J. M., J. W. Otves, D. P. Stevenson, and C. O. Wagner, *Ind. Eng. Chem.*, **45**, 1480 (1953).
15. Yang, K. H., and O. A. Hougen, *Chem. Eng. Progr.*, **46**, 146 (1950).

Vapor-liquid–equilibrium Data for the Ternary System Cyclohexane-heptane-toluene

H. S. MYERS

C. F. Braun and Company, Alhambra, California

Previous papers have reported equilibrium data for the binary systems cyclohexane-heptane, heptane-toluene, and cyclohexane-toluene. This present study gives similar data for the ternary system cyclohexane-heptane-toluene and compares the activity coefficients with those predicted from the three limiting binaries.

The ternary activity coefficients fall well in line between the limiting-binary data. Distribution is about as would be predicted by the ternary Margules equations. As an approximation, if the coefficients are plotted as a function of the aromatic concentration only, without consideration of the ratio of naphthenes to paraffins, reasonably good correlation is observed.

Previous papers (*1, 3, 4*) have reported equilibrium data for the binary systems cyclohexane-heptane, heptane-toluene, and cyclohexane-toluene. This work gives ternary equilibrium-data for the system cyclohexane-heptane-toluene and compares the computed activity coefficients with those predicted from the three limiting-binaries.

APPARATUS

The equilibrium apparatus, Figure 1, has been described in detail in an earlier article (*1*). It is of the vapor-recirculating type and uses a vapor jacket to maintain adiabatic operation. All parts are glass except for the Teflon sample valves. The heating elements, which are fused into a borosilicate glass tube, are completely enclosed with glass. Except for sampling, operation is entirely automatic.

PURIFICATION OF HYDROCARBONS

All three of the hydrocarbons used in this work were purified before use. Complete details concerning the source, the method of purification, and the physical properties are given in earlier articles (*2, 3*).

ANALYSIS

Normally, the chief problem involved in studying a ternary system is that of analysis. The system cyclohexane-heptane-toluene is ideal for a naphthene-paraffin-aromatic study, because it can be analyzed simply and accurately. As

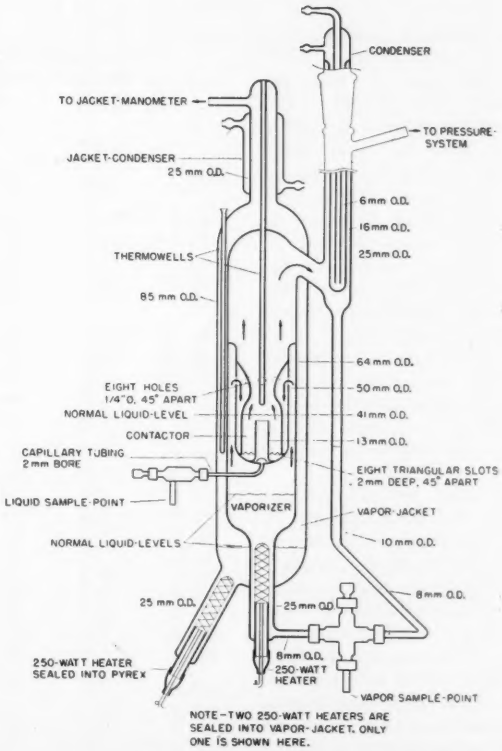

Fig. 1. Vapor-recirculating still.

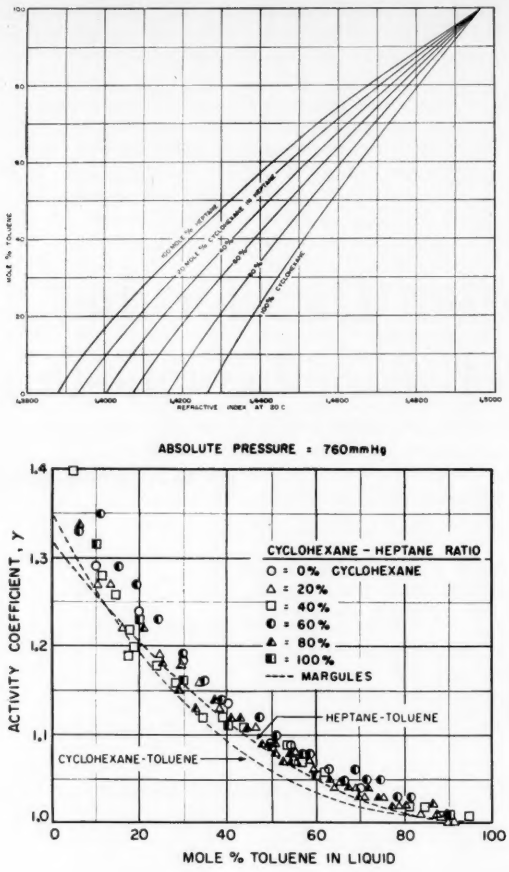

toluene can be removed quantitatively from cyclohexane and heptane with concentrated sulfuric acid at room temperature without affecting either the cyclohexane or the heptane, it is possible to analyze mixtures of these three hydrocarbons by reading the refractive index before and after acid extraction. Calibration curves, shown in Figure 2, were made up with known mixtures. In addition to these curves, one requires the refractive-index–composition curve for the cyclohexane-heptane binary, which was determined previously (*4*).

Extractions were made in cream-test bottles with an acid-to-hydrocarbon ratio of 10 to 1. Fifteen minutes in the laboratory shaker was found to be sufficient time for complete toluene extraction.

Tests made with known mixtures showed that the acid-extraction step in the analytical procedure does not appreciably decrease the precision. Accuracy is limited primarily by the reproducibility in refractometer readings. The worst case is represented by the cyclohexane-heptane binary, where there is a spread of 385 fourth-place points on the refractometer between the pure components. Refractometer readings can be reproduced to ±1 point, an accuracy of about ±0.25%.

RANGE

All three of the limiting-binary mixtures for this ternary system had been studied earlier (*1, 3, 4*). In order to cover the entire range of intermediate ternary compositions, mixtures containing 20 mole % cyclohexane in heptane, 40 mole %, 60%, and 80% were blended. Each of these mixtures was then studied in the still with varying amounts of toluene.

Fig. 2. Toluene analysis, cyclohexane-heptane-toluene mixtures.

All work was carried out isobarically at 760 mm. Hg absolute pressure.

RESULTS

Experimental equilibrium data for the ternary system, along with computed activity coefficients, are listed in Tables 1, 2, 3, and 4. Similar data for the three limiting binaries were reported earlier (*1, 3, 4*).

Fig. 3. Toluene activity coefficients, system—cyclohexane, heptane, toluene. Absolute pressure = 760 mm. Hg.

Toluene

Figure 3 is a plot of the activity coefficients for toluene computed from the experimental data.

The binary coefficients for toluene in cyclohexane and in heptane are also

Table 1

Vapor-liquid-equilibrium Data, Cyclohexane-Heptane-Toluene Ratio—Cyclohexane to Heptane = 0.25 in Charge to Still Absolute Pressure = 760 mm. Hg

Temp.,	Composition, mole % Liquid		Vapor		Activity coefficient		
°C.	CH	C7	CH	C7	CH	C7	Tol
95.0	15.7	81.8	23.3	74.8	0.99	1.01	1.20
95.6	14.4	75.2	21.7	69.8	0.99	1.01	1.27
96.1	14.0	69.5	21.2	65.8	0.98	1.01	1.22
96.75	12.3	62.8	19.0	61.3	0.98	1.02	1.19
97.2	11.3	58.8	17.8	57.5	0.99	1.01	1.18
97.65	10.6	55.5	17.1	56.0	1.00	1.03	1.16
98.15	9.7	52.0	16.1	53.8	1.01	1.04	1.13
98.75	9.2	47.8	15.7	50.3	1.02	1.04	1.12
99.1	8.7	45.3	14.6	48.9	1.00	1.06	1.11
99.7	7.9	41.2	14.0	44.7	1.03	1.07	1.09
100.25	7.3	37.6	12.9	43.1	1.02	1.08	1.08
100.25	7.5	36.6	13.4	32.5	1.02	1.10	1.07
100.8	6.7	34.6	11.9	40.9	1.02	1.10	1.07
100.9	7.2	33.2	12.7	39.8	1.00	1.12	1.06
101.35	6.1	31.4	11.3	38.3	1.04	1.12	1.06
101.5	6.0	30.0	11.4	37.5	1.05	1.14	1.04
101.9	5.4	29.1	10.4	36.4	1.06	1.13	1.05
102.4	5.3	26.0	10.3	33.7	1.06	1.15	1.04
102.8	4.9	24.1	9.7	31.8	1.07	1.16	1.03
103.6	4.2	20.1	8.6	27.7	1.07	1.19	1.03
104.8	3.3	16.5	6.9	24.3	1.07	1.23	1.02
105.7	2.7	13.4	5.7	20.0	1.06	1.21	1.01
106.5	2.2	10.5	4.8	16.9	1.07	1.28	1.01
107.0	1.9	8.7	4.2	14.8	1.11	1.32	1.00
107.6	1.4	7.1	3.5	12.4	1.18	1.35	1.00

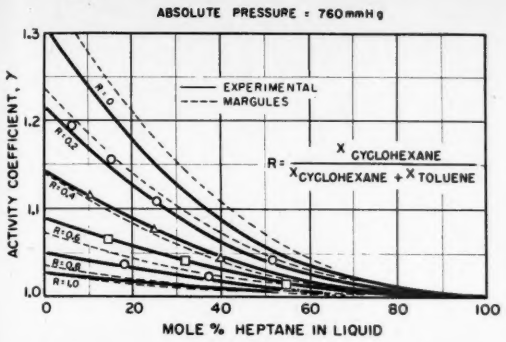

Fig. 4. Heptane activity coefficients, system—cyclohexane, heptane, toluene. Absolute pressure = 760 mm. Hg.

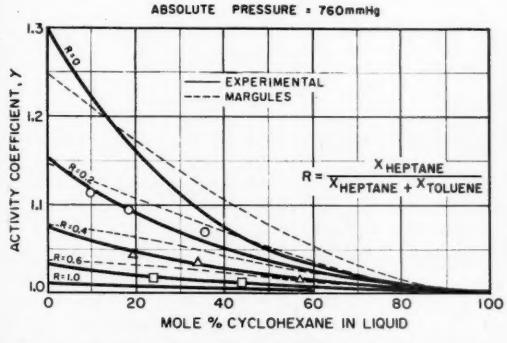

Fig. 5. Cyclohexane activity coefficients, system—cyclohexane, heptane, toluene. Absolute pressure = 760 mm. Hg.

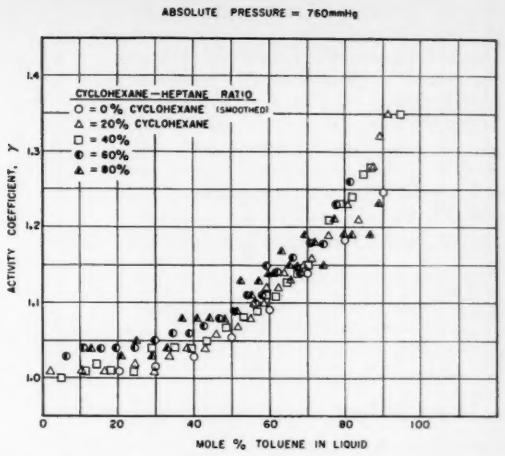

Fig. 6. Heptane activity coefficients, system—cyclohexane, heptane, toluene. Absolute pressure = 760 mm. Hg.

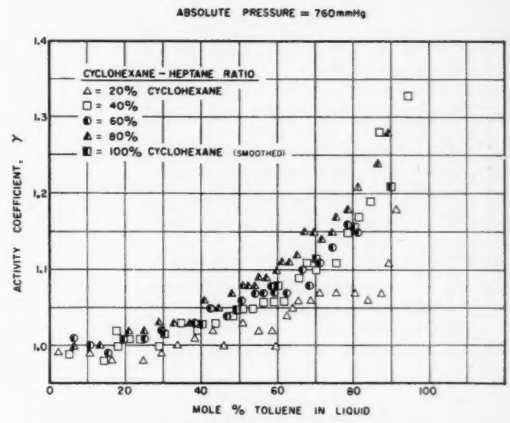

Fig. 7. Cyclohexane activity coefficients, system—cyclohexane, heptane, toluene. Absolute pressure = 760 mm. Hg.

plotted. It can be seen from this plot that the activity-coefficient curve for toluene is essentially the same in cyclohexane as in heptane and in all ternary mixtures with cyclohexane and heptane that were studied.

The activity coefficients discussed here are defined as $\pi Y/PX$ where π is the total pressure of the system and P is the vapor pressure of the pure component at the system temperature. Vapor pressures were taken from data published by the National Bureau of Standards, A.P.I. Project 44 (1953).

Heptane

The binary activity-coefficient curve for heptane in toluene is quite different from the curve for heptane in cyclohexane, as can be seen in Figure 4. As would be expected, the ternary activity coefficients for heptane fall between the curves for the two limiting binaries. The lines shown in Figure 4 as representing the binary activity coefficients are smoothed curves. The data points have been omitted for

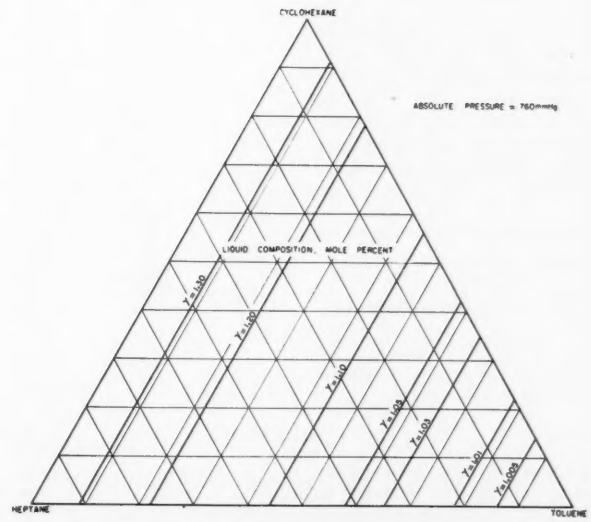

Fig. 8. Toluene activity coefficients—cyclohexane, heptane, toluene. Absolute pressure = 760 mm. Hg.

sake of clarity but are shown later in Figure 11. The ternary points shown in Figure 4 represent experimental values but cannot be plotted directly from the tabulated data. First the heptane activity coefficients from Tables 1 to 4 are plotted against percentage of heptane, with the various cyclohexane-heptane ratios as parameters. Then, with the same parameters, the activity coefficients are plotted against the ratio of heptane to heptane

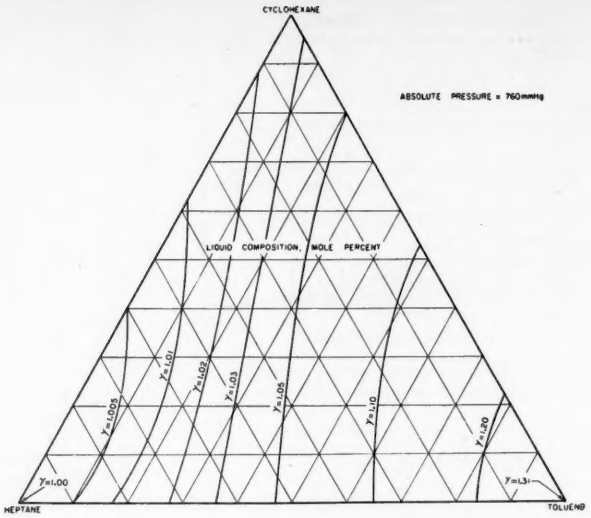

Fig. 9. Heptane activity coefficients, cyclohexane, heptane, toluene. Absolute pressure = 760 mm. Hg.

plus toluene. From these two plots, Figure 4 can be constructed.

Cyclohexane

Figure 5 shows the corresponding activity-coefficient curves for cyclohexane. As is the case for heptane, the ternary points fall in line between the limiting-binary curves.

Approximate Correlation

Another way of plotting the activity coefficients for cyclohexane and heptane is to plot them as a function of the toluene concentration only; that is, the effect

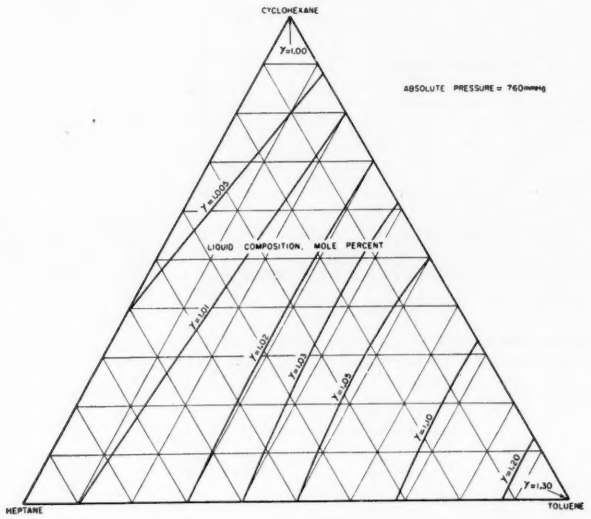

Fig. 10. Cyclohexane activity coefficients, cyclohexane, heptane, toluene. Absolute pressure = 760 mm. Hg.

of the varying naphthene-paraffin ratio is neglected. Figure 6 shows such a plot for heptane. There is some scatter in the points but they fall in a fairly narrow band.

For cyclohexane, in Figure 7, the scatter is worse, but there is still a rough correlation.

The value of such an approximate correlation does not, of course, lie in predicting ternary data. There are better procedures for ternaries. But when the designer is faced with a multicomponent problem on a mixture containing all three molecular types, he either must assume that the mixture is ideal, or he must

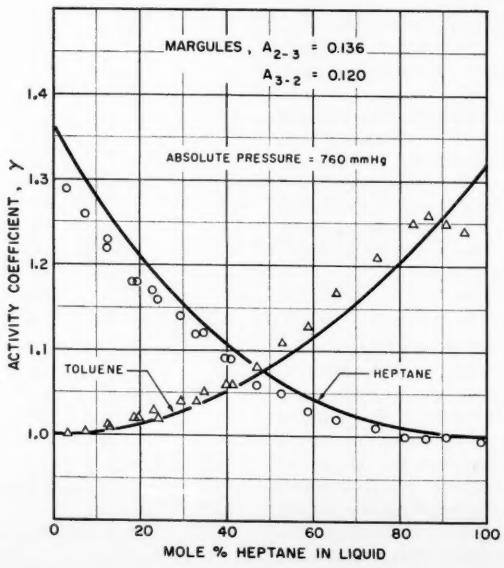

Fig. 11. Activity coefficients, heptane-toluene.

assign some arbitrary values for the activity coefficients. Here is a reasonable basis for choosing these values.

Alternative Plot

An alternative method of plotting ternary activity coefficients is shown in Figures 8, 9, and 10, in which lines of constant activity coefficient are plotted on a triangular diagram. There are advan-

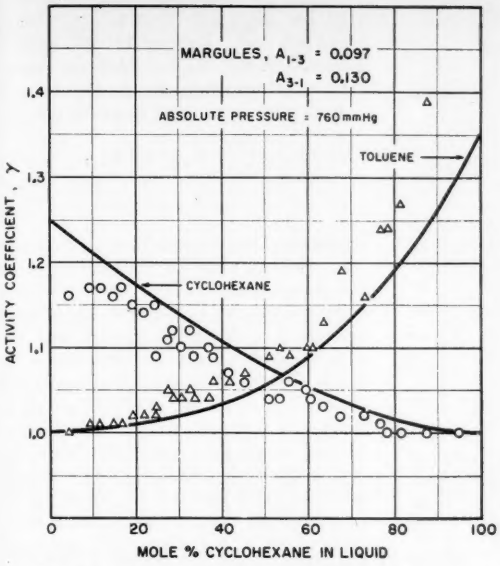

Fig. 12. Activity coefficients, cyclohexane-toluene.

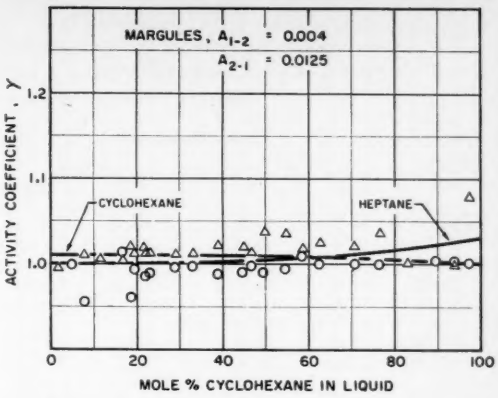

Fig. 13. Activity coefficients, cyclohexane-heptane.

tages for both types of plots. The first type, Figures 3, 4, and 5, is usually better for working up experimental data. Interpolation is normally more obvious than with a triangular plot. If only the limiting-binary data are known, the intermediate activity-coefficient lines can be sketched in by eye between the binary curves as a rough approximation.

For actually using the activity-coefficient curves, however, as in making tray calculations, the triangular plots are more convenient. Activity coefficients can be read directly as a function of the ternary composition, not as a ratio of compositions.

Ternary Curves from Binary Data

Complete vapor-liquid-equilibrium data for ternary systems are rare in the literature, and quaternary data are practically nonexistent. When designers need such information, they frequently attempt to predict the ternary or quaternary system from binary data by means of one of the thermodynamic equations. The ternary and quaternary Margules equations derived by Wohl and described by Perry (*5*) are most commonly used. These equations are derived from the two-constant, binary Margules equations and make the same simplifying assumptions plus one or two more. Nowhere in the literature have they been checked with experimental data. The present data, on a hand-picked system of a naphthene, a paraffin, and an aromatic seemed to offer a good opportunity of checking the theoretical equations.

The first step in predicting ternary activity coefficients from binary data by the Margules equations is to evaluate the Margules constants for each of the three limiting binaries. Figures 11, 12, and 13 show how this was done for heptane-toluene, cyclohexane-toluene, and cyclohexane-heptane. For each system the lines represent what were considered the best pair of Margules curves through the data points. This, of course, is somewhat a matter of personal interpretation, but in general the philosophy is to get the best average fit over the widest possible area without too much reliance on data points near the pure materials, where the accuracy is poorest. The constants for each binary are listed on the plots and are numerically equal to the logarithms of the terminal activity coefficients indicated by the Margules curves.

The dotted lines on Figures 3, 4, and 5 show the ternary activity coefficients

Table 2
Vapor-liquid-equilibrium Data, Cyclohexane-heptane-toluene
Ratio—Cyclohexane to Heptane = 0.67 in Charge to Still
Absolute Pressure = 760 mm. Hg

Temp.,	Composition, mole % Liquid		Vapor		Activity coefficient		
°C.	CH	C7	CH	C7	CH	C7	Tol
91.2	36.1	58.9	48.4	47.7	0.99	1.00	1.40
91.8	33.8	55.0	46.3	45.7	0.99	1.01	1.28
92.65	31.2	50.8	43.9	43.3	1.00	1.01	1.22
92.8	30.5	51.0	43.5	43.5	1.01	1.01	1.20
92.45	30.4	51.8	43.75	44.05	1.02	1.01	1.19
92.3	32.6	53.0	44.6	45.0	0.98	1.02	1.26
93.4	28.2	47.8	41.2	42.0	1.01	1.01	1.18
94.05	27.0	44.0	39.4	40.2	1.00	1.04	1.16
94.65	24.5	40.9	37.5	38.6	1.03	1.05	1.12
95.45	22.7	38.1	35.4	36.6	1.02	1.04	1.12
96.15	21.0	35.2	33.7	34.8	1.03	1.05	1.11
96.85	19.3	32.2	31.9	32.8	1.04	1.07	1.09
97.2	18.1	31.3	30.4	32.3	1.05	1.07	1.09
97.7	16.9	29.3	28.9	31.0	1.05	1.08	1.09
98.3	15.9	27.4	27.8	29.8	1.06	1.09	1.07
98.85	14.8	25.7	26.3	28.8	1.06	1.11	1.07
99.4	13.9	24.2	25.1	27.6	1.06	1.11	1.06
100.0	12.6	22.2	23.6	26.3	1.09	1.13	1.05
100.5	11.6	20.6	22.5	25.0	1.11	1.14	1.04
101.1	10.8	19.2	21.2	23.8	1.10	1.15	1.03
102.1	8.8	15.9	17.8	21.4	1.11	1.21	1.03
102.8	7.6	13.7	16.2	19.3	1.15	1.23	1.02
103.7	6.5	11.8	14.3	17.2	1.17	1.24	1.02
104.55	5.4	9.9	12.5	15.0	1.19	1.27	1.02
105.35	4.2	8.6	10.8	13.3	1.28	1.28	1.01
107.7	1.8	3.9	5.1	6.8	1.33	1.35	1.01

TABLE 3

VAPOR-LIQUID-EQUILIBRIUM DATA, CYCLOHEXANE-HEPTANE-TOLUENE
RATIO—CYCLOHEXANE TO HEPTANE = 1.5 IN CHARGE TO STILL
ABSOLUTE PRESSURE = 760 MM. HG

Temp.,	Composition, mole % Liquid		Vapor		Activity coefficient		
°C.	CH	C7	CH	C7	CH	C7	Tol
88.0	51.7	42.1	64.5	31.3	1.01	1.03	1.33
88.7	49.0	40.0	61.3	31.0	1.00	1.04	1.35
89.3	46.6	37.9	59.5	30.0	0.99	1.04	1.29
89.95	44.2	36.1	57.6	29.0	1.00	1.04	1.27
90.65	41.3	34.3	55.5	28.2	1.01	1.04	1.23
91.45	38.2	32.0	52.9	27.3	1.02	1.05	1.19
92.15	35.4	30.1	50.7	26.5	1.03	1.06	1.16
92.9	32.9	28.3	48.6	25.5	1.03	1.06	1.14
93.6	30.7	26.4	46.6	24.6	1.05	1.07	1.12
94.35	28.5	24.4	44.0	23.4	1.04	1.08	1.12
95.15	26.4	22.7	42.4	22.4	1.06	1.09	1.10
95.8	24.6	21.3	40.4	21.8	1.07	1.11	1.09
96.3	23.1	20.1	38.5	21.3	1.07	1.10	1.08
96.7	22.0	19.6	37.5	20.7	1.08	1.11	1.08
97.0	21.6	18.8	36.8	20.4	1.07	1.15	1.07
97.8	19.9	18.5	34.8	19.6	1.07	1.14	1.06
98.45	17.9	15.8	32.8	18.4	1.10	1.16	1.05
99.1	16.7	14.7	30.4	17.1	1.08	1.14	1.06
99.8	15.1	13.3	28.8	16.4	1.11	1.18	1.05
100.55	13.5	12.0	26.7	15.1	1.13	1.18	1.05
101.6	11.3	10.2	23.8	13.7	1.16	1.23	1.03
102.7	9.7	8.8	20.9	12.4	1.15	1.26	1.03

TABLE 4

VAPOR-LIQUID-EQUILIBRIUM DATA, CYCLOHEXANE-HEPTANE-TOLUENE
RATIO—CYCLOHEXANE TO HEPTANE = 4.0 IN CHARGE TO STILL
ABSOLUTE PRESSURE = 760 MM. HG

Temp.,	Composition, mole % Liquid		Vapor		Activity coefficient		
°C.	CH	C7	CH	C7	CH	C7	Tol
84.55	72.7	21.0	81.4	14.8	1.00	1.08	1.34
85.7	67.3	19.3	78.3	13.7	1.00	1.04	1.27
86.9	61.1	17.9	74.5	13.0	1.02	1.03	1.22
87.6	57.9	17.0	72.6	12.9	1.02	1.05	1.18
88.4	54.7	16.2	70.6	12.3	1.03	1.03	1.15
89.1	51.9	15.1	68.5	11.9	1.03	1.04	1.13
90.0	48.4	14.3	65.3	12.0	1.03	1.08	1.14
90.7	45.6	13.5	63.4	11.6	1.06	1.08	1.12
91.45	42.7	12.9	61.1	11.3	1.05	1.08	1.11
92.2	39.6	12.4	58.9	11.1	1.07	1.08	1.09
92.9	37.3	11.6	57.0	10.8	1.08	1.09	1.08
93.1	36.0	11.4	55.8	11.0	1.08	1.13	1.07
93.5	35.0	11.0	54.6	10.6	1.08	1.11	1.08
93.85	33.7	10.8	53.6	10.5	1.09	1.11	1.07
94.25	32.7	10.3	52.5	10.3	1.09	1.13	1.07
94.9	30.7	9.5	50.5	9.8	1.10	1.14	1.06
95.3	29.3	9.1	49.4	9.5	1.11	1.14	1.06
95.8	28.2	8.6	48.3	9.3	1.11	1.17	1.05
96.4	26.4	8.3	46.3	9.0	1.12	1.15	1.05
96.85	24.5	7.8	44.6	8.6	1.15	1.15	1.04
97.5	23.0	7.1	42.8	8.2	1.15	1.19	1.03
98.3	21.4	6.7	40.2	7.9	1.14	1.18	1.04
99.1	19.5	6.3	38.0	7.4	1.15	1.15	1.03
100.0	17.3	5.5	35.1	6.9	1.17	1.21	1.02
100.7	15.9	5.2	32.9	6.6	1.18	1.19	1.02
101.6	13.7	4.6	29.8	6.0	1.21	1.19	1.02
103.65	9.8	3.4	23.1	4.7	1.24	1.10	1.02
104.7	7.9	2.8	19.7	4.1	1.28	1.23	1.01

that are predicted when the six binary constants from Figures 11, 12, and 13 are used in the ternary Margules equation. The constant C in the ternary equation was computed from the relation

$$C = \tfrac{1}{2}(A_{2-1} - A_{1-2} + A_{1-3} - A_{3-1} + A_{3-2} - A_{2-3})$$

where the A's are the six binary constants.

Agreement between the predicted and the experimental curves for the ternary system is about as good as the agreement between the Margules curves and the experimental curves for the three binaries. The chief cause of disagreement is believed to be the effect of changing temperature on the activity coefficients. Earlier work (*4*) has shown that the various thermodynamic consistency equations sometimes do not fit isobaric data, even though similar isothermal data, determined in the same equipment, are fitted closely.

CONCLUSIONS

Vapor-liquid-equilibrium data for the ternary system cyclohexane-heptane-toluene fall in line among the data for the three limiting binaries. The ternary Margules equation is able to predict the ternary activity-coefficients from the binary data with about the same precision as the binary Margules fits the binary data, but the agreement is not very good. This lack of agreement is believed due to the effect of changing temperature on the activity coefficients. Unfortunately, the addition of a temperature-correction term to the Margules equations, even if the proper correction term were known, makes the equations extremely difficult to use for ternary or multicomponent mixtures. The uncorrected equations are probably satisfactory for isothermal data or for isobaric data where the temperature spread is small, but they should be used with caution over wide temperature ranges.

For the cyclohexane-heptane-toluene system, if the activity coefficients are plotted only as a function of the aromatic concentration, without consideration of the ratio of naphthenes to paraffins, an approximate correlation is observed. This is probably true for all ternary mixtures of naphthenes, paraffins, and aromatics.

LITERATURE CITED

1. Hipkin, H. G., and H. S. Myers, *Ind. Eng. Chem.*, **46**, 2524 (1954).
2. Myers, H. S., *Ind. Eng. Chem.*, **47**, 2215 (1955).
3. *Ibid.*, **48**, 1104 (1956).
4. Myers, H. S., *Petroleum Refiner*, **36**, No. 3 (1957).
5. Perry, J. H., "Chemical Engineers' Handbook," 3 ed., p. 529, McGraw-Hill Book Company, Inc., New York (1950).

Heats of Vaporization of Hydrogen-bonded Substances

A. BONDI and DONALD J. SIMKIN

Shell Development Company, Emeryville, California

A new method is proposed for the calculation of the heat of vaporization of hydroxylated compounds to an accuracy of about ±0.5 kcal./mole from no more data than the molecular structure and a boiling point. The older methods, by comparison, achieved an accuracy of about ±1 kcal./mole with a far greater computational effort, since they required the (usually hypothetical) critical temperature and critical pressure in addition to a boiling point.

The method is here applied to aliphatic and aromatic alcohols, to ether-alcohols (e.g., the cellosolves), and to alcohols containing keto or aldehyde groups (e.g., salicylaldehyde) and supersedes previous correlations covering the heats of vaporization of these compounds. The method can also be used to assess the quality of vapor-pressure data of the compounds covered by it.

The method is based on the assumption that the heat of vaporization consists of two terms, the dispersion energy and the hydrogen-bond increment (close but not equal to the hydrogen-bond strength). The first term is calculated from a knowledge of the heat of vaporization of the equistructural hydrocarbon, now easily available from the Tables of A.P.I. Research Project 44. The hydrogen-bond term is calculated from a set of rules given in the report.

The application of the increment method of this report to other properties and other functional groups is the subject of a continuing investigation.

PURPOSE AND SCOPE

The recurrent need for heat-of-vaporization data of increasingly complex synthetic oxygenated compounds and the discovery of some inconsistencies in previous correlations prompted a short inquiry into regularities which could be used as basis for improved calculation. The choice between the direct calculation of the heat of vaporization and the older path of calculating the entropy of vaporization has been resolved in favor of the first route, since it could be shown from basic principles that more information is required to estimate the entropy of vaporization from liquids with strongly oriented molecules than to assess the extra force of cohesion caused by hydrogen bonds.

Exploratory calculations (*10, 48, 49, 51, 57*) had shown that the difference between the heat of vaporization of a hydroxylic compound and that of its hydrocarbon (or otherwise nonpolar) homomorph* constitutes a good measure of hydrogen-bond strength (*12*). This path could now be pursued in detail because of the availability of extensive and reliable heat-of-vaporization data in the A.P.I.-44 tabulation (*3*) on a wide variety of hydrocarbons that could serve as homomorphs of oxygenated compounds.

Donald J. Simkin is with Marquardt Aircraft Company, Van Nuys, California.

*A homomorph is a compound of similar molecular geometry; e.g., ethane is a homomorph of methanol, toluene of phenol, etc.

BASIC PRINCIPLES

The Hydrogen Bond

The interaction (in a condensed phase) between a hydrogen atom which is chemically bound to an atom of electronegativity ≥ 3 e.v. (Pauling's scale) and an atom of high electronegativity bound to another (or the same) molecule has in many respects more the character of a chemical bond than of nonspecific van der Waals attraction. The *hydrogen bond*, as this interaction is called, can therefore be characterized by a bond strength which is essentially independent of its environment and should depend primarily on the nature of the atoms to which the hydrogen atom is bound.

Contribution of Hydrogen Bond to Heat of Vaporization

In comparison with other chemical bonds the hydrogen bond is rather weak

and only rarely survives the transition from condensed to vapor phase. The contribution which the hydrogen bond makes to the strength of cohesion of condensed phases is therefore a good measure of its strength (*51*).

The separation of the hydrogen-bond term from all other factors which determine the magnitude of the cohesive forces in liquids requires, in principle, a detailed calculation of the dispersion and dipole forces between the molecules of the liquid. In order to avoid this laborious and, of necessity, inexact calculation, it is here proposed to substitute for the dispersion forces between the molecules of a hydroxylic compound the (readily available) heat of vaporization ΔH_v* of its hydrocarbon homomorph at the same reduced temperature; the dipole interaction is absorbed into the hydrogen-bond–strength increment δ(OH) of the total heat of vaporization ΔH_v of a liquid, and specific intramolecular interactions are represented as Δ, or formally as

$$\Delta H_v|_T = \Delta H_v^*|_{T_R} + \Sigma\delta(OH)|_T + \Sigma\Delta \qquad (1)$$

In this procedure it is implicit that the dispersion-energy contribution of the functional groups of a molecule is equal to that of a methyl or methylene group. The correctness of this assumption has been previously proved (*9*).

Since the increment δ(OH) is a measure of (but not identical with) the heat of formation of the hydrogen bond, and decreases with increasing temperature, comparison at the boiling point means that δ(OH) is not a constant but depends upon the absolute temperature level at which the hydroxyl compound is being considered. Such a reference curve for δ(OH) has been constructed from the heat-of-vaporization data of water (by subtraction of the dispersion-force contribution) and is shown, together with the data from other alcohols, in Figure 1. The upper curve for the hydrogen-bond increment of water may be considered as representing the upper limit of hydrogen-bond increments in liquids. The proximity of the curve for the hydrogen-bond increment of the monohydric alcohols to that of water is a bit surprising, since the proton is attached far more strongly (by about 13 kcal.) to the water oxygen than to that of the alcohols. It will be seen that vicinal effects on the hydrogen-bond strength cannot be ignored in the case of phenols, where the electron attraction of the benzene ring reduces the charge separation which is largely responsible for hydrogen bonding. It is noteworthy that the average value of $d\delta(OH)/dT$ along the water and alcohol curve (10 cal./°K.) is similar to that found spectroscopically for the hydrogen bond of isopropyl alcohol (6.6 cal./°K.) (*42*).

An examination of the temperature coefficient of ΔH_v of the homomorph provides some information regarding the error which could be made by incorrect choice of the appropriate reduced temperature in Equation (1). This is an actual problem with many hydroxylic compounds of interest, the critical temperature of which cannot be measured but only established by means of various empirical correlations (*59*). If one then assumes that the maximum error in estimating the critical temperature is about $0.1T_R$ ($\sim$ 50°C.), the error in ΔH_v of the homomorph can be estimated by means of the equation of Watson (*32*)

$$\Delta H_v^*(T_R) = \Delta H_v(b)\left(\frac{1 - T_R}{1 - T_R(b)}\right)^{0.38} \qquad (2)$$

as of the order of $0.1\Delta H_v$ of the homomorph. Since the heat of vaporization of the homomorph is usually about 4 to 10 kcal./mole, the maximum error in δ(OH) due to very poor choice of T_c for the hydroxyl compound is about 0.4 to 1 kcal./mole. Actual errors are likely to be less than this amount since mistakes of more than ±50°C. are not very probable, nor will the discrepancy between the "true" corresponding temperatures and the temperature chosen for equal vapor pressure approach that amount.

Effect of Molecular Structure on the Hydrogen-bond Increment

The hydrogen-bond increment δ(OH) is approximately the same for a wide range of hydroxylated compounds. However, in certain types of molecule systematic variations can be observed, many of which can fortunately be assigned to rational causes and some even calculated from independent measurements. The following paragraphs will treat, in order, the monofunctional primary alcohols and phenols, then the strong intra- and intermolecular interactions due to other functional groups in the molecule, and finally the shielding effect of hydrocarbon chains adjacent to the hydroxyl group.

Primary Aliphatic Alcohols. The properties of the members of this series form the backbone of this report not only because of the simplicity of their structure and the proximity of their hydrogen-bond increments to those of the "standard hydroxyl group," namely water, but also because their data have been determined more accurately than those of any other group of hydroxyl compounds. The data, which form the basis of Figure 1, are assembled in Table 1. Combined with the curve for water, they suggest that the increment δ(OH) is essentially independent of the size of the hydrocarbon radical at temperatures above 25°C. and that the trend with absolute temperature is a measure of the temperature coefficient of δ(OH).* The data for *n*-amyl alcohol were not included because their accuracy was suspected.

Table 1. Hydrogen-bond Increments for Lower Primary *n*-Aliphatic Alcohols

Alcohol \ Temp., °C.	−10	0	20	60	100
Methyl	5.7	5.6	5.6	5.4	*5.2*
Ethyl	5.7	5.7	5.6	5.2	*5.0*
n-Propyl	6.0	5.9	5.7	5.4	*4.8*

Phenols. The hydroxyl group attached to a benzene ring is subject to very strong electron withdrawal forces, as is evident by the far more acidic character of the phenol than of the aliphatic alcohols. More important is perhaps the strong attraction of the benzene ring (due to its high polarizability) for the proton of the phenolic OH group, as is shown by comparison of the infrared spectra in the series methanol, phenol, *o*-phenyl phenol (*46*, *50*, *51*, *66*). The strength of the interaction between hydroxyl groups and benzene rings is also evident from the fact that for both methanol and phenol at infinite dilution the heat of solution in benzene is about 0.8 to 1 kcal./mole lower than in aliphatic hydrocarbons (*46*). This is about the amount by which δ(OH) is lower for the three unhindered phenols of Table 2 than for aliphatic alcohols at the same temperature. The attraction of the proton by the benzene ring may therefore be the dominating effect. Independent evidence regarding the possible effect of electron withdrawal from the OH group on δ(OH) can be obtained by heat-of-vaporization measurements on perfluoro and perchloro alcohols.

Table 2. Heats of Vaporization of Phenols and Their Homomorphs at T_b

Compound	ΔH_v, kcal.	Homomorph	ΔH_v, kcal.	$\delta(\Delta H_v)$	Data sources
Phenol	10.95	Toluene	8.00	2.95	*21*
p-Cresol	11.34	*p*-Xylene	8.62	2.72	*21*
3,4-Xylenol	12.33	Pseudocumene	9.38	2.95	*21*

Multifunctional Alcohols, General Principles. The comparison between normal aliphatic alcohols and the phenols (and benzylalcohol) has shown the effect of competitive intramolecular interactions on the hydrogen-bond increment $\delta\Delta H_v$. One would expect, therefore, that additional functional groups in an alcohol molecule which are capable of strong intramolecular interaction with hydroxyl groups also would reduce $\delta\Delta H_v$. The conditions for effective intramolecular

*Close inspection of Figure 1 reveals a trend toward increasing steepness of the δ(OH)-vs.-temperature curves with increasing molecular size. More accurate vapor-pressure data are required to ascertain the reality of this trend.

bonding of the hydroxyl group can be anticipated intuitively:

1. The interaction energy between the functional group and the hydroxyl group has to be of the same order as that of the OH–OH interaction. A feel for the magnitude of such competitive interaction can be obtained by inspection from the excess free energy of mixing F^E of alcohols with hydrocarbons and with solvents containing the functional groups in question (Table 3). The magnitude of the interaction between hydroxyl, ether, and carbonyl groups has also been measured spectroscopically (*41, 44, 46, 51, 63, 66*).

Table 3. Solutions of Alcohol in Hydrocarbons and in Oxygenated Solvents (760 mm.)

(1)	(2)	Log γ_{12}^{∞}	F^E cal./mole	Data sources
Ethanol–*n*-hexane		1.12	1,800	*35*
Ethanol–ethyl ether		0.42	670	*52*
Ethanol–ethyl acetate		0.38	610	*24*
Methanol–*n*-heptane		1.313	2,200	*7*
Methanol–acetone		0.25	420	*52*

2. Since the bonding interaction decreases very rapidly with distance, unhindered mutual approach of the interacting groups is a prerequisite of intramolecular interaction. Ideally, a six-or-more–membered ring has, therefore, to be obtainable in the manner

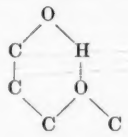

if any effect of the group (here –O–) on $\delta\Delta H_v$ is to be expected. A weak effect is sometimes noted (as will be seen below) even when only a five-membered ring can be formed.

3. When the intramolecular bond formed is stable, no effect on ΔH_v could be expected. The factors determining this stability are still somewhat elusive, but some features can be discerned. The entropy decrease ΔS_c that accompanies ring formation has to be compensated for by the heat of formation of the hydrogen bond ΔH_c so that the free energy of formation of the hydrogen bond is zero or smaller. An estimate of ΔS_c, obtained by a comparison of S^0 for alkene-1 and cycloalkane gives $\Delta S_c = -13$ e.u. for the five-membered ring and $\Delta S_c = -20$ to -22 e.u. for six- to eight-membered rings. Hence at 300°K. ΔH_c must be ≥ 6 kcal./mole to give a significant fraction of intramolecularly bonded molecules.

Monohydric Ether and Keto Alcohols. Only a limited amount of vapor-pressure data among the members of this class of compounds was good enough to permit valid conclusions to be drawn from the resulting heats of vaporization, shown in Table 4. All of these could have formed six-membered rings in intramolecular hydrogen-bond formation, and although infrared spectroscopic evidence points to relatively high concentrations of bonded hydroxyl groups in the dilute solution of 3-ethoxypropanol-1 (*63*) and of diacetone alcohol (*51*), the observed heats of vaporization are in rather good agreement with those calculated on the assumption of an unbonded hydroxyl group in the vapor phase.* The absence of extensive internal ring formation in the vapor phase suggested by the data of Table 4 is in agreement with the probable magnitude of ΔH_f for the O–H$\cdots$O bond as compared with the $\geq$ 6 kcal./mole required to compensate for the large entropy of ring formation mentioned in the introduction to this section. No acceptable reconciliation between the vapor pressure and the infrared spectral observation has yet been found.

A large number of monohydric ether alcohols derived from ethylene oxide are made commercially. The remarkable discordance among the many published vapor-pressure measurements on these compounds suggests that most of the available samples may have been impure. Since most of the probable impurities, especially water, are likely to decrease the heat of vaporization below its true value, one may consider the data leading to the highest value of ΔH_v (shown in Table 5) as perhaps more reliable than the others. There is a suggestion of a systematic lowering of about 1 kcal. of the hydrogen-bond contribution to ΔH_v below the typical value of δ(OH) especially as the size of the group tied to the far end of the ether oxygen increases beyond that of the ethyl group. The likelihood of impurities being responsible for the lowering of ΔH_v of these products is very high because of notorious difficulty involved in their purification. Lowering of ΔH_v as a result of a finite width of boiling range may be a general phenomenon worthy of further investigation. Until more reliable data have been obtained, one can only record this information but can hardly use it for generalizations.

Aliphatic Polyhydric Alcohols. Intramolecular bonding of hydroxyl groups might be expected to lower $\delta\Delta H_v$ significantly, since there is ample evidence for its occurrence from infrared-absorption-spectra (*46*), electron (*5*), and X-ray-diffraction data (*5*) as well as for various physical properties (*5, 6, 56*). But the

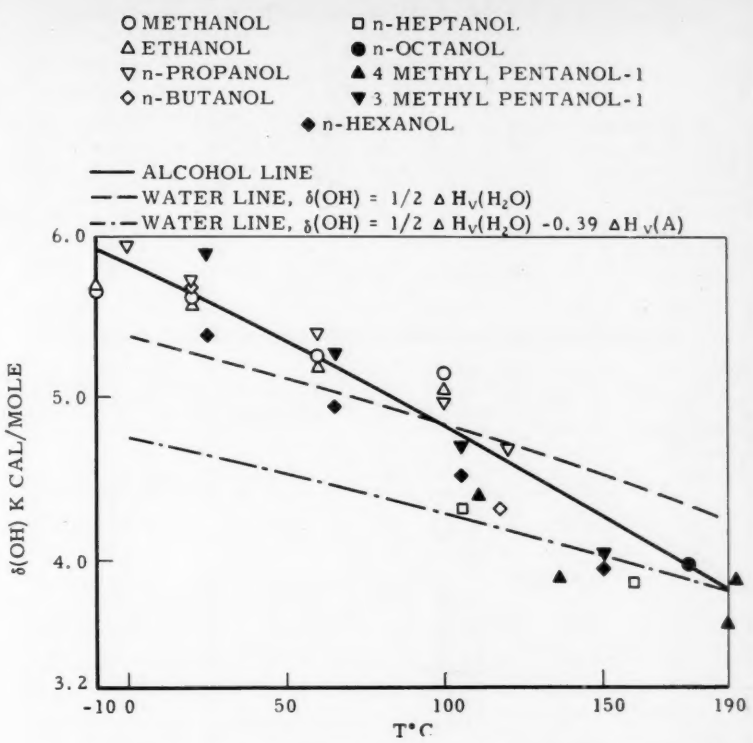

Fig. 1. Hydrogen-bond increments δ(OH) of primary aliphatic alcohols and water.

*The assumption of dimer formation in the vapor phase would reconcile the infrared and the vapor-pressure data and would lead to values of ΔH_v(calc.) which while invariably higher than observed would almost all be within the experimental error of the observed data.

Table 4. Heats of Vaporization of Monohydric Ether and Keto Alcohols

Compound	T_b, °C.	ΔH_v	ΔH_v*	δ(OH) from ΔH_v* Fig. 1	ΔH_v* + δ(OH), calc.	ΔH_D D = dimer	Data sources
3 Methoxybutanol-1	161.1	11.8	7.36	4.08	11.42	~12.2	*22, 60*
3 Ethoxypropanol-1	162–3	11.5	7.58	4.08	11.66	~12.4	*2, 63*
3 Methoxypropanol-1	~150	11.1	6.90	4.18	11.18	11.4	*2, 58*
Diacetone alcohol	~166	11.4	7.41	4.05	11.46	12.7	*57*
Acetyl acetone	~135	10.3	7.41	4.2	11.6	~12.5	*18, 22, 40*
4-Hydroxypentanone-2	~176	11.4	7.05	3.98	11.03	~12.5	*45, 47*
4 Me 4 hydroxy-pentanone-2	~187	12.4	7.82	3.94	11.76	12.7	*45*

Table 5. Heats of Vaporization of Monohydric Ether Alcohols

Compound	T_b, °C.	ΔH_v, kcal. (exptl.)	δ(OH)*	Homomorph ΔH_v*, kcal.	ΔH_v* + δ(OH)	Data sources
Glycol ethers (cellosolve)						
Methyl	124.6	9.13	4.4	6.16	10.6	*15*
		9.39				*26*
		9.60				*15*
		10.16				*14*
		10.3				*26, 27*
Ethyl	135.6	9.41	4.3	6.90	11.2	
		9.46				*14*
		9.85				*15*
		10.93				*20*
		11.13				*15*
n-Hexyl	208.1	9.59	3.6	9.39	13.0	*15*
		11.34				*14*
		11.94				*15*
Diglycol ethers (carbitols)						
Methyl	193.6	11.5	3.8	8.22	12.0	*14*
		11.30				*15*
		10.88				*15*
		12.08				*14*
Ethyl	201.9	12.90	3.7	8.82	12.5	*19*
n-Butyl	230.4	10.00	3.4	9.92	13.3	*15*
		11.99				*15*
		12.62				*14*
n-Hexyl	259.1	13.75	3.1	10.91	14.0	*15*
		12.84				*15*
		13.51				*14*
		12.8				*14*

*From Figure 1.

Table 6. Hydrogen-bond Increment in Aliphatic Polyols

Compound	T_b, °C.	ΔH_v, kcal.	Homomorph	ΔH_v*, kcal.	$\delta\Delta H_v$, kcal.	Decrease in ΔH_v, kcal. Total	Per OH group	Data sources
Ethylene glycol	197.2	12.58	Butane	5.35	7.23	0.4	0.2	*1, 17, 19, 25*
Propylene glycol	187.4	12.90	2-Methyl butane	5.90	7.00	0.6	0.3	*17, 19*
1,3-Butanediol	207.5	13.97	2-Methyl pentane	6.64	7.33	~0	~0	*19*
Pentaerythritol	256*	24*	3,3-Diethyl pentane	10.8	13.2	~0	~0	*11, 31*
Glycerol	290.5	~16	3-Methyl pentane	6.7	9.3	~0	~0	*19*

*At the melting point.

data assembled in Table 6 indicate that the vapor concentration of internally bonded molecules is not large. One would probably predict the heat of vaporization of aliphatic polyols to within the experimental error if one assigned the full value of δ(OH) per OH group present.

Aliphatic Polyhydric Ether Alcohols. The polyhydric ether alcohols can be divided into two groups: (1) those with single hydroxyl groups on either side of an ether linkage, as in diethyleneglycol, and (2) those with more than one adjacent hydroxyl group on one or both sides of an ether linkage as in glycerol-α-ethyl ether or in diglycerol, respectively. Inspection of the possible structures in Figure 2 clearly shows the difference between the two types of compounds. The diethylene or triethyleneglycol type would hardly be expected to behave very differently from the monohydric ether alcohols of the same class. The data of Table 7 indicate that this is indeed the case in every respect. The range of reported ΔH_v value is large, within the probable range of error, and one again finds only small deviations from the behavior of monohydric alcohols, equivalent to but small concentrations of internally bonded molecules in the vapor phase.

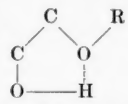

Di- or triethylene glycol structure

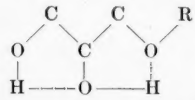

Glycerol-α-ether structure

Fig. 2. Types of polyhydric ether alcohol structures.

The structure of the glyceryl ether type, on the other hand, suggests mutual reinforcement of the interacting groups OH---OH---O. It is not surprising to find, therefore, that in all the α-glyceryl ethers only one out of two hydroxyl groups contributes its full share, δ(OH), to the heat of vaporization, or, in other words, that here the vapor concentration of internally bonded molecules is quite high.

Multifunctional Phenols

In spite of the much older technology, far fewer physical-property data are available on phenol derivatives than on the relatively recent aliphatic alcohols. This paucity of information coupled with the early dates of the reported measurements should be kept in mind whenever the data of this section are used as a basis for further extrapolation.

Phenols with Orthocarbonyl Groups. The classical example of intramolecular hydrogen bonding is salicyl aldehyde, by spectral evidence (*51*) as well as in terms of its heat of vaporization, as shown by the data of Table 8. Methyl salicylate likewise exhibits just the ΔH_v of its hydrocarbon homomorph, indicating essentially complete internal binding of the hydroxyl group.

The reason for the exceptionally strong interaction between the phenolic OH group and the adjacent carbonyl oxygen may be the planarity of the ring system and the consequent lack of hindering barriers in the path of the interacting groups. Stabilization of hydrogen bond by resonance among various possible electronic configurations may also play a role here.

Dihydroxy Benzenes. The data of Table 9 show the expected pattern. The interaction between adjacent (ortho) hydroxyl groups reduces ΔH_v by about the same amount found for the glycols (about 0.5 kcal./OH group). The meta- and para-oriented OH groups do not interact.

SHIELDING EFFECTS

Methyl or other shielding groups located adjacent to or near the hydroxyl group of a molecule reduce the intermolecular hydrogen bonding (*51*) in the liquid and thereby the heat of vaporization of an alcohol. Even a cursory inspection of the extensive data on isomeric butanols, hexanols (*34*), and octanols (*54*) in the literature reveals that essentially two different types of shielding can be discerned: one group (*A*) for which the difference Δ between the observed hydrogen-bond increment and that of Figure 1 is about 0.5 to 1.5 kcal. and essentially temperature independent and another group (*B*) for which the observed hydrogen-bond increment is about 1 to 2 kcal./mole nearly independently of temperature; hence the decrement Δ is about 4 kcal./mole of room temperature, decreasing to about 2 kcal./mole at 160°C.

All the alcohols of group *B* have a methyl group at three carbon atoms' distance from the hydroxyl group. Typical examples are listed in group *B* of Table 10. The weak hydroxyl bonding among the members of this group must be due to the hindrance which the attached propyl group presents to the formation of OH-association chains. The maximum observed value of Δ is—in accordance with this view—of the order of the barrier to internal rotation of a methyl-methylene couple.

Group *A* contains a wide variety of isomers. Several of its members would have been classed intuitively in group *B* because they possess methyl groups three carbon atoms removed from the hydroxyl group; however, one finds in each case that either the interacting methyl group or the hydroxyl group has been locked into some fixed position in space, thus apparently permitting more ready access to intermolecular hydrogen bonding. Typical examples have been enumerated under group *A*-2 in Table 10. Other members of group *A* are the alcohols with OH groups attached to tertiary and secondary carbon atoms.

Shielding effects are difficult to separate from interaction effects in aliphatic polyols. Using the shielding decrements given in Table 10, one can estimate $\delta(\Delta H_v)$ for 2-methyl-2, 4 pentanediol [$\delta(\Delta H_v)$ calc. = 5.8 kcal./mole] and 2-ethyl-1, 3 hexanediol [$\delta(\Delta H_v)$ calc. = 6.2 kcal./mole] without appeal to hydroxyl interaction, as shown by comparison with the data of Table 11.

A somewhat larger effect of shielding groups is noted with phenols (Table 12), where the orthomethyl group reduces δ(OH) by about 1 kcal./mole. The larger effect here may be due to the rigidity of the molecule which precludes close approach of a colliding molecule to the OH group by bending of the carbon skeleton. With the aliphatic compounds, on the other hand, rotation around the C–C axis is relatively free, thus reducing the shielding effect of the alkyl group adjacent to the hydroxyl.

Table 7. Heat of Vaporization of Polyhydric Ether Alcohols

Compound	T_b, °C.	ΔH_b, kcal./mole	$\sum\delta$(OH) (Fig.1)	Homomorph, ΔH_v*, kcal./mole	$\Delta H_v^* + \sum\delta$(OH)	Data sources
Diethylene glycol	245.0	15.92	6.6	7.58	14.4	*19*
		12.49				*25*
		11.36				*19*
Triethylene glycol	289.8	14.93	5.6	9.39	15.0	*19*
		17.07				*25*
Glycerol ethyl ether	224	12.40	7.0	8.10	15.1	*57*
Glycerol α-isopropyl ether	226	12.3	7.0	8.50	15.5	*57*
Glycerol α-allyl ether	245	12.9	6.6	8.79	15.4	*57*

Table 8. Heats of Vaporization of Phenols With Ortho Carbonyl Groups

Compound	T_b, °C.	ΔH_v, kcal./mole	ΔH_v^*, kcal./mole	Data sources
Salicylaldehyde	196	9.14	9.29	*40, 21*
Methyl Salicylate	223.3	9.58	9.94	*62, 21*

Table 9. Hydrogen Bond Increments For Dihydroxy Benzenes

Compound	T_b, °C.	ΔH_v	Homomorph	ΔH_v^*	$\delta\Delta H_v$	Decrease in $\delta\Delta H_v$	Data sources
o-Dihydroxybenzene	245.5	13.95	*o*-Xylene	8.80	5.13	0.9	*4, 21*
m-Dihydroxybenzene	276.5	16.29	*m*-Xylene	8.71	7.58	—	*4, 21*
p-Dihydroxybenzene	268.2	16.38	*p*-Xylene	8.62	7.76	—	*61, 21*

Table 10. Shielding Effects in Aliphatic Alcohols

Group	Compound	t, °C.	$\delta(\Delta H_v)$, kcal./mole	Δ, kcal./mole
A-1 Secondary alcohols	*n*-butanol-2			
	n-hexanol-2	110	3.1–4.0	1.0 ± 0.5
	n-octanol-2	140	3.3–3.9	0.5 ± 0.3
	n-octanol-4			
A-2 Tertiary alcohols	*t*-butanol	25	4.3	1.4
	2-methyl pentanol-2	70	3.4–4.0	1.4 ± 0.3
	2-methyl heptanol-2	150	2.1–3.2	1.3 ± 0.5
A-3 "Locked" propyl interaction	3-methyl heptanol-3			
	2,2 dimethyl butanol-3	25	4.3–4.7	1.2 ± 0.2
	2-methyl heptanol-3	60	3.7–4.2	1.3 ± 0.3
	3-methyl pentanol-2	150	2.2–3.0	1.4 ± 0.4
	2-methyl pentanol-3			
B Propyl interaction	*n*-hexanol-3			
	n-octanol-3			
	2-methyl heptanol-5			
	2-methyl heptanol-1	25	1.2–2.2	4.0 ± 0.5
	3-methyl heptanol-2	60	1.1–2.1	3.6 ± 0.5
	3-methyl heptanol-4	150	1.2–1.9	2.4 ± 0.3
	3-methyl heptanol-5			
	4-methyl heptanol-3			

Table 11. Shielding Effects in Aliphatic Compounds

Compound	T_b, °C.	ΔH_v, kcal.	Homomorph	ΔH_v^*, kcal.	$\delta\Delta H_v$, kcal.	Data sources
2-Methyl-2,4-pentanediol	197.1	13.66	2,2,4-Trimethyl-pentane	7.44	6.25	*19*
2-Ethyl-1,3-hexanediol	244.2	14.95	9-Ethyl-4-methylheptane	9.00	5.95	*19*

Table 12. Shielding Effects in Phenols

Compound	T_b, °C.	ΔH_v, kcal./mole	Homomorph	ΔH_v^*, kcal./mole	$\delta\Delta H_v$	Decrease in δ(OH)	Data sources
Phenol	181.7	10.95	Toluene	8.00	2.95	0	*21*
o-Cresol	191.0	10.72	*o*-Xylene	8.80	1.92	1	*21*
m-Cresol	202.2	11.32	*m*-Xylene	8.71	2.61	~0.3	*21*
p-Cresol	201.9	11.34	*p*-Xylene	8.62	2.72	~0.2	*21*
2,3-Xylenol	218.0	11.33	Hemimellitene	9.57	1.76	~1.2	*21*
3,4-Xylenol	225.0	12.33	Pseudocumene	9.38	2.95	0	*21*

Table 13. Hydrogen Bond and Strong Dipole Increments

Functional group	Increment, δ at 100°C. kcal./mole	$-d\delta/dT$, cal. mole(°K.)	Number of compounds investigated
–OH (aliphatic)	4.6 ± 0.2	10	>10
$-NH_2$ (aliphatic)	1.6 ± 0.2	4.5	5
–NH (aliphatic)	~0	—	3
–C≡N (aliphatic)	2.1 ± 0.4	7.0	10
$-NH_2$ (aromatic)	2.6 ± 0.2	—	3
–C(=O)H (aliphatic)	1.4 ± 0.2	2.9	9

SUMMARY OF HEAT-OF-VAPORIZATION INCREMENTS

In surveying the results of this investigation, one is struck by the simplicity of the relationships obtained. Much of this simplicity is hardly real but must be ascribed to the crudeness of most of the published data. Many trends in deviations may have to be accepted as real, once better data are available, which now fall within the bounds of experimental uncertainty.

In the meantime the hydroxyl-bond increments of Figure 1 may be considered as directly applicable to normal aliphatic alcohols, monohydric ether alcohols (Tables 4 and 5), monohydric keto alcohols (Table 4), polyhydric ether alcohols (Table 7), and with very small increments to aliphatic polyols (Table 6). Fairly large deviations for intramolecular hydrogen bonding, namely −0.8 δ(OH)/glyceryl group, are found with α-glycerol ethers (Table 7). Steric shielding effects are most prominent with the larger aliphatic alcohols, all of which are assembled in Table 10. Similar but less well established rules are found to hold for aromatic hydroxyl compounds and can easily be deduced from the data of Tables 2 (basic increments), 8 (intramolecular bonding), 9 (dihydroxy interaction), and 11 (shielding effects).

EVALUATION OF EXPERIMENTAL DATA

The correlations for predicting ΔH_v also provide a means for critically analyzing existing data. This analysis may be desirable for assessing the accuracy of vapor-pressure data or of a calorimetric technique. Even though the values predicted by the correlations of this report may be in error by 0.5 kcal., the differences between reported ΔH_v are so great that one can sharply delineate between the reasonable values and the impossible ones by the methods outlined here. An example of this technique is shown for the case of diethylene glycol. Literature values of ΔH_v have been given in kilocalories as 12.49 (*25*), 13.6 (*19*), and 15.92 (*1*). The difference between the highest and lowest value is great, being 3.43 kcal. The present method predicts a ΔH_v of 14.4 to 15.5 kcal. The evidence seems clear here that the 12.49 value is quite unreasonable.

When miscellaneous vapor-pressure data are used to estimate the heat of vaporization, a wide divergence of values can often be obtained. A case in point is diglycerol. The vapor-pressure data of eleven investigations were collected and plotted as log P vs. $1/T$. Using different sets of points, the extremes of which were widely separated in $1/T$ value, one can estimate ΔH_v at the boiling point to be between 18.4 and 51.4 kcal. The "best" line through the points gave a value of 22.5 kcal.; the group increment method predicts a value of 17.3 to 23.2 kcal.

FURTHER APPLICATIONS OF THE METHOD

An exploratory investigation has shown that the contribution of other hydrogen-bonding and strong dipole groups to the heat of vaporization can also be treated as addition to the heat of vaporization of the hydrocarbon homomorph. The resulting increments, collected in Table 13, are supported by much less experimental evidence than has been available for the hydroxylic compounds and should therefore be used with caution.

Description of the application of the principles outlined above to the calculation of vapor pressure, viscosity, etc., of hydroxylic compounds would obviously exceed the scope of this paper and must therefore be deferred.

ACKNOWLEDGMENT

The authors are indebted to R. B. McConaughy for the machine computation of many of the aliphatic alcohol data.

APPENDIX

A. Calculation of Boiling Point and of Critical Temperature

The method of calculation described in the paper requires knowledge of either the atmospheric boiling point or the critical temperature of the alcohol. If the boiling point is known, the critical temperature can be calculated by any one of the many variants of Guldberg's rule [Ref. 32, pp. 71–72; L. Riedel, *Chem. Ing. Tech.*, **24**, 353 (1952); or R. Herzog, *Ind. Eng. Chem.*, **36**, 997 (1944)].

In the absence of experimental boiling-point data for the alcohol a method must be found to estimate them. Following the technique of the paper, one can estimate the boiling point of an alcohol T_B by reference to that of its hydrocarbon homomorph T_B^* through the relation

$$T_B/T_B^* = a + b/(T_B^*)^2$$

where a and b are constants characteristic of a (homologous) series. Furthermore, b is proportional to the ratio $(\delta(OH) - \Delta)/\Delta S_v$, where ΔS_v $(= \Delta H_v/T_B)$ is the entropy of vaporization of the alcohol. Since the constants a and b are readily determined empirically for the more important series of alcohols, the need to use the awkward relation of b to the physical constants to be determined arises only for the adjustment of b for isomer and other structure effects. In that case

$$b(\text{isomer})/b(\text{normal}) = [\delta(OH)_i - \Delta_i] \cdot \Delta S_v(n)/\delta(OH)_n \cdot \Delta S_v(i)$$

where one obviously must make some guesses, which need not be very accurate, regarding the anticipated magnitude of T_B for the "isomer." Empirical, and still tentative, values for a and b are

	a	$b \times 10^4$ (°K.²)
Normal aliphatic monohydric alcohols	0.925	3.2
Aliphatic glycols	0.98	5.5
Phenols	0.96	3.4

Combination of the calculated boiling point with the heat of vaporization calculated by the method outlined in the body of the paper makes it possible now to estimate the vapor-pressure curve of a new polar compound from no more information than its molecular structure. The basic tools are the A.P.I.-44 tables and the hydrogen-bond (or dipole interaction) correlation presented in the paper.

B. Calculation of Heat of Vaporization

1. Calculate the heat of vaporization at the atmospheric boiling point.

a. The atmospheric boiling point of the alcohol is known:

Step 1: Write down the molecular structure and select the appropriate hydrocarbon homomorph.

Step 2: Find the heat of vaporization (at boiling point of the homomorph (ΔH_v^*) in the A.P.I.-44 tables (*3*).

Step 3: Take δ(OH) from *Figure* 1 at the boiling point of the alcohol or extrapolate, if necessary, with $d\delta(\mathrm{OH})/dT \doteq -10$ cal./°C.

Step 4: Find the appropriate value of Δ from the requisite table of the paper. (See Summary of Heat-of-vaporization Increments for guidance.)

Step 5: Calculate $\Delta H_v = \Delta H_v^* + n\delta(\mathrm{OH}) - n\Delta$ where n = number of OH groups in molecule.

(*b*) The atmospheric boiling point of alcohol is not known:

Step 1: Same as in (a).

Step 2: Same as in (a).

Step 3: Calculate the atmospheric boiling point of the alcohol T_B by means of the procedure given in Appendix A.

For the balance of the calculation, follow the procedure from step 3 under (a) onward.

2. Calculate the heat of vaporization at a fixed temperature T:

(a) The critical temperature of the alcohol is known:

Step 1: Same as in 1(a).

Step 2: Find critical temperature T_c^* and heat of vaporization ΔH_v^* of homomorph in the A.P.I.-44 tables.

Step 3: Calculate the reduced temperature T/T_c for the alcohol.

Step 4: Calculate ΔH_v^* for the reduced temperature $T^*/T_c^* = T/T_c$, by means of Equation (2) in the paper.

Step 5: Take δ(OH) from *Figure* 1 for the temperature T, or extrapolate if necessary.

Steps 6 and 7: Same as steps 4 and 5 under 1(*a*).

(b) The critical temperature of the alcohol is not known:

Step 1: Same as under 1(a).

Step 2: Calculate the critical temperature T_c of the alcohol. If the atmospheric boiling point of the alcohol is known, use the methods referred to in the first paragraph of Appendix A. If no physical property of the alcohol is known, the boiling point calculated according to the method of Appendix A may be substituted for the experimental datum point in the calculation of T_c by the usual methods.

All subsequent steps are the same as under 2(a).

NOTATION

F^E = excess free energy of mixing, cal./mole
ΔH_v = heat of vaporization
ΔS_c = entropy due to ring formation, e.u.
ΔS_V = entropy of vaporization, e.u.
T = temperature, °C. or °K.
T_B = boiling point, °C. or °K.
T_c = critical temperature, °K.
T_R = reduced temperature, T/T_c
V = molal volume, cc./mole

Greek Letters

γ_{12}^{∞} = activity coefficient of alcohol at infinite dilution
δ(OH) = hydrogen-bond increment as defined by Equation (1)
Δ = structural contribution to the heat of vaporization
$\delta(\Delta H_v)$ = change in heat of vaporization due to polar or structural effects

Superscripts

* = physical property of hydrocarbon homomorph

LITERATURE CITED

1. *Allied Chemical & Dye Tech. Bull.* G4 and H4.
2. Anderson, E. P., et al., *J. Am. Chem. Soc.*, **68**, 1294 (1946).
3. Anon., *Am. Petroleum Inst. Research Project* 44, Carnegie Institute of Technology, Pittsburgh, Pennsylvania.
4. Anschutz, and Reitter, "Die destillation unter vermindertem Druck im Laboratorium," 2 ed., Cohen, Bonn (1895).
5. Bastiansen, O., *Acta Chem. Scand.*, **3**, 415 (1949).
6. Batuev, M. I., and G. S. Landsberg, *Usepekhi Khim*, **10**, 416 (1941).
7. Benedict, Manson, et al., *Trans. Am. Inst. Chem. Engrs.*, **41**, 375 (1945).
8. Blacet, A. F. E., B. A. Leighton, and E. P. Bartlett, *J. Phys. Chem.*, **35**, 1935 (1931).
9. Bondi, A. and D. J. Simkin, *J. Chem. Phys.*, **25**, 1073 (1956).
10. Bondi, A., *Annals N. Y. Acad. Sciences*, Series II, **53**, 805 (1951).
11. Bradley, R. S., and S. Cotson, *J. Chem. Soc.*, 1684 (1953).
12. Briegleb, G., *Z. Electrochem.*, **50**, 35 (1944).
13. Butler, J. A. V. et al., *J. Chem. Soc.*, 280 (1935).
14. Carbide and Carbon Chemicals Co., personal communication (March 12, 1956).
15. ———, *Tech. Booklet* F-4765B (1954).
16. *Carbon and Carbide Bull.* F-4541 (September, 1940).
17. *Ibid.*, F-8327 (June, 1954); (April, 1955).
18. *Ibid.*, F-4767C.
19. Curme, G. O., and F. Johnston, "Glycols," Reinhold Publishing Corp., New York (1952).
20. Doolittle, A. K., *Ind. Eng. Chem.*, **27**, 1172 (1935).
21. Dreisbach, R. R., "Physical Properties of Chemical Compounds," *Am. Chem. Soc.*, Washington, D. C. (1955).
22. Eastman Kodak Organic Chemicals Lists 39 and 40.
23. Evans, H. D., W. N. Lacey, and B. H. Sage, *Ind. Eng. Chem.*, **31**, 767 (1939).
24. Furnas, C. C. and W. B. Leighton, *ibid.*, **27**, 396 (1937).
25. Gallaugher, A. F., and J. Hibbert, *J. Am. Chem. Soc.*, **59**, 2523 (1937).
26. Gardner, G. S., *ibid.*, **32**, 226 (1940).
27. ———, and J. E. Brewer, *Ind. Eng. Chem.*, **29**, 179 (1937).
28. "Handbook of Chemistry and Physics," 32 ed., Chemical Rubber Publishing Co., Cleveland, Ohio.
29. Hildebrand, J. H., and R. L. Scott, "Solubility of Nonelectrolytes," 3 ed., Reinhold Publishing Corp., New York (1951).
30. Hood, G. C., Shell Development Company, personal communication.
31. Hoshino, S., and S. Nagasaki, *Bull. Chem. Soc. Japan*, **23**, 80 (1950).
32. Hougen, O. A., and K. M. Watson, "Chemical Process Principles," John Wiley and Sons, New York (1943).
33. Hough, E. W., D. M. Mason, and B. H. Sage, *J. Am. Chem. Soc.*, **72**, 5775 (1950).
34. Hovorka, F., et al., *J. Am. Chem. Soc.*, **55**, 4820 (1933); **60**, 820 (1938); **62**, 183, 1096 (1940); **63** (1941).
35. Ishii, Naojiro, *J. Soc. Chem. Ind. (Japan)*, **38**, 661 (1935).
36. Kemp, J. D., and C. J. Egan, *J. Am. Chem. Soc.*, **60**, 1521 (1938).
37. Kistiakowsky, V. A., *J. Russ. Phys. Chem. Soc.*, **53**, I 247 (1921).
38. ———, *Z. physik Chem.*, **107**, 65 (1923).
39. Landolt Bornstein, "Physikalisch Chemische Tabellen," Erg. 1, 721; Erg. 2, 1221.
40. Lange, N. A., Handbook of Chemistry, 8th Edition (1952).
41. Lasettre, E. N., *Chem. Rev.*, **20**, 259 (1937).
42. Lippincott, E. R., and J. N. Finch, *J. Chem. Phys.*, **24**, 908 (1956).
43. Luttke, W., and R. Mecke, *Z. physik. Chem.*, **196**, 56 (1950).
44. ———, *Z. Electrochem.*, **53**, 241 (1949).
45. McAllister, S. H., and E. F. Bullard, Shell Development Company, personal communication.
46. Mecke, R., *Z. Electrochem.*, **52**, 269 (1948).
47. Nerdel, F., et al., *J. prakt. Chemie*, **4**, 156 (1956).
48. Nitta, I., and S. Seki, *J. Chem. Soc. Japan*, **69**, 141 (1948).
49. Nitta, I. et al., *Bull. Chem. Soc. Japan*, **24**, 63 (1951).
50. Pauling, L., *J. Am. Chem. Soc.*, **58**, 94 (1936).
51. Pauling, L., "Nature of the Chemical Bond," Cornell University Press, Ithica (1940).
52. Perry, J. H., "Chemical Engineers' Handbook," 3 ed., McGraw-Hill Book Co., New York (1950).
53. Prey, V., and H. Berbalk, *Monatsh.*, **82**, 990 (1951).
54. Reid, E. E., et al., *J. Am. Chem. Soc.*, **63**, 3100 (1941).
55. Sage, B. H., and W. N. Lacey, *Ind. Eng. Chem.*, **27**, 1484 (1935).
56. Satoh, J. S., *Bull. Inst. Phys. Chem. Research (Tokyo)*, **21**, 18 (1942).
57. Shell Development Data Sheets DS-47:14; DS-47:13; SC:53-65, 6829.
58. Shell Development Organic Chemicals List, 4 ed.
59. Simkin, D. J., paper presented at Am. Inst. Chem. Engrs. meeting, Seattle, (June 9-12, 1957).
60. Simkin, D. J., Vapor Pressures measured in These Laboratories," Shell Development Company.
61. Stelzner, Dissertation, Erlangen (1901).
62. Timmermans, J., "Physico-Chemical Constants of Pure Organic Compounds," Elsevier Publishing Co., New York (1950).
63. Wall, F. T., and W. F. Calussen, *J. Am. Chem. Soc.*, **61**, 2679 (1939).
64. Wiebe, R., K. H. Hubbard, and M. J. Brevoort, *J. Am. Chem. Soc.*, **52**, 611 (1930).
65. Witt, R. K., and J. D. Kemp, *J. Am. Chem. Soc.*, **59**, 273 (1937).
66. Wulf, O. R., et al., *J. Am. Chem. Soc.*, **58**, 2287 (1936); **57**, 1464 (1935).

Presented at A.I.Ch.E. Seattle meeting

Continuous Centrifugation in a Disk Centrifuge

STANLEY H. JURY and W. L. LOCKE

Union Carbide Nuclear Company, Oak Ridge, Tennessee

The design of conical disk centrifuges and interpretation of data therefrom is far from being straightforward. Smith (*3*) and Ambler (*1*) discuss semiempirical methods used in certain applications by centrifuge manufacturers in estimating capacity of a machine. Maloney (*2*) in his review of twenty-three references states that "of the recognized Unit Operations, this one has been the subject of few articles." He finally concludes that the engineering schools in the country are in excellent position to help in developing a sound theoretical background for this unit operation.

Theoretical solutions to the problem of conical disk centrifuges have been found and tested, and it is the purpose of this paper so to report.

KINETIC MECHANISM OF CENTRIFUGATION

In Figure 1 there is shown a schematic diagram of the stack of cones contained in a conical-disk type of centrifuge. The N cones of inner radius R_1 and outer radius R_2 form an angle θ with the vertical and enclose $N - 1$ spaces of thickness s. Feed slurry is fed as indicated, and during the course of its progress up through the $N - 1$ spaces it is centrifuged with angular velocity ω radian/sec. into two cuts, the dilute top cut and the concentrated bottom cut.

In the kinetic mechanism of centrifugation, it is assumed for the moment that the feed slurry contains fluid of density ρ_f and viscosity η and particles of diameter D and density ρ_s, where

$$\rho_s > \rho_f$$

The feed slurry approaches its angular velocity, ω, as it enters the $N - 1$ spaces and moves at the flow rate q or lineal velocity v up through each space.

A given particle, say P, moves laterally with a velocity v_s relative to the fluid. The components of this velocity are v_s' and v_s'', wherein the contribution of gravity is neglected because of its negligible effect in strong centrifugal fields. It is immediately apparent that whether the particle P moves up or down through a space is determined by whether $v - v_s'$ is positive or negative. Negative values of this quantity are associated with low capacities and are of no particular interest here, although subsequent mathematical treatment includes this case as well as that for positive values.

On the assumption that the particle P moves up through a space, then its trajectory involves an increase along the x coordinate as its position along the r coordinate decreases in value.

Any particle P entering at B will appear in the bottom cut if its trajectory does not cross a vertical line drawn through point A; otherwise the particle will appear in the top cut.

If the trajectories are relatively flat, as shown in Figure 1, there will be a limiting trajectory passing through point A. If the trajectories have much more curvature than that shown in Figure 1, then there will be a limiting trajectory which is tangent to a vertical line drawn through A. In any event the limiting trajectory also passes through the entrance B at some point x, say x_0. The fraction of solids from the feed recovered in the bottom cut is $(s - x_0)/s$ and this fraction can be calculated if the mathematical expression for the trajectory under consideration is known.

RESULTS

The mathematical details are contained in the Appendix. Suffice it to say here that two solutions have been developed for the case in which Stokes free settling in a centrifugal field is applicable. The feed slurry and cuts are assumed sufficiently dilute that hindered settling does not play an important role.

The first solution is

$$\frac{s - x_0}{s} = \frac{\cos\theta}{s}\left\{\frac{b}{2}\ln\left[\left(\frac{b + R_2}{b - R_2}\right)\cdot\left(\frac{b - R_1}{b + R_1}\right)\right] - (R_2 - R_1)\right\} \qquad (1)$$

which is an approximate analytical solution in the sense that in order to avoid insuperable mathematical difficulty the approximate expression for v, i.e.,

$$v \simeq \frac{q}{2\pi rs} \qquad (2)$$

has been used. The dimensionless groups $\cos\theta$, b/s, R_2/s, R_1/s, b/R_2 and b/R_1 determine the recovery efficiency of the centrifugation.

Equation (1) is plotted in Figure 2 for the case of a Merco centrifuge with specifications as follows: $N = 24$, $\theta = 45°$, $s = 0.16838$ cm., $R_1 = 5.12$ cm., $R_2 = 7.62$ cm., $\omega = 859.85$ radian/sec. (8,210 rev./min.). Of course, θ, s, R_1, and R_2 are the only variables that need be known for plotting. It is obvious from this figure that until b reaches a value of 21.7 (approximately) all particles are recovered. When b is increased beyond this value, losses set in accordingly until the recovery finally approaches zero as b approaches infinity.

The second solution is a numerical solution to the differential equation which has been converted to finite difference form thus

$$\frac{x_{n+1} - x_n}{r_{n+1} - r_n} = \frac{\cos \Theta}{1 - \frac{6b^2}{r_n^2}\left[\frac{x_n}{s} - \frac{x_n^2}{s^2}\right]} \quad (3)$$

No simplifying assumptions have been made concerning v. This solution is also plotted in Figure 2.

It is obvious from Figure 2 that the analytical solution is a fairly good approximation to the numerical solution, particularly at the smaller values of b.

The solutions may be applied to a feed having a distribution of particle sizes. One simply plots the fraction by weight vs. particle-size distribution curve. For a selected value of D on this curve, there is a corresponding point on the curve of Figure 2. The value of $(s - x_0)/s$ associated with the latter point multiplied by the selected weight fraction from the first curve gives the fractional recovery of size D. By repeating this procedure, one may tabulate enough values of [(wt. fraction)$\cdot(s - x_0)/s$] vs. D so as to form a plot of these and then determine the area under the curve which is the total fractional recovery for the mixture of particle sizes. This procedure has been tested on a pilot run with a Merco centrifuge of the foregoing specifications. In this run $\Delta\rho = 1.988 - 0.945 = 1.043$ g./cc., $\eta = 0.03$ poise, $Q = 2.5$ gal./min. total feed rate to centrifuge. It can be shown that

$$q = \frac{\frac{o}{V}}{\frac{o}{V} + 1} \cdot Q \cdot 2.743 \text{ cc./sec. passage}$$

Also

$$d = D \cdot 10^4$$

By material balance one can also show that

$$\frac{o}{V} = \frac{C_B - C_F}{C_F - C_T}$$

In the run

$$C_F = 46.17 g/L$$

$$C_T = 0.274 g/L$$

$$C_B = 202.3 g/L$$

The feed-particle-size analysis and calculated values of b along with $(s - x_0)/s$ from Figure 2 and the calculated value of

$$\left[\frac{s - x_0}{s}\right][\text{wt. fraction}]$$

are tabulated in Table 1, which shows that the predicted recovery of particles

TABLE 1

ANALYSIS OF FEED AND PREDICTED RECOVERY

d, μ	Fraction by wt. of particles in feed	Calculated values of b	$\left[\frac{s - x_0}{s}\right]$ Fig. 2 by numerical integration	$\left[\frac{s - x_0}{s}\right]$ [Fraction by wt.]
1	0.0000530	27.9	0.560	0.0000297
2	0.00141	14.0	1.00	0.00141
3	0.00660	9.31	1.00	0.00660
4	0.0173	6.98	1.00	0.0173
5	0.0366	5.59	1.00	0.0366
6	0.0669	4.65	1.00	0.0669
7	0.111	3.99	1.00	0.111
8	0.161	3.49	1.00	0.161
9	0.143	3.10	1.00	0.143
10	0.131	2.79	1.00	0.131
11	0.0891	2.54	1.00	0.0891
12	0.0876	2.33	1.00	0.0876
13	0.0745		1.00	0.0745
14	0.0188		1.00	0.0188
15	0.0117		1.00	0.0117
16	0.00710		1.00	0.00710
>16	0.0363		1.00	0.0363

The predicted recovery = 1.0000000 − 0.0000297 = 0.9999703.

in the underflow from the feed is 99.997%. The actual measured recovery in the run was 99.935%, which suggests pretty fair agreement between theory and practice.

One might wonder how particles migrate back down the upper cone surface to appear in the bottom cut once they arrive at the cone surface. The answer lies in the fact that, at the two extremities of s, the value of v is zero, while toward the center of s, the value of v reaches a maximum. Thus a particle of diameter D migrates up through a space until $v - v_s'$ goes through zero and becomes negative, when it begins to migrate downward to appear as the bottom cut. Again the mathematical details appear in the Appendix, but the fraction of s occupied by y, the thickness of the sludge stream flowing down the top cone wall, is

$$\frac{y}{s} = \frac{1 - \left(1 - \frac{2}{3}\left[\frac{r \sin \Theta}{b}\right]^2\right)^{1/2}}{2} \quad (4)$$

The film thickness is determined by the dimensionless groups, $\sin \theta$ and r/b. While this treatment is valid only for small values of y, it is valuable in that it shows, for example, that in order to keep y small for a given centrifuge and

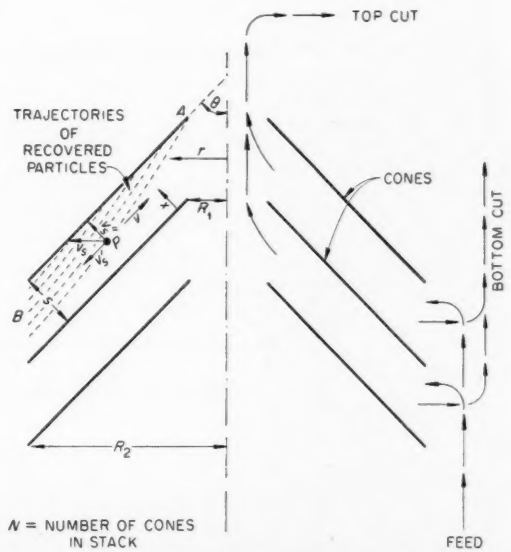

Fig. 1. Schematic drawing of cones.

particle size, one must operate with large b. Also, as one passes from R_2 to R_1, the film thickness decreases for a given particle size.

Ambler (*1*) empirically modified the theory for a simple rotating cylinder centrifuge with end caps to try to make it conform to the operation of a conical disk centrifuge. His result is

$$Q=\frac{2\Delta\rho D^2(N-1)\pi\omega^2(R_2^3-R_1^3)}{27\eta\tan\Theta} \quad (5)$$

This formula according to the author is limited to calculating a value of D for the smallest particle that will be recovered. Accuracy is not claimed for the formula and experience in its application is emphasized. A direct comparison with the formula developed in this paper is not obvious.

NOTATION

b = $\left(\frac{9q\eta\sin\Theta}{s\pi\Delta\rho D^2\omega^2}\right)^{1/2}$, cm.
C = concentration, g. solid/liter slurry
D = particle diameter, cm.
d = particle diameter, μ
F = force, g.-force
g_c = 980.665 (g.-mass)(cm./g.-force)(sec.^{2})
N = total number of cones in centrifuge
o = overflow rate, gal./min.
p = pressure, g./sq. cm.
q = flow rate through a single passage, cc./sec. of passage
Q = total slurry feed rate to centrifuge, gal./min.
r = radial position measured normal to axis of centrifuge, cm.
R = radius of top or bottom of a cone, cm.
s = distance between cones, cm.
t = time, sec.
v = fluid velocity at a point in a passage, cm./sec.
v_s = particle velocity relative to fluid, cm./sec.
v_s', v_s'' = components of v_s, cm./sec.
V = underflow rate, gal./min.
x = lineal distance normal to and measured from top side of a cone, cm.
y = sludge film thickness, cm.

Greek Letters

ρ = density, g./cc.
θ = cone angle
η = viscosity, poise (g./cm.)(sec.)
ω = angular velocity, radians/sec.
ϕ = lineal distance measured along cone, cm.

Subscripts

1 = top end of cone, or the first in a series
2 = bottom end of cone, or the second in a series
s = solid phase
f = fluid phase
n = independent variable in finite differences
o on x = x at B in Figure 2 for the limiting trajectory
F = feed
T = top cut or overflow
B = bottom cut or underflow
R = used with a force due to fluid resistance in Stokes settling
S = used with a force due to a centrifugal field

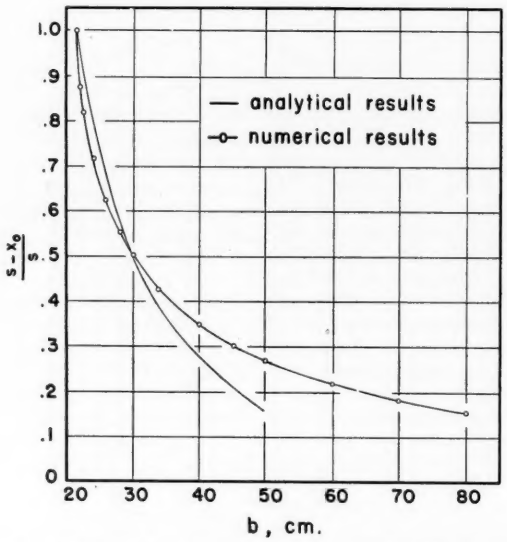

Fig. 2. Solutions to the equations governing centrifugation.

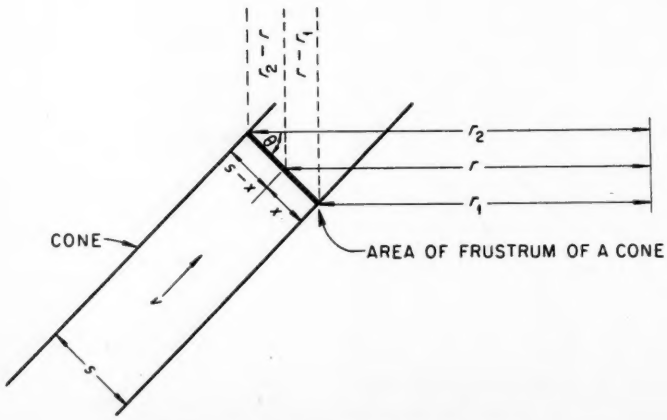

Fig. 3. The cross area of the annular space.

LITERATURE CITED

1. Ambler, C. M., *Chem. Eng. Progr.*, **48**, 150 (1952).
2. Maloney, J. O., *Ind. Eng. Chem.*, **38**, 24, 37 (1946).
3. Smith, J. C., *ibid.*, **39**, 474 (1947).

APPENDIX

Fractional Recovery of Particle Size D—Approximate Analytical Solution

The particle velocity relative to cone wall along x is defined as

$$\frac{dx}{dt}=v_s'' \quad (A1)$$

and along r is defined as

$$\frac{dr}{dt}=v_s-v\sin\Theta \quad (A2)$$

The ratio of Equation (A1) to (A2) is

$$\frac{dx}{dr}=\frac{v_s''}{v_s-v\sin\Theta} \quad (A3)$$

The problem is to express v_s'', v_s, and v as functions of x and r so that integration

of Equation (A3) becomes possible. To simplify integration, v may be approximated by the ratio of q to the cross area through which the slurry flows. The cross area under consideration is indicated in Figure 3. The area is

$$\pi(r_2 + r_1)s \qquad \text{(A4)}$$

but

$$\frac{r_2 - r}{s - x} = \cos\Theta; \qquad \frac{-r + r_1}{x} = -\cos\Theta \qquad \text{(A5)}$$

adding Equation (A5) shows that

$$r_2 + r_1 = 2r + (s - 2x)\cos\Theta \qquad \text{(A6)}$$

Therefore

$$v = \frac{q}{\pi[2r + (s - 2x)\cos\Theta]s} \qquad \text{(A7)}$$

and since

$$2r \gg (s - 2x)\cos\Theta$$

one finds that

$$v \simeq \frac{q}{2\pi rs} \qquad \text{(A8)}$$

The effective force operating on a spherical particle of diameter D in a centrifugal field is

$$g_c F_S = \frac{\pi}{6}\Delta\rho D^3\omega^2 r \qquad \text{(A9)}$$

According to Stokes's Law for free settling, the force resisting motion of the particle through the fluid is

$$g_c F_R = 3\pi\eta D v_s \qquad \text{(A10)}$$

At equilibrium the two forces F_S and F_R are equivalent if one assumes negligible the force due to the rate of change of momentum of the particle. Thus

$$v_s = \frac{\Delta\rho D^2\omega^2 r}{18\eta} \qquad \text{(A11)}$$

Also,

$$v_s'' = \frac{\Delta\rho D^2\omega^2 r}{18\eta}\cos\Theta \qquad \text{(A12)}$$

The differential equation (3A) becomes

$$\int_{x_0}^{s} dx = -\cos\Theta\int_{R_2}^{R_1}\frac{r^2\,dr}{b^2 - r^2} \qquad \text{(A13)}$$

where

$$b = \left(\frac{9q\eta\sin\Theta}{s\pi\Delta\rho D^2\omega^2}\right)^{1/2} \qquad \text{(A14)}$$

and the solution is

$$\frac{s - x_0}{s} = \frac{\cos\Theta}{s}\left\{\frac{b}{2}\ln\left[\left(\frac{b + R_2}{b - R_2}\right)\cdot\left(\frac{b - R_1}{b + R_1}\right)\right] - (R_2 - R_1)\right\} \qquad \text{(A15)}$$

Sludge Film Thickness for Particle Size D

The definition of laminar viscosity is

$$g_c\frac{\text{force}}{\text{area}} = \eta\frac{dv}{dx} \qquad \text{(A16)}$$

If the lineal distance along the surface of a cone normal to x is designated as ϕ, then over an elemental section $d\phi$ there will be a corresponding pressure drop dp. If s is small:

$$g_c\ \text{force} \simeq \frac{dp}{2}(s - 2x)2\pi r \qquad \text{(A17)}$$

and

$$\text{area} = 2\pi r\,d\phi \qquad \text{(A18)}$$

Substituting in Equation (16), one has

$$g_c\frac{1}{2}\frac{dp}{d\phi}\int_0^x (s - 2x)\,dx = \eta\int_0^v dv \qquad \text{(A19)}$$

or

$$g_c\frac{1}{2}\frac{dp}{d\phi}[sx - x^2] = \eta v \qquad \text{(A20)}$$

For small s one has that v rises to its maximum value at

$$x = \frac{s}{2} \qquad \text{(A21)}$$

From Equation (A20) then

$$g_c\frac{1}{2}\frac{dp}{d\phi}\frac{s^2}{4} = \eta v_{max} \qquad \text{(A22)}$$

The ratio of Equation (A20) to (A22) produces the result:

$$v = 4v_{max}\frac{sx - x^2}{s} \qquad \text{(A23)}$$

For small s

$$q = 2\cdot 2\pi r\int_0^{s/2} v\,dx \qquad \text{(A24)}$$

Substituting A23 in A24 and integrating gives

$$q = v_{max}\frac{4\pi r}{3}s \qquad \text{(A25)}$$

Eliminating v_{max} between Equations (A23) and (A25), one finds the velocity distribution in the annulus to be

$$v = \frac{3q}{\pi r}\frac{sx - x^2}{s^3} \qquad \text{(A26)}$$

The free settling velocity v_s is

$$v_s = \frac{\Delta\rho D^2\omega^2 r\sin\Theta}{18\eta} \qquad \text{(A27)}$$

At some distance,

$$x = y \qquad \text{(A28)}$$

the velocities v and v_s become equal and Equations (A27) and A25) may be combined to show that

$$\frac{y}{s} = \frac{1 - \left[1 - \frac{2}{3}\left(\frac{r}{b}\sin\Theta\right)^2\right]^{1/2}}{2} \qquad \text{(A29)}$$

The thickness y is that of the sludge film flowing down the cone wall. Equation (A29) may also be derived by setting

$$\frac{dr}{dx} = \cos\Theta; \qquad r = R_1$$

in the differential equation.

FRACTIONAL RECOVERY OF PARTICLE SIZE D, NUMERICAL SOLUTION

If one employs Equations (A11), (A12), and (A26) to eliminate the velocities from Equation (A3), he finds that

$$\frac{dx}{dr} = \frac{\cos\Theta}{1 - \frac{6b^2}{r^2}\left[\frac{x}{s} - \frac{x^2}{s^2}\right]} \qquad \text{(A30)}$$

This equation is difficult to solve in closed analytical form. It may however be solved by numerical methods if written in finite difference form thus

$$\frac{x_{n+1} - x_n}{r_{n+1} - r_n} = \frac{\cos\Theta}{1 - \frac{6b^2}{r_n^2}\left[\frac{x_n}{s} - \frac{x_n^2}{s^2}\right]} \qquad \text{(A31)}$$

It will be noted from Equation (A30) that if

$$\frac{dr}{dx} = 0; \qquad r = R_1$$

then

$$1 - \frac{6b^2}{R_1^2}\left[\frac{x}{s} - \frac{x^2}{s^2}\right] = 0 \qquad \text{(A32)}$$

or in the finite difference case

$$\frac{x_n}{s} = \frac{1 + \left[1 - \frac{2}{3}\left(\frac{R_1}{b}\right)^2\right]^{1/2}}{2} \qquad \text{(A33)}$$

Equation (A33) was the starting point for numerical calculation of a trajectory. By substituting s, R_1, and b, one can calculate the point x_1 on the vertical line drawn through A of Figure 2. This is the point of tangency of the limiting trajectory. If one substitutes x_1, R_1, b, s and Θ in Equation (A31) and selects an interval for Δx, then r_2 can be calculated. This process is simply repeated to obtain r_3, r_4, etc.

For

$$\Delta x = -0.09935; \qquad b = 80$$

the fractional recovery was 0.1802. When Δx was cut in half, the recovery became 0.1728. When halved three more times, the recovery became 0.1660, 0.1615 and 0.1610 respectively. The latter calculation for this and the other values of b lead to the data which form the basis of the plot in Figure 2.

Fluid Friction in Noncircular Ducts

J. E. WALKER, G. A. WHAN, and R. R. ROTHFUS

Carnegie Institute of Technology, Pittsburgh, Pennsylvania

Pressure drop due to fluid friction has been measured in a smooth tube; in six smooth concentric annuli; and between smooth, parallel, flat plates. The data cover the viscous, transition, and lower turbulent ranges of flow. Friction factors are in agreement with theory in the viscous range and can be correlated uniquely in the fully turbulent range by means of a modified hydraulic radius concept. Limits of the transition region in annuli are functions of the ratio of inner and outer radii. Correlations in the fully turbulent range permit friction factors for the noncircular ducts to be predicted within the uncertainty of smooth-tube data. Such factors can be used for the purpose of correlating other variables as well as for direct calculation of pressure drop.

The characteristics of fluid friction in smooth tubes are well known through many experimental studies. Particularly in the realm of isothermal flow, the empirical data are sufficient to establish the limits of the viscous, transition, and turbulent regimes as well as the Reynolds-number effect on friction within each region.

Unfortunately, the same is not true for isothermal flow in noncircular conduits. Taken in total, the data are numerous, but none of the common cross sections, considered individually, has been investigated as thoroughly as the circular tube. It is the purpose of this paper to present friction data for flow in concentric annuli and between parallel plates which are as consistent and precise as typical tube data and numerous enough to be meaningful.

The present investigation deals with the isothermal, steady, uniform flow of water at room temperature. Pressure-drop measurements have been made in conduits having only uniformly smooth brass, copper, and steel surfaces. The data cover the viscous, transition, and lower turbulent ranges of flow in a tube, in six concentric annuli of various radius ratios, and between parallel flat plates.

PRELIMINARY DISCUSSION

Basic Relationships

The pressure drop due to friction in a tube or pipe can be represented by means of the Fanning equation

$$\Delta p = \frac{2f\rho V^2 L}{g_0 D} \tag{1}$$

Dimensional considerations indicate that the friction factor f should be a function of the Reynolds number alone in tubes of negligible roughness. It is usual to define the Reynolds number in the manner

$$N_{Re} = \frac{DV\rho}{\mu} \tag{2}$$

largely as a matter of convenience. Other characteristic lengths and velocities could be chosen in establishing a criterion for the onset of turbulent flow if it should prove advantageous to do so.

In dealing with steady, uniform flow through uniform conduits of noncircular cross section, it is customary to write Equations (1) and (2) with an "equivalent diameter" D_e replacing the tube diameter D. By analogy with the tube, the equivalent diameter is taken to be four times the cross-sectional area occupied by the fluid divided by the wetted perimeter on which the fluid exerts skin friction. Since the latter ratio is known as the *hydraulic radius* of the conduit,

$$D_e = 4R_H \tag{3}$$

Therefore, for tubes and noncircular conduits alike,

$$N_{Re} = \frac{D_e V\rho}{\mu} \tag{4}$$

and

$$\Delta p = \frac{2f\rho V^2 L}{g_0 D_e} \tag{5}$$

The problem, of course, is to set forth the correct relationship between the friction factor and Reynolds number within each stable flow regime for each type of conduit. In the absence of an adequate theory of turbulence, the experimental problem is enormous. It, therefore, becomes a practical nesessity to seek correlations of fluid friction in noncircular ducts with that in tubes at predetermined conditions. In the realm of fully viscous flow, theoretical expressions for the friction factors can be developed on the basis of zero slip at the conduit walls.

Geometrical Considerations

Smooth, concentric annuli have certain characteristics which prove advantageous in the study of fluid friction. Symmetry dictates that the skin friction should be uniform over either of the two boundaries taken separately. On the other hand, the skin friction on the inner surface, or core, is greater than that on the outer surface by an amount depending on the ratio of the surface radii. Thus geometrical differences can be studied without the additional complication of point-to-point variations in the boundary conditions. Furthermore, from the standpoint of friction, tubes and parallel plates are limiting cases of annular cross sections; therefore, all the conduits studied in the present investigation can be considered annuli of various radius ratios.

When the entire stream is taken as the basis of definition, the equivalent diameter of an annulus is simply the difference in diameters of the outer and inner boundaries, that is,

$$D_e = D_2 - D_1 \tag{6}$$

G. A. Whan is at present at the University of New Mexico, Albuquerque, New Mexico.

For the limiting case of tubes, where the core is made vanishingly small, $D_e = D_2$. On the other hand, for the limiting case of parallel plates of infinite extent $D_e = 4b$ where b is the half clearance between the plates.

Viscous Flow

When the flow in a concentric annulus is entirely viscous, theory predicts that combination of Equations (4), (5), and (6) should yield

$$f = \frac{16}{N_{Re}} \psi_1\left(\frac{r_1}{r_2}\right) \qquad (7)$$

$$= \frac{16}{N_{Re}} \left[\frac{1 - 2\left(\frac{r_1}{r_2}\right) + \left(\frac{r_1}{r_2}\right)^2}{1 + \left(\frac{r_1}{r_2}\right)^2 + \frac{1 - \left(\frac{r_1}{r_2}\right)^2}{\ln\left(\frac{r_1}{r_2}\right)}} \right]$$

For a tube the bracketed term is 1.00 and for parallel plates it is 1.50. Values at intermediate radius ratios can be obtained from Table 1.

Senecal and Rothfus (*10*) measured pressure gradients in smooth tubes and found Equation (7) to be obeyed exactly at Reynolds numbers of less than 1,200. Prengle and Rothfus (*7*), using a dye technique, found viscous flow at every point in smooth tubes when the Reynolds number was less than 1,225. On the other hand, their results for concentric annuli indicate an initial deviation from entirely viscous flow at Reynolds numbers in the vicinity of 700. The pressure-drop data of Carpenter and coworkers (*2*) for one annulus confirm Equation (7) up to a Reynolds number of about 800.

Transition Flow

Senecal and Rothfus have demonstrated that the reproducibility of transition-range friction factors in tubes can be made equal to that in the fully turbulent range with sufficient care. The only other requirement is a normally high level of disturbance in the tube entry.

At Reynolds numbers between 1,200 and 2,030 in smooth tubes Senecal and Rothfus observed a slight progressive departure from the friction-factor equation for viscous flow. The principal transition region lay between the lower critical Reynolds number of 2,030 and an upper critical value of 2,750. The dye experiments of Prengle and Rothfus indicated sinuous flow in the main stream at Reynolds numbers between 1,225 and 2,100. Large disturbance eddies were cast off with increased frequency as the Reynolds number was increased from 2,100 to 2,800. Above the latter value, both pressure-drop and dye studies suggested fully turbulent motion throughout the main stream.

In the case of concentric annuli as well as parallel plates the limits of the tran-

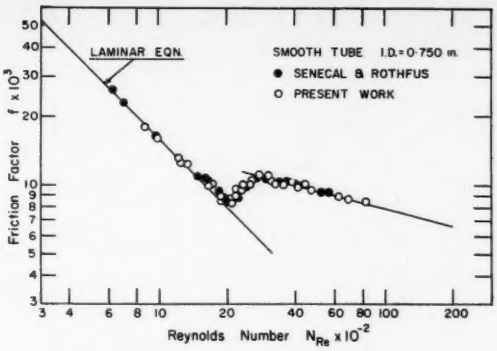

Fig. 1A.

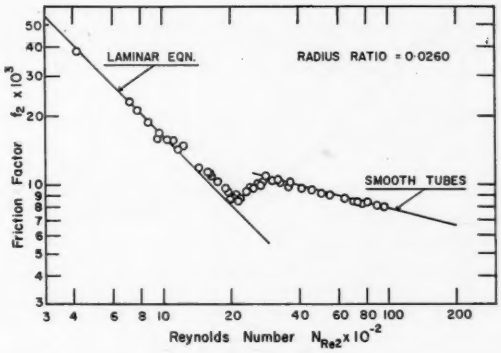

Fig. 1B.

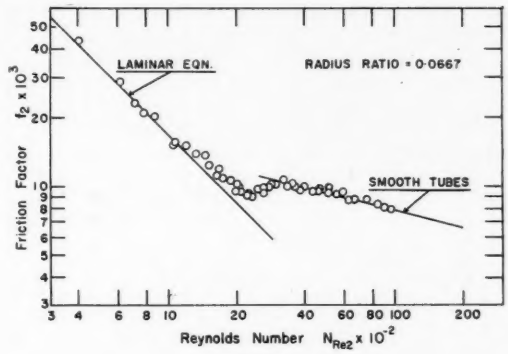

Fig. 1C.

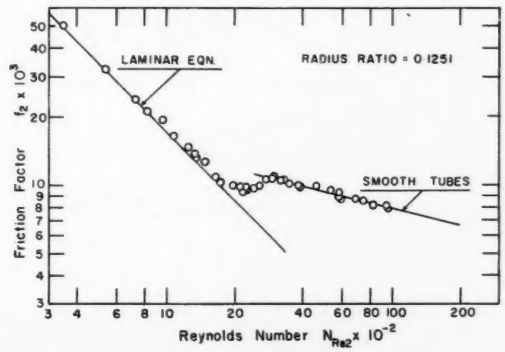

Fig. 1D.

Fig. 1. Fanning friction factors for tubes, parallel plates, and the outer surfaces of annuli.

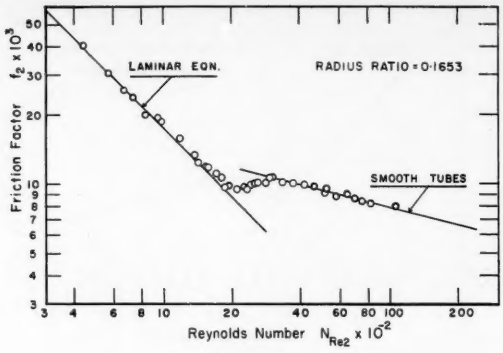

Fig. 1E.

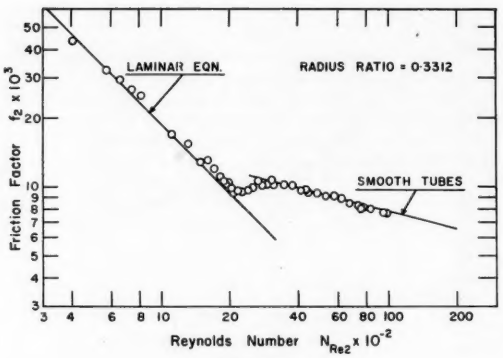

Fig. 1F.

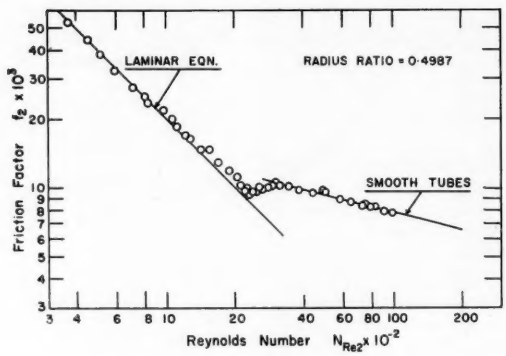

Fig. 1G.

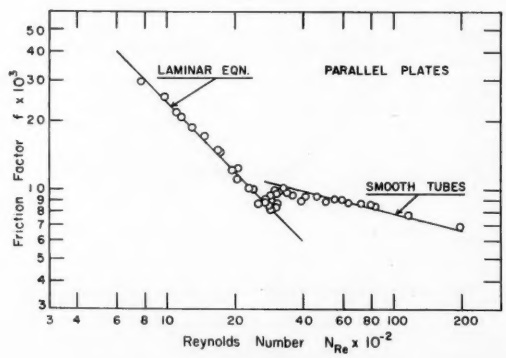

Fig. 1H.

Fig. 1 (*continued*).

TABLE 1

EFFECT OF GEOMETRY ON VISCOUS-FLOW FRICTION FACTORS IN CONCENTRIC ANNULI

r_1/r_2	0.0	0.1	0.2	0.4	0.6	0.8	1.0
$\psi_1(r_1/r_2)$, Equation (7)	1.00	1.40	1.44	1.48	1.49	1.50	1.50
$\psi_2(r_1/r_2)$, Equation (19)	1.00	1.06	1.11	1.21	1.31	1.41	1.50

sition region and the friction factor behavior within that region have not been established adequately. A few consistent data, such as Carpenter's, are available, but no single investigator has obtained precise data over a wide range of radius ratios. The dye studies of Prengle and Rothfus indicated a progressive spread of sinuous flow over the main stream in annuli at Reynolds numbers above 700. Although this behavior was similar to that in smooth tubes, the authors could not extend their data to establish the Reynolds number at which the first disturbance eddy was cast off.

Turbulent Flow

It is customary to deal with friction in fully turbulent flow through noncircular ducts by applying the hydraulic radius concept to the entire stream. In brief, this assumes that the friction factor in Equation (5) can be obtained from the smooth-tube correlation at the Reynolds number defined in Equation (4).

A force balance on the entire stream shows that if the skin friction is equal at all points on the wetted perimeter,

$$\frac{\Delta p g_0}{L} = \frac{\tau_0 g_0}{R_H} = \frac{4\tau_0 g_0}{D_e} \qquad (8)$$

The balance can also be written in the form of Equation (5) through the introduction of the appropriate friction factor. If the skin friction varies from point to point around the perimeter of the conduit, the corresponding local friction factors must also change. The over-all friction factor of Equation (5) represents the integrated effect of the local values on the pressure drop and may bear a complex relationship to the physical situation. It is, therefore, rather unlikely that the hydraulic-radius method should be completely successful unless the stipulation of uniform skin friction is fulfilled. Parallel plates, however, meet this requirement and thus stand a good chance of being handled satisfactorily by means of the empirical procedure.

On the other hand, a force balance on the entire stream in an annular duct shows that

$$\frac{\Delta p g_0}{L} = \frac{2(r_1\tau_1 g_0 + r_2\tau_2 g_0)}{(r_2^2 - r_1^2)} \qquad (9)$$

The two skin frictions therefore, would have to be averaged in order to reproduce the form of Equation (8). It seems

unlikely that any more than a rough approximation of the actual pressure drop would be forthcoming from the over-all application of hydraulic radius.

At Reynolds numbers between 3,000 and 100,000 in smooth tubes the Fanning friction factor is closely correlated by the Blasius equation (*1*)

$$f = 0.079/(N_{Re})^{0.25} \qquad (10)$$

Sage and coworkers (*3*, *5*, *6*) have obtained friction data for flow between parallel plates which are in approximate agreement with Equation (10) at Reynolds numbers from 6,960 to 53,200. It should be noted that infinite parallel plates are simulated in practice by rectangular passages of large-aspect ratio. It is exceptionally difficult to isolate conditions in the central portion of such ducts from side effects; therefore, it is not surprising that friction factors for parallel plates are generally measured with less precision than those for tubes.

Early measurements of friction in concentric annuli reviewed by Wiegand and Baker (*11*) show conflicting deviations from Equation (10) with varying radius ratios. More recent data on local velocities as well as friction (*4*, *8*) have pointed toward a more consistent dependence of friction factor on the geometry of the conduit.

EXPERIMENTAL EQUIPMENT

Static pressure gradients were measured in a brass tube and six concentric annuli formed by fitting the tube with metallic cores of various radii. Pressure drops were also obtained in a brass duct of rectangular cross section. Principal dimensions of the various conduits are summarized in Table 2. Upstream calming lengths varied from 167 to 450 equivalent diameters.

The test fluid was water at room temperature. Isothermal flow was maintained by means of heat exchangers installed in the external piping system through which the water was circulated steadily and continuously.

The pressure differences were indicated on vertical U-tube manometers designed to minimize contamination of the liquid-liquid interface. Use of a micromanometer was avoided through the selection of monochlorobenzene as a manometer fluid. Since the specific gravity of monochlorobenzene at 20°C. is 1.1084 referred to water at 20°C., the desired degree of multiplication was obtained in the manometer readings at low pressure differences. For larger differences in pressure, carbon tetrachloride was used as the manometer fluid.

BASIS OF CORRELATION

The steady, uniform, isothermal flow of an incompressible fluid through any smooth, concentric annulus will be considered, including the limiting cases of tubes and parallel plates. At some radial distance r_m from the center of the configuration, the velocity profile goes through a maximum point and the local shearing stress reaches zero. In fully viscous flow, the force balance on a differential element of fluid predicts that

$$r_m^2 = \frac{r_2^2 - r_1^2}{\ln\left(\frac{r_2}{r_1}\right)^2} \qquad (11)$$

Katz and Knudsen (*4*) and Rothfus, Monrad, and Senecal (*8*) have shown by velocity measurements that the same relationship serves to represent r_m in fully turbulent flow as well as in the viscous range. Rothfus and coworkers (*9*) have used drag measurements at the core to show that the radius of maximum velocity does not, however, obey Equation (11) in the transition range. Exceptions to this are the limiting cases of tubes and parallel plates where symmetry forces the point of maximum velocity to remain undisturbed.

If a portion of the fluid lying between the radius of maximum velocity and an arbitrary radius r is considered, the hydraulic radius for this segment may be defined in the usual manner. The cross-sectional area occupied by the fluid is $\pi(r^2 - r_m^2)$ and the perimeter over which fluid shear is exerted is simply $2\pi r$, since no shear exists at the radius of maximum velocity. Thus

$$R_{H_r} = \frac{r^2 - r_m^2}{2r} \qquad (12)$$

If r is taken to be r_1 or r_2, the radii of the inner and outer surfaces, respectively, the definite hydraulic radii R_{H_1} and R_{H_2} can be specified through Equation (12). For example,

$$R_{H_2} = \frac{r_2^2 - r_m^2}{2r_2} \qquad (13)$$

It is apparent that R_{H_1} loses significance as the core is made vanishingly small. The portion of the fluid between the radius of maximum velocity and the outer surface of the annulus is of more immediate concern for purposes of correlation.

The pressure gradient due to friction is related to the skin friction, $\tau_2 g_0$, at the outer boundary through the force balance

$$\frac{\Delta p g_0}{L} = \frac{\tau_2 g_0}{R_{H_2}} = \frac{4\tau_2 g_0}{D_{e_2}} \qquad (14)$$

which is the equivalent of Equation (8). By analogy with Equation (5), a friction factor f_2 for the outer surface can be defined in such manner as to make

$$\Delta p = \frac{2f_2\rho V^2 L}{4g_0 R_{H_2}} = \frac{2f_2\rho V^2 L}{g_0 D_{e_2}} \qquad (15)$$

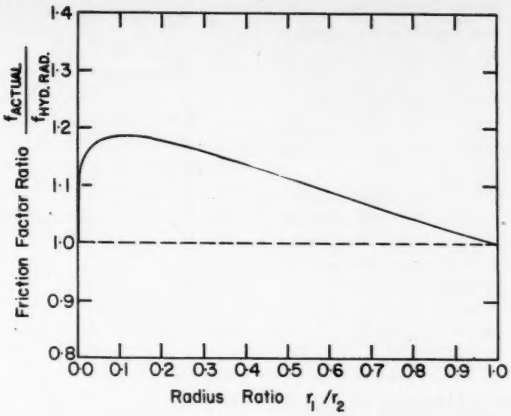

Fig. 2. Comparison of over-all friction factors in the lower turbulent range with those calculated by means of hydraulic radius applied to the whole annular stream.

TABLE 2
DIMENSIONS OF EXPERIMENTAL CONDUITS

Conduit	Outer tube Material	r_2, in.	Inner tube Material	r_1, in.	(r_1/r_2)	$r_2 - r_1$, in.	r_m, in.
Tube	brass	0.3750	—	—	0.0000	—	0.000
Annulus 1	brass	0.3750	Steel	0.0098	0.0260	0.365	0.139
2	brass	0.3750	Steel	0.0250	0.0667	0.350	0.161
3	brass	0.3750	Steel	0.0469	0.1251	0.328	0.182
4	brass	0.3750	Steel	0.0620	0.1653	0.313	0.195
5	brass	0.3750	Copper	0.1242	0.3312	0.251	0.238
6	brass	0.3750	Copper	0.1870	0.4987	0.188	0.276
Parallel plates*	brass	∞	Brass	∞	1.0000	0.700	

*Rectangular passage, 14 in. wide by 0.700 in. clearance.

It is, therefore, reasonable to investigate the merit of the hydraulic-radius method of correlating fully turbulent friction by applying the concept to that part of the fluid lying outside the radius of maximum velocity. Only in the cases of tubes and parallel plates is this the same as dealing with the entire stream.

Extending the hydraulic radius concept in this manner implies that the friction factor f_2 at the outer wall should be obtained from the smooth-tube correlation at the Reynolds number

$$N_{Re_2} = \frac{2(r_2^2 - r_m^2)V\rho}{r_2\mu} \qquad (16)$$

provided that the flow is fully turbulent. Thus at Reynolds numbers in the lower turbulent range,

$$f_2 = 0.079/(N_{Re_2})^{0.25} \qquad (17)$$

for annuli and parallel plates as well as tubes.

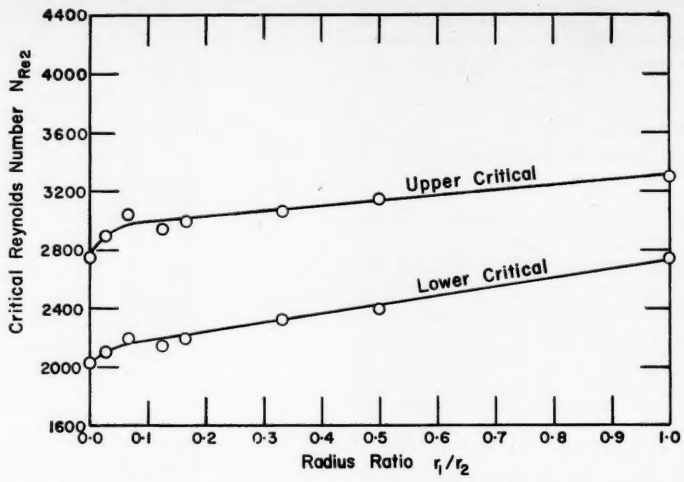

Fig. 3. Effect of radius ratio on critical Reynolds numbers.

RESULTS AND DISCUSSION

The experimental data* are summarized in Figure 1 as graphs of f_2 against N_{Re_2} on logarithmic coordinates. The abscissae have been calculated from Equation (16) and the ordinates from Equation (15). The radius of maximum velocity has been obtained from Equation (11) over the whole Reynolds-number range, since the behavior of r_m in the transition region is not well known.

Comparison of Equations (5) and (15) shows that

$$f_2 = f\left(\frac{D_{e_2}}{D_e}\right) = f\left(\frac{N_{Re_2}}{N_{Re}}\right) \qquad (18)$$

Therefore, in fully viscous flow, combination of Equations (7) and (18) yields the theoretical expression

$$f_2 = \frac{16}{N_{Re_2}}\psi_2\left(\frac{r_1}{r_2}\right) \qquad (19)$$

$$= \frac{16}{N_{Re_2}}\left[\frac{(r_2^2 - r_m^2)^2}{r_2^2(r_2^2 + r_1^2 - 2r_m^2)}\right]$$

Values of the bracketed term at various radius ratios are shown in Table 1. The experimental data are in exact agreement with Equation (19) at low Reynolds numbers where entirely viscous flow can reasonably be expected.

In the fully turbulent range the friction factors for all three cross sections obey Equation (17) very closely. The parallel-plate data deviate from the tube curve somewhat more than do the data for annuli. Since the experimental uncertainty is greater in the case of parallel plates, as previously mentioned, Equation (17) can still be taken to represent these data adequately. In addition to the wide range of radius ratios covered by the present data, Rothfus, Monrad, and Senecal have observed that their data for annuli having radius ratios of 0.1625 and 0.650 also obey Equation (17) in the lower turbulent range. It can, therefore, be concluded that a unique correlation for all concentric annuli is attainable through application of the hydraulic radius concept to the portion of the fluid lying between the outer boundary of the conduit and the radius of maximum velocity.

Since the friction factor at the outer surface is so accurately correlated in this manner, it is of interest to inquire what magnitude of error would be incurred by using the equivalent diameter for the whole stream in the usual way. In this case the over-all friction factor f, defined by Equations (5) and (6), is assumed to obey Equation (10) with the Reynolds number calculated by means of Equation (4). On the other hand, the actual values of f must be related to the experimental values of f_2 through Equation (18). Combination of Equations (10), (17), and (18) shows the actual over-all friction factor to be related to the friction factor predicted from over-all hydraulic radius by the equation

$$\frac{f \text{ actual}}{f \text{ hydraulic radius}} = \left[\frac{2\left(1 - \frac{r_1}{r_2}\right)\ln\frac{r_2}{r_1}}{\left(\frac{r_1}{r_2}\right)^2 - 1 + 2\ln\frac{r_2}{r_1}}\right]^{1.25} \qquad (20)$$

It is, therefore, apparent that the friction factor calculated by means of over-all hydraulic radius must differ from the actual friction factor by an amount dependent on the radius ratio of the conduit. There is also a small effect of Reynolds number since the value of the exponent in the last equation is related to the slope of the logarithmic friction-factor–Reynolds-number correlation.

The friction-factor ratio of Equation (20) is shown at various radius ratios in Figure 2. It is apparent that the error due to using the over-all hydraulic-radius method reaches a maximum value at $r_1/r_2 = 0.11$. Since many commercial annuli have radius ratios between 0.5 and 1.0, the error incurred may not be very serious if pressure drop alone is the important variable. On the other hand, at lower radius ratios or where precise friction data are required as a basis for other correlations, the application of hydraulic radius to the whole stream may not be sufficiently accurate. In any case the correction obtained from Equation (20) or Figure 2 very simply reduces the error to a negligible percentage in the lower turbulent range.

Even at Reynolds numbers above 100,000 it is recommended that f_2 be obtained from the smooth-tube correlation at N_{Re_2} and the pressure drop calculated by means of Equation (15). The friction factor f_1 at the inner surface, defined by Equation (15) with the equivalent diameter

$$De_1 = 4R_{H_1} = \frac{2(r_m^2 - r_1^2)}{r_1} \qquad (21)$$

replacing the equivalent diameter De_2, can easily be related to the friction factor f_2. As shown by Rothfus, Monrad, and Senecal,

*Complete tabular material has been deposited as document 5438 with the American Documentation Institute, Photoduplication Service, Library of Congress, Washington 25, D. C., and may be obtained for $6.25 for photoprints or $2.50 for 35-mm. microfilm.

$$\frac{f_1}{f_2} = \frac{\tau_1 g_0}{\tau_2 g_0} = \frac{r_2\,(r_m^2 - r_1^2)}{r_1\,(r_2^2 - r_m^2)} \qquad (22)$$

The last equation is valid at all Reynolds numbers since it is nothing more than a combination of force balances. In the fully viscous and fully turbulent regions, the radius of maximum velocity can be obtained from Equation (11).

The friction factors shown in Figure 1 serve to mark the limits of the transition range. In every case a dip occurs in the correlations for the noncircular ducts in much the same manner as for smooth tubes. The upper and lower critical Reynolds numbers marking the maxima and minima in the transition friction factors are shown as functions of the radius ratio in Figure 3. Except for annuli having very small cores a linear relationship adequately represents the data.

It should be noted that the Reynolds numbers in Figure 3 are calculated with the radius of maximum velocity indicated in Equation (11). Rothfus and coworkers (9) have found that r_m is greater than the computed value at the lower critical Reynolds number. Therefore, the actual lower critical value is somewhat smaller than shown in Figure 3. The same appears to be true at the upper critical Reynolds number to a lesser degree. Any firm conclusion, however, must be postponed until accurate velocity distributions have been obtained experimentally.

The data of Figure 1 also indicate a small upward deviation from the viscous relationship at Reynolds numbers below the lower critical point. The behavior of the friction factors in this range of flow is similar to that in smooth tubes. The data are consistent with the results of previous dye studies, which indicate that a regime of sinuous flow proceeds the initial formation of disturbance eddies in annuli as well as in tubes.

The friction data suggest that the Reynolds number at which viscous flow first becomes unstable depends on the radius ratio. Although pressure drop is an insensitive indication of sinuous flow, there is some tendency for the first deviation from viscous behavior to appear at lower and lower Reynolds numbers as the radius ratio is increased. No conclusion can be drawn in the absence of velocity distributions, but it is likely that the Reynolds number of 700 reported by Prengle and Rothfus is only a rough approximation of the actual values at which sinuous flow begins in annular ducts.

In view of the experimental results and the foregoing discussion, it is possible to predict the frictional pressure drop for isothermal, steady, uniform flow through smooth concentric annuli with about the same precision as in the case of smooth tubes. If the flow is fully viscous or fully turbulent, the individual skin frictions at the inner and outer surfaces of the conduit can also be computed. If the fluid is in transitional flow, only the skin friction at the outer wall can be obtained from the present data. The limits of the transition region have been established experimentally over the whole range of radius ratios as shown in Figures 1 and 3.

In order to calculate pressure drops or individual skin frictions, the flow regime should be established by calculating the radius of maximum velocity from Equation (11) and the Reynolds number from Equation (16). Interpolation in Figure 1 then indicates whether viscous, transition, or turbulent flow can be expected to prevail under the predetermined conditions of operation. If the flow is entirely viscous, the friction factor at the outer wall f_2 can be obtained from Equation (19) and the pressure drop can then be calculated by means of Equation (15). The friction factor at the inner wall f_1 can be calculated, in turn, from Equation (22). Then the skin frictions at the two surfaces can be obtained separately from their defining equations

$$\tau_1 g_0 = \frac{f_1}{2}\,\rho V^2 \qquad (23)$$

and

$$\tau_2 g_0 = \frac{f_2}{2}\,\rho V^2 \qquad (24)$$

If the flow is fully turbulent, the outer wall friction factor f_2 can be obtained at the Reynolds number N_{Re_2} from Figure 1 or a similar graph of friction factor against Reynolds number for smooth tubes. The pressure drop can then be calculated from Equation (15), the inner wall friction factor from Equation (22), and the individual skin frictions from Equations (23) and (24). If the flow is transitional, the value of f_2 is best obtained by interpolating in Figure 1. The pressure drop can then be calculated by means of Equation (15).

NOTATION

b = half clearance between parallel flat plates, ft.

D = diameter of tube, ft.; D_1 = inner diameter of annular space, ft.; D_2 = outer diameter of annular space, ft.

D_e = equivalent diameter of noncircular duct based on hydraulic radius of the whole stream, ft.; D_{e_1} and D_{e_2} = equivalent diameters based on hydraulic radii R_{H_1} and R_{H_2} respectively, ft.

f = Fanning friction factor defined in Equations (1) and (5), dimensionless; f_1 and f_2 = friction factors for the inner and outer surfaces, respectively, of an annular conduit, dimensionless

g_0 = conversion factor = 32.2 (lb. mass)(ft.)/(lb. force)(sec.^{2})

L = length of conduit, ft.

N_{Re} = Reynolds number defined in Equations (2) and (4), dimensionless; N_{Re_2} = Reynolds number for annuli defined in Equation (16), dimensionless

Δp = pressure drop due to fluid friction, lb. force/sq. ft.

r = radius from center of configuration to a point in the fluid stream, ft.; r_1 = inner radius of annular space, ft.; r_2 = outer radius of annular space, ft.

r_m = radius from center of configuration to the point of maximum local fluid velocity, ft.

R_H = hydraulic radius (i.e., cross-sectional area of fluid + wetted perimeter) for the whole stream, ft.; R_{H_1} = hydraulic radius of the fluid between r_m and r_1, ft.; R_{H_2} = hydraulic radius of the fluid between r_m and r_2, ft.; R_{H_r} = hydraulic radius of the fluid between r_m and r, ft.

V = bulk average linear velocity of the fluid, ft./sec.

Greek Letters

μ = viscosity of the fluid, lb. mass/(sec.)(ft.)

ρ = density of the fluid, lb. mass/cu. ft.

τ = local shearing stress at a point in the fluid stream, lb. force/sq. ft.; τ_0 = skin friction at the wall of a conduit, lb. force/sq. ft.; τ_1 and τ_2 = skin frictions at the inner and outer surfaces, respectively, of an annular space, lb. force/sq. ft.

ψ_1, ψ_2 = geometrical functions defined in Equations (7) and (19), dimensionless

LITERATURE CITED

1. Blasius, H., *Mitt. Forschungsarb.*, **131**, 1 (1913).
2. Carpenter, F. G., A. P. Colburn, E. M. Schoenborn, and A. Wurster, *Trans. Am. Inst. Chem. Engrs.*, **42**, 165 (1946).
3. Corcoran, W. H., F. Page, Jr., W. G. Schlinger, and B. H. Sage, *Ind. Eng. Chem.*, **44**, 410 (1952).
4. Knudsen, J. G., and D. L. Katz, *Proc. Midwestern Conf. on Fluid Dynamics*, 1st Conf., No. 2, 175 (1950).
5. Page, F., Jr., W. H. Corcoran, W. G. Schlinger, and B. H. Sage, *Ind. Eng. Chem.*, **44**, 424 (1952).
6. Page, F., Jr., W. G. Schlinger, D. K. Breaux, and B. H. Sage, *ibid.*, **44**, 419 (1952).
7. Prengle, R. S., and R. R. Rothfus, *ibid.*, **47**, 379 (1955).
8. Rothfus, R. R., C. C. Monrad, and V. E. Senecal, *ibid.*, **42**, 2511 (1950).
9. Rothfus, R. R., C. C. Monrad, K. G. Sikchi, and W. J. Heidger, *ibid.*, **47**, 913 (1955).
10. Senecal, V. E., and R. R. Rothfus, *Chem. Eng. Progr.*, **49**, 533 (1953).
11. Wiegand, J. H., and E. M. Baker, *Trans. Am. Inst. Chem. Engrs.*, **38**, 569 (1942).

Mass Transfer Between Two Liquids with Chemical Reaction

RICHARD SEARLE and KENNETH F. GORDON, University of California, Berkeley, California

The subject of mass transfer between two phases with chemical reaction is only partially developed, as shown by the fact that absorption and extraction processes with chemical reaction are apparently designed on the basis of laboratory and pilot plant runs rather than on more basic premises. Examples of the processes would be found in the Solvay process, the manufacture of dry ice, and the production of nitric acid.

Whitman and several coauthors (*18, 19, 20*) set forth the fundamentals of mass transfer between two phases on the basis of the two-film theory, in which the resistance of each phase was represented by an equivalent film. More recently several authors (*5, 10*) have shown evidence for the existence of an appreciable interfacial resistance at high rates of transfer. Several years ago Danckwerts (*4*) suggested another model for the process of interphase mass transfer. Instead of an equivalent two-film picture he postulated an unsteady state situation with eddies of one fluid momentarily resting at the interface until displaced by other eddies coming from the bulk of the same fluid phase. During the period when the eddy rests at the interface unsteady state mass transfer takes place. This viewpoint, known as the penetration theory, results in equations of the same general form as those of the film theory. The available evidence does not indicate which picture is closer to the truth. Probably both views have partial validity, and a more accurate picture may well be a compromise between the two.

Hatta (*8*) pioneered with the application of the two-film concept to the case of absorption of carbon dioxide in potassium hydroxide and showed how the concept could qualitatively explain the experimental results. In their fairly recent text Sherwood and Pigford (*15*) devote a chapter to the subject of mass transfer with chemical reaction, giving an excellent summary of the mathematical and experimental developments in the field. Recently several studies on gas absorption with chemical reaction (*1, 14, 16*) have been published. There seems to be much less experimentation in liquid-liquid extraction with chemical reaction.

The steady state picture of two solutes A and B diffusing through stagnant films close to the interface between phases W and I, where W contains B and I has A, and undergoing instantaneous reaction in one of the films results in the following equations:

for reaction in phase W

$$\frac{k_{AW}}{k_{AW}'} - 1 = \frac{D_{BW}C_{BW}}{D_{AW}C_{AW_i}} \qquad (1)$$

and for reaction in phase I

$$\frac{k_{BI}}{k_{BI}'} - 1 = \frac{D_{AI}C_{AI}}{D_{BI}C_{BI_i}} \qquad (2)$$

Naturally, for the case of reaction in phase W the transfer coefficient k_{AI} equals k_{AI}'. The other coefficient in W, namely k_{BW}, which is greater than k_{BW}', follows from k_{AW}, k_{BW}', and the film concept. The parallel derivation holds for reaction in phase I.

The other picture, that of unsteady diffusion into an eddy which is momentarily resting at the interface, gives the same numerical result if the molecular diffusivities of each solute are equal.

The main difference between the two pictures of the transfer process without chemical reaction is that the strict film theory indicates that the individual transfer coefficient should be proportional to the first power of the molecular diffusivity while the penetration or transient state theory yields the result that the individual-phase mass transfer coefficient should vary as the square root of the molecular diffusivity.

An exact solution is available for the equations which result when the case of second-order infinitely rapid irreversible reaction is considered by the penetration theory (*2, 3, 4*). The solution is complicated and so makes an approximation convenient to use. Peaceman (*13*) and Sherwood and Pigford (*15*) have found that a close approximation is given if the square root of the molecular diffusivities is substituted for the first power in Equations (1) and (2). Thus for reaction in phase W a good approximation is

$$\frac{k_{AW}}{k_{AW}'} - 1 = \sqrt{\frac{D_{BW}}{D_{AW}}}\frac{C_{BW}}{C_{AW_i}} \qquad (1a)$$

and for reaction in phase I

$$\frac{k_{BI}}{k_{BI}'} - 1 = \sqrt{\frac{D_{AI}}{D_{BI}}}\frac{C_{AI}}{C_{BI_i}} \qquad (2a)$$

In the present sodium hydroxide–acetic acid system where $D_{BW}/D_{AW} = 1.6$, when $D_{BW}\ C_{BW}/D_{AW}\ C_{AW_i}$ or $D_{AI}\ C_{AI}/D_{BI}\ C_{BI_i}$ is unity, Peaceman has found that these approximations are good to within 10% and to within 5% when the ratios are greater than ten. They continue to become even better as the ratios increase.

The purpose of this study is not to choose one model as being preferable but to determine the value of the equations in predicting and correlating data for extraction with chemical reaction. A rapid irreversible reaction is the neutralization reaction between sodium hydroxide and acetic acid. In a study of this system with an apparatus very similar to that used in the present investigation, Osborne (*12*) working with T. K. Sherwood and K. F. Gordon has found mass transfer rates higher than would be predicted by theory. When the concentration of each component was about $0.45N$, transfer rates were found to be more than twice as great as those which would be predicted by the two-film theory. His data were all for a concentration of about $0.45N$ acetic acid, so only a partial picture of the behavior of this system was obtained.

The reaction was studied in a system consisting of a layer of alcohol-saturated water containing sodium hydroxide beneath a layer of water-saturated 2-methyl-1-propanol (isobutanol) containing acetic acid. The distribution coefficients $m = C_I/C_W$ were 0.0051 for the sodium hydroxide and 1.18 (*6*) for the acetic acid. As shown in Figure 1, the solvents were in a cylinder having a stirrer with a single arm in each phase rotating at such a speed that the interface was smooth and of known constant area. Values for the individual transfer coefficients k_W' and k_I' were obtained by a previously described technique (*7*). To obtain the individual transfer coefficients, thirteen runs without chemical reaction were made with five solutes.

APPARATUS

The apparatus, similar to one previously described (*7*), consisted of a glass cylinder, 6.09 in. I.D. suspended in a constant-temperature bath at 25°C. The stirring arms, of 3/16 in. stainless steel rod, were mounted at right angles in a 5/16-in.-diam. circular stainless steel shaft. The upper arm was 4 in. long, mounted with its center line 2¾ in. above the lower end of the rod while the lower stirrer, 2⅞ in. long, with its center line ½ in. above the end of the rod, was placed at a right angle to the upper stirrer. The shaft ended ½ in. from the center of the floor of the glass cylinder which was slightly curved, being ¼ in. higher at the center than at the edge. The end of the rod and the stirrer arms were slightly beveled. The

Richard Searle is at present with Rocketdyne Division of North American Aviation, Inc., Canoga Park, California, and Kenneth F. Gordon with the University of Michigan, Ann Arbor, Michigan.

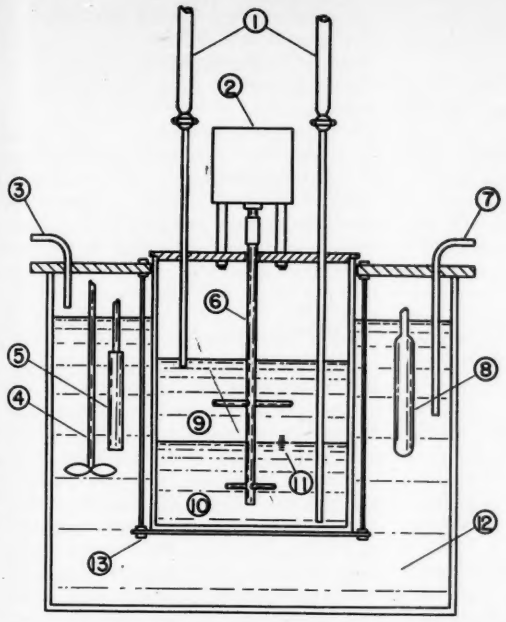

Fig. 1. Schematic diagram of apparatus. (1) burets; (2) stirrer motor; (3) water inlet to bath; (4) bath stirrer; (5) immersion heater; (6) reaction vessel stirrer; (7) constant head siphon; (8) mercury thermostat; (9) isobutanol phase; (10) water phase; (11) etched scale on reaction vessel; (12) thermostat bath; (13) reaction vessel supports.

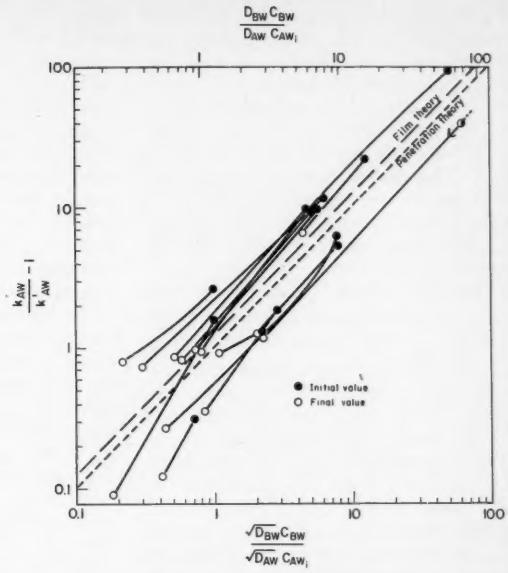

Fig. 2. Experimental increase of aqueous-phase mass transfer coefficient vs. theoretical increase.

stirrer was driven at 75 rev./min. by a constant-speed motor.

Extended tips from burettes containing solvent ran into each phase.

PROCEDURE

One liter of the alcohol phase, containing the acetic acid, was added to the cylinder, and the water containing the sodium hydroxide was placed slowly beneath the alcohol through a bent glass tube from a separatory funnel so that there was a minimum of initial mass transfer between the two phases. The stirrer was started, and periodically 10-ml. samples of each phase were taken and solvent was added to the phase in order to keep the total phase volume constant. Usually samples were taken every 10 min., but when the transfer rate was high the interval would be 5 min. or even as low as 2 min.

In order to reduce the possible interference of solvent transfer on the transfer process being studied the solvents were 90 vol. % saturated with the second solvent when the initial solutions were being prepared; likewise the replacement solvents were also 90% saturated.

All samples were diluted with neutralized 50 vol. % ethanol in water and titrated with sodium hydroxide or hydrochloric acid in 50 vol. % ethanol. This avoided titrations involving two phases.

RESULTS

The values for the over-all transfer resistance of various solutes were plotted against the distribution coefficient. The solutes were acetic acid, valeric acid, tetraethanol ammonium hydroxide, tetramethylammonium hydroxide, and sodium hydroxide. A straight line of intercept equal to the resistance of one phase and of slope equal to the resistance of the other phase resulted. This is to be expected from the equations for the additivity of resistances. As the solutes had various diffusivities the result would be more accurate if a correction for differences in diffusivity were made. This is done by converting each resistance to that for a solute with a molecular diffusivity of 3.6×10^{-2} sq. cm./hr. This value, while arbitrary, is an intermediate value of those solutes used. The factor used to make this correction is the ratio of the square root of the diffusivities. Thus $1/K_{corrected}$ is equal to $(1/K)(D/3.6 \times 10^{-2})^{1/2}$.

The experimental values for the individual transfer coefficients were 9.5 cm./hr. for k'_I and 10.0 cm./hr. for k'_W for a substance having a diffusivity of 3.6×10^{-2} sq. cm./hr. These values may be compared with the values of 9.0 and 10.4 cm./hr. (7) for the respective values in a similar, but not quite identical, apparatus after a minor correction for the difference in stirrer speeds.

For the runs with chemical reaction, as broad a range as possible was taken for concentrations and concentration ratios. Analytical techniques limited the lower concentration, and the effect of solute concentration on properties such as viscosity and density, which would in turn affect the hydrodynamics, limited the upper concentration, which was arbitrarily set as $1.4N$, for all but one run.

A total of twenty-four reaction runs was made. In fourteen the initial acetic acid concentration was greater than that of the sodium hydroxide. In one of these runs the reaction zone, which was initially in the isobutanol phase because of the high diffusivity of sodium hydroxide, moved into the water phase as the ratio of the acetic acid concentration to that of the sodium hydroxide increased. In the other thirteen runs of this set the reaction zone remained in the aqueous phase. Nine runs were made where the sodium hydroxide concentration was larger than that of the acetic acid, and one was made where it was equal, and so reaction took place entirely in the alcohol phase for these runs.*

On a hydrodynamical basis there is no clear choice between the film and penetration theories. However, the evidence from transfer without chemical reaction indicates that the transfer coefficient is more nearly proportional to the square root of the molecular diffusivity as required by the penetration theory, rather than to the first power (7). In the present systems the conditions postulated by either theory could exist. Therefore, the results will be considered in the light of both views.

The results in Figure 2 are plotted as suggested by the penetration theory [Equations (1*a*) and (2*a*)]. This plot shows all the runs which, according to theory, occurred in the aqueous phase, the solid circles representing values at the beginning of a run and the open

*Supplementary data may be obtained as document 4834 from the American Documentation Institute, Photoduplication Service, Library of Congress, Washington 25, D. C., for $2.50 for photoprints or $1.75 for 35-mm. microfilm.

circles conditions later in the run. This figure contains the complete data for thirteen runs and part of the data for the single run where the reaction zone, which was originally in the isobutanol phase, crossed the interface to the water phase. It is the latter portion which is shown here. The dotted line represents that predicted by the penetration theory. It will be noticed that many of the lines are straight and nearly parallel to the theoretical line.

The runs where the reaction took place in the isobutanol phase are shown in Figure 3. The vertical line at $\sqrt{D_{AW}}\,C_{AI}/\sqrt{D_{BW}}\,C_{BI_i} = 642$ shows where the bulk concentrations of each phase are equal. Runs where the reaction zone moves toward the water phase and eventually enters it would lie to the right of this. The line for the run where the bulk concentration of each phase is equal plots as a vertical line. The curve for that run connects the two points shown on the plot, but, instead of being a vertical line, it lies to the right of the vertical except at the terminal points, because the bulk concentrations did not remain precisely equal except fortuitously at both terminal points. It is noticeable that the slopes of the connecting lines between initial and subsequent values tend toward the vertical as the dotted line is approached. For the case of almost equal bulk concentration of each reactant where

$$\sqrt{D_{AW}}C_{AI}/\sqrt{D_{BW}}C_{BI_i} = 642$$

the deviation between theory and experiment decreases as the reactants are consumed. Here the reaction is in the alcohol phase and the reaction product, sodium acetate which has a distribution coefficient $m < 0.1$ in favor of the water phase, is transferred to the aqueous phase as the reaction proceeds, and total solute concentration in the alcohol phase decreases as does the deviation.

Except for data close to the dividing-line region, the discrepancy between the calculated and experimental values seems to be independent of the value of $D_{BW}C_{BW}/D_{AW}C_{AW_i}$ or $D_{AI}C_{AI}/D_{BI}C_{BI_i}$.

The theoretical equations for mass transfer with chemical reaction, Equations (1*a*) and (2*a*), suggest that

$$\left(\frac{k_{AW}}{k_{AW}'} - 1\right)\Big/\sqrt{\frac{D_{BW}}{D_{AW}}}\,\frac{C_{BW}}{C_{AW_i}}$$

and

$$\left(\frac{k_{BI}}{k_{BI}'} - 1\right)\Big/\sqrt{\frac{D_{AI}}{D_{BI}}}\,\frac{C_{AI}}{C_{BI_i}}$$

should equal unity. In Figures 4 and 5 the value of the appropriate function at the beginning is plotted against the bulk concentration in the phase where the reaction takes place. For most runs subsequent values during a run would fall on about the same point as the initial value or a little lower.

Figures 6 and 7 show the effect of bulk concentration on the fractional increase in mass transfer coefficient at constant interfacial concentration. Figures 8 and 9 show the effect of interfacial concentration on the fractional increase in mass transfer coefficient at constant bulk concentration. The constant concentrations were chosen to give the maximum number of data points.

The deviation of the experimental fractional increase from the simple theoretical is seen to be a strong function of the bulk concentration in the phase in which reaction is taking place, as shown by the results in Figures 4 and 5 and by the slopes appreciably different from unity in Figures 6 and 7, but to have much less correlation with the interfacial concentration, as shown by the slopes close to -1 in Figures 8 and 9.

These results may be compared with those of Stephens and Morris (*16*), who found that for the absorption of chlorine in aqueous ferrous chloride the fractional increase in transfer coefficient was proportional to $(C_{BW}/C_{AW_i})^{0.83}$, and with those of Roper (*14*), who for the absorption of chlorine by carbon tetrachloride solutions of 2-ethylhexene-1 or oleic acid found the fractional increase to be proportional to $(k_eC_B/C_{A_i})^{0.5}$. The reaction rate constant k_e is fairly high, 152 to 3,200 liters/(g. mole)(sec.), but Roper suggests that the exponent might approach unity for a very rapid reaction.

Before these correlations are considered further, it would be well to examine the basic equations used to obtain the data which are plotted in Figures 2 and 3. At higher values of $(k_{AW}/k_{AW}') - 1$

$$\left(\frac{k_{AW}}{k_{AW}'} - 1\right) \rightarrow \frac{k_{AW}}{k_{AW}'}$$

$$= \frac{N_A}{AC_{AW_i}k_{AW}'} = \frac{N_A}{AC_{AW_i}}\ \text{(constant)} \tag{3}$$

and

$$\frac{D_{BW}C_{BW}}{D_{AW}C_{AW_i}} = \frac{C_{BW}}{C_{AW_i}}\ \text{(constant)} \tag{4}$$

Thus, if data are correlated by the methods used here, by Stephens and Morris, and by Roper, essentially N_A/AC_{AW_i} is plotted as a function of C_{BW}/C_{AW_i}.

For reactions occurring near the interface large fluctuations in C_{AW_i}, with relatively smaller changes in N_A and C_{BW}, produce large parallel shifts of data points in a single run with a 45-deg. slope on a log-log plot. This effect is seen clearly in Figures 2 and 3. The most interesting characteristic of the present data is the deviation from the theoretical line. As mentioned above in the discussion of Figures 4 to 9, the bulk concentration seems to be the significant factor in the deviation rather than the interfacial concentration.

From Figures 2 through 5 it is seen that, for this particular system, the penetration or transient-state theory predicts values for $(k/k') - 1$ which are about 100% high at 0.005 N bulk concentration, correct at about 0.1N, and about 60% low at 1N.

DISCUSSION

It is seen that theory has good qualitative agreement with the present experimental results; however, at very low concentrations it gives predictions which are too high, and at the higher concentrations the theoretical results are too low. At the higher concentrations the viscosity would be greatest and the molecular diffusivity would be smallest. Both of these effects would be expected to reduce the experimentally observed fractional increase below the theoretically calculated value rather than to increase it. The more obvious explanations for possible discrepancies between theoretical and calculated transfer coefficients lead to the expectation of theoretical coefficients higher than experimental, but the reverse is true at concentrations above about 0.1N.

It would be wise to consider the possible errors that might arise from the use of an incorrect diffusivity. The values used for the diffusivities D_{AW} and D_{BW} were taken from the International Critical Tables after employing the Stokes-Einstein equation for a temperature correction. Allowances were made for the variation of diffusivity with concentration. The square root of the diffusivity was always within 3% of the mean value.

The diffusivities enter into the calculation of the interfacial concentration by means of an equation of the form

$$C_{BI_i} = \frac{k_{BW}'C_{BW} - k_{AI}'C_{AI}}{k_{BI}' + \dfrac{k_{BW}'}{m_B}} \tag{5}$$

A diffusivity correction to k_W and k_I must be made to obtain values for k_{AW}', k_{BW}', k_{AI}', and k_{BI}'. This may be derived from the two-film theory as shown in the Appendix. As mentioned earlier the interfacial concentration appears in both ordinates and abscissas in Figures 2 and 3. The effect of using different values for the diffusivity would be to shift the data points along a 45-deg. line. For the few points where k/k' is appreciably different from $(k/k') - 1$ the angle would be somewhat different from 45-deg. Errors in diffusivity would also alter the scale of the abscissas in those figures. As the most significant point about the data is not the absolute values of the data but rather the deviation from

the theoretical line, moderate errors in diffusivity will not be important.

In the calculation of the individual transfer coefficients a correction for the diffusivity differences is made for both the water- and isobutanol-phase coefficients. In making the correction for the isobutanol-phase transfer coefficient it is necessary to know the ratio of the appropriate diffusivities in both water and isobutanol. The ratios are assumed to be the same in both phases, an assumption that is probably valid for members of a homologous series, where the association effects might be expected to be similar. This assumption is used for the ratio of the diffusivities for sodium hydroxide or acetic acid to those of the various carboxylic acids used to make the runs for mass transfer without chemical reaction which gave values for the individual phase transfer coefficients. The assumption is probably fairly good for acetic acid, for sodium hydroxide with its dissociation and possible variable solvation the accuracy is not known.

For reaction in the water phase, the diffusion coefficient for acetic acid through isobutanol is required to obtain the interfacial concentration using the counterpart of Equation (5). The small diffusivity correction for acetic acid is believed accurate. All the other diffusivities required are those in the water phase, which are also believed to be known accurately enough for the present calculation. Thus for reaction in the water phase it seems impossible to explain the discrepancy between theory and experiment on the basis of diffusivity if constant hydrodynamics are assumed. It is most likely that the similar deviation which results when reaction takes place in the isobutanol phase is due to the same cause rather than to erroneous diffusivities of the pure components in the pure solvents.

The calculations for this study have been made by use of the diffusivities of the pure components. This method cannot be precisely correct, for as soon as reaction starts there will be reaction product, sodium acetate in this case. It is known that the diffusivity of sodium hydroxide, an ionic material, should be affected by the presence of sodium acetate, another ionic material. Here the hydroxide and acetate ions may be diffusing while the sodium ions may not be diffusing. Thus the ionic diffusivities become important.

A paper by Sherwood and Wei (*15a*) provides a helpful insight to the problem. They show calculations based on the theory of diffusion in mixed electrolytes including some for the aqueous-phase reaction between sodium hydroxide in water and acetic acid being absorbed or extracted from another phase. They calculate that for the case when the ratio of sodium hydroxide to sodium acetate bulk concentration is low the rate of mass transfer will be about 2.4 times

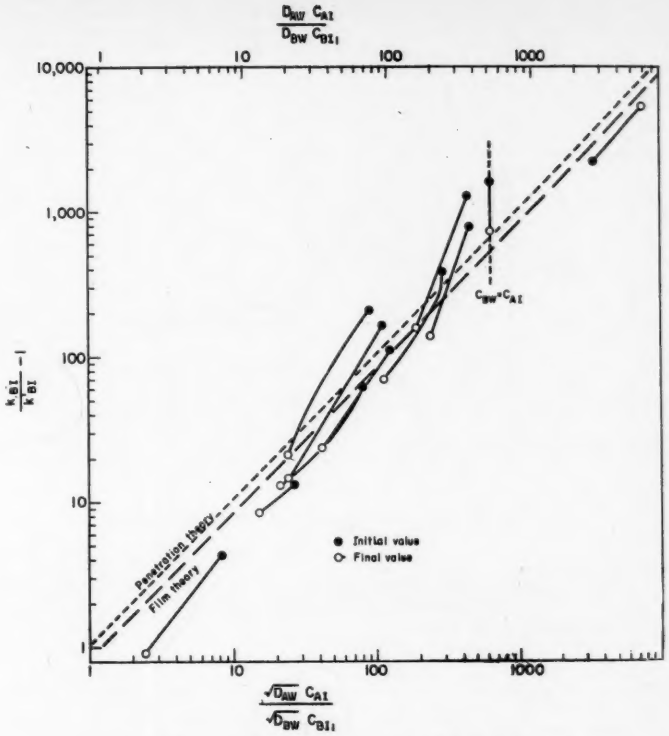

Fig. 3. Experimental increase of alcoholic-phase mass transfer coefficient vs. theoretical increase.

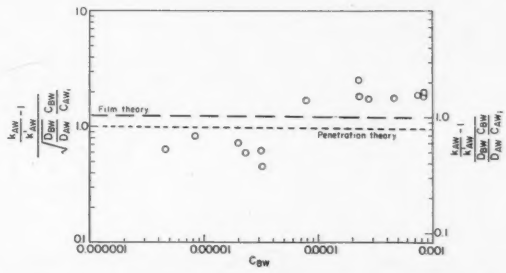

Fig. 4. Effect of bulk aqueous-phase concentration on the ratio of experimental to theoretical increase of aqueous-phase mass transfer coefficient.

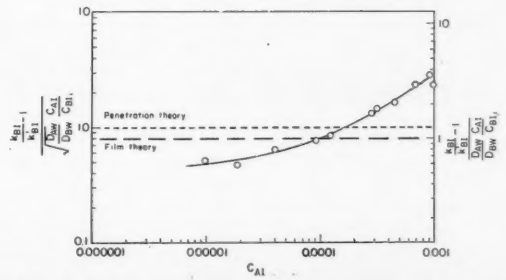

Fig. 5. Effect of bulk alcoholic-phase concentration on the ratio of experimental to theoretical increase of alcoholic-phase mass transfer coefficient.

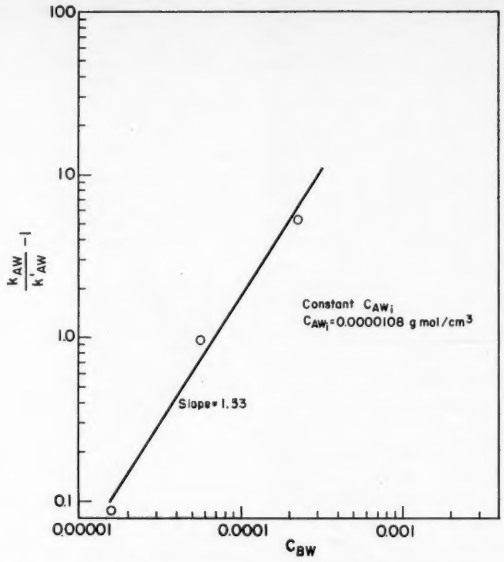

Fig. 6. Effect of bulk aqueous-phase concentration on increase of aqueous-phase mass transfer coefficient.

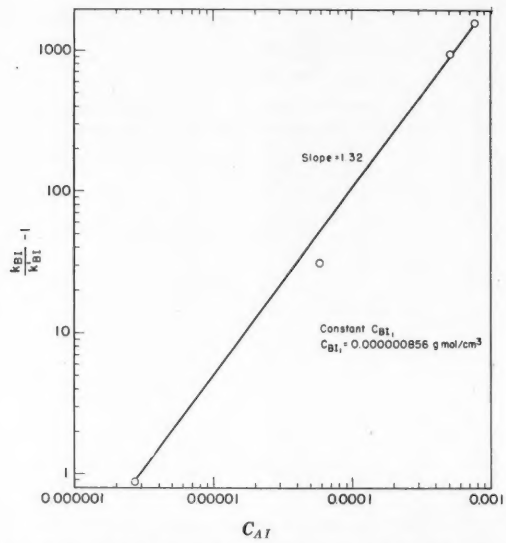

Fig. 7. Effect of bulk alcoholic-phase concentration on increase of alcoholic-phase mass transfer coefficient.

that predicted from the film theory. As the ratio of sodium hydroxide to sodium acetate becomes very large this ratio becomes about 1.5. The increase in transfer rate is due to an increase in the effective diffusivity.

They point out the difficulty in applying these results for a film to a moving or agitated liquid and conclude that for the sodium hydroxide–acetic system "the effect of ion diffusion might be expected to be minor because ionization is small in the region near the interface, where the diffusivity is important."

Thus far the experimental results have been compared with the predictions of the penetration theory. As pointed out earlier, instead of exact solutions of the penetration theory, approximations are used which are good to within 10% for all the data and within 5% for most of it. For comparison of the results with the two-film theory, by use of half-power diffusivity corrections for the individual film coefficients, $(k_{AW}/k_{AW}') - 1$ could be plotted against $D_{BW}C_{BW}/D_{AW}C_{AW_i}$ as indicated by Equation (1). This could be demonstrated in Figure 2 by shifting the abscissa of each data point to a value identical to that derived by multiplying by $(D_{AW}/D_{BW})^{1/2}$, and keeping the same line for the theoretical line of both theories. It is convenient to show the equivalent operation by multiplying the scale of the abscissa by the factor $D_{BW}/D_{AW})^{1/2}$. As the factor varies over the limited range 0.785 to 0.814, it will be taken as 0.80. This is shown on the upper scale. The theoretical line predicted by the penetration theory is given by the dotted line. The data may be compared with either theory on the same plot. Figure 3 is treated in a parallel manner. Similar reasoning, with adjustments to the ordinates rather than the abscissas, yields the theoretical lines of the penetration theory in Figures 4 and 5.

It is seen that the discrepancy between theory and experiment remains for both theoretical views.

A calculation using the enthalpy of reaction, the rate of reaction, and the analogy between heat and mass transfer with two-thirds exponents on the Schmidt and Prandtl numbers will show that a temperature difference of up to about 1.4°C. would be sufficient to transfer all the heat evolved across the equeous resistance. This is for the case where the concentrations and rates of transfer are highest. Presumably this represents a maximum temperature rise in the water phase because it would be expected that the heat of reaction would be dissipated in two directions. The maximum so calculated for the isobutanol phase is 3.6°C. What effect this temperature rise should have on the fluid dynamics and the mass transfer coefficient is not yet known. It may be noted that the higher the concentration of reactants the higher will be the temperature rise and, as the experimental results show, the greater the increase in transfer rate over that predicted by theory, which assumes constant fluid dynamics without added thermal convection.

There is no evidence to support the two-thirds exponent on the Schmidt and Prandtl groups for a liquid-liquid system. If half-power exponents are used, then the temperature rise would be about 2.4 times larger. If the half power is used on the Schmidt group and two thirds on the Prandtl group, a temperature difference three times larger would result. Thus a temperature difference of up to 11°C. might be calculated as the rise due to chemical reaction. These values are given solely to show an order of magnitude and are not meant to imply any reliability.

It is of interest to note that another case has been reported where mass transfer with chemical reaction gives coefficients higher than would be expected. Peaceman (*13*) studied the desorption of chlorine from water where the chlorine is in the form of chlorine, hydrochloric acid, and hypochlorous acid. Basing his liquid film coefficients on the total chlorine present, that is as chlorine, hydrochloric acid, and hypochlorous acid, he obtained liquid-phase mass transfer coefficients higher than those obtained without

chemical reaction. The coefficients without chemical reaction were obtained from the desorption of carbon dioxide from water and the desorption of chlorine from hydrochloric acid, which represses the reaction to form hydrochloric acid and hypochlorous acid. After a diffusivity correction the carbon dioxide data were in excellent agreement with the chlorine data.

Peaceman's data for the desorption of chlorine from water showed that the liquid-film mass transfer coefficient, based on the total chlorine present, approaches zero as the concentration of chlorine approaches zero, equals the maximum expected value at about a total chlorine concentration of 0.06 g. mole/liter, and continues to increase with increasing concentration. This behavior is very surprising, for the reaction between hydrochloric acid and hypochlorous acid to form chlorine would be expected to constitute a chemical resistance which would reduce the liquid-phase coefficient if it had any effect. The diffusivity used by Peaceman for hydrochloric acid is about twice that for chlorine or hypochlorous acid. This prevents an elucidation based on differences of diffusivities. He could offer no explanation for the anomalous behavior of this system.

CONCLUSIONS

For the case of extraction with rapid second-order chemical reaction between sodium hydroxide and acetic acid, the two-film theory and the transient-state theory give a good qualitative picture of the experimental results. However, theory predicts values for $(k/k') - 1$ which are about 100% high at $0.005N$, correct at $0.1N$, and about 60% low at $1N$. The magnitude of the discrepancy appears to be a function of the bulk concentration of the phase in which the reaction is occurring rather than the interfacial concentration.

NOTATION

A = area for mass transfer, sq. cm.
C = concentration, g. moles/cu. cm.
D = diffusivity, sq. cm./hr.
k' = individual mass transfer coefficient without chemical reaction, cm./hr.
k = individual mass transfer coefficient with chemical reaction, cm./hr.
m = distribution coefficient, C_{SI}/C_{SW} at equilibrium
N = mass transfer rate across interface, g. moles/hr.

Subscripts

A = of component A or acetic acid
B = of component B or sodium hydroxide
I = of or in component I or isobutanol
i = at the interface
S = of solute S
W = of or in component W or water

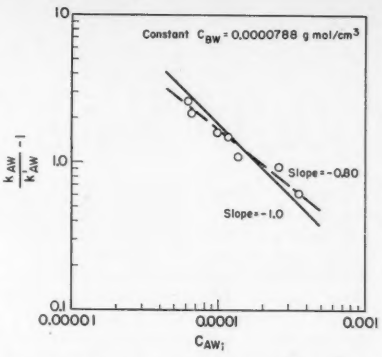

Fig. 8. Effect of aqueous-phase interfacial concentration on aqueous-phase mass transfer coefficient.

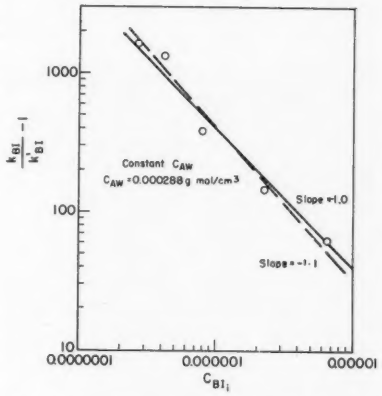

Fig. 9. Effect of alcoholic-phase interfacial concentration on alcoholic-phase mass transfer coefficient.

LITERATURE CITED

1. Caudle, P. G., and K. G. Denbigh, *Trans. Faraday Soc.*, **49**, 39 (1953).
2. Danckwerts, P. V., *loc. cit.*, **46**, 300 (1950).
3. *Ibid.*, 701.
4. ———, *Ind. Eng. Chem.*, **43**, 1460 (1951).
5. Emmert, R. E., and R. L. Pigford, *Chem. Engr. Progr.*, **50**, 87 (1954).
6. Gordon, K. F., *Ind. Eng. Chem.*, **45**, 1813 (1953).
7. ———, and T. K. Sherwood, *Chem. Eng. Progr. Symposium Series*, No. 10, **50**, 15 (1954).
8. Hatta, S., *Tech. Repts., Tohoku Imp. Univ.*, **8**, 1 (1928–29).
9. Heertjes, P. M., W. A. Holve, and H. Talsma, *Chem. Eng. Sci.*, **3**, 122 (1954).
10. Higbie, R., *Trans. Am. Inst. Chem. Engrs.*, **31**, 365 (1935).
11. Lewis, J. B., A.E.R.E. C.E./R. 1120. Atomic Energy Establishment, Harwell, England (1954), quoted by T. K. Sherwood and K. F. Gordon, *A.I.Ch.E. Journal*, **1**, 129 (1955).
12. Osborne, R., M.S. thesis, Mass. Inst. Technol., Cambridge, Mass. (1951).
13. Peaceman, D., Sc.D. thesis, Mass. Inst. Technol., Cambridge, Mass. (1951).
14. Roper, G. H., *Chem. Eng. Sci.*, **2**, 18, 247 (1953).
15. Sherwood, T. K., and R. L. Pigford, "Absorption and Extraction," 2 ed., McGraw-Hill Book Company, Inc., New York (1952), and correction sheet.

15a. Sherwood, T. K., and J. C. Wei, *A.I.Ch.E. Journal*, **1**, 522 (1955).

16. Stephens, E. J., and G. A. Morris, *Chem. Eng. Progr.*, **47**, 232 (1951).
17. Wang, J. H., C. V. Robinson, and I. S. Edelman, *J. Am. Chem. Soc.*, **75**, 466 (1952).
18. Whitman, W. G., *Chem. Met. Eng.*, **29**, No. 4, p. 146 (July 23, 1923).
19. ———, and D. S. Davis, *Ind. Eng. Chem.*, **16**, 1233 (1924).
20. ———, and W. K. Lewis, *loc. cit.*, 1215.

Presented at A.I.Ch.E. New York Meeting.

APPENDIX

Calculation of Transfer Coefficients Without Chemical Reaction

Calculation of the Over-all Transfer Coefficient for a Run. The calculation of K for a run is elementary when a continuous analysis of each phase is available without sample removal. If, as is often the case, the analyses are taken by removing a sample of each phase and replacing it with pure solvent, a correction must be made for the solute removed from the phase in sampling.

Let

C^* = concentration of one phase that would be in equilibrium with the other, g. moles/cc.
p = number of intervals
v = volume of sample removed from the phase, cc.
Θ = volume of a phase, cc.
V = time, hr.

K_W for Transfer from Water to Isobutanol:

$$N = K_W A(C_W - C_W^*) \quad \text{(A-1)}$$

Remembering $m = C_I/C_W^*$ and $V_I = V_W$ = constant and letting the zero subscript refer to the beginning of the interval being considered, one obtains from a substitution of C_I/m for C_W^* followed by a substitution of $C_{I_0} + C_{W_0} - C_W$ for C_I, based on a total material balance,

$$N = K_W A\left[\frac{1+m}{m} C_W - \frac{1}{m}(C_{W_0} + C_{I_0})\right] \quad \text{(A-2)}$$

Considering the interval from n to $n+1$, at $n+1$

$$N = K_W A\left[\frac{1+m}{m} C_{W_{n+1}}' - \frac{1}{m}(C_{W_0}' + C_{I_0}')\right] \quad \text{(A-3)}$$

where the primes on the concentrations refer to the actual concentrations of the phases at the beginning and end of the interval.

The rate of transfer from the water phase

$$N = -V_W \frac{dC_W}{d\Theta} \qquad \text{(A-4)}$$

Substituting this in Equation (A-3), collecting concentration terms, and integrating over the interval n to $n + 1$ gives

$$\ln \frac{\left(1 + \frac{1}{m}\right)C_{W_n}' - \frac{1}{m}(C_{I_n}' + C_{W_n}')}{\left(1 + \frac{1}{m}\right)C_{W_{n+1}}' - \frac{1}{m}(C_{I_n}' + C_{W_n}')} = \left(1 + \frac{1}{m}\right)K_W \frac{A}{V}(\Theta_{n+1} - \Theta_n) \qquad \text{(A-5)}$$

Let the unprimed concentrations refer to those given by the actual analysis of samples taken at the beginning and end of each interval. In the interval n to $n + 1$ the concentrations at the beginning will be $(V - v)/V$ times the concentration just given by analysis because the fraction v/V of the volume of each phase is removed in sampling and is immediately replaced by pure solvent. Therefore

$$C_{W_n}' = \frac{V - v}{V} C_{W_n}$$

and

$$C_{I_n}' = \frac{V - v}{V} C_{I_n}$$

At the end of the interval the actual concentration is that given by the analsyis making

$$C_{W_{n+1}}' = C_{W_{n+1}} \quad \text{and} \quad C_{I_{n+1}}' = C_{I_{n+1}}$$

Substituting the foregoing results in Equation (A-5) gives

$$\ln \frac{\left(\frac{V - v}{V}\right)\left[\left(1 + \frac{1}{m}\right)C_{W_n} - \frac{1}{m}(C_{I_n} + C_{W_n})\right]}{\left(1 + \frac{1}{m}\right)C_{W_{n+1}} - \frac{1}{m}(C_{I_n} + C_{W_n})\left(\frac{V - v}{V}\right)} = \left(1 + \frac{1}{m}\right)K_W \frac{A}{V}(\Theta_{n+1} - \Theta_n) \qquad \text{(A-6)}$$

Owing to solute removal during sampling

$$\left(\frac{V - v}{V}\right)(C_{I_n} + C_{W_n}) = C_{I_{n+1}} + C_{W_{n+1}} \qquad \text{(A-7)}$$

Substituting Equation (A-7) in the denominator of Equation (A-6) and writing similar equations for each of p periods or intervals and adding gives

$$\ln \left(\frac{V - v}{V}\right)^p \frac{\left(1 + \frac{1}{m}\right)C_{W_n} - \frac{1}{m}(C_{I_n} + C_{W_n})}{\left(1 + \frac{1}{m}\right)C_{W_{n+p}} - \frac{1}{m}(C_{I_{n+p}} + C_{W_{n+p}})} = \left(1 + \frac{1}{m}\right)K_W \frac{A}{V}(\Theta_{n+p} - \Theta_n) \qquad \text{(A-8)}$$

If the time intervals are of equal length

$$\Theta_{n+p} - \Theta_n = p(\Theta_{n+1} - \Theta_n)$$

and Equation (A-8) can be written

$$K_W = \frac{V}{\left(1 + \frac{1}{m}\right)A} \left\{ \frac{\ln \frac{V - v}{V}}{\Theta_{n+1} - \Theta_n} - \frac{\Delta\left\{\ln\left[\left(1 + \frac{1}{m}\right)C_W - \frac{1}{m}(C_I + C_W)\right]\right\}}{\Delta\Theta} \right\} \qquad \text{(A-9)}$$

The second term in the braces is the slope of a plot of ln $(C_W - C_W^*)$ vs. Θ and the first term is a correction to allow for solute being removed from both phases, which decreases the driving force without any interphase transfer. Equation (A-9) is written so that it is dependent on C_W, for $(C_I + C_W)$ changes slowly. A similar equation could be written dependent on C_I. It could be used when the percentage of C_I changes more rapidly than that of C_W. This would give greater accuracy than Equation (A-9). There the numerator of the second term in the braces would be

$$\Delta\left\{\ln\left[(C_{I_n} + C_{W_n}) - \left(1 + \frac{1}{m}\right)C_{I_n}\right]\right\}$$

K_W for Transfer from Isobutanol to Water: A similar derivation yields

$$K_W = \frac{V}{\left(1 + \frac{1}{m}\right)A} \left\{ \frac{\ln \frac{V - v}{V}}{\Theta_{n+1} - \Theta_n} - \frac{\Delta\left\{\ln\left[\left(1 + \frac{1}{m}\right)C_{I_n} - (C_{W_n} + C_{I_n})\right]\right\}}{\Delta\Theta} \right\} \qquad \text{(A-10)}$$

K_I:

K_I is obtained from $mK_I = K_W$ (A-11)

Calculation of Individual Transfer Coefficients. From the equations for the additivity of individual phase resistances

$$\frac{1}{K_W'} = \frac{1}{k_W'} + \frac{1}{mk_I'} \qquad \text{(A-12)}$$

$$\frac{1}{K_I} = \frac{1}{k_I'} + \frac{m}{k_W'} \qquad \text{(A-13)}$$

it is seen that for a series of solutes a plot of the over-all resistance against the distribution coefficient $1/K_W$ vs. $1/m$ and $1/K_I$ vs. m should yield straight lines, the slope of which equals the resistance of one phase and the intercept that of the other. Also the slope of one plot should equal the intercept of the other.

For greater accuracy a correction is made for the variation in K due to diffusivity by taking K as being proportional to the square root of the molecular diffusivity and putting all resistances on the basis of the same diffusivity.

Calculation of Mass Transfer Coefficient with Chemical Reaction

First the rate is calculated. The logarithm of the concentration of each phase is plotted against time in order to allow interpolation and to check for consistency.

The rate at

$$\Theta = \frac{\Theta_{n+1} + \Theta_n}{2}$$

is taken as

$$N = \left[\frac{\frac{V - v}{V}C_n - C_{n+1}}{\Theta_{n+1} - \Theta_n}\right]V \qquad \text{(B-1)}$$

where $(V - v)/V$ allows for the dilution on sampling.

Two sets of values for N may be obtained, one from each phase. Both are plotted as log N vs. Θ. The data are usually in good agreement, yielding a straight line allowing N to be read with adequate precision.

For instantaneous reaction in the W phase where one molecule of A reacts with one of B

$$k_{AI}'A(C_{AI} - C_{AI_i}) = N_A = N_B = k_{AW}'A\left[C_{AW_i} + \left(\frac{D_{BW}}{D_{AW}}\right)^{1/2} C_{BW}\right] \qquad \text{(B-2)}$$

As $C_{AI_i} = m_A C_{AW_i}$, this yields

$$C_{AW_i} = \frac{k_{AI}'C_{AI} - k_{BW}'C_{BW}}{k_{AW}' + k_{AI}'m_A} \qquad \text{(B-3)}$$

Then the value for k_{AW} is obtained from

$$N_A = k_{AW}A(C_{AW_i} - O) \qquad \text{(B-4)}$$

In a similar way values for k_{BI} for reaction in the I phase may be obtained after calculating C_{BI_i} from

$$C_{BI_i} = \frac{k_{BW}'C_{BW} - k_{AI}'C_{AI}}{k_{BI}' + \frac{k_{BW}'}{m_B}} \qquad \text{(B-5)}$$

In all cases k' is obtained from the runs to determine the individual transfer coefficients with the assumption that k' is proportional to the square root of the molecular diffusivity.

Continuous-flow Stirred Tank Reactors: Solid-liquid Systems

R. V. MATTERN, OLEGH BILOUS and EDGAR L. PIRET

University of Minnesota, Minneapolis, Minnesota

The theory and design of continuous stirred tank reactors are extended to the complex but industrially important field of continuous-heterogeneous-reaction systems. The present investigation is concerned with the elementary process occurring when solid particles and a liquid flow into and from a single reactor or a chain of these reactors. The equations are developed for dissolution processes, and the theoretical size distributions and specific areas are confirmed experimentally. Performance is also related to operating conditions and reactor design.

Continuous stirred tank reactors (*CSTR*) have important industrial as well as laboratory possibilities which need to be exploited. The theory however has not been extended to the continuous processing of solid-liquid systems. In many cases the high agitation levels required preclude the use of tubular installations for these systems.

The present investigation extends the previously reported work of this laboratory on homogeneous systems (*1, 6, 4*) to solid-liquid systems. As a basis for similar studies on heterogeneous reactions a simple solid-liquid dissolution system has been chosen for this study. This has an important experimental advantage over liquid- and gas-liquid systems in that the interphase contact area is definite and readily measurable. This paper is concerned with the theory and experimental investigation of the dissolution process occurring in continuous stirred tank reactors.

In a continuous solid-liquid reaction system the solid particles can remain unchanged in size during the reactions, as, for example, in catalytic reactions, ion exchange, or leaching; increase in size, as in polymerization and crystallization; or decrease in size, as in dissolution or other similar reaction processes.

With continuous flow of liquid through a stirred tank reactor, three methods of solid operation can be used: an *open solid-flow system*, where solid particles enter and leave the reactor continuously; a *choked solid-flow system*, where solid particles enter continuously but are physically prevented from leaving the reactor; and an *enclosed solid-flow system*, where the solid is placed initially in the reactor but no solid particles enter or leave after that time.

R. V. Mattern is with Shell Chemical Corporation, New York, New York, and Olegh Bilous with Laboratoires Centrales des Poudres, Paris, France.

ELEMENTARY THEORY

The essentials of the reactor systems to be considered are shown diagrammatically in Figure 1. The unit reactor consists of an agitated vessel into which flow a liquid and an essentially continuous stream of solid particles. The location and design of inlets and outlets and the method of agitation and transport in the assembly of reactors depend on the particular effects desired and the preferred over-all design. The liquid, and in some operations the solid, products also flow out continuously from the unit reactors. For greater volumetric efficiency and high conversion several reactors may be placed in series in vertical-tower or horizontal arrangements. The solid and liquid flo s can be concurrent or countercurrent if separators are interposed.

The bases of the development are that steady state prevails, there are many small solid particles in the feed and in the reactor, and agitation is sufficient to make the liquid concentration essentially uniform around each particle and equal to the concentration in the effluent. Usually these are common, practical conditions for operation. They may be attained even in a basket type of design which retains the agitated solid and through which the solution flows rapidly.

While the solid-liquid ratio in an open solid-flow reactor may differ from that in the effluent, and the solid may or may not be uniformly distributed within the reactor volume, the approximation will be made in the following discussion that every solid particle has an equal probability of leaving the reactor. That is, there is no size selection and the holding

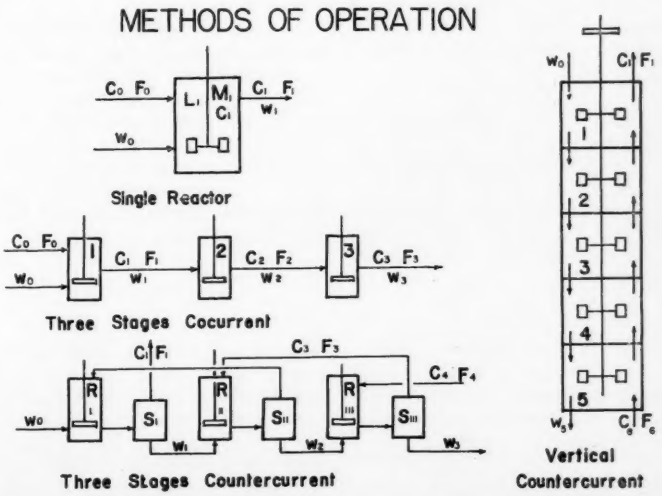

Fig. 1. Continuous-flow stirred-tank-reactor systems for two-phase operations.

time for the solid is assumed independent of particle size. For this condition it is necessary that the solid agitation level be sufficient to circulate even the largest particles rapidly to the outlet. This approximation must of course be examined or verified experimentally for each installation.

In a choked solid or enclosed solid-flow system the situation is simpler. It is not essential that the solid be circulated to the outlet or throughout the reactor; it is necessary only that each solid particle be exposed to the same reaction conditions and that liquid mixing be uniform.

The basic equations governing these methods of operation will now be developed and experimental evidence presented which supports the bases and conclusions of the theoretical development.

Open Solid-flow System

Figure 1 shows a single continuous-flow stirred tank reactor operating with feed and effluent streams containing solid particles and liquid. For the present, all the feed particles are assumed to be identical in size.

In the steady state, and with the same completely uniform dispersion of solid in the reactor and in the effluent stream, the mass rate of withdrawal of solid particles, $-(dM_1/dt)$, is equal to the mass of particles in the reactor M_1, multiplied by the ratio of the liquid effluent rate F_1 to the liquid mass in the reactor L_1.

$$-\left(\frac{dM_1}{dt}\right) = M_1 \frac{F_1}{L_1} = w_1 \qquad (1)$$

In the steady state the rate w_1 is independent of time.

Equation (1) holds only if the mass ratio of solid to liquid in the effluent is equal to that in the reactor. However, when these ratios are not equal, as is often the case in such systems, a modifying factor is required. The modifying factor, α, is defined as the solid-to-liquid mass ratio in the effluent divided by the solid-to-liquid mass ratio in the reactor

$$\alpha_1 = \frac{w_1/F_1}{M_1/L_1} = \frac{L_1/F_1}{M_1/w_1} \qquad (2)$$

Two holding times are distinguishable, namely, a liquid holding time, θ_{L_1}, defined as the ratio L_1/F_1, and a solid holding time, θ_{s_1}, defined as the ratio M_1/w_1. By the definitions of the holding times,

$$\alpha_1 = \frac{\theta_{L_1}}{\theta_{s_1}} \qquad (3)$$

Rewriting Equation (1) to take account of nonuniform dispersion of the solid in the reactor and in the effluent stream and inserting Equation (3) results in

$$-\left(\frac{dM_1}{dt}\right) = \alpha_1 M_1 \frac{F_1}{L_1} = w_1$$

or

$$-\frac{dM_1}{M_1} = \alpha_1 \frac{dt}{\theta_{L_1}} = \frac{dt}{\theta_{s_1}} \qquad (4)$$

If only the set of solid particles which are present in the reactor at an arbitrary zero time is considered, the integral of Equation (4) will give the mass fraction of this particular set of solid particles still remaining in the reactor at any future time t.

$$\frac{M_{1_t}}{M_{1_0}} = y_t = e^{-t/\theta_{s_1}} \qquad (5)$$

The subscripts 0 and t refer to the above-mentioned arbitrary time interval but, since steady state prevails, these equations also hold for any and all time intervals. Thus, y_t is the mass fraction of the solid contents of the reactor which have a residence time of t or longer. This mass

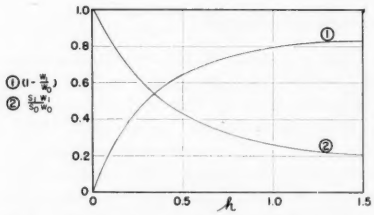

Fig. 2. Computation aid for reactor design, Equations (13*a*) and (15*a*).

fraction is equivalent to the number fraction under the ideal purging conditions assumed, as M_1 and w_1 have the same size distributions. Also

$$d(1 - y_t) = \frac{1}{\theta_{s_1}} e^{-t/\theta_{s_1}}\, dt \qquad (6)$$

represents the fraction of the particles which have a residence time between t and $t + dt$.

The application of Equation (6) to a reaction process wherein the solid mass is changing will be considered next. While the operation may be steady state, and so the sizes of the particles in the effluent remain constant with time, the masses of the individual particles in the reactor change during their passage through the reactor. In general the rate equation governing the process is

$$-\frac{dm}{dt} = f(m, a, C) \qquad (7)$$

where m and a are the mass and surface area of the solid at time t in a liquid concentration C. The surface area of a particle may be related empirically to the particle mass, so that in the steady state where the liquid concentration is a constant, Equation (7) reduces to $-dm/dt = f'(m)$ and integrates to

$$m/m_0 = g(t) \qquad (8)$$

where m_0 is the initial mass of a particle.

The product of m/m_0 and $d(1 - y_t)$ equals the fraction of the feed which leaves the reactor at time t, i.e., the ratio of the differential solid effluent rate, dw_1, to the solid feed rate, w_0.

$$\frac{dw_1}{w_0} = \frac{1}{\theta_{s_1}} g(t) e^{-t/\theta_{s_1}}\, dt$$

With T the time at which the particle disappears by reaction or simple dissolution as calculated by Equation (8), then, because the lifetime T is the longest time any particle can remain in the reactor, the total solid effluent rate w_1 is

$$\frac{w_1}{w_0} = \frac{1}{\theta_{s_1}} \int_0^T g(t) e^{-t/\theta_{s_1}}\, dt \qquad (9)$$

Although Equations (7), (8), and (9) are written in terms of mass changes, similar equations can also be written in terms of other characteristics which change during the process, such as specific surface, size distribution, activity of catalysts, or saturation of adsorbents.

These equations will be applied in this work to a dissolution process, and the validity of the final equations will be verified experimentally. It is assumed that the rate of mass transfer for dissolution of the solid is expressed by the equation

$$-\frac{dm}{dt} = ka\Delta \qquad (10)$$

with

$$\Delta = (C_s\rho_s - C\rho)$$

where a solid of mass m at time t is being dissolved in a liquid of concentration $C\rho$ (mass per unit volume). The term $C_s\rho_s$ is the saturation concentration, and k is an experimentally determined coefficient dependent on the level of agitation, temperature, and the usual rate-determining properties of the liquid and solid (*8*). An equation of the form of (10) can describe the rate of certain heterogeneous reactions with rates proportional to the surface of the solid and to some function of the reactant concentrations; hence the subsequent development can also be applied to these chemical reaction processes.

For a particle which retains its original shape, the surface area remains proportional to the $\frac{2}{3}$ power of its mass.

$$-\frac{dm}{dt} = kbm^{2/3}\Delta \qquad (10a)$$

where b is an area proportionality factor. Integration gives

$$\frac{m}{m_0} = \left(1 - \frac{t}{T}\right)^3 = g(t) \qquad (11)$$

where

$$T = \frac{3}{kbm_0^{-1/3}\Delta} = \frac{3}{ks_0\Delta} \qquad (12)$$

s_0 being the initial specific surface of the particle. Substituting in Equation (9) for integration yields

$$\frac{w_1}{w_0} = \frac{1}{\theta_{s_1}} \int_0^T \left(1 - \frac{t}{T}\right)^3 e^{-t/\theta_{s_1}}\, dt \qquad (13)$$

If

$$h_1 = \frac{\theta_{s_1}}{T} = \left(\frac{k_1 s_0 \Delta_1 L_1}{3\alpha_1 F_1}\right)$$

integration gives

$$1 - \frac{w_1}{w_0} = 3h_1[1 - 2h_1 + 2h_1^2(1 - e^{-1/h_1})] \qquad (13a)$$

Equation (13a) relates analytically the effluent solid rate, w_1, in terms of the liquid-concentration difference, Δ_1, solid-feed rate, w_0, solid holding time, θ_{s_1}, and initial specific surface, s_0. It can be used to calculate the mass transfer coefficient k_1 from experimental data, or, if k and α can be estimated, the equation can be used to predict the performance of a proposed reaction unit.

The specific surface of the solid in the reactor or the effluent can also be calculated by an equation similar to (9). By a previous assumption, $a/a_0 = (m/m_0)^{2/3}$, and from Equation (11)

$$\frac{a}{a_0} = \left(1 - \frac{t}{T}\right)^2 \qquad (14)$$

Proceeding in the same manner as in deriving Equation (13) gives the ratio of the total surface leaving to that entering as

$$\frac{\text{leaving surface}}{\text{entering surface}} = \frac{s_1 w_1}{s_0 w_0} = \frac{1}{\theta_{s_1}} \int_0^T \left(1 - \frac{t}{T}\right)^2 e^{-t/\theta_{s_1}}\, dt \qquad (15)$$

Integration gives

$$\frac{s_1 w_1}{s_0 w_0} = 1 - 2h_1 + 2h_1^2(1 - e^{-1/h_1}) \qquad (15a)$$

The equation relates the outgoing total surface $s_1 w_1$ to the operating variables and to the rate coefficient k_1.

From a plot of Equation (13a), Figure 2, a value of h_1 is obtained from the value of w_1/w_0. Then from a plot of Equation (15a), also on Figure 2, this value of h_1 may be used to obtain s_1/s_0. Thus the specific surface of the solid in the reactor and in the effluent is obtained when only the ratio of the solid flow rates w_1/w_0 and the initial specific surface s_0 are known. This value of h_1 can also be used to obtain the rate coefficient k_1 from the operating data by means of the expression

$$k_1 = \frac{3h_1 w_1}{s_0 \Delta_1 M_1} \qquad (16)$$

From Equations (13a) and (15a)

$$\frac{s_1 w_1}{s_0 w_0} = \frac{1 - \dfrac{w_1}{w_0}}{3h_1} = \frac{w_0 - w_1}{w_0 K_1 \theta_{s_1}}$$

Then by substitution from Equation (12)

$$k_1 = \frac{w_0 - w_1}{s_1 \Delta_1 M_1} \qquad (17)$$

Equation (17) expresses the solid-flow rates in terms of internal reactor conditions. It also follows directly from a material balance if the same coefficient

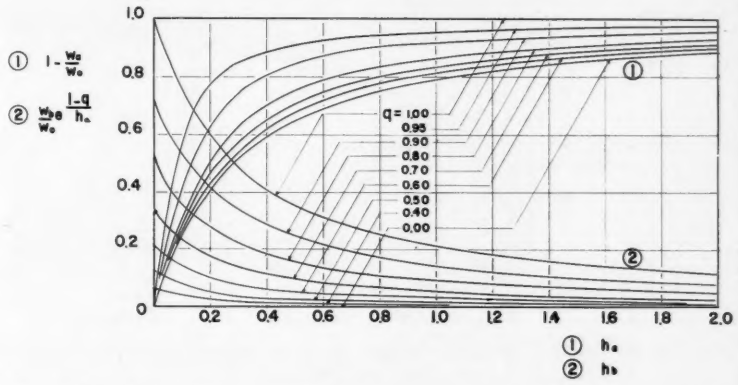

Fig. 3. Computation aid for reactor design, two-group theory, solid-flow-rate equations (33) and (34).

k_1 is assumed to hold when applied to the over-all reactor conditions.

$$w_0 - w_1 = C_1F_1 - C_0F_0 = k_1A_1\Delta_1 = k_1s_1M_1\Delta_1 \qquad (17a)$$

The use of Equation (16) involves the assumption that the size distributions of the effluent w_1 and the reactor contents M_1 are the same and that the transfer coefficient k_1 is independent of particle size. Experimentally this will be checked by comparing calculated and measured specific surfaces of the effluent solid.

To arrive at the size distribution of the effluent solid if no change in particle shape during dissolution is again assumed, the linear dimensions of a particle will be represented by $(x/x_0) = (m/m_0)^{1/3}$ where x is the selected linear dimension of the particle. Combining with Equation (11) results in the relation between particle size and reaction time

$$\frac{x}{x_0} = \left(1 - \frac{t}{T}\right) \qquad (18)$$

where x_0 is the size of the feed particle. By use of Equation (6) and (18), the differential size distribution in the reactor and effluent is expressed by

$$Y(x) = \frac{100w_0}{h_1 w_1}\frac{x^3}{x_0^4} \cdot \exp\left\{-\left(\frac{x_0 - x}{h_1 x_0}\right)\right\} \qquad (19)$$

where $Y(x)\,dx$ is the weight percentage of the particles which have a size between x and $x + dx$. Equation (19) is applied in the experimental section.

Choked Solid-flow System

Liquid flows into and out of the stirred reactor and a stream of solid particles enters continuously, but the particles are prevented from leaving the reactor, for example, by a screen. The effluent solid rate w_1 being zero for this method of operation, a material balance for the solid gives

$$C_1 = \frac{C_0F_0 + w_0}{F_0 + w_0} \qquad (20)$$

That is, the outgoing liquid concentration C_1 is independent of internal reactor conditions. However, since the effluent liquid concentration C_1 must be less than the saturation concentration C_s, the ratio w_0/F_0 is limited as follows:

$$\frac{w_0}{F_0} < \frac{C_s - C_0}{1 - C_0} \qquad (21)$$

If this relation is not satisfied, the solid accumulates in the reactor and steady state cannot be attained.

As no particles escape before complete dissolution, the total solid mass in the reactor is

$$M_1 = \int_0^T m\frac{w_0}{m_0}\, dt$$

and substituting from Equation (11) gives

$$\frac{M_1}{w_0} = \int_0^T \left(1 - \frac{t}{T}\right)^3 dt \qquad (22)$$

which reduces to

$$\frac{M_1}{w_0} = \frac{T}{4} \qquad (22a)$$

The ratio of the solid surface in the reactor s_1M_1 to the surface in the solid feed s_0w_0 is

$$\frac{s_1M_1}{s_0w_0} = \int_0^T \left(1 - \frac{t}{T}\right)^2 dt \qquad (23)$$

$$\frac{s_1M_1}{s_0w_0} = \frac{T}{3} \qquad (23a)$$

Combining (22a) and (23a) yields

$$\frac{s_1}{s_0} = \frac{4}{3} \qquad (24)$$

Thus in the steady state the ratio of the specific surface of the solid in a choked reactor to that of the feed is a constant, provided that the particles retain their shape throughout dissolution and dissolve under the same concentration gradient. Experimentally, relation (24) was checked by stopping all the feed and effluent streams and letting the holdup mass M_1 dissolve to a value M_1' corresponding to saturation. From a mass balance on the solid

$$M_1 - M_1' = L_1 \frac{C_s - C_1}{1 - C_s} \qquad (25)$$

and the initial specific surface s_1 is related to the final measured value s_1', by

$$\frac{s_1}{s_1'} = \left(\frac{M_1'}{M_1}\right)^{1/4} \qquad (26)$$

The batch dissolution up to saturation requires theoretically an infinite time which, along a fictitious dissolution path with constant concentration difference Δ_1, is equivalent to a finite time t_s, independent of initial particle size. Thus the final mass m' of a particle which arrived in the reactor at time t before flow was stopped is

$$\frac{m'}{m_0} = \left(1 - \frac{t + t_s}{T}\right)^3$$

Then

$$\frac{M_1'}{M_1} = \frac{4}{T}\int_0^{T-t_s} \left(1 - \frac{t + t_s}{T}\right)^3 dt = \left(1 - \frac{t_s}{T}\right)^4$$

$$\frac{s_1'M_1'}{s_1M_1} = \frac{3}{T}\int_0^{T-t_s} \left(1 - \frac{t + t_s}{T}\right)^2 dt = \left(1 - \frac{t_s}{T}\right)^3$$

and relation (26) results.

Choked solid operation is a limiting case of an open solid-flow process for low solid-discharge rates. This occurs when the holding time θ_s is large compared with the dissolution time T, under which conditions the parameter h becomes large. Limiting expressions which may be used as approximations are, when h is large,

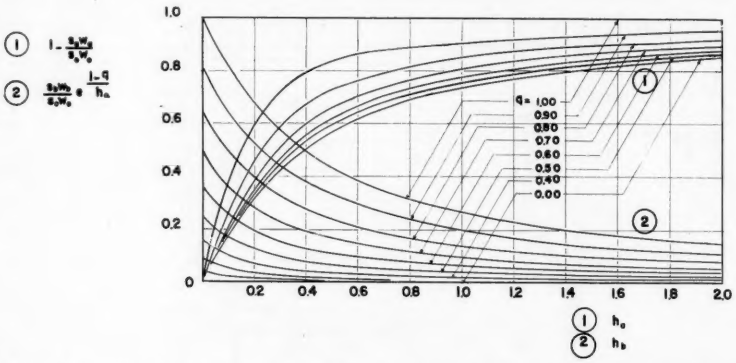

Fig. 4. Computation aid for reactor design, two-group theory, Surface-area equations (35) and (36).

$$\frac{w_1}{w_0} \cong \frac{1}{4h_1}, \qquad \frac{M_1}{w_0} \cong \frac{T}{4}\left(1 - \frac{1}{5h_1}\right), \qquad \frac{s_1w_1}{s_0w_0} \cong \frac{1}{3h_1}$$

For nearly insoluble material and low holding times, h is small and the following approximations hold:

$$\frac{w_1}{w_0} \cong 1 - 3h_1,$$

$$\frac{M_1}{w_0} \cong \theta_s(1 - 3h_1),$$

$$\frac{s_1w_1}{s_0w_0} \cong 1 - 2h_1$$

Two modifications of choked design which can be expected in practice are the basket type and the partially choked reactor. In a basket-type reactor the larger solid particles are retained by a screened container in a limited portion of the vessel. In a partially choked reactor a screen is placed at the outlet of the reactor but its openings are so large that particles of an appreciable size escape into the outlet tube.

Under the reactor conditions uniformly sized particles of lifetime T are fed to the reactor and held exposed to optimum liquid circulation by the screen basket. After a residence time T_B in the basket which brings their dimensions to the screen hole dimension, d_B, the particles escape through the screen openings and then undergo normal purging from the remaining reactor volume.

$$T - T_B = \frac{3}{k_Bbp\Delta} d_B = \lambda d_B \qquad (27)$$

where p is the shape factor in the relation $x = pm^{1/3}$. By equations similar to (22) and (23) the holdup mass and the specific surface ratio in the basket are found to be

$$\frac{M_B}{w_0} = \frac{T}{4}\left[1 - \left(1 - \frac{T_B}{T}\right)^4\right]$$

$$\frac{s_B}{s_0} = \frac{4}{3}\frac{\left[1 - \left(1 - \frac{T_B}{T}\right)^3\right]}{\left[1 - \left(1 - \frac{T_B}{T}\right)^4\right]}$$

The solid effluent rate w_B from the basket is

$$w_B = w_0\left(1 - \frac{T_B}{T}\right)^3$$

These equations may be applied to a partially choked reactor if the particles escape immediately after reaching size d_B.

The equations for open solid flow hold in the main body of the reactor outside the basket, with an appropriate holding time θ_s and a particle life T_R.

$$T_R = \frac{k_B}{k_R}(T - T_B)$$

The dissolution coefficients in the reactor and the basket, k_R and k_B, may be slightly different owing to different flow conditions. The total mass transfer in the reactor is

$$w_0 - w_1 = (k_Bs_BM_B + k_Rs_RM_R)\Delta$$

where

$$\frac{s_RM_R}{s_0w_0} = \theta_s\left(1 - \frac{T_B}{T}\right)^2[1 - 2h_R + 2h_R^2(1 - e^{-1/h_R})]$$

and

$$\frac{w_1}{w_0} = \left(1 - \frac{T_B}{T}\right)^3\{1 - 3h_R[1 - 2h_R + 2h_R^2(1 - e^{-1/h_R})]\}$$

with

$$h_R = \frac{\theta_s}{T_R}$$

Enclosed Solid-flow System

An approach to steady state operation is possible with this method if the solid is essentially unchanged during the reaction. For mass transfer

$$C_1F_1 - C_0F_0 = k_1s_0M_0(C_s\rho_s - C_1\rho_1) \qquad (28)$$

If the density change of the liquid in the reaction is small and if the factor D is the fractional approach to equilibrium of the effluent liquid, there results

$$D = \frac{C_1 - C_0}{C_s - C_0} = \frac{1}{1 + \frac{F_0}{k_1s_0M_0\rho_s}} \qquad (29)$$

Batch System

Agitated reactors, of course, may also be operated by the batch method for both solid and liquid. The following equation, which may be used for calculating mass transfer coefficients for this method of operation, is derived from Equation (10*a*).

$$\int_{C_0}^{C} \frac{dC}{(1-C)^2\left(1+\frac{L_0}{M_0}\frac{C_0-C}{1-C}\right)^{2/3}(C_s\rho_s - C\rho)} = \frac{ks_0M_0t}{L_0(1-C_0)} \qquad (30)$$

In the experimental section coefficients for nonflow or batch experiments obtained by Equation (30) will be compared with the coefficients for flow experiments.

EXTENSIONS OF THE THEORY

Two-group Theory

Experimental evidence shows that if the agitation is insufficient, the coefficient α and therefore θ_s depend upon the size of the solid particles. The preceding elementary theory can still be applied within limits under these conditions by using an average value of θ_s. However a more detailed treatment may be useful where effects of size are important.

When feed particles of uniform size x and mean residence time θ_a reach a size x', their mean residence time becomes θ_b. If T and T' represent the lifetimes corresponding to sizes x and x' under the reactor conditions, the residence time distribution is then described by

$$y = e^{-t/\theta_a} \qquad t < T - T' \qquad (31)$$

$$y = \exp\left\{-(T-T')\left(\frac{1}{\theta_a}-\frac{1}{\theta_b}\right)\right\}e^{-t/\theta_b} \qquad T - T' < t < T \qquad (32)$$

where the holding times are defined as

$$\theta_a = \frac{M_a}{w_a}, \qquad \theta_b = \frac{M_b}{w_b}$$

a and b referring to the fractions of the holdup mass and the effluent solid, which consist of particles having a size respectively larger and smaller than x'. Then, as in Equation (13),

$$\frac{w_a}{w_0} = \int_0^{T-T'}\left(1-\frac{t}{T}\right)^3\frac{1}{\theta_a}e^{-t/\theta_a}\,dt$$

$$\frac{w_b}{w_0} = \int_{T-T'}^{T}\left(1-\frac{t}{T}\right)^3\frac{1}{\theta_b}\cdot\exp\left\{-(T-T')\left(\frac{1}{\theta_a}-\frac{1}{\theta_b}\right)\right\}e^{-t/\theta_b}\,dt$$

Integration yields

$$\frac{w_a}{w_0} = 1 - 3h_a + 6h_a^2 - 6h_a^3 - e^{-(1-q)/h_a}[q^3 - 3h_aq^2 + 6h_a^2q - 6h_a^3] \qquad (33)$$

$$\frac{w_b}{w_0} = e^{-(1-q)/h_a}[q^3 - 3h_bq^2 + 6h_b^2q - 6h_b^3(1-e^{-q/h_b})] \qquad (34)$$

where

$$h_a = \frac{\theta_a}{T}, \quad h_b = \frac{\theta_b}{T}, \quad q = \frac{T'}{T} = \frac{x'}{x}$$

Experimental evidence for the use of two different holding times could be obtained by screening the effluent at a reasonable value of q and comparing the values of θ_a and θ_b given by Equations (33) and (34). For convenience plots of $1 - (w_a/w_0)$ and $(w_b/w_0)\,e^{(1-q)/h_a}$ vs. h_a and h_b for different values of q are shown on Figure 3.

Having determined the θ_a and θ_b which best describe the purging process, one obtains the surface area in the reactor from

$$s_1M_1 = \theta_a(s_aw_a) + \theta_b(s_bw_b)$$

with

$$M_1 = \theta_aw_a + \theta_bw_b$$

and

$$\frac{s_aw_a}{s_0w_0} = \int_0^{T-T'}\left(1-\frac{t}{T}\right)^2\frac{1}{\theta_a}e^{-t/\theta_a}\,dt$$

$$\frac{s_bw_b}{s_0w_0} = \int_{T-T'}^{T}\left(1-\frac{t}{T}\right)^2\frac{1}{\theta_b}\cdot\exp\left\{-(T-T')\left(\frac{1}{\theta_a}-\frac{1}{\theta_b}\right)\right\}e^{-t/\theta_b}\,dt$$

Integration gives

$$\frac{s_aw_a}{s_0w_0} = 1 - 2h_a + 2h_a^2 - e^{-(1-q)/h_a}(q^2 - 2h_aq + 2h_a^2) \qquad (35)$$

$$\frac{s_bw_b}{s_0w_0} = e^{-(1-q)/h_a}[q^2 - 2h_bq + 2h_b^2(1-e^{-q/h_b})] \qquad (36)$$

Plots of these expressions are shown in Figure 4.

This treatment can be extended to several size groups or to a continuous model if sufficient experimental data are available.

Equations for Nonuniform Feeds

In the preceding derivations the particles in the entering stream were uniform in size. The size distribution within the reactor and in the effluent stream has been expressed for this condition by Equation (19). In practice the feed to a reactor may be nonuniform in size. In any event the effluent from a unit in a chain of reactors will have a size distribution which must be taken into account to predict the performance of succeeding reactors. It is therefore desirable for sequential reactor design to solve the general problem of nonuniform feeds.

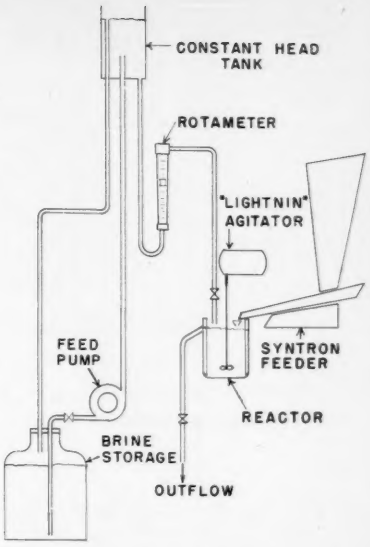

Fig. 5. Experimental arrangement for continuous operation.

If $Y_0(x)$ represents the differential size distribution of the solid feed, $Y_0(x)$ is related to $P_0(x)$, the cumulative weight percentage passing the screen of size x, by

$$P_0(x) = 100\int_{x_0}^{x} Y_0(\xi)\,d\xi \qquad (37)$$

where x_0 is the smallest size of particle present in the feed.

Equation (12) can be written in the form

$$T = \lambda x_0 \qquad (38)$$

where $\lambda = 3/kbp\Delta$ and p is the shape factor, $p = xm^{-1/3}$. The function $X_0(T)$ representing the weight fraction of the feed particles which have dissolution times between T and $T + dT$ is then

$$X_0(T) = \frac{1}{\lambda}\,Y_0\left(\frac{T}{\lambda}\right)$$

This lifetime distribution, $X_0(T)$, has been introduced here instead of the usual particle-size distribution, $Y_0(x)$, for consistency with the preceding derivations.

For an open-solid-flow reactor Equation (13) becomes

$$\frac{w_1}{w_0} = \int_{T_a}^{T_b} X_0(T)\left[\int_0^T\left(1-\frac{t}{T}\right)^3\cdot\frac{1}{\theta_s}e^{-t/\theta_s}\,dt\right]dT$$

where T_a and T_b correspond to the smallest and largest particle sizes in the feed. Substituting from Equation (13*a*) yields

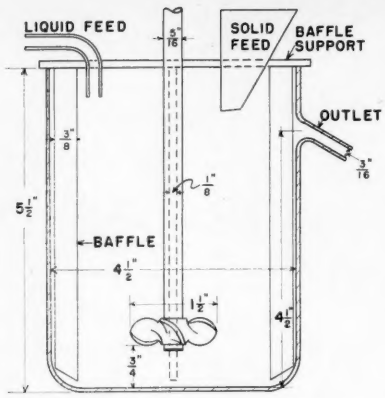

Fig. 6. Detail of experimental reactor.

$$\frac{w_1}{w_0} = \int_{T_a}^{T_b} X_0(T)\left[1 - 3\,\frac{\theta_s}{T} + 6\,\frac{\theta_s^2}{T^2} - 6\,\frac{\theta_s^3}{T^3} + 6\,\frac{\theta_s^3}{T^3}\,e^{-T/\theta_s}\right] dT \qquad (39)$$

And for specific surfaces from (15)

$$\frac{s_1 w_1}{s_0 w_0} = \frac{\displaystyle\int_{T_a}^{T_b} X_0(T)\left[\int_0^T \frac{1}{\theta_s}\left(1 - \frac{t}{T}\right)^2 e^{-t/\theta_s}\,dt\right]\frac{dT}{T}}{\displaystyle\int_{T_a}^{T_b} X_0(T)\,\frac{dT}{T}}$$

or

$$\frac{s_1 w_1}{s_0 w_0} = \frac{\displaystyle\int_{T_a}^{T_b} X_0(T)\left[1 - 2\,\frac{\theta_s}{T} + 2\,\frac{\theta_s^2}{T^2} - 2\,\frac{\theta_s^2}{T^2}\,e^{-T/\theta_s}\right]\frac{dT}{T}}{\displaystyle\int_{T_a}^{T_b} X_0(T)\,\frac{dT}{T}} \qquad (40)$$

For the choked solid case the same method gives the following expressions:

$$M_1 = \frac{w_0}{4}\int_{T_a}^{T_b} T X_0(T)\,dT \qquad (41)$$

$$\frac{s_1 M_1}{s_0 w_0} = \frac{1}{3\displaystyle\int_{T_a}^{T_b} X_0(T)\,\frac{dT}{T}} \qquad (42)$$

The size distribution of the solid effluent from a reactor receiving a feed of distribution $X_0(T)$ is obtained by integrating

$$X_0(T)\,\frac{1}{\theta_{s_1}}\left(1 - \frac{t}{T}\right)^3 e^{-t/\theta_{s_1}}\,dt\,dT$$

at constant effluent lifetime T_1, with $T_1 = T - t$, over the range of T:

$$X_1(T_1) = \frac{w_0}{w_1}\int_\Omega X_0(T)\,\frac{1}{\theta_{s_1}} \cdot \left(\frac{T_1}{T}\right)^3 \exp\left\{-\frac{T - T_1}{\theta_{s_1}}\right\} dT \qquad (43)$$

where the range of integration Ω is

from T_a to T_b for $0 < T_1 < T_a$

from T_1 to T_b for $T_a < T_1 < T_b$

Formal integration of Equation (43) can be made for the cases of a Gaudin or a log-probability distribution in the feed. Graphical or approximate procedures can of course also be used.

Multiple Reactors

The problem of sequential reactor design is now completely solved in theory. An example is the design of a series of reactors to dissolve a given amount of solid per unit time. If the size distribution of the initial solid is given, Equation (39) gives θ_{s_1}, the solid holding time in the first reactor, and Equation (40) gives the total surface area in the first reactor. The concentration difference is calculated from Equation (17*a*), which also gives the required liquid flow rate. The reactor volume can then be calculated from experimental values of α. The size distribution $X_1(T_1)$ of the feed to the second reactor is given by Equation (43). The solid holding time in the second reactor θ_{s_2} is obtained by the substitution of $X_1(T_1)$ in Equation (39), the subscript designations being increased by 1. This procedure is repeated for all the reactors in the chain. Concurrent, countercurrent, or mixed operation can be calculated by this step-by-step procedure.

EXPERIMENTAL

The experimental part of this study is divided into mixing and mass transfer sections. In the mixing section the effect of physical variables on the continuous mixing of sand and water was examined. These experiments provided needed insight into the mixing process and aided in the planning of the mass transfer experiments.

The mass transfer (dissolution) experiments were carried out to verify the previously derived equations relating mass transfer coefficient, surface area, and size distribution. For this purpose a relatively simple system—sodium chloride and concentrated brine—was chosen. The use of the brine instead of water was required to provide sufficient effluent solid for surface and size determinations even though its use may have decreased the accuracy of the mass transfer coefficients to a small extent. Although most of the runs were made by use of the open solid-flow method of operation, choked solid flow and batch were also investigated briefly.

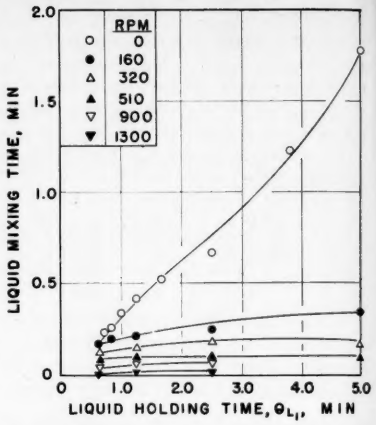

Fig. 7. Liquid mixing time for a dye injected into the feed stream of the reactor.

A vibratory feeder, Syntron Company model FM-0-10, produced a substantially continuous stream of solid particles from a hopper, with rate variations to the reactor of about 5% and very little particle breakage. The solid particles dropped into the open top reactor through a small funnel located above the liquid surface (Figures 5 and 6). The metered liquid entered the reactor through the feed tube also located slightly above the surface of the liquid.

The glass, flat-bottomed, 1.3-liter reactor (Figure 6) had four ⅜- by ⅛-in. brass baffles spaced 90 deg. apart along its inside periphery. Agitation was supplied by a commercial stainless steel 45-deg. pitch three-bladed, marine-type propeller 1½ in. in diam., which rotated so as to force the solution downward.

The air-permeability apparatus used to determine the solid specific surface has been previously described in detail (*3*). For the batch experiments a rapid sampling device was used which consisted of a vacuum manifold with six constricted glass sample tubes of about 5-ml. capacity dipping into the liquid and connected to the vacuum through stopcocks (*10*). Small wads of glass wool were placed in the tubes to prevent the solid from entering the samples. When a stopcock was rotated, a liquid sample was quickly obtained.

A commercially available salt, Morton's Bakers' *A*, consisting of uniform cubic crystals of sodium chloride, was used. After being screened into three fractions, 20/30, 30/40, and 40/50 U. S. mesh sizes, the salt was dried at 150°F. to facilitate free flow. An 87% saturated brine was used as the liquid feed.

Open Solid-flow System

The average duration of a run after establishment of steady flow conditions was about 20 min. During this time at least six 250- to 500-ml. samples were obtained by

directing the effluent into a Büchner funnel to separate the solid rapidly from the liquid. The solid from the steady state samples (normally four of the six) was combined and used in the screen analyses and surface measurements. Runs made at a liquid feed rate of 500 g./min. or less did not reach steady state but continued to build up solid throughout the run.

At the end of a run the feeds and outflow were stopped and the reactor contents agitated for several hours. The mass of solid in the reactor at steady state could be calculated from the final conditions by the increase in concentration plus the mass of solid remaining.

The densities of the liquid samples were measured by pycnometer, and their salt content was determined by evaporation. The solid samples were dried and screened in 3-in.-diam. screens and their specific surface was determined by the air-permeability method.

Choked Solid-flow System

The procedure for this type of operation was the same as for the open-solid method except that a 270-mesh Tyler screen was placed just inside the reactor outlet to restrict the solid outflow.

Batch System

The initial solid was dropped into the reactor with the impeller rotating. Samples were then taken at 10-sec. intervals by momentarily opening each stopcock in turn. The samples were again analyzed for salt content by evaporation.

MIXING IN SOLID-LIQUID FLOW SYSTEMS

Two agitation levels prevail in a continuous-flow stirred tank reactor, one pertaining to the solid phase, the other to the liquid. Contributions to these levels come from the impellers and also from the kinetic energy of the inlet streams (*4*). In the case of ideal mixing in a multiphase *CSTR* the distribution of residence times for each phase is expressed by an equation of the form $y = e^{-t/\theta}$. Under such conditions *CSTR* operation can be described by the elementary theory. If agitation and outlet conditions are so favorable that θ_s is entirely independent of particle size, θ_s is also equal to θ_L, i.e., $\alpha = 1.0$. Since this is not usually attained, θ_s, as used in the elementary theory, is a mean solid holding time and is usually different from θ_L. The use of a mean θ_s seems justified in view of the good agreement of the experimental and calculated size-distribution curves for the effluent solid.

In the experiments reported, the whole reactor volume (Figure 6) was accessible to the particles. Except where otherwise indicated in the mixing experiments, the feeds were water and sand, where the sand had a density of 2.65 g./cc. and a size distribution of 33% between 30 and 40 mesh, 66% between 40 and 50 mesh, and 1% less than 50 mesh.

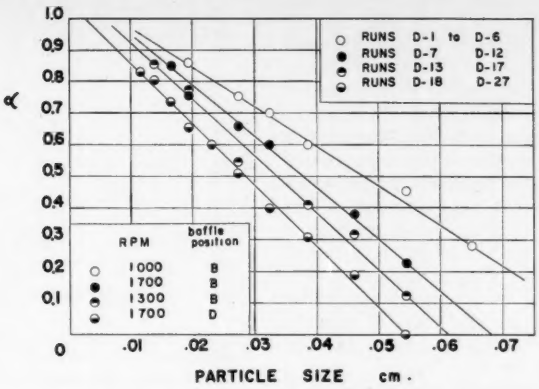

Fig. 8. Effect of particle size on holding time ratio.

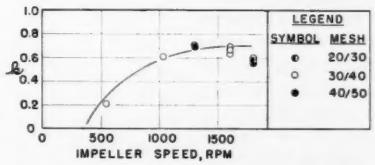

Fig. 9. Batch system, mass transfer coefficients.

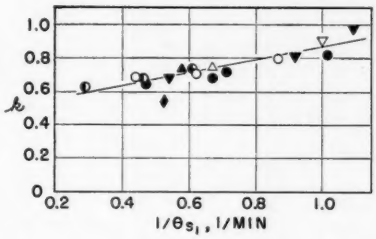

Fig. 10. Open solid-flow system. Mass transfer coefficients. Equation (16) vs. reciprocal holding time.

Liquid- and Solid-mixing Times

The liquid-mixing time was determined by an experimental method previously reported (*4*), wherein a small amount of dye solution was injected into the liquid feed and the time for uniform mixing observed. At impeller speeds above 900 rev./min. this liquid-mixing time was found to be a small fraction of the liquid holding time, except when the rate of liquid feed was high (Figure 7). The assumption of a uniform liquid concentration throughout the reactor is, therefore, closely approached when applied to the liquid phase in solid-liquid mixing.

The time for solid mixing was also found to be short (Table 1*). The time recorded was the interval between the start of the impeller in the reactor at rest containing 50 g. of sand, and the time when the mean solid-flow pattern was no longer seen to change; for example, at 810, 1,400, and 1,800 rev./min. the time interval is only 3.0, 1.2, and 0.7 sec. respectively.

The instantaneous solid-flow pattern fluctuates continually in a continuous-flow solid-liquid reactor. Clouds of particles swirl in a pulsating manner about the reactor and into the outlet tube. These particle clouds are usually less than 1 in. in diameter and recur roughly once or twice a second at impeller speeds of 1,000 rev./min. and higher. Effluent samples, therefore, must be taken for a time which is long in terms of the frequency of the pulsations. Similar fluctuations of concentration have been observed in the effluent of a *CSTR* with a homogeneous chemical reaction (*4*).

*The tables and remaining figures are on file as document 5325 with the American Documentation Institute, Photoduplication Service, Library of Congress, Washington 25, D. C., and may be obtained for $2.50 for photoprints or $1.75 for 35-mm. microfilm.

Holding-time Ratio

For design purposes the solids content at steady state in a *CSTR* unit usually must be known, since it determines the total area of contact between the phases in the reactor. An extensive investigation would be required to obtain a generalized quantitative correlation of the solids content with the numerous design and operating variables. Shown here in a general way are the effects of a few of the more important variables.

The holding-time ratio α is defined by Equation (2) as the ratio of solid to liquid in the effluent divided by this ratio in the reactor. Not only is α a measure of the uniformity of solid mixing, but it is indicative of the sampling process occurring at the outlet. In the mixing experiments α at steady state was found to vary widely with the impeller position, baffle position, particle size, impeller speed, and solid- and liquid-flow rate. These variations, illustrated by Figures 8 to 13 and Tables 2 and 4,* indicate trends to be expected by the designer.

Although the location of the outlet nozzle would be an important variable in a study of the kind, a simple top outlet only was used. This location prevents clogging or settling which might be expected to occur with other outlet locations. For a top outlet an α approaching unity indicates good mixing and usually corresponds to desirable operating conditions. Accordingly, the variables of baffle position and impeller location were set at the maxima obtained in the runs.

The effect of particle size on α is illustrated in Figure 8 by use of closely sieved fractions of crushed sand. Increasing the impeller speed increases the rate of circulation, decreases the thickness of the clear area near the surface, and increases α.

Low values of α, and hence operating conditions less than optimum, are encountered for sand at low solid-flow rates or high liquid-flow rates. In the mass transfer experiments, however, at high liquid-flow rates little change in α is observed when the liquid-flow rate is varied. Limiting operating conditions occur at very high solid-flow rates or low liquid-flow rates when the reactor overloads with solid. These overloaded flooding conditions occurred when the mass of solid salt in the 1,300-cc. reactor was above about 150 g. Although the speed of the impeller was maintained, there was little solid turnover. The solid collected in the reactor bottom and continued to increase indefinitely.

MASS TRANSFER RESULTS

Open Solid-flow System

Rate coefficients. The mass transfer coefficient k of each run (Tables 3 and 4*) was calculated by Equation (16) and corrected to 25°C. For purposes of comparison the coefficients were also calculated by Equation (17), and the very good agreement (2.5% deviation) of the sets verifies the equivalence of the two equations.

All the coefficients were in the range from 0.6 to 1.0 g./(min.)(sq. cm.)(g./cc.), but contrary to expectations no discernible correlation with impeller speed was obtained. (All runs were made at 1,000 rev./min. or above.) The average of the coefficients of the runs at each impeller speed (1,000, 1,300, 1,600, and 1,800 rev./min.) varied only between 0.70 and 0.78. An error of about 15% could be expected in the k values because the expressions involve the differences of nearly equal quantities. The small particle sizes probably explain the lack of correlation of k with impeller speed. Because of the rapid circulation of the particles in the reactor, the relative velocity between the liquid and the particles is much less sensitive to impeller speed than is the case with large particles.

The batch results (Table 5* and Figure 9) also show an insensitivity of k to impeller speed at speeds above 1,000 rev./min. The batch coefficients agree well with the open-solid-flow coefficients and show no appreciable effect of particle size. This is in accord with the results of other investigators working with larger sized particles (*2, 5, 9, 10*). The average within variation for the batch runs was about 5%.

The quantity $1/\theta_s$ is a measure of the rate of solid turnover in the reactor and as such should represent a contribution to the reactor mixing conditions. A plot of $1/\theta_s$ vs. k (Figure 10) shows the small but definite effect of this factor.

Although all runs were at a nominal steady state (shown by concentration vs. time plots), random fluctuations in feed rates and especially in mixing pattern resulted in minor discrepancies in the material balances calculated by Equation (17*a*). The average of the discrepancies for all runs was 2.5%.

Particle-surface Area. The equations developed depend on the assumption that the surface area of the particles varies as the $\frac{2}{3}$ power of the mass. However, rounding off of the particles and fragmentation are possible, and so an experimental verification of this assumption is desirable. Brine of known concentration containing varying amounts of 30/40 mesh salt was saturated by agitation in a beaker. The residual solid was dried and its specific surface determined by air permeability. The results when plotted on logarithmic coordinates (Figure 11) show a variation in area as the 0.70 power of the mass, which is close to the assumed 0.67.

In the continuous-flow mass transfer

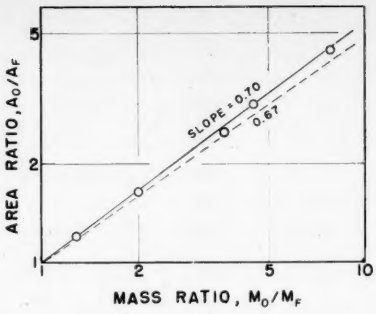

Fig. 11. Batch experiment, comparison of calculated and measured variation of surface area with mass in dissolution.

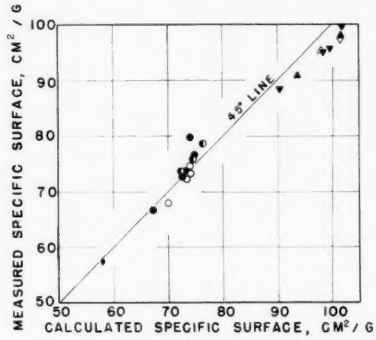

Fig. 12. Open solid-flow system, comparison of calculated and measured specific surface of outlet solid.

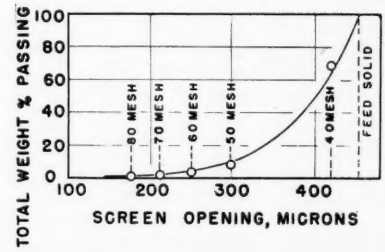

Fig. 13. Comparison of calculated curve and experimental size measurements of outlet solid, run C-3.

*See footnote on page 503.

*See footnote on page 503.

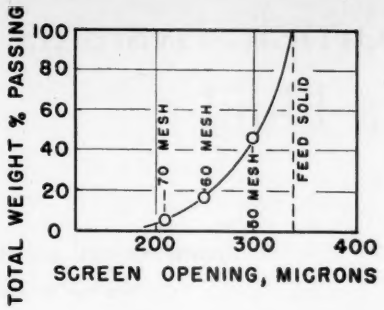

Fig. 14. Comparison of calculated curve and experimental size measurements of outlet solid. Run C-14.

experiments, the specific surface of the effluent solid from the reactor was calculated by use of Equation (15*a*) in conjunction with a plot of Equation (13*a*). These calculated areas are compared in Table 6* and Figure 12 to the specific surface measured by air permeability. There is good agreement (2.5%), confirming Equation (15*a*), which permits the calculation of the surface of the outgoing solid when only the feed and effluent rates and the feed specific surface are known.

Size Distribution. A basic assumption in the derivation of the equations of the elementary theory is that there is no size selection at the outlet. This assumption was confirmed by use of the sand-water system and also by the results described below.

The size distributions of the effluent solid of the runs were calculated by Equation (19). When these calculated distributions were compared with the measured distributions, surprisingly good agreement was obtained in view of the inherent errors in screening. The results for some typical runs are shown in Table 7* and Figures 13 and 14. The size of the feed was calculated by the relation $x_0 = 6/s_0\rho$.

Choked Solid-flow System

Several runs were performed with this method of operation (Tables 8 and 9*) in order to test the validity of the eqlations developed. The rate coefficients were calculated by the relation $k = w_0/s_1\Delta_1 M_1$ and Equation (24). All coefficients were in the range from 0.97 to 1.14, and there is again no apparent effect of impeller speed.

The average coefficient for this method of operation is 1.08, which is appreciably higher than the average coefficients of the other methods. A troublesome problem in the choked solid runs was the rapid build-up of solid particles on the outlet screen. A significant portion of the reactor solid was held on the screen in spite of frequent scraping with a spatula. It is believed that a major cause of the higher coefficients obtained in these runs is the very rapid dissolution of the particles on the screen resulting from the high liquid velocities through the miniature packed bed. Another contributing factor, although quite minor, was fines passing through the screen and subsequently dissolving in the sample flasks.

The values of C calculated by Equation (20) checked the measured values very closely, with an average deviation of only 0.0011 g./g.

The specific surface of the reactor solid was calculated by Equation (26) by use of the measured surface of the residual solid remaining after saturation of the solution. The ratio of the steady state specific surface to that of the feed solid is predicted by Equation (24) to be 4/3. The measured ratios were in good agreement, being 1.27, 1.26, 1.33, and 1.31 for the four runs having residual solid.

*See footnote on page 503.

ACKNOWLEDGMENT

This project was in part supported by Research Grant G449 of the National Science Foundation and by a fellowship granted by the Minnesota Mining and Manufacturing Company.

NOTATION

a = effective surface area of a single solid particle, sq. cm.
A = effective surface area of total reactor solid, sq. cm.
b = area proportionality constant = $m^{-2/3}a$, cm^{2}g.$^{-2/3}$
C = liquid concentration, g. solute/solution
d_B = basket screen hole dimension, cm.
D = degree of reaction
F = liquid flow rate, g./min.
h = ratio of solid holding time to particle lifetime = θ_s/T
k = mass transfer coefficient, g./(min.)(sq. cm.)(g./cc.)
L = liquid holdup in reactor, g.
M = solid holdup in reactor, g.
m = mass of a single solid particle, g.
p = shape factor = $m^{-1/3}x$, cm. g.$^{-1/3}$
q = parameter in two-group theory ($q = T'/T$)
s = specific surface of solid, sq. cm./g.
t = time, min.
T = time of complete dissolution (lifetime) of a solid particle, min.
w = solid flow rate, g./min.
x = selected dimension of particle, cm.
y_t = fraction of reactor contents having a residence time of t or longer
α = holding time ratio, θ_L/θ_s
Δ = concentration difference = $(C_s\rho_s - C\rho)$, g./cc.
λ = lifetime to size proportionality constant, min./cm.
ρ = density of solution, g./cc.
θ_L = liquid holding time, L/F, min.
θ_s = solid holding time, W/w, min.
ξ = integration variable

Subscripts

0 = feed to first reactor or to zero time or to feed
1 = the contents and effluent of the first vessel
a, b = size groups separated by size x' (lifetime T') in two-group theory; or smallest and largest size of feed particles
B = basket-type reactor
R = reaction space outside of basket
s = saturation

LITERATURE CITED

1. Eldridge, J. W., and Edgar L. Piret, *Chem. Eng. Progr.*, **46**, 290 (1950).
2. Hixson, A. W., and S. J. Baum, *Ind. Eng. Chem.*, **33**, 478, 1433 (1941); **34**, 120, 194 (1942).
3. Kwong, J. W. S., J. T. Adams, Jr., J. F. Johnson, and Edgar L. Piret, *Chem. Eng. Progr.*, **45**, 508 (1949).
4. MacDonald, R. W. and Edgar L. Piret, *ibid.*, **47**, 363 (1951).
5. Mack, D. E., and R. A. Marriner, *ibid.*, **45**, 545 (1949).
6. Mason, D. R., and Edgar L. Piret, *Ind. Eng. Chem.*, **42**, 817 (1950); **43**, 1210 (1951).
7. Rushton, J. H., and J. Y. Oldshue, *Chem. Eng. Progr.*, **49**, 267 (1953).
8. Sherwood, T. K., and R. L. Pigford, "Absorption and Extraction," 2 ed., p. 74, McGraw-Hill Book Company, Inc., New York (1952).
9. Wilhelm, R. H., *Chem. Eng. Progr.*, **45**, 208 (1949).
10. ———, L. H. Conklin, and P. C. Sauer, *Ind. Eng. Chem.*, **33**, 453 (1941).

Presented at A.I.Ch.E. San Francisco meeting

Viscous Flow in Multiparticle Systems: Motion of Spheres and a Fluid in a Cylindrical Tube

JOHN HAPPEL and HOWARD BRENNER

New York University, New York, New York

An approximate theory for the behavior of multiparticle systems suspended in a viscous fluid is developed, based on a rigorous treatment for the case of a single sphere occupying any position in a cylindrical tube. The results obtained include estimates of the effect of some of the parameters involved on the particle velocities and spatial distribution of particles in very dilute sedimenting and fluidized beds as well as on the pressure drop resulting from passage of fluid. The conclusions presented are in agreement with such experimental data as are available and suggest a basis for more exact treatment of these systems.

The theoretical investigation reported here is a continuation of studies previously published (*8, 9*) having as their general objective a fundamental solution of the hydrodynamic relationships underlying low Reynolds-number phenomena involving particles suspended in a fluid. As in the case of the earlier studies the so-called *creeping-motion* equations are employed in conjunction with spherical-shaped particles in a cylindrical tube to furnish the idealization necessary for mathematical analysis. This limits the validity of the results to low Reynolds numbers. In the following treatment the simplest possible approximation is explored as a means of relating the phenomena of sedimentation, fluidization, and pneumatic conveying. Thus it will be expected to apply only in very dilute systems, but it is here (*8*) that the necessary boundary surface which laterally confines any actual bed is of greatest importance.

Attention is confined to the purely hydrodynamic aspects of the behavior of the particulate systems involved. Accordingly, approximations are presented for the effect of the various parameters involved on the particle velocities and spatial distribution of particles as well as the pressure drop experienced by passage of fluid. For any given system these parameters include the physical dimensions of spheres and cylinder, the specific gravity of the spheres, the viscosity and specific gravity of the fluid, fluid velocity, and geometrical distribution of particles entering the system. Only hydrodynamic forces are considered though in some cases interparticle friction and electrostatic effects (*10, 14*) may assume great importance. The treatment here should furnish a framework for further studies on systems possibly including heat, mass transfer, and chemical-reaction effects.

SINGLE-SPHERE BEHAVIOR

The procedure adopted here is first to develop the behavior of a single sphere in a cylinder and then to extend the treatment to more complicated cases involving more than one sphere. In order to furnish a suitable basis the case must be treated for a sphere which is free to occupy any position in a tube. Previously (*8*) the behavior of a single sphere suspended at the axis of a cylindrical tube was treated. Figure 1 illustrates the more general case now to be considered. The sphere moves with an arbitrary constant velocity U relative to the cylinder wall in the direction of Z positive, parallel to the axis of the cylinder, while the fluid is in laminar flow with a velocity U_{OF} (with respect to the cylinder wall) at the axis of the cylinder (average or superficial velocity $\frac{1}{2}U_{OF}$) at a sufficiently great distance from the sphere where the pattern is parabolic. The sphere radius is a, the cylinder radius is R_0, and the center of the sphere is located at a distance b from the cylinder axis. Cylindrical coordinates (R, Φ, Z) are employed that have their origin at the cylinder axis at the same elevation as the sphere center.

The equations of motion to be satisfied are, in vector notation,

$$\nabla^2 \mathbf{v} = \frac{1}{\mu} \nabla p \qquad (1)$$

together with the continuity equation for incompressible fluids,

$$\nabla \cdot \mathbf{v} = 0 \qquad (2)$$

where $\mathbf{v}$ is the fluid velocity with respect to an origin which moves with the sphere. The boundary conditions which define the field $\mathbf{v}$ are

$$\mathbf{v} = 0 \quad \text{at} \quad r = a \qquad (3)$$

$$\mathbf{v} = -\mathbf{i}_z U \quad \text{at} \quad R = R_0 \qquad (4)$$

At large distances from the sphere $z = \pm\infty$, the disturbance propagated by the sphere vanishes, and the fluid-velocity distribution becomes Poiseuillian. Hence, as an additional boundary condition,

$$\mathbf{v} = \mathbf{i}_z \left[U_{OF}\left(1 - \frac{R^2}{R_0^2}\right) - U \right] \qquad (5)$$

As in the previous study, this boundary-value problem is solved by the method of reflections, the solution consisting of the sum of a series of velocity fields all of which satisfy Equations (1) and (2) and each partially satisfies the boundary conditions as follows:

$$\mathbf{v}_0 = \mathbf{i}_z \left[U_{OF}\left(1 - \frac{R^2}{R_0^2}\right) - U \right] \qquad (6)$$

$$\mathbf{v}_1 = \begin{cases} -\mathbf{v}_0 \text{ at } r = a \\ 0 \text{ at } z = \pm\infty \text{ (i.e. } r = \infty) \end{cases} \qquad (7)$$

$$\mathbf{v}_2 = \begin{cases} -\mathbf{v}_1 \text{ at } R = R_0 \\ 0 \text{ at } Z = \pm\infty \end{cases} \qquad (8)$$

$$\mathbf{v}_3 = \begin{cases} -\mathbf{v}_2 \text{ at } r = a \\ 0 \text{ at } z = \pm\infty \text{ (i.e. } r = \infty), \end{cases} \qquad (9)$$

etc.

with as many such fields taken as needed for an appropriate degree of approximation. The field $\mathbf{v}$ satisfying the boundary conditions (3), (4), and (5) is then obtained in the form

$$\mathbf{v} = \mathbf{v}_0 + \mathbf{v}_1 + \mathbf{v}_2 + \mathbf{v}_3 + \cdots$$

and the corresponding pressure field,

$$p = p_0 + p_1 + p_2 + p_3 + \cdots.$$

The field $\mathbf{v}_1$, corresponding to a sphere suspended in a field which becomes parabolic at an infinite distance from it,

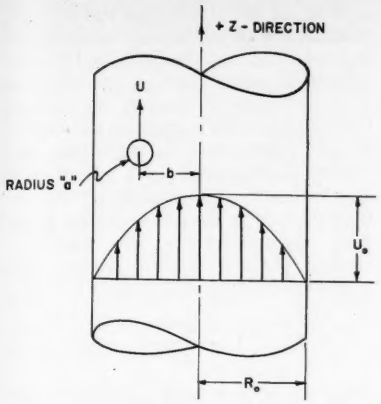

Fig. 1. Definition sketch—single sphere.

has been given by Simha (*18*) and Brenner (*1*). General expressions for additional reflections have been developed by Brenner and Happel (*2*), and details for the first two reflections are given in a supplement to this paper.*

For the present treatment only the first reflection is considered for the velocity field and the first two reflections are considered for pressure drop. In this approximation the effect of (a/R_0) is not evaluated and the "zeroth" approximation for drag and pressure drop is obtained as follows:

$$W = -6\pi\mu a \cdot \left[U - U_{OF}\left(1 - \frac{b^2}{R_0^2}\right)\right] \qquad (10)$$

$$\Delta P = \frac{12\mu a}{R_0^2}\left(1 - \frac{b^2}{R_0^2}\right) \cdot \left[(U_{OF} - U) - U_{OF}\frac{b^2}{R_0^2}\right] \qquad (11)$$

The expression for pressure drop corresponds to the energy dissipation experienced by a sphere moving in an unbounded medium with the same approach velocity.

MULTIPLE SPHERES

Relationships developed for a single sphere can be applied to the study of the behavior of more than one sphere by use of the same reflection technique. In order to illustrate this a simple case, involving the sedimentation of two spheres along the axis of a cylinder, is developed. The treatment, detailed in the supplement,* is confined to terms in first powers in a/R_0, and the investigation of Happel and Byrne (*8*) is used to obtain the velocity field generated by one of the spheres. More complicated cases can be developed by use of the same principle but substantial numerical calculations are involved.

For the case of multiple spheres the velocity contribution to the n-th sphere is obtained by summing the effects developed by each of the other $n - 1$ spheres. In the development which follows, the "zero" order approximation represented by Equations (10) and (11) is employed. Thus it is assumed that terms of the first power in a/R_0 and a/l may be omitted. (l is the distance between any two spheres.) The velocity field then will consist of the original undisturbed Poiseuille flow, except at the ends of the tube containing the spheres. The drag exerted on each particle will be given by Stokes's Law. Pressure drop due to each particle will depend solely upon its location and velocity.

Additional simplifications worth special attention result from the adoption of this simple hydrodynamic model. Since there is no interaction between particles, no prediction is possible of the effect of changes in the void volume between particles. It is assumed that the particles are sufficiently far apart so that such changes may be neglected. Actual bed depth corresponding to a given number of particles and fluid velocity must be specified independently. Similarly, on purely hydrodynamic grounds each particle will move only in an axial direction. No collisions are assumed and the pattern of motion continues unchanged along the entire tube length.

It is assumed that the particles suspended in a cylinder extend for an infinite distance axially. Boundary conditions at the inlet and outlet control the particle distribution which prevails in the tube. This particle distribution together with particle terminal settling velocity and fluid velocity constitute the three basic variables which influence the behavior of an assemblage. It is believed that a study of these idealized models will lead to a better understanding of the phenomena involved, though their quantitative application must be confined to assemblages of small particles located at relatively large distances from each other.

FIXED RELATIVE PARTICLE POSITION—UNIFORM DISTRIBUTION

First the simplest type of assemblage behavior will be considered, namely the case in which the particles suspended in a cylinder do not move relative to each other and in which they are randomly distributed throughout the cylinder cross section for an infinite distance axially. In practice this case is realized in sedimentation of a mass of particles in a quiescent fluid. The particles all fall at the same velocity and so maintain a fixed position relative to each other. This case also corresponds to the experiments of Happel and Epstein (*9*) in which pressure drop through rigid assemblages of particles was measured.

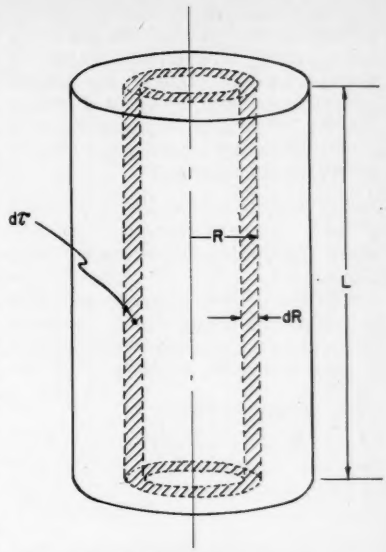

Fig. 2. Element of volume.

The number of particles N of radius a per unit volume is sufficient to characterize the behavior of such an assemblage. Since the particles do not influence each other by interaction fields, it is not necessary to know their exact arrangement as long as they are uniformly distributed.

A calculation will first be made for the velocity of such an assemblage by means of the annular volume $d\tau$ bounded by the radii R and $R - dR$ denoted in Figure 2.

The volume $d\tau = L(2\pi R\, dR)$, and the number of spheres contained in this volume is $NL(2\pi R\, dR)$. For this rigid assemblage the drag due to the presence of each sphere at position R is, Equation (10),

$$W = 6\pi\mu a\left[(U_{OF} - U) - U_{OF}\frac{R^2}{R_0^2}\right] \qquad (10a)$$

Hence the drag resulting from the particles in $d\tau$ is

$$dW_S = NL(2\pi R\, dR) \cdot 6\pi\mu a\left[(U_{OF} - U) - U_{OF}\frac{R^2}{R_0^2}\right] \qquad (12)$$

Integration gives the total drag,

$$W_S = NL(2\pi)(6\pi\mu a) \cdot \int_0^{R_0}\left[(U_{OF} - U)R - U_{OF}\frac{R^3}{R_0^2}\right] dR$$

whence

$$W_S = 6\pi\mu a \cdot N\pi R_0^2 L\left[\frac{U_{OF}}{2} - U\right] \qquad (13)$$

*Complete tabular material has been deposited as document 5441 with the American Documentation Institute, Photoduplication Service, Library of Congress, Washington 25, D. C., and may be obtained for $3.75 for photoprints or $2.00 for 35-mm. microfilm.

$U_{OF}/2$ is of course the average velocity of fluid in the cylinder and the result above is simply the equivalent of applying Stokes's Law to each of the spheres present. In terms of the terminal settling velocity of each of the particles it is readily shown by equating the drag to gravitational force that

$$U = U_{MF} - U_{TS}$$

where $U_{MF} = U_{OF}/2$, the mean fluid velocity.

A similar derivation for pressure drop is obtained by noting that the pressure drop due to a single sphere located at a distance R from the center is

$$\Delta P = \frac{12\mu a}{R_0^2}\left(1 - \frac{R^2}{R_0^2}\right) \cdot\left[(U_{OF} - U) - U_{OF}\frac{R^2}{R_0^2}\right] \qquad (11a)$$

Hence the pressure drop resulting from the particles in $d\tau$, with reference to Figure 3, is

$$d(\Delta P_S) = NL(2\pi R\, dR) \cdot\left(\frac{12\mu a}{R_0^2}\right)\left(1 - \frac{R^2}{R_0^2}\right) \cdot\left[(U_{OF} - U) - U_{OF}\frac{R^2}{R_0^2}\right] \qquad (14)$$

Integration between the limits of zero and R_0 gives the total pressure drop

$$\Delta P_S = NL8\pi\mu a\left(U_{MF} - \frac{3U}{4}\right) \qquad (15)$$

Here as in the remainder of this paper pressure drops due to the flow of fluid (Poiseuille's Law) and the effect of static head of the fluid are not included in the term ΔP_S, which refers only to the disturbance due to the presence of particles. For the case of sedimentation, where $U_{MF} = 0$, the pressure drop corresponds to the summation of the drag on the individual particles.

The case where particle velocity $U = 0$ gives the pressure drop through a rigid assemblage which does not move. If there are q particles contained in a volume of cylinder of length L and radius R_0, the following applies for the fractional void volume ϵ,

$$(1 - \epsilon) = \frac{\frac{4}{3}q\pi a^3}{\pi R_0^2 L} \qquad (16)$$

Thus the number of particles per unit volume N is

$$N = \frac{q}{\pi R_0^2 L} = \frac{3(1 - \epsilon)}{4\pi a^3} \qquad (17)$$

If this expression is substituted for N in Equation (15) and U is set equal to zero,

$$\Delta P_S = 6(1 - \epsilon)\frac{\mu U_{MF} L}{a^2} \qquad (18)$$

This expression differs from the exactly similar one derived by Happel and Byrne (*8*) and given by their Equation (64) by the constant, i.e., 9 instead of 6 as above. The assumption of Stokes's Law to compute the pressure drop would result in a factor of 4.5. Actual data on dilute assemblages by Happel and Epstein (*9*), as shown in their Figure 5 when extrapolated to infinite dilution, agree better with Equation (18) than either of the other values, providing confirmation for the present theoretical treatment.

MOBILE RELATIVE PARTICLE POSITION

Next the case will be considered in which the spheres are free to move relative to each other in an axial direction. In cases of practical interest radial distribution of particles may vary depending on end conditions, though distribution axially at any given radial location is assumed fixed. The general case for an arbitrary radial distribution will first be developed.

The frictional force, in the direction of flow, experienced by a sphere translating in the same direction with a constant velocity u when the fluid flows with a mean velocity $U_{MF} = \frac{1}{2}U_{OF}$ is given by Equation (10*a*). The gravitational force (corrected for the buoyancy of the fluid) experienced by the particle is

$$F_g = \frac{4\pi a^3(\rho_S - \rho_F)g}{3}$$

which, if Stokes's Law is valid for the terminal settling velocity in the quiescent fluid, is equivalent to

$$F_g = 6\pi\mu a U_{TS}$$

When no net force acts on the particle it will move with a constant velocity u, which is obtained by equating the drag and gravitational forces. The result obtained is

$$u = U_{OF}\left(1 - \frac{R^2}{R_0^2}\right) - U_{TS} \qquad (19)$$

which gives the equilibrium velocity of a particle situated at a distance R from the cylinder axis. Where all particles are free to move, a parabolic particle-velocity pattern thus results, as shown in Figure 3. Equation (19) implies that there is a radius s, $R_0 > s > 0$, for which the particle velocity $u = 0$. This radius might aptly be termed the *stagnation* radius and corresponds physically to the point at which the gravitational and frictional forces exactly balance one another. Upon putting $u = 0$ and $R = s$ in Equation (19) one obtains

$$\frac{s}{R_0} = \left(1 - \frac{U_{TS}}{U_{OF}}\right)^{1/2} \qquad (20)$$

In the region $R_0 \geq R > s$, which is hereafter termed the *outer annular area*, it is found from Equation (19) that $u < 0$, an indication that the particles in the vicinity of the tube wall have a downward motion. Similarly, in the *inner cylindrical space*, where $s > R \geq 0$, $u > 0$, corresponding to an upward motion of the solid particles in the vicinity of the cylinder axis. In the former case the net gravitational forces exceed those due to friction, as a result of the low fluid velocity in the neighborhood of the wall, accounting for the downward motion. The reverse effect predominates in the inner cylindrical space.

$$U_{OF}\left(1 - \frac{R^2}{R_0^2}\right) - u(R)$$

is the slip velocity and is constant with a value of U_{TS}, the terminal settling velocity.

The pressure drop through such an assemblage is for each sphere, situated at a distance R from the axis,

$$\Delta P_S = \frac{12\mu a}{R_0^2}\left(1 - \frac{R^2}{R_0^2}\right)U_{TS} \qquad (21)$$

Hence the pressure drop in the differential element of volume $d\tau$ is

$$d(\Delta P) = \frac{24\pi\mu a L}{R_0^2} \cdot U_{TS}\left(1 - \frac{R^2}{R_0^2}\right)nR\, dR \qquad (22)$$

Integration between the limits of zero and R_0 gives the over-all pressure drop. (L is assumed to be very large so that end effects may be neglected.) The number n of particles per unit volume at any radial location R is determined from end conditions. A general solution is possible without specific information regarding the dependence of n upon R, as follows. If ψ is the net number of particles transported per unit time in a positive axial direction, then

$$\int_0^{R_0} n \cdot u 2\pi R\, dR = \psi \qquad (23)$$

Whence,

$$2\pi\int_0^{R_0}\left[U_{OF}\left(1 - \frac{R^2}{R_0^2}\right) - U_{TS}\right]nR\, dR = \psi \qquad (24)$$

And finally

$$\int_0^{R_0}\left(1 - \frac{R^2}{R_0^2}\right)nR\, dR = \frac{\psi}{2\pi U_{OF}} + \frac{U_{TS}}{2\pi U_{OF}} \cdot\int_0^{R_0} n2\pi R\, dR \qquad (25)$$

However, if N_M is taken as the mean number of particles per unit volume averaged over the assemblage,

$$N_M \pi R_0^2 = \int_0^{R_0} n 2\pi R \, dR \qquad (26)$$

Thus the pressure drop is expressible as follows:

$$\Delta P = \frac{24\pi\mu a L}{R_0^2} U_{TS} \cdot \left[\frac{\psi}{2\pi U_{OF}} + \frac{U_{TS} N_M R_0^2}{2U_{OF}} \right] \qquad (27)$$

For the case of no net transport of particles, where total flow of particles upward balances downward flow, $\psi = 0$ and Equation (27) reduces to

$$\Delta P = N_M L 12\pi\mu a \frac{U_{TS}^2}{U_{OF}} \qquad (28)$$

If desired, a formula for pressure drop corresponding to fractional void volume may be readily obtained by appropriate substitution for N_M from Equation (17),

$$\Delta P = \frac{9\mu L U_{TS}^2 (1 - \epsilon)}{2U_{MF} a^2} \qquad (29)$$

Since the terminal settling velocity is given by

$$U_{TS} = \frac{2a^2 g}{9\mu} (\rho_S - \rho_F) \qquad (30)$$

and the weight of the bed of solid particles w, corrected for buoyancy, is given by

$$w = g(\rho_S - \rho_F) L (1 - \epsilon) \pi R_0^2 \qquad (31)$$

there results

$$\Delta P = \frac{U_{TS}}{U_{MF}} \times \frac{w}{\pi R_0^2} \qquad (32)$$

$\Delta P(\pi R_0^2)$ is the force F required to cause flow (above the Poiseuille Law pressure drop). Hence

$$F = w \times \frac{U_{TS}}{U_{MF}} \qquad (33)$$

Thus general expressions for velocity of particles and pressure drop have been developed. Next the effect of particle distribution will be considered. It should be noted that particle distribution will not affect particle velocity or pressure drop, except as it fixes the relationship between U_{TS} and U_{OF} required for specified particle transport ψ.

MOBILE BEDS

Uniform Particle Distribution

The simplest case for particle distribution in moving assemblages is that in which the radial particle distribution is uniform. One way in which this condition can be realized is by mixing particles and fluid uniformly at both ends and assuming that a steady state flow pattern is immediately established. The fluid entering a given zone in the tube will then contain a uniform particle concentration. This situation may be approximated in practice when both fluid and particles are introduced into the system simultaneously as in pneumatic conveying, pumping of slurries, and some sedimenting systems.

It is also likely that in fluidized systems where the velocity of fluid is close to the particle velocity, motion of particles at ends and other locations will cause fluid mixing so that a uniform particle distribution results.

In this case the variable concentration $n = n(R)$ is replaced by the constant concentration N. Equation (24) becomes

$$2\pi \int_0^{R_0} \left[U_{OF} \left(1 - \frac{R^2}{R_0^2} \right) - U_{TS} \right] N 2\pi R \, dR = \psi \qquad (34)$$

which is readily integrated. Upon setting $U_{OF}/2 = U_{MF}$, the simple result

$$U_{MF} - U_{TS} = \frac{\psi}{N\pi R_0^2} \qquad (35)$$

is obtained. For the case of no net particle transport, the "teeter" condition, $\psi = 0$ and

$$U_{MF} = U_{TS} \qquad (36)$$

Pressure drop through a uniform assemblage under appropriate restrictions upon ψ or U_{TS} may be determined by employing Equations (35) or (36) in conjunction with Equations (27) or (28) respectively. Thus for no net particle transport

$$\Delta P = NL6\pi\mu a U_{TS} = NL6\pi\mu a U_{MF} \qquad (37)$$

That is, the pressure drop is simply the equivalent of the Stokes's Law resistance corresponding to the terminal velocity of the particles.

Uniform Particle Flux

As noted above any radial distribution of particles is possible, depending on the conditions prevailing at the bed entrance and exit. It is desired to consider end conditions here which might be especially applicable in the case of fluidized beds, where the particles at entrance and exit conditions move independently of the fluid motion. In such beds the majority of particles are supported on a screen or other perforated device through which the fluid enters the bed. As circulation of particles occurs, the particles moving down are stopped abruptly at the screen and are redistributed. Again, fluid escapes from the top of the bed and the particles moving upward are redistributed as they assume a downward course. The present theory does not predict the depth of bed corresponding to a given number of particles because this necessitates a consideration of interaction effects

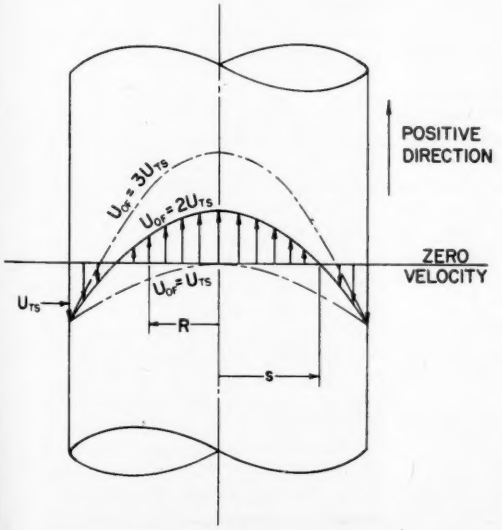

Fig. 3. Particle velocity pattern.

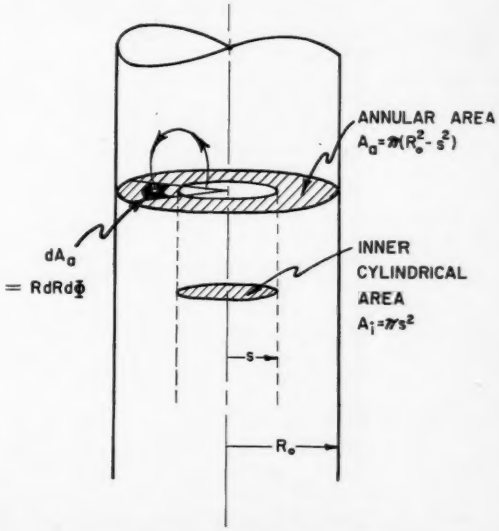

Fig. 4. Effect of end distribution.

among particles. However, the spatial distribution of particles, frequency of recirculation, and pressure drop can be computed on the presumption of random mixing of particles and fluid at the discontinuities appearing at the top and bottom of the bed.

In the development of the treatment to follow, it is assumed that a particle leaving the inner cylindrical space at the top of the bed has an equal probability of entering the outer annular space, down which particles are moving, at *any point*. The same reasoning applies for a particle leaving the annular space at the bottom of the tube and entering the inner cylindrical space. Other assumptions might be made, but it is believed that this assumption corresponds most closely to the facts in the present instance.

Conditions at the top of a bed are as shown in Figure 4. When a particle leaves the inner cylindrical space and enters the annular space, the probability that it enters the area dA_a if the particles are mixed is

$$\frac{dA_a}{A_a} = \frac{R\,dR\,d\Phi}{\pi(R_0^2 - s^2)} \qquad (38)$$

The relative distribution of particles to any differential area will be given by this fraction. If u is the particle velocity at any point, then the average particle velocity will be obtained by summing local velocities over the area and dividing by the total area through which they flow. In the case of a continuous distribution

$$U_{MS} = \frac{\int_A u\,dA}{A} \qquad (39)$$

Thus the average velocity of fall of a particle in the annular space will be

$$(U_{MS})_a = \frac{-\int_0^{2\pi}\int_{R=s}^{R=R_0} uR\,dR\,d\Phi}{\pi(R_0^2 - s^2)} \qquad (40)$$

$$= \frac{-2}{R_0^2 - s^2}\int_s^{R_0}\left[U_{OF}\cdot\left(1 - \frac{R^2}{R_0^2}\right) - U_{TS}\right]R\,dR \qquad (41)$$

$$= \frac{-2}{R_0^2 - s^2}\left[(U_{OF} - U_{TS})\cdot\frac{(R_0^2 - s^2)}{2} - \frac{U_{OF}}{R_0^2}\cdot\frac{(R_0^4 - s^4)}{4}\right] \qquad (42)$$

After further reduction,

$$(U_{MS})_a = -\left[\frac{U_{OF}}{2}\cdot\left(1 - \frac{s^2}{R_0^2}\right) - U_{TS}\right] \qquad (43)$$

whence, upon substitution of the value of s given in Equation (20),

$$(U_{MS})_a = \frac{U_{TS}}{2} \qquad (44)$$

A similar analysis is applicable to determine the velocity of particles in the inner cylindrical space

$$(U_{MS})_i = \frac{\int_0^{2\pi}\int_{R=0}^{R=s} uR\,dR\,d\Phi}{\pi s^2} \qquad (45)$$

$$= \frac{2}{s^2}\int_0^s\left[U_{OF}\cdot\left(1 - \frac{R^2}{R_0^2}\right) - U_{TS}\right]R\,dR \qquad (46)$$

$$= \frac{2}{s^2}\left[(U_{OF} - U_{TS})\cdot\frac{s^2}{2} - \frac{U_{OF}}{R_0^2}\cdot\frac{s^4}{4}\right] \qquad (47)$$

Consequently,

$$(U_{MS})_i = \frac{U_{OF} - U_{TS}}{2} \qquad (48)$$

The number of particles passing up through the entire inner cylindrical area per unit time, designated as ψ_i, will be a constant under steady state conditions. The number of particles passing down per unit time in the annulus will equal ψ_a. The number of particles passing a given area per unit time divided by their average velocity will give the number of particles contained in a unit length of path. The sum of these concentrations for upward- and downward-flowing particles must equal the average particle content of a unit length of bed. Thus

$$\frac{2\psi_i}{U_{TS}} + \frac{2\psi_a}{U_{OF} - U_{TS}} = N_M(\pi R_0^2) \qquad (49)$$

This provides a relation similar to Equation (35). The particle transport over the entire tube $\psi = \psi_i - \psi_a$. Thus in order to establish a relationship between U_{TS} and U_{OF}, ψ must be specified. To illustrate the procedure, the case for no net particle transport, $\psi = 0$, will be developed here. This results in $\psi_i = \psi_a$ expressed as follows:

$$\psi_i = \psi_a = \frac{N_M(\pi R_0^2)U_{TS}(U_{OF} - U_{TS})}{2U_{OF}} \qquad (50)$$

The inner cylindrical area may be expressed as

$$A_i = \pi s^2 = \frac{U_{OF} - U_{TS}}{U_{OF}}\pi R_0^2 \qquad (51)$$

Therefore the flux or number of particles per unit area per unit time passing through the inside area is

$$\frac{\psi_i}{A_i} = \frac{N_M U_{TS}}{2} \qquad (52)$$

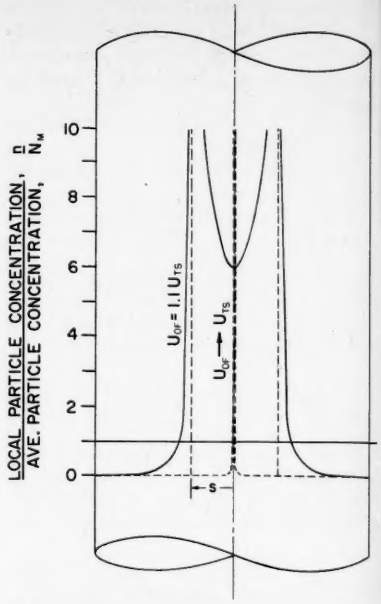

Fig. 5. Particle distribution—limit for upward transport.

This flux is constant over the cross-sectional area since equal distribution of particles was assumed over a given area of flow.

Similarly the area of the annular space is

$$A_a = \pi(R_0^2 - s^2) = \pi R_0^2\frac{U_{TS}}{U_{OF}} \qquad (53)$$

Therefore the flux through the annular space is

$$\frac{\psi_a}{A_a} = \frac{N_M(U_{OF} - U_{TS})}{2} \qquad (54)$$

The spatial distribution of particles may now be determined by noting that the flux at a given radial location is obtained by multiplying the local particle velocity by local concentration. Thus, for the annulus

$$\frac{\psi_a}{A_a} = \frac{N_M(U_{OF} - U_{TS})}{2} = n_a\left[U_{TS} - U_{OF}\left(1 - \frac{R^2}{R_0^2}\right)\right] \qquad (55)$$

whereupon

$$n_a = \frac{N_M(U_{OF} - U_{TS})}{2\left[U_{TS} - U_{OF}\left(1 - \frac{R^2}{R_0^2}\right)\right]}; \quad R_0 \geq R \geq s \qquad (56)$$

The number of particles per unit volume becomes very large (infinite) at the point $R = s$, where the particles are stationary.

Similarly the number of particles per unit volume in the inner cylindrical space n_i is

$$n_i = \frac{N_M U_{TS}}{2\left[U_{OF}\left(1 - \frac{R^2}{R_0^2}\right) - U_{TS}\right]}; \quad s \geq R \geq 0 \qquad (57)$$

Here again the number of particles per unit volume becomes very large at $R = s$.

Particle distribution in a system of this type will depend on the relative velocities U_{TS} and U_{OF}. It will be impossible to establish a condition of no net transport unless $U_{OF} = 2U_{MF} \geq U_{TS}$, because, as shown in Figure 3, no particle would have an upward velocity at lower fluid velocities. For this limiting case the particle concentration will be very high at the axis of the tube and fall off toward the walls, as illustrated in Figure 5. Cases have been reported in which this situation can be approached. Thus, Parent et al. (*17*) report "boiling," or aeration, at rates less than required to sweep even the finest particles of the contents out of a container.

The case where $U_{MF} = U_{TS}$ is of interest as this corresponds to the teeter condition for a bed of uniformly distributed particles. Pressure drop will be the same in both cases, though, as shown in Figure 6, particle distribution will be decidedly different. There is no theoretical upper limit to the value of U_{MF}, except that caused by difficulty in maintaining appropriate end conditions. Particle buildup at the walls becomes pronounced, as shown in Figure 6. This type of buildup of downward-moving particles in the vicinity of the walls has been repeatedly observed for fluidized beds (*4, 5, 11, 12, 15, 20*). In commercial fluidized beds velocities U_{MF} much higher than the terminal settling velocity have been observed (*6, 22*).

It is interesting to note that with the mechanism described here an increase in fluid velocity will result in a reduction in pressure drop for a given total bed weight supported, once $U_{TS} \geq U_{MF}$. This phenomenon was observed in experiments conducted by Lewis and Bowerman (*13*) in which cracking catalysts were fluidized at low velocities with liquid hydrocarbons. Pressure drops relative to bed weight of solids decreased 20% while the average fluid velocity increased threefold from the point of incipient fluidization. Further velocity increase by another tenfold factor resulted in a gradual approach of pressure drop to that required for $F = w$. Circulation can thus explain how particles without touching each other can cause pressure drop less than the weight of bed supported. In most commercial operations, where velocities are much higher than corresponds to incipient fluidization, the pressure drop is maintained approximately equal to the weight of suspended solids (*13, 14, 19*). Reduction in pressure drop with increase in velocity according to the mechanism treated here is an unstable phenomenon resulting from corresponding increase in particle segregation. Eventually a readjustment would occur owing to movement of particles back toward the middle of the tube, perhaps in an intermittent fashion as discussed by Miller and Logwinuk (*16*), with consequent increase in pressure drop. Of course, as more concentrated assemblages are employed, wall effects present in dilute suspensions assume a smaller relative importance in determining pressure drop, and so these analogies must be viewed with caution.

For the determination of pressure drop as a function of particle transport one may employ Equation (49) or (50) in conjunction with Equation (27) or (28) respectively. For the case of no net particle transport, $\psi = 0$, an expression for ΔP in terms of either U_{MF} or U_{OF} involves the additional parameter of particle circulation rate $\psi_i = \psi_o$. The greater the circulation rate, the larger will be the ratio of U_{MF} to U_{TS} required.

It is of some interest in connection with dilute fluidized beds to calculate the frequency of solids recirculation f for the case of no net transport $\psi = 0$. This quantity is defined as the number of complete cycles in the over-all circulation pattern which an average particle makes per unit time. In a bed of length L the average residence time of a particle falling in the annular space is, from Equation (44),

$$t_a = \frac{L}{U_{TS}/2} \qquad (58)$$

Similarly, the average residence time in the inner cylinder space, obtained from Equation (48), is

$$t_i = \frac{L}{(U_{OF} - U_{TS})/2} \qquad (59)$$

Thus, the average time required to complete one cycle is

$$t = t_a + t_i = \frac{2LU_{OF}}{U_{TS}(U_{OF} - U_{TS})} \qquad (60)$$

from which it follows that the frequency of recirculation is

$$f = \frac{1}{t} = \frac{U_{TS}(U_{OF} - U_{TS})}{2LU_{OF}} \qquad (61)$$

If θ is the nominal holdup time of the fluid as it traverses the bed,

$$\theta = \frac{L}{U_{MF}} = \frac{2L}{U_{OF}} \qquad (62)$$

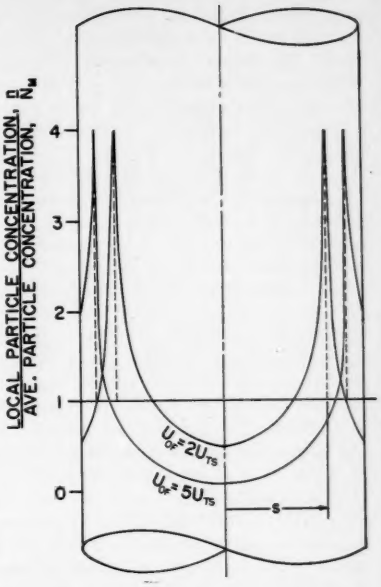

Fig. 6. Particle distribution—fluidized systems.

then the dimensionless parameter,

$$f\theta = \frac{U_{TS}}{U_{OF}}\left(1 - \frac{U_{TS}}{U_{OF}}\right) = \eta\left(\frac{U_{TS}}{U_{OF}}\right) \qquad (63)$$

may be of use in the correlation of backmixing effects.

DISCUSSION

The derivations above have been based on a simple set of consistent postulates in order to emphasize the basic conclusions. It is likely that certain other assumptions would provide better agreement with one or another set of empirical data. Thus one might choose to satisfy the continuity equation more exactly at higher solids concentrations by the assumption that instead of the original fluid velocity remaining undisturbed, it would be increased by a factor of $1/\epsilon$, (*3, 7*). This assumption in effect assumes complete shielding of each particle and is open to the objection that while it might approximate results at high concentrations of particles, its applicability would probably be questionable in dilute systems where wall effects might be important. Another more tenable assumption might involve removing the singularity noted in Equations (56) and (57) due to infinite particle concentration occurring at $R = s$. This could be done by noting that the concentration of particles could not occur to a greater extent than corresponds to fractional void volume of $\epsilon = 0.48$, the loose bed density (*9*). However, this would be

inconsistent with the assumption of no particle interaction employed in developing the theory. Application of these semiempirical concepts in a sound way awaits further experimental validation.

The cases considered above were all concerned with the ideal case of steady flow in a vertical cylindrical tube of infinite length. In effect the system is assumed to be sufficiently dilute so that a wide range of particle concentrations might exist. It is hypothesized that some means must be provided at the ends of the tube to effect the particle distributions assumed for the cases of moving particles. Nothing in the theory developed explains how and where the top and bottom interfaces are produced in the case of a bed of finite length. In the laboratory screens could be provided at both bottom and top of a given section to accomplish this. In beds which are relatively short the effect of entrance and exit boundaries and fluid-flow patterns would also require consideration. Preliminary studies indicate that a possible way to take such effects into account would be to assume that the fluid flow to and from a bed would be produced by point sources and sinks rather than by an established parabolic flow pattern of fluid motion.

It should also be emphasized that the treatment applies only in very dilute systems and for the slow viscous flow region, that is essentially the range where Stokes's Law applies. Extension to higher concentrations could be accomplished by taking into account additional reflections as discussed in the supplement. To form a quantitative estimate of the range of concentration for which the present theory is applicable, it would be necessary to develop at least the first interaction between spheres and cylinder walls.

The assumption of a parabolic distribution of fluid is also consistent with the idealization of no interaction of spheres with each other or the cylinder walls. Another extreme of behavior of exceedingly dilute systems would involve the case where the particle surface once was extremely large compared with that of the walls, in which case the average fluid velocity would be uniform. To determine the combined effect it would again be necessary to develop the first interaction. For cases of higher velocity where inertial effects cannot be neglected, the linearized form of the Stokes-Navier equations exployed here will not be adequate. However, it should be noted that often the motion of particles relative to fluid will be very small even though rate of movement of particles and fluid with respect to container walls is substantial.

It is thought that, in spite of many qualifications, the theory is of interest in providing a start toward a unified picture of the phenomena of fluidization and sedimentation based on fundamental fluid dynamic considerations. This is considered worthwhile because many laboratory-scale investigations do not appear to take into account the numerous variables which exist in commercial applications of these processes.

For dilute beds where depth is great enough so that entrance and exit effects are not important, the present theory can be employed to predict other characteristics of interest in the application of moving-bed systems. Thus, given an appropriate bed depth corresponding to a definite concentration of particles, one may estimate such items as fraction of particles present in annular space and in internal cylindrical space and time of contact of fluid with particles in the bed.

CONCLUSIONS

It has been demonstrated that a simple hydrodynamic theory based on the motion of a dilute system of spherical particles in a cylinder through which fluid is slowly passing may throw some light on phenomena observed in practical applications involving behavior of particles suspended in fluids.

Thus recirculation effects and distribution of particles can be examined in a qualitative fashion. Pressure drops are shown to be greatest relative to bed weight supported in the case of fixed assemblages. Recirculation of a uniformly dispersed suspension results in a lowering of pressure drop. If redistribution as well as recirculation occurs, still lower pressure drops are attainable but an unstable condition results.

Further work in progress aims to continue these studies from both theoretical and experimental approaches. It is believed that this paper represents progress in understanding the microscopic effects involved, as contrasted with statistical or empirical approaches to the problem.

ACKNOWLEDGMENT

The authors are grateful to the Research Corporation and the National Science Foundation for providing support for this investigation.

NOTATION

(Consistent Absolute Units)

a = radius of spherical particle
A = area
b = distance of sphere center from cylinder axis
F = force required to maintain fluid flow due to presence of spheres
F_g = gravitational force (corrected for buoyancy) acting on a spherical particle
f = frequency of particle recirculation
g = acceleration of gravity
l = distance between two spheres
L = length of an assemblage of spheres
n = number of spheres per unit volume at a given point location
N = constant number of spheres per unit volume
N_M = mean number of spheres per unit volume averaged over entire assemblage
p = viscous pressure at any location
ΔP = pressure drop due to presence of sphere or spheres
q = number of particles in a cylinder of length L and radius R_0
R = perpendicular distance from longitudinal axis of cylinder
R_0 = radius of cylinder
s = distance from cylinder axis at which there is no relative motion of sphere with respect to cylinder wall
t = average residence time of a particle
u or U = velocity of sphere or spheres in $+Z$ direction with respect to cylinder wall
U_{OF}, U_{OS} = axial velocity of fluid or spheres, respectively, in direction of Z positive with respect to cylinder wall
U_{MF}, U_{MS} = mean velocity of fluid or spheres, respectively, in direction of Z positive with respect to cylinder wall
U_{TS} = terminal settling velocity in direction of Z negative with respect to cylinder wall
w = weight of assemblage of particles corrected for buoyancy
W = frictional force in $+Z$ direction

Greek Letters

ϵ = fractional void volume
η = function in Equation (62)
θ = nominal holdup time of fluid
μ = viscosity
π = constant, 3.14159 $\cdots$
ρ = density
τ = volume
ψ = particle flux, particles per unit time

Vector Quantities

∇ = gradient
$\nabla\cdot$ = divergence
∇^2 = Laplace operator
$\mathbf{i}$ = unit vector; subscript indicates direction of vector
$\mathbf{v}$ = fluid velocity at any point

Subscripts

0, 1, 2, $\cdots$ = different velocity fields
a = outer annular area, where particles are moving down
A = a sphere
B = a sphere
F = fluid
i = inner cylindrical space where particles are moving up
m = mean value

0 = axial position
R_0 = evaluation of the function at $R = R_0$
S = sphere

LITERATURE CITED

1. Brenner, Howard, unpublished papers.
2. ———, and John Happel, *J. Fluid Mechanics*, to be published.
3. Burke, S. P., and W. B. Plummer, *Ind. Eng. Chem.*, **20**, 1196 (1928).
4. Dow, W. M., and Max Jakob, *Chem. Eng. Progr.*, **47**, 637 (1951).
5. Gamson, B. W., *ibid.*, **47**, 19 (1951).
6. Gohr, E. J., in "Fluidization in Practice," by D. F. Othmer, D. Van Nostrand, New York (1954).
7. Happel, John, *Ind. Eng. Chem.*, **41**, 1161 (1949).
8. ———, and B. J. Byrne, *ibid.*, **46**, 1181 (1954).
9. Happel, John, and Norman Epstein, *ibid.*, 1187.
10. Hariu, O. H., and M. C. Molstad, *ibid.*, **41**, 1148 (1949).
11. Leva, Max et al., *Chem. Eng. Progr.*, **44**, 511 (1948).
12. Leva, Max, et al., *ibid.*, **45**, 563 (1949).
13. Lewis, E. W., and E. W. Bowerman, *ibid.*, **48**, 603 (1952).
14. Lewis, W. K., E. R. Gilliland, and W. C. Bauer, *Ind. Eng. Chem.*, **41**, 1104 (1949).
15. McCune, L. K., and R. H. Wilhelm, *ibid.*, **41**, 1124 (1949).
16. Miller, C. O., and A. K. Logwinuk, *ibid.*, **43**, 1220 (1951).
17. Parent, J. D., N. Yagel, and C. S. Steiner, *Chem. Eng. Progr.*, **43**, 429 (1947).
18. Simha, Robert, *Kolloid. Z.* **76**, 16 (1936).
19. Toomey, R. D., and H. F. Johnstone, *Chem. Eng. Progr.*, **48**, 220 (1952).
20. Van Heerden, C., A. P. P. Nobel, and D. W. van Krevelen, *Ind. Eng. Chem.*, **45**, 1237 (1953).
21. Wilhelm, R. H., "Proceedings of Second Midwestern Conference on Fluid Mechanics," Ohio State Univ. (1952).
22. ———, and Mooson Kwauk, *Chem. Eng. Progr.*, **44**, 201 (1948), discussion by L. J. Friend, on p. 218.

Unsteady State Heat Transfer in Stationary Packed Beds

PARK M. REILLY

Polymer Corporation, Limited, Sarnia, Ontario, Canada

A new solution is presented of the differential equations describing unsteady state heat transfer in stationary beds of small granular solid particles through which a fluid is flowing. Arbitrary initial solid temperature distribution and arbitrary variation of inlet gas temperature are allowed. The solution presented appears easier to apply in practice than those previously published and affords an example of the versatility of Fourier integrals and series. An application of the solution to the regeneration of Dow type-B butylene dehydrogenation catalyst is described.

Passage of a fluid through a bed of granular solid is of common occurrence in chemical engineering practice. Several mathematical treatments of unsteady state heat transfer in this situation have been published. Schumann (*1*) developed the basic differential equations and presented a solution for the case of uniform initial solid temperature and constant entering fluid temperature. His work was extended by Furnes (*2*), Goldstein (*3*), and others. More general cases have been covered by Amundson (*4*, *5*). One (*4*) considers the unsteady state with arbitrary initial solid temperature and also arbitrary inlet fluid temperature at any time. This publication was presented as a solution to a problem in adsorption, but the mathematical statement is identical with that for the heat transfer problem. A more recent publication by Amundson (*5*) covers much more general cases where heat may be produced or absorbed in the bed, simultaneously transferred through the wells of the containing vessel, etc.

All solutions published to date have been in terms of Bessel functions or other functions which are published for limited ranges of variables or at best for relatively widely separated values. Also, in most practical cases the more general solutions are quite laborious to apply. Presented here are two solutions of the same problem as that treated by Amundson (*4*), but they are derived from Fourier integrals and Fourier series. The resulting mathematical forms are consequently easy to apply. Convergence is rapid in most cases. The series form of solution is an approximation but in most practical cases it is a very good one. In general, it is easier to use than the integral form, which however is exact.

The problem concerns a bed in the shape of a right porous prism (or cylinder) of granular material the initial temperature of which is an arbitrary function of distance into the bed. A fluid, the inlet temperature of which is an arbitrary function of time, is allowed to pass lengthwise through the bed at a uniform rate of flow, the sides of the bed being impervious to the fluid and to heat. The problem is to find the distribution of temperature in the solid material and in the fluid for all time if it is assumed that

1. The gas and solid temperature are uniform across any section perpendicular to the axis of the prism.
2. The solid particles are so small or have such high thermal diffusivity that any given particle may be considered as being at a uniform temperature at any instant.
3. Compared with the transfer of heat from fluid to solid, the transfer of heat by conduction, convection, or mixing in the fluid itself or in the solid itself is small and may be neglected.
4. The rate of heat transfer from fluid to solid at any point is proportional to the difference in temperature between fluid and solid at that point.
5. Change in volume of fluid and solid due to change in temperature may be neglected.
6. The thermal constants are independent of the temperature.
7. There is no generation or absorption of heat as latent heat, heat of chemical reaction, etc.

DERIVATION OF EQUATIONS

The basic differential equations describing the problem, as derived by Schumann (*1*), are

$$\frac{\partial t_g}{\partial \theta} + \frac{g}{\rho_g f}\frac{\partial t_g}{\partial x} = -\frac{hs}{C_g \rho_g f}(t_g - t_s) \quad (1)$$

$$\frac{\partial t_s}{\partial \theta} = \frac{hs}{\rho_s C_s}(t_g - t_s) \quad (2)$$

Changing the independent variables to y and z gives

$$\frac{\partial t_g}{\partial y} = t_s - t_g \quad (3)$$

$$\frac{\partial t_s}{\partial z} = t_g - t_s \qquad (4)$$

and from these

$$\frac{\partial t_s}{\partial z} = -\frac{\partial t_g}{\partial y} \qquad (5)$$

By differentiating (3) with respect to z and (4) with respect to y and substituting (5) in both cases, one obtains the following two equations:

$$-\frac{\partial^2 t_g}{\partial y \partial z} = \frac{\partial t_g}{\partial y} + \frac{\partial t_g}{\partial z} \qquad (6)$$

$$-\frac{\partial^2 t_s}{\partial y \partial z} = \frac{\partial t_s}{\partial y} + \frac{\partial t_s}{\partial z} \qquad (7)$$

BOUNDARY CONDITIONS

The boundary conditions are that the initial temperature distribution of the solid is an arbitrary function of position in the bed and that after the datum point in time the temperature of the gas entering the bed is another arbitrary function of time. Expressed mathematically, these are

$$t_s = F_1(y); \qquad z = 0 \qquad (8)$$

$$t_g = F_2(z); \qquad y = 0 \qquad (9)$$

SOLUTION

The solution is obtained by first finding a solution for both t_s and t_g consistent with boundary condition (8) and assuming datum inlet gas temperature. Another solution is found consistent with boundary condition (9) and assuming datum initial solid temperature. The sum of these two solutions satisfies both boundary conditions for any temperature datum.

A solution of Equation (7) is found, by the method of separation of variables, to be

$$t_s = \left[a \cos c\left(y - \frac{z}{1+c^2}\right) + b \sin c\left(y - \frac{z}{1+c^2}\right)\right] \exp \frac{-c^2 z}{1+c^2}$$

where a, b, and c are arbitrary constants. When $z = 0$, this reduces to $t_s = a \cos cy + b \sin cy$. This form is the correct one for the formation of a Fourier integral which will converge to $F_1(y)$ at $z = 0$ as required by boundary condition (8). It can be shown that this expansion is normally permissible under the conditions of this problem.

The solution shown above has no term containing t_g. In order to produce a solution of this type consistent with datum inlet gas temperature, a means is used which can best be explained from a physical point of view. A bed of solid, infinitely long, and initially at uniform datum temperature throughout is imagined to lie ahead of the real solid bed. This will have the effect of adjusting the gas temperature entering the real bed to the datum temperature. The mathematical justification for this step will be indicated later. Also, to make the Fourier integral converge, the solid from the outlet end of the real bed to infinity in the positive direction is considered to be at datum temperature. Boundary condition (8) can then be expressed, in complete form, as follows:

$$\begin{aligned} t_s(y, 0) &= 0 && y < 0 \\ &= F_1(y) && 0 < y < Y \\ &= 0 && Y < y \end{aligned}$$

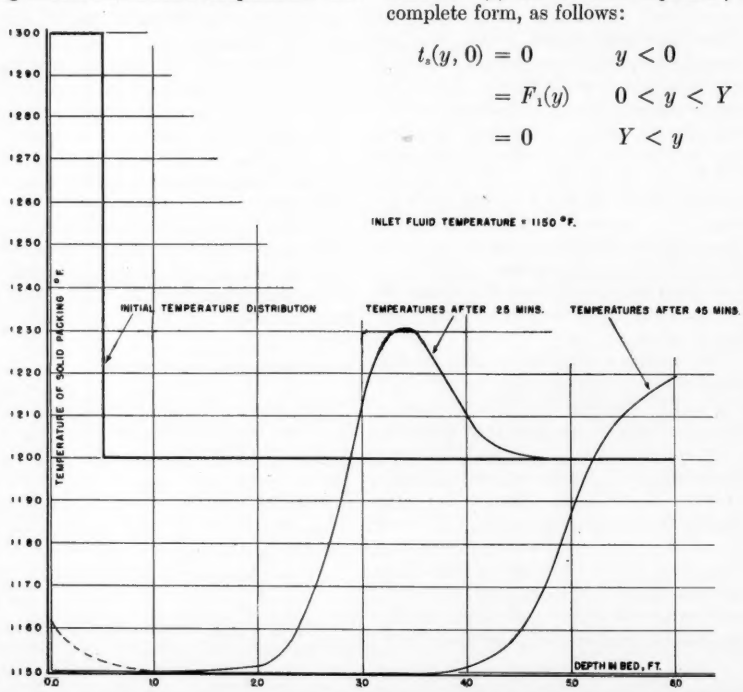

Fig. 1. Calculated temperatures of solid packing. Inlet fluid temperature = 1,150°F.

A solution of Equation (7) consistent with this condition can be made by properly choosing the constants a, b, and c to expand the solution into Fourier integral form, which is

$$t_s = \frac{1}{\pi}\int_0^\infty \left[g(\alpha) \cos\left(y\alpha - \frac{z\alpha}{1+\alpha^2}\right) + h(\alpha) \sin\left(y\alpha - \frac{z\alpha}{1+\alpha^2}\right)\right] \cdot \exp - \frac{z\alpha^2}{1+\alpha^2}\, d\alpha \qquad (10)$$

where

$$g(\alpha) = \int_0^Y F_1(n) \cos \alpha\eta \, d\eta$$

and

$$h(\alpha) = \int_0^Y F_1(n) \sin \alpha\eta \, d\eta$$

If Equation (10) is differentiated with respect to z and substituted into Equation (4), the following expression for t_g results.

$$t_g = \frac{1}{\pi}\int_0^\infty \left[\frac{g(\alpha) - \alpha h(\alpha)}{1+\alpha^2} \cdot \cos\left(y\alpha - \frac{z\alpha}{1+\alpha^2}\right) + \frac{h(\alpha) + \alpha g(\alpha)}{1+\alpha^2} \cdot \sin\left(y\alpha - \frac{z\alpha}{1+\alpha^2}\right)\right] \cdot \exp - \frac{z\alpha^2}{1+\alpha^2}\, d\alpha \qquad (11)$$

It can be shown that for all positive z, the preceding expression converges to $t_g = 0$ at $y = 0$. This is the mathematical justification for the assumption of an infinite imaginary bed initially at datum temperature ahead of the real one.

By a method similar to that used to develop Equations (10) and (11), expressions for t_s and t_g can be developed for datum initial solid temperature based on Equation (6) and boundary condition (9). The condition of datum initial solid temperature is achieved by a device analogous to the imaginary bed used previously. Here it is assumed that gas of datum temperature has flowed through the actual bed for an infinite time before the zero of time. The following equations result:

$$t_s = \frac{1}{\pi}\int_0^\infty \left[\frac{p(\alpha) - \alpha q(\alpha)}{1+\alpha^2} \cdot \cos\left(z\alpha - \frac{y\alpha}{1+\alpha^2}\right) + \frac{q(\alpha) + \alpha p(\alpha)}{1+\alpha^2}\right.$$

$$\cdot \sin\left(z\alpha - \frac{y\alpha}{1+\alpha^2}\right)\Bigg]$$

$$\cdot \exp - \frac{y\alpha^2}{1+\alpha^2}\, d\alpha \qquad (12)$$

$$t_g = \frac{1}{\pi}\int_0^\infty \left[p(\alpha)\cos\left(z\alpha - \frac{y\alpha}{1+\alpha^2}\right) + q(\alpha)\sin\left(z\alpha - \frac{y\alpha}{1+\alpha^2}\right)\right] \cdot \exp - \frac{y\alpha^2}{1+\alpha^2}\, d\alpha \qquad (13)$$

$p(\alpha)$ and $q(\alpha)$ are as defined below.

For any temperature datum, the expressions for t_s will be the sum of Equations (10) and (12). Similarly, t_g is given by the sum of Equations (11) and (13). The final solution, then, which satisfies Equations (6) and (7) and boundary conditions (8) and (9) for any temperature datum is

$$t_s = \frac{1}{\pi}\int_0^\infty \left[g(\alpha)\cos\left(y\alpha - \frac{z\alpha}{1+\alpha^2}\right) + h(\alpha)\sin\left(y\alpha - \frac{z\alpha}{1+\alpha^2}\right)\right] \cdot \exp - \frac{z\alpha^2}{1+\alpha^2}\, d\alpha + \frac{1}{\pi}\int_0^\infty \left[\frac{p(\alpha) - \alpha q(\alpha)}{1+\alpha^2} \cdot \cos\left(z\alpha - \frac{y\alpha}{1+\alpha^2}\right) + \frac{q(\alpha) + \alpha p(\alpha)}{1+\alpha^2} \cdot \sin\left(z\alpha - \frac{y\alpha}{1+\alpha^2}\right)\right] \exp - \frac{y\alpha^2}{1+\alpha^2}\, d\alpha \qquad (14)$$

$$t_g = \frac{1}{\pi}\int_0^\infty \left[p(\alpha)\cos\left(z\alpha - \frac{y\alpha}{1+\alpha^2}\right) + q(\alpha)\sin\left(z\alpha - \frac{y\alpha}{1+\alpha^2}\right)\right] \cdot \exp - \frac{y\alpha^2}{1+\alpha^2}\, d\alpha + \frac{1}{\pi}\int_0^\infty \left[\frac{g(\alpha) - \alpha h(\alpha)}{1+\alpha^2} \cdot \cos\left(y\alpha - \frac{z\alpha}{1+\alpha^2}\right) + \frac{h(\alpha) + \alpha g(\alpha)}{1+\alpha^2} \cdot \sin\left(y\alpha - \frac{z\alpha}{1+\alpha^2}\right)\right] \cdot \exp - \frac{z\alpha^2}{1+\alpha^2}\, d\alpha \qquad (15)$$

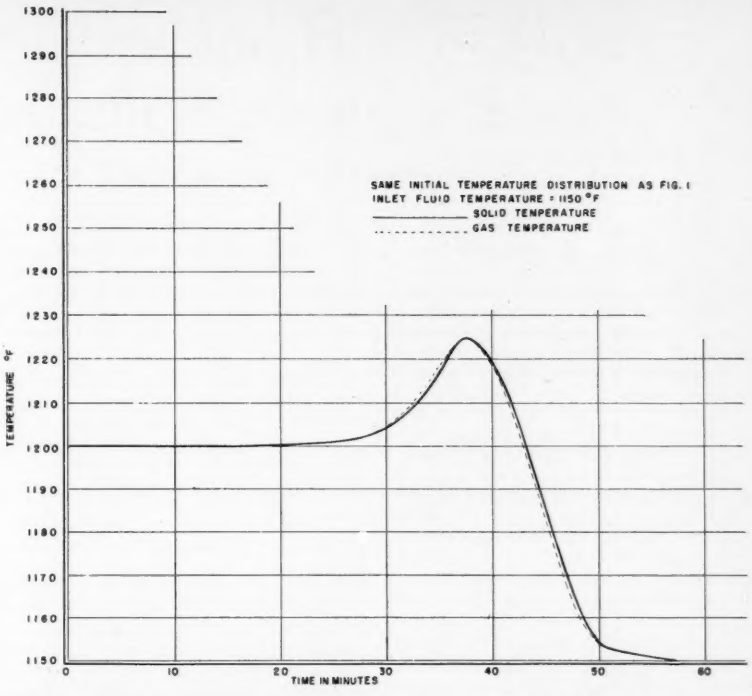

Fig. 2. Calculated temperature of solid packing and gas at a point 5 ft. from fluid entrance into bed. Same initial temperature distribution as Figure 1. Inlet fluid temperature = 1,150°F. ———— solid temperature, - - - - - - - gas temperature.

where

$$g(\alpha) = \int_0^Y F_1(\eta)\cos\alpha\eta\, d\eta \qquad p(\alpha) = \int_0^Z F_2(\gamma)\cos\alpha\gamma\, d\gamma$$

$$h(\alpha) = \int_0^Y F_1(\eta)\sin\alpha\eta\, d\eta \qquad q(\alpha) = \int_0^Z F_2(\gamma)\sin\alpha\gamma\, d\gamma$$

This solution can be shown to be mathematically identical to that of Amundson (*4*), and Schumann's solution (*1*) can be shown to be a special case of that above.

In practice, the integrals involved in the solution are usually best evaluated graphically.

FOURIER-SERIES FORMS

An approach similar to those used in obtaining the foregoing exact forms can be used to produce approximate solutions derived from Fourier series. A solution for t_s and t_g is found for datum inlet gas temperature as before by assuming an imaginary bed of solid at datum temperature ahead of the real bed. Because of the finite range of convergence of Fourier series this bed can be of only finite length, and so the gas is brought only approximately to datum temperature. In actual cases the approximation is very good for y and z less than Y. For y and z greater than Y the approximation fails completely. In practice, this is not usually an important limitation because values of y greater than Y are never of interest and those of z are not usually interesting.

Similarly, the device of obtaining datum initial solid temperature by treatment of the solid with gas of datum temperature is true only as a good approximation and for y and z less than Y.

The Fourier series forms are

$$t_s = \frac{g_0}{2} + \sum_{n=1}^{\infty}\left[g_n\cos\left(c_n y - \frac{c_n z}{1+c_n^2}\right) + h_n\sin\left(c_n y - \frac{c_n z}{1+c_n^2}\right)\right] \cdot \exp - \frac{c_n^2 z}{1+c_n^2} + \frac{p_0}{2} + \sum_{n=1}^{\infty}\left[\frac{p_n - c_n q_n}{1+c_n^2} \cdot \cos\left(c_n z - \frac{c_n y}{1+c_n^2}\right) + \frac{q_n + c_n p_n}{1+c_n^2} \cdot \sin\left(c_n z - \frac{c_n y}{1+c_n^2}\right)\right] \cdot \exp - \frac{c_n^2 y}{1+c_n^2} \qquad (16)$$

$$t_g = \frac{p_0}{2} + \sum_{n=1}^{\infty}\left[p_n\cos\left(c_n z - \frac{c_n y}{1+c_n^2}\right) + q_n\sin\left(c_n z - \frac{c_n y}{1+c_n^2}\right)\right]$$

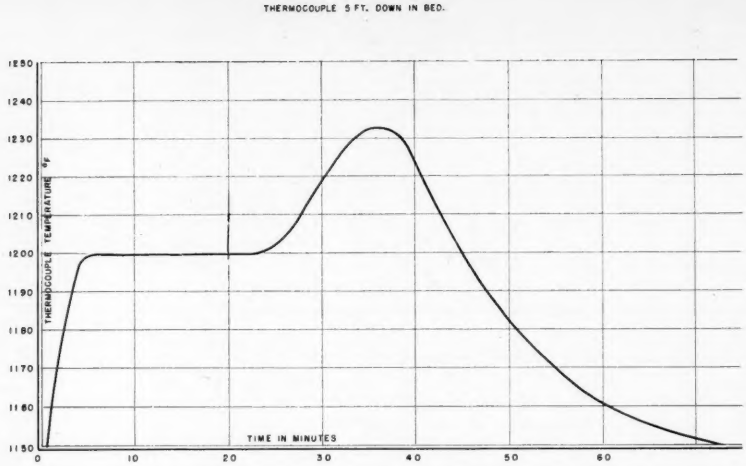

Fig. 3. Typical regeneration pattern for Dow type-B catalyst (observed). Thermocouple 5 ft. down in bed.

$$\cdot \exp - \frac{c_n^2 y}{1 + c_n^2}$$

$$+ \frac{g_0}{2} + \sum_{n=1}^{\infty} \left[\frac{g_n - c_n h_n}{1 + c_n^2} \right.$$

$$\cdot \cos \left(c_n y - \frac{c_n z}{1 + c_n^2} \right) + \frac{h_n + c_n g_n}{1 + c_n^2}$$

$$\left. \cdot \sin \left(c_n y - \frac{c_n z}{1 + c_n^2} \right) \right]$$

$$\cdot \exp - \frac{c_n^2 z}{1 + c_n^2} \cdot \qquad (17)$$

where

$$c_n = \frac{n\pi}{Y} \quad p_n = \frac{1}{Y} \int_0^Y F_2(\gamma) \cos c_n \gamma \, d\gamma$$

$$g_n = \frac{1}{Y} \int_0^Y F_1(\eta) \cos c_n \eta \, d\eta$$

$$q_n = \frac{1}{Y} \int_0^Y F_2(\gamma) \sin c_n \gamma \, d\gamma$$

$$h_n = \frac{1}{Y} \int_0^Y F_1(\eta) \sin c_n \eta \, d\eta$$

APPLICATION TO A COMMERCIAL REACTOR

The series form of solution has been applied to a system in which a mixture of steam and air is flowing downward through a bed of $\frac{3}{16}$ in. cylindrical pellets of Dow type B butylene dehydrogenation catalyst under the following conditions:

$C_g = 0.48$ B.t.u./(lb.)(°F.)
$f = 0.366$
$X = 6$ ft.
$\rho_s = 62.5$ lb./cu. ft.
$C_s = 0.24$ B.t.u./(lb.)(°F.)
$g = 225$ lb./sq. ft.)(hr.)
$\rho_g = 0.0714$ lb./cu. ft.

The initial conditions used were that the solid was at 1,300°F. for the top 6 in. and 1,200°F. for the remainder of the bed.

Figure 1 shows the solid temperature throughout the bed initially and as calculated after the elapse of 25 and 45 min. with the steam-air mixture entering at 1150°F. The heat transfer constant hs used in the calculation of Figure 1 was 3,500 B.t.u./(cu. ft.)(hr./°F.). This is the approximate value indicated by the method of analogy with mass transfer quoted by McAdams (7). The broken line applies to the temperatures calculated at 45 min. and arises because z is greater than Y for this line. For this reason the broken part of the calculated line at 45 min. is incorrect.

Figure 2 is a plot of the calculated solid and gas temperatures at a point 5 ft. into the bed shown against a time base. Figure 3 shows a typical temperature history of a thermocouple shielded by a metallic well, at a point 5 ft. down in the bed under study. The solid temperature curve of Figure 2 was calculated in an attempt to explain the shape of the curve of Figure 3. There is reason to believe that very shortly after the beginning of the regeneration of the catalyst as described in a previous paper (6), the catalyst pellets are at temperatures approximately as described for the initial condition used for calculating Figures 1 and 2 and that little or no heat is produced or absorbed in the bed during the remainder of the regeneration period. The fact that the curve of Figure 3 is of the same general shape as the calculated one in Figure 2 substantiates the postulate that the temperature "surges" as shown in Figure 3 are largely the result of a band of high pellet temperature passing down through the bed by heat transfer.

GENERALIZATION

Certain problems in mass transfer, such as some cases of chromatography, some ion exchange processes, and some cases of drying by desiccant beds, are analogous to unsteady state heat transfer in packed beds. Where the analogy holds, the solutions developed here can be applied with appropriate changes in definition of the variables.

ACKNOWLEDGMENT

Acknowledgment is due Polymer Corporation, Limited, for cooperation in the preparation of this paper and for permission to publish it and to Dr. L. C. Eagleton of the University of Pennsylvania for criticism of some of the mathematical demonstrations.

NOTATION

C_g = specific heat of fluid, B.t.u./(lb.)(°F.)
C_s = specific heat of solid, B.t.u./(lb.)(°F.)
f = void fraction of bed, dimensionless
$F_1(y) = t_s$ at $z = 0$
$F_2(z) = t_g$ at $y = 0$
g = mass velocity of fluid, lb./(sq. ft.)(hr.)
h = surface heat transfer coefficient, B.t.u./(sq. ft.)(hr./°F.)
s = effective heat transfer area per unit bulk volume of solid, ft.$^{-1}$
t_g = temperature of fluid, °F. above datum
t_s = temperature of solid, °F. above datum
x = distance into bed in direction of fluid flow, ft.
X = total length of bed in direction of fluid flow, ft.
$y = \frac{hsx}{gC_g}$, dimensionless
$Y = \frac{hsX}{gC_g}$ dimensionless, the maximum value of y to be considered
$z = \frac{hs}{\rho_s C_s} \left(\theta - \frac{\rho_s f x}{g} \right)$, dimensionless
Z = maximum value of z to be considered
ρ_g = density of fluid lb./cu. ft.
ρ_s = bulk density of solid lb./cu. ft.
θ = time, hr.

LITERATURE CITED

1. Schumann, T. E. W., *J. Franklin Inst.*, **208**, 405 (1929).
2. Furnas, C. C., *Ind. Eng. Chem.*, **22**, 721 (1930).
3. Goldstein, S., *Proc. Royal Soc. (London)*, **219A**, 151 (1953).
4. Amundson, N. R., *J. Physical & Colloid Chem.*, **54**, 812 (1950).
5. ———, *Ind. Eng. Chem.*, **48**, 26 (1956).
6. Reilly, P. M., *Chemistry in Canada*, p. 25, (March, 1953).
7. McAdams, W. H., "Heat Transmission," 3 ed., p. 294, McGraw-Hill Book Company, Inc., New York, (1954).

Vapor-liquid Equilibria and Heat of Mixing: *n*-Octane–ethylbenzene–Cellosolve System

P. S. MURTI and MATTHEW VAN WINKLE, University of Texas, Austin, Texas

Vapor-liquid equilibria of the systems *n*-octane–Cellosolve, ethylbenzene-Cellosolve, and *n*-octane–ethylbenzene–Cellosolve were determined at 760 mm. Hg. The activity coefficient data of Yang and Van Winkle (*23*) for the system *n*-octane–ethylbenzene and the data of this work on other systems were expressed by Wohl's three-suffix Margules equations. The ternary data are predicted satisfactorily from the binary constants and no noticeable ternary effects seem to exist for this ternary system.

Heat-of-mixing data at 25°C. were determined for the ternary and the three related binary systems, and attempts were made to predict ternary heat-of-mixing data from those of the component binaries by the method of Scatchard et al. (*15*).

Yang and Van Winkle (*23*) presented vapor-liquid equilibrium data for the binary system *n*-octane–ethylbenzene at various subatmospheric pressures. Their data indicate that the relative volatility of *n*-octane with respect to ethylbenzene is very low, particularly at high concentrations of *n*-octane. This was observed in some hydrocarbon-nonhydrocarbon systems studied by Thoronton and Garner (*19*).

The present investigation was carried out to find the influence of a third component on the relative volatility of *n*-octane with respect to ethylbenzene and to present heat-of-mixing data for the binaries and the ternary system.

PURITY OF COMPOUNDS

Pure-grade *n*-octane, supplied by Phillips Petroleum Company, was fractionated in a 4-ft. glass column packed with ¼-in. glass helices at a reflux ratio of approximately 20:1. The first and last fractions, each approximately one-sixth of the charge, were discarded and the heart cut was used for experimental work. Ethylbenzene, supplied by the same company, was used directly without further purification. Carbide and Carbon Chemical Company Cellosolve, supplied by Baker Chemical Company, was fractionated twice in this column and a heart cut was taken for experimental work. Proper precautions minimized absorption of atmospheric moisture by cellosolve. The physical properties of the purified materials are listed in Table 1.

METHODS OF ANALYSIS

Density was used as a basis for analysis of the unknown mixtures of *n*-octane and Cellosolve, and compositions of the ethylbenzene-Cellosolve mixtures were determined at 30°C. by refractive index with a Bausch and Lomb precision refractiometer using monochromatic light from a sodium lamp. The densities were determined with a 10.0-ml. pycnometer.

The analysis of the ternary system was based upon the method of Carlson, Schubert and Fenske (*1*), which consisted essentially of determining one physical property of the mixture, extracting the Cellosolve with water, and finding the same or another physical property of the raffinate phase, i.e., the residual liquid. From the results of these two determinations, it is possible to fix the composition of the mixture.

Known mixtures of the three components were prepared by weighing the components and mixing them in 50-ml. conical flasks provided with ground-glass stoppers. The densities of the mixtures were determined with a 10.0-ml. pycnometer. About ten determinations were made on each mixture in which the mole percentage of *n*-octane on a Cellosolve-free basis was maintained constant, and in all about ninety determinations were made in order to describe the entire composition range of the ternary. A plot of density vs. mole percentage of Cellosolve in the ternary with mole percentage of *n*-octane on Cellosolve-free basis as parameter was prepared. From this a cross plot of density vs. mole percentage of *n*-octane on a Cellosolve-free basis with mole percentage of Cellosolve in the ternary as a parameter was then made. This plot is shown in Figure 1.

To analyze each unknown mixture, the following data were obtained: (1) the density of the mixture and (2) the refractive index of raffinate phase. From a knowledge of (2), the mole percentage of *n*-octane in the *n*-octane–ethylbenzene system on a Cellosolve-free basis was obtained from a plot of refractive index vs. composition based on the data of Yang and Van Winkle (*23*). With the latter information and the density of the mixture, the composition could be established by referring to Figure 1. Five determinations were made on known mixtures of the three components to test the accuracy of the method.

TABLE 1
PHYSICAL PROPERTIES OF THE COMPOUNDS

Compound	Boiling point, °C. Exp.	Boiling point, °C. Lit. (*20*)	Density$^{25/4}$ Exp.	Density$^{25/4}$ Lit. (*20*)	Ref. Inc. 25°C. Exp.	Ref. Inc. 25°C. Lit. (*20*)
(1) *n*-Octane	125.7	125.665	0.69856	0.69849	1.39510	1.39505
(2) Ethylbenzene	136.2	136.187	0.86274	0.86264	1.49337	1.49330
(3) Cellosolve*	135.3	135.3†	0.92595	—	1.40812	1.4080‡

*Reference 8.
†Reference 2.
‡At 20°C.

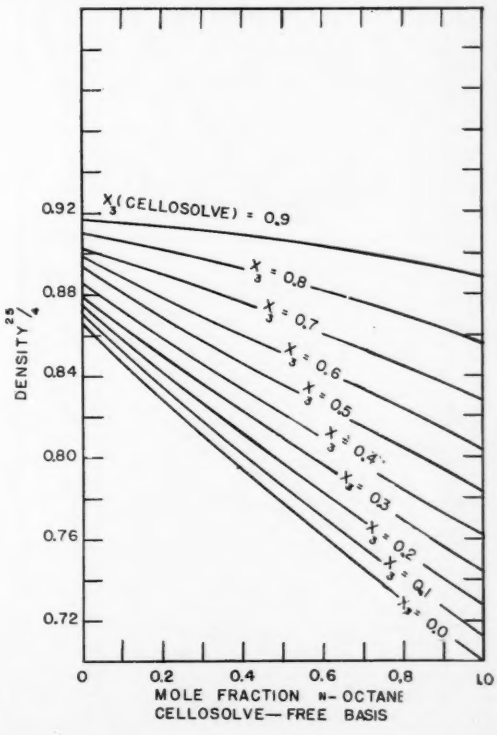

Fig. 1. Analytical diagram for the system *n*-octane–ethylbenzene–Cellosolve.

P. S. Murti is at Andhra University, Waltair, India.

APPARATUS AND PROCEDURE

The modified Colburn equilibrium still (*6*) and its operation to obtain vapor-liquid equilibrium data were described in an earlier paper (*11*), and the calorimeter, its accessories and its operation to obtain heat of mixing data, was also described previously (*12*).

ACTIVITY COEFFICIENTS

The activity coefficients were calculated from experimental vapor-liquid equilibrium data by means of the equation

$$\log_{10}\gamma_1 = \log_{10}\frac{P_T y_1}{P_1 x_1} + \frac{(\beta_{11} - v_{11})(P_T - P_1)}{2.303RT} \qquad (1)$$

(This assumes additivity of partial volumes in a gaseous mixture.) Vapor-pressure data for *n*-octane and ethylbenzene were calculated by means of the Antoine equations by Weissberger et al. (*20*). The vapor-pressure data available for Cellosolve were presented in the literature (*2*) as graphs, which could not be read with sufficient accuracy; hence, vapor pressures for this compound were determined in the Colburn still. The Berthelot equation of state was used to calculate the second virial coefficients.

$$\beta = \frac{9RT_c}{128P_c} - \frac{27RT_c^3}{64P_cT^2} \qquad (2)$$

The critical properties for *n*-octane and ethylbenzene were obtained from the reviews of Kobe and Lynn (*7*) and those for cellosolve were estimated by the method of Lyderson (*10*). The liquid molal volumes for *n*-octane and ethylbenzene were estimated from the density-temperature data given by Rossini (*14*). Data for Cellosolve, which were not available in literature, were approximated by Hanson's method (*4*).

TABLE 2

EXPERIMENTAL VAPOR-LIQUID EQUILIBRIUM DATA AT 760 mm. Hg PRESSURE SYSTEM:

(1) *n*-octane–(3) Cellosolve

x_1	y_1	t, °C.	γ_1	γ_3
0.0100	0.0640	133.6	5.161	0.997
0.0240	0.1475	131.1	5.298	0.994
0.0375	0.2000	129.6	4.788	0.993
0.0535	0.2605	127.75	4.598	0.993
0.0775	0.3300	125.5	4.278	0.996
0.1075	0.3855	123.45	3.815	1.011
0.1575	0.4540	121.95	3.200	1.000
0.2230	0.4975	119.55	2.653	1.083
0.3020	0.5395	118.4	2.196	1.150
0.4010	0.5675	117.45	1.788	1.303
0.5250	0.6020	117.0	1.468	1.538
0.6510	0.6300	117.05	1.237	1.942
0.7475	0.6625	117.25	1.123	2.430
0.7790	0.6800	117.05	1.115	2.652
0.8800	0.7455	119.0	1.023	3.622
0.9475	0.8690	122.6	1.000	3.763

x_1 = mole fraction *n*-octane in liquid.
y_1 = mole fraction *n*-octane in vapor.
t°C. = temperature in °C.

TABLE 3

EXPERIMENTAL VAPOR-LIQUID EQUILIBRIUM DATA AT 760 mm. Hg PRESSURE SYSTEM:

(2) ethylbenzene–(3) Cellosolve

x_3	y_3	t, °C.	γ_3	γ_2
0.0460	0.1190	133.55	2.724	0.992
0.0950	0.2028	131.9	2.372	0.990
0.1650	0.2845	129.9	2.038	1.018
0.2345	0.3450	129.0	1.732	1.042
0.3345	0.4035	128.2	1.508	1.121
0.4675	0.4730	127.8	1.283	1.247
0.5160	0.4960	127.9	1.216	1.308
0.6040	0.5475	128.1	1.137	1.427
0.6715	0.5860	128.5	1.080	1.557
0.7470	0.6400	129.2	1.037	1.723
0.7580	0.6540	129.0	1.051	1.741
0.8540	0.7520	131.1	1.003	1.952
0.8825	0.7895	131.3	1.012	2.047
0.9385	0.8725	133.2	0.992	2.248
0.9705	0.9340	134.15	0.998	2.364

x_3 = mole fraction cellosolve in liquid.
y_3 = mole fraction cellosolve in vapor.
γ_2 = activity coefficient, ethylbenzene.

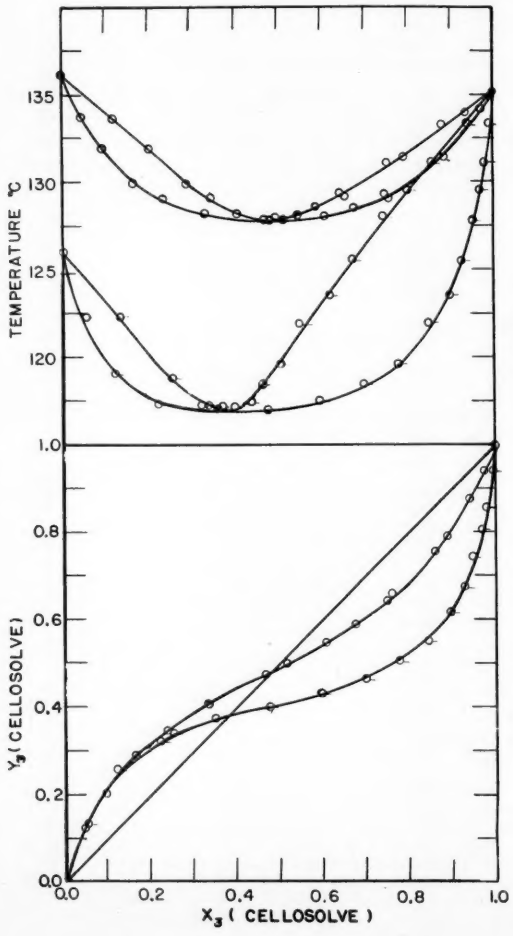

Fig. 2. Boiling-point and equilibrium diagrams: o, ethylbenzene-Cellosolve; o-, octane-Cellosolve.

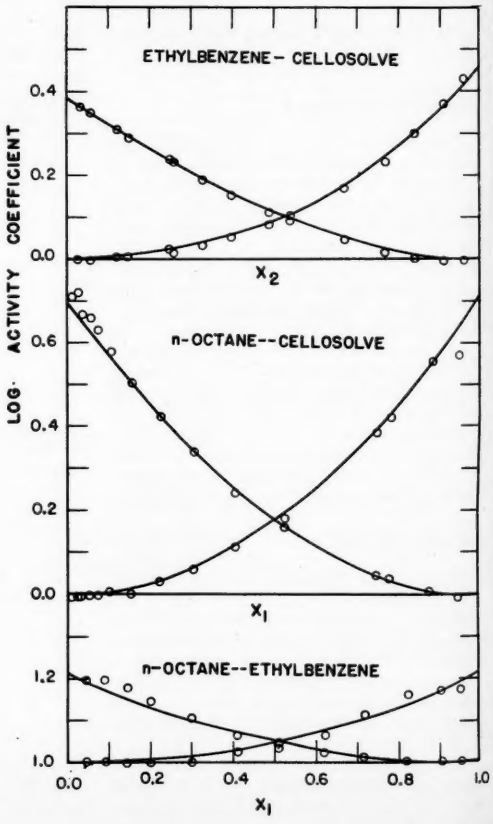

Fig. 3. Activity coefficients.

CORRELATIONS OF VAPOR-LIQUID EQUILIBRIUM DATA

The experimental activity-coefficient data for the binary systems were related by the Margules three-suffix equations modified by Wohl (*21*).

$$\log \gamma_1 = x_2^2[A + 2(B - A)x_1] \quad (3)$$

$$\log \gamma_2 = x_1^2[B + 2(A - B)x_2] \quad (4)$$

Therefore

$$\lim_{x_1 \to 0} \log \gamma_1 = A \quad (5)$$

and

$$\lim_{x_2 \to 0} \log \gamma_2 = B \quad (6)$$

The values for A and B were obtained by extrapolating the log-γ-vs.-x curves.

Wohl (*21*) developed Equation (7) as a means of representing ternary activity-coefficient data:

$$\begin{aligned}\log \gamma_1 = {} & x_2^2[A_{12} + 2x_1(A_{21} - A_{12})] \\ & + x_3^2[A_{13} + 2x_1(A_{31} - A_{13})] \\ & + x_2x_3[A_{21} + A_{13} - A_{32} \\ & + 2x_1(A_{31} - A_{13}) \quad (7) \\ & + 2x_3(A_{32} - A_{23}) - C(1 - 2x_1)]\end{aligned}$$

The rotation principle can be used to express the constants for the other two components. He (*22*) modified his original equations and developed Equation (8).

$$\begin{aligned}\log \gamma_1 = {} & x_2^2[A_{12} + 2x_1(A_{21} - A_{12})] \\ & + x_3^2[A_{13} + 2x_1(A_{31} - A_{13})] \\ & + x_2x_3[\tfrac{1}{2}(A_{21} + A_{12} + A_{31} \\ & + A_{13} - A_{23} - A_{32}) \\ & + x_1(A_{21} - A_{12} + A_{31} - A_{13}) \\ & + (x_2 - x_3)(A_{23} - A_{32}) \\ & - (1 - 2x_1)C^*] \quad (8)\end{aligned}$$

where the A's are the end values in log-γ-vs.-x plots of the component binary systems, and C and C^* are the ternary constants.

The relation between C and C^* was shown by Severens, Sesonske, Perry, and Pigford (*17*) to be

$$\begin{aligned}C^* = {} & C + \tfrac{1}{2}(A_{12} - A_{21} + A_{23} \\ & - A_{32} + A_{31} - A_{13}) \quad (9)\end{aligned}$$

Equation (8) was used to correlate the ternary vapor-liquid equilibrium data.

CORRELATIONS OF HEAT-OF-MIXING DATA

The heat-of-mixing data for binary systems were satisfactorily correlated by means of the empirical expressions of the type used by Scatchard et al. (*15*):

$$\begin{aligned}\Delta H_x^M = {} & x_1x_2[A_0 + A_1(x_1 - x_2) \\ & + A_2(x_1 - x_2)^2 + \cdots] \quad (10)\end{aligned}$$

The choice of the number of constants depends upon the accuracy of the experimental data and the dissymmetry of the system under investigation.

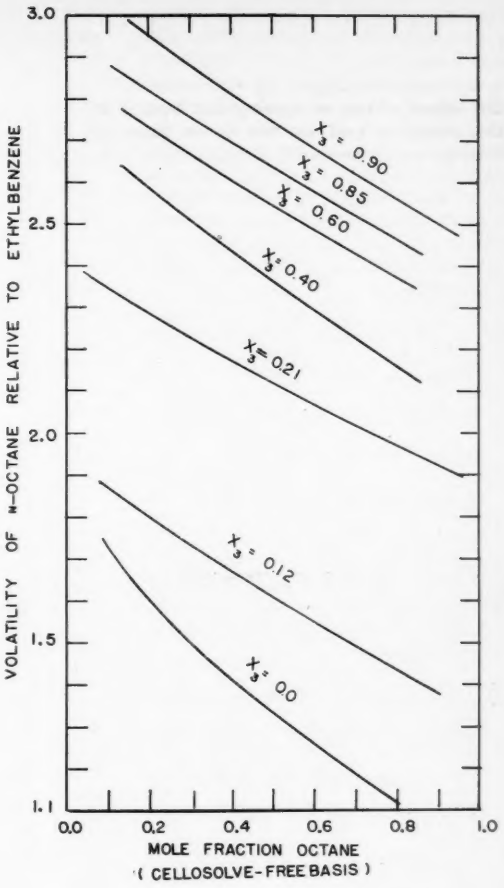

Fig. 4. Relative volatility. Parameter: mole fraction Cellosolve in ternary mixture.

It is desirable to predict the ternary heat-of-mixing data from the component binary heat-of-mixing data if possible. Based on free-energy analogy, Scatchard et al. proposed an equation of the type:

$$\begin{aligned}\Delta H_{x_{123}}{}^M = {} & x_1x_2[A_{0_{12}} + A_{1_{12}}(x_1 - x_2) \\ & + A_{2_{12}}(x_1 - x_2)^2 + \cdots] \\ & + x_1x_3[A_{0_{13}} + A_{1_{13}}(x_1 - x_3) \\ & + A_{2_{13}}(x_1 - x_3)^2 + \cdots] \\ & + x_2x_3[A_{0_{23}} + A_{1_{23}}(x_2 - x_3) \\ & + A_{2_{23}}(x_2 - x_3)^2 + \cdots] \quad (11)\end{aligned}$$

Equation (11) involved the assumption that the heat of mixing of a ternary mixture could be expressed as a sum of

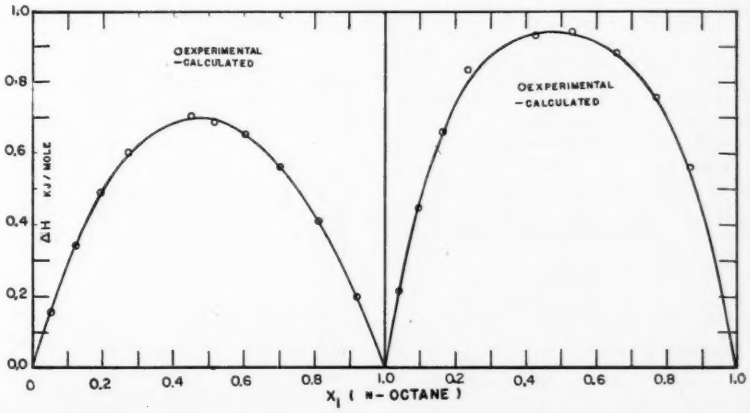

Fig. 5. Heat of mixing at 25°C., *n*-octane–ethylbenzene.

Fig. 6. Heat of mixing at 25°C., *n*-octane–Cellosolve.

the heats of mixing of the related binary systems. This is true only when the contribution from the triple interactions is very small or negligible. To account for the effect of one or more polar liquids in the mixture and at the same time to eliminate the necessity for a ternary constant, Scatchard et al. (*16*) proposed a form of Equation (12) in terms of volume fractions (Redlich and Kister (*13*) expressed it in terms of mole fraction) and found fairly good agreement with experimental data:

$$\Delta H_{x_{1_2}}{}^{M} = x_1x_2[A_{0_{1_2}} + A_{1_{1_2}}(x_1 - x_2) + A_{2_{1_2}}(x_1 - x_2)^2 + \cdots] + x_1x_3[A_{0_{1_3}} + A_{1_{1_3}}(1 - 2x_3) + A_{2_{1_3}}(1 - 2x_3)^2 + \cdots] + x_2x_3[A_{0_{2_3}} + A_{1_{2_3}}(1 - 2x_3) + A_{2_{2_3}}(1 - 2x_3)^2 + \cdots] \quad (12)$$

They also suggested that it might be advantageous to replace $(x_1 - x_2)$ by $(1 - 2x_2)$ for certain cases. This results in Equation (13):

$$\Delta H_{x_{1_2}}{}^{M} = x_1x_2[A_{0_{1_2}} + A_{1_{1_2}}(1 - 2x_2) + A_{2_{1_2}}(1 - 2x_2)^2 + \cdots] + x_1x_3[A_{0_{1_3}} + A_{1_{1_3}}(1 - 2x_3) + A_{2_{1_3}}(1 - 2x_3)^2 + \cdots] + x_2x_3[A_{0_{2_3}} + A_{1_{2_3}}(1 - 2x_3) + A_{2_{2_3}}(1 - 2x_3)^2 + \cdots] \quad (13)$$

Prediction of ternary heat-of-mixing data through binary data was attempted by use of Equations (11) and (13) and the following Equation (14):

$$\Delta H_{x_{1_2}}{}^{M} = x_1x_2[A_{0_{1_2}} + A_{1_{1_2}}(x_1 - x_2) + A_{2_{1_2}}(x_1 - x_2)^2 + \cdots] + x_1x_3[A_{0_{1_3}} + A_{1_{1_3}}(1 - 2x_3) + A_{2_{1_3}}(1 - 2x_3)^2 + \cdots] + x_2x_3[A_{0_{2_3}} + A_{1_{2_3}}(x_2 - x_3) + A_{2_{2_3}}(x_2 - x_3)^2 + \cdots] \quad (14)$$

When none of these equations adequately represent the ternary heat-of-mixing data, probably because of extreme dissymmetry of the system, it is necessary to introduce one or more ternary constants.

$$\Delta H_{x_{1_2}}{}^{M} = \text{Equation (11)} + Cx_1x_2x_3 \quad (15)$$

RESULTS AND DISCUSSION

Vapor-liquid Equilibria

The vapor-liquid equilibrium data of the binary and ternary systems are given in Tables 2 through 4 and the boiling-point diagrams and the equilibrium

TABLE 4

EXPERIMENTAL VAPOR-LIQUID—EQUILIBRIUM DATA AT 760 mm. HG PRESSURE SYSTEM:

(1) *n*-Octane–(2) ethylbenzene–(3) Cellosolve
Composition on Mole-fraction Basis

					(γ_1)		(γ_2)		(γ_3)	
t, °C.	x_1	x_2	y_1	y_2	Exp.	Calc.	Exp.	Calc.	Exp.	Calc.
125.35	0.4116	0.5061	0.4442	0.3753	1.089	1.077	1.0001	1.027	2.955	2.835
123.00	0.3289	0.4541	0.3835	0.3300	1.252	1.221	1.027	1.043	1.950	2.087
122.35	0.2515	0.3734	0.3386	0.2799	1.471	1.459	1.092	1.125	1.531	1.571
122.75	0.1673	0.2831	0.3071	0.2492	1.984	1.909	1.267	1.305	1.202	1.250
124.00	0.1218	0.2120	0.2642	0.2119	2.267	2.369	1.387	1.486	1.234	1.127
125.25	0.0786	0.1483	0.2250	0.1797	2.896	2.947	1.623	1.711	1.055	1.055
128.15	0.0448	0.0985	0.1711	0.1389	3.581	3.562	1.729	1.935	1.003	1.021
130.70	0.0230	0.0529	0.1094	0.0904	4.179	4.168	1.972	2.147	1.000	1.006
123.7	0.4724	0.4046	0.4866	0.2872	1.086	1.102	1.005	1.037	2.652	2.702
122.0	0.4154	0.3738	0.4470	0.2603	1.187	1.180	1.039	1.045	2.115	2.205
121.3	0.3137	0.2984	0.4007	0.2200	1.436	1.436	1.109	1.127	1.525	1.585
121.8	0.2158	0.2296	0.3609	0.1905	1.854	1.865	1.232	1.295	1.243	1.264
123.2	0.1411	0.1698	0.3208	0.1670	2.428	2.417	1.400	1.513	1.093	1.116
125.5	0.0791	0.1163	0.2663	0.1443	3.389	3.119	1.646	1.777	1.005	1.042
127.7	0.0481	0.0732	0.2012	0.1083	3.967	3.707	1.856	1.989	1.000	1.017
130.4	0.0264	0.0429	0.1347	0.0751	4.513	4.397	2.041	2.162	0.969	1.003
122.2	0.5639	0.3997	0.5492	0.2160	1.063	1.079	1.032	1.050	2.360	2.831
120.7	0.4917	0.2735	0.4965	0.1060	1.154	1.171	1.049	1.056	2.156	2.199
120.1	0.3695	0.2229	0.4559	0.1630	1.430	1.429	1.140	1.135	1.523	1.583
120.7	0.2486	0.1718	0.4132	0.1433	1.899	1.892	1.283	1.314	1.220	1.249
122.1	0.1638	0.1256	0.3603	0.1242	2.419	2.461	1.454	1.536	1.104	1.107
124.1	0.1008	0.0874	0.3037	0.1051	3.141	3.102	1.668	1.776	1.037	1.043
121.3	0.6636	0.2022	0.6201	0.1454	1.050	1.061	1.082	1.069	2.730	2.974
119.7	0.6072	0.1928	0.5562	0.1267	1.077	1.110	1.037	1.065	2.619	2.508
119.2	0.4443	0.1494	0.5036	0.1037	1.349	1.399	1.157	1.132	1.566	1.640
119.85	0.2918	0.1118	0.4575	0.0945	1.833	1.884	1.327	1.320	1.234	1.248
121.35	0.1845	0.0798	0.4016	0.0815	2.440	2.530	1.534	1.466	1.097	1.097
123.75	0.1067	0.0541	0.3420	0.0683	3.370	3.247	1.795	1.833	1.016	1.034
126.8	0.0625	0.0341	0.2544	0.0525	3.951	3.837	1.977	2.039	1.000	1.012
120.1	0.7366	0.1186	0.6496	0.0897	1.024	1.052	1.174	1.084	2.928	3.043
118.65	0.6519	0.1084	0.6002	0.0754	1.113	1.124	1.127	1.074	2.304	2.393
118.2	0.4866	0.0875	0.5497	0.0679	1.383	1.374	1.274	1.138	1.461	1.631
118.85	0.3338	0.0662	0.5065	0.0563	1.824	1.843	1.370	1.310	1.237	1.259
120.75	0.2006	0.0463	0.4460	0.0490	2.535	2.566	1.611	1.585	1.068	1.069
123.2	0.1254	0.0317	0.3763	0.0413	3.204	3.212	1.850	1.823	1.011	1.035
119.65	0.8267	0.0528	0.7265	0.0303	1.031	1.029	1.167	1.111	3.198	3.418
117.75	0.6963	0.0464	0.6344	0.0320	1.129	1.122	1.147	1.083	2.291	2.384
117.5	0.5284	0.0367	0.5756	0.0286	1.361	1.368	1.306	1.141	1.624	1.645
125.5	0.0769	0.4675	0.1437	0.4090	1.877	1.769	1.160	1.225	1.334	1.336
124.25	0.1241	0.4759	0.2146	0.3765	1.796	1.603	1.09	1.163	1.447	1.449
122.9	0.2115	0.4014	0.3011	0.3134	1.532	1.514	1.117	1.142	1.474	1.564
118.65	0.5119	0.1289	0.5440	0.0919	1.284	1.320	1.155	1.102	1.735	1.814
119.9	0.4711	0.2309	0.4961	0.1601	1.230	1.238	1.081	1.076	1.884	1.952
121.5	0.4100	0.3341	0.4492	0.2366	1.224	1.221	1.054	1.058	1.904	2.030
126.45	0.3092	0.5918	0.3623	0.4555	1.150	1.142	1.007	1.017	2.394	2.598
124.4	0.2558	0.5569	0.3177	0.3923	1.234	1.257	1.001	1.043	1.858	1.996
123.3	0.1982	0.4351	0.2834	0.3493	1.522	1.483	1.140	1.125	1.476	1.556
123.1	0.1367	0.3347	0.2510	0.2964	1.966	1.889	1.260	1.289	1.254	1.263
124.65	0.0905	0.2458	0.2193	0.2589	2.493	2.409	1.435	1.499	1.098	1.120
126.4	0.0668	0.1783	0.1775	0.2148	2.604	2.880	1.564	1.682	1.060	1.061
128.5	0.0350	0.1083	0.1393	0.1686	3.696	3.596	1.905	1.953	1.000	1.061
127.0	0.2227	0.6507	0.2762	0.5045	1.198	1.192	1.000	1.017	2.234	2.360
125.6	0.1914	0.4860	0.2485	0.4515	1.266	1.293	1.033	1.045	1.826	1.941
124.4	0.1490	0.4962	0.2228	0.3896	1.547	1.497	1.043	1.123	1.541	1.554
124.65	0.1029	0.3844	0.1970	0.3441	1.967	1.898	1.222	1.283	1.244	1.269
125.7	0.0680	0.2794	0.1706	0.3101	2.503	2.405	1.469	1.493	1.074	1.123
127.0	0.0455	0.2036	0.1422	0.2483	3.017	2.912	1.561	1.690	1.046	1.059
128.8	0.0262	0.1234	0.1092	0.1934	3.841	3.582	1.956	1.938	0.9982	1.020
128.6	0.1441	0.7429	0.1978	0.5966	1.224	1.217	0.988	1.012	2.224	2.344
126.9	0.1300	0.6769	0.1771	0.5315	1.351	1.299	1.006	1.036	1.942	1.986
125.5	0.0936	0.5411	0.1547	0.4453	1.661	1.563	1.098	1.139	1.487	1.490
125.7	0.0720	0.4571	0.1422	0.4123	1.979	1.812	1.197	1.243	1.274	1.312
126.2	0.0517	0.3346	0.1245	0.3590	2.373	2.282	1.400	1.438	1.116	1.150
127.45	0.0350	0.2510	0.1021	0.2964	2.784	2.799	1.548	1.642	1.060	1.070
129.30	0.0193	0.1534	0.0788	0.2366	3.714	3.446	1.854	1.887	1.000	1.026
130.8	0.0680	0.8400	0.0984	0.7391	1.259	1.240	1.000	1.008	2.014	2.370
128.55	0.0568	0.7600	0.0833	0.6254	1.354	1.328	1.000	1.056	1.95	1.971
127.2	0.0440	0.6405	0.0753	0.5593	1.641	1.517	1.106	1.110	1.487	1.579
126.75	0.0331	0.5191	0.0662	0.4927	1.948	1.802	1.219	1.231	1.281	1.328
127.45	0.0227	0.3763	0.0558	0.4139	2.342	2.296	1.400	1.436	1.105	1.151
128.3	0.0121	0.2408	0.0447	0.3336	3.438	2.983	1.732	1.710	1.02	1.055

curves for the two binary systems studied in this work are shown in Figure 2. The activity coefficients calculated from the experimental data of the three binary systems are shown in Figure 3, in which the solid curve represents the values calculated by means of Wohl's three-suffix Margules equations.

n-Octane–ethylbenzene System

Data on this system at various pressures were reported by Yang and Van Winkle (*23*). No attempt was made to rerun these data as they are thermodynamically consistent and are available at the pressure required for this work. Yang and Van Winkle found that the van Laar equation fits the data more closely than the Margules or Redlich and Kister equations. However, for reasons explained earlier, the activity-coefficient data were again fitted by Wohl's three-suffix Margules equations, and it was observed that the variation of activity coefficients is symmetrical with respect to composition.

n-Octane–Cellosolve System

Data on this system were not reported in the literature. The experimental data at 760 mm. Hg total pressure show that the system is both nonideal and azeotropic in its behavior. The azeotropic conditions with regard to temperature and pressure were established by distilling a mixture of the two components of approximately the same composition as the azeotrope in a 4-ft. glass column packed with ¼-in. glass helices with a reflux ratio of approximately 20:1. The fraction boiling at constant temperature was collected and the distillation was repeated with this heart cut. A heart cut of this distillate was analyzed by means of density and found to have the following composition:

Total pressure	Temperature, °C.	Mole % *n*-octane	Density$^{25/4}$
650 mm. Hg	116.1	60.9	0.75922

Lecat's data (*9*) as reported by Horsley (*5*) show good agreement with respect to temperature (116°C.) but the composition (38% Cellosolve on weight basis) as reported by them does not seem to be correct. Streiff et al. (*18*) gave the composition as approximately equal to 28 wt. % Cellosolve but did not report the temperature.

Ethylbenzene–Cellosolve System

Vapor-liquid equilibrium data on this system were reported by Kieffer and Grabiel (*8*) at 735 mm. Hg total pressure; however, they did not report the equilibrium temperatures. Although methods are available (*3*) for the calculation of equilibrium temperature from a knowledge of *x-y* relations in binary systems, it was not done in this case either, as the total pressure of the present work was 760 instead of the 735 mm. Hg at which the data were reported. In order that accurate prediction of ternary data may be made, the method should be based upon the equilibrium measurements of the binary systems under the same conditions.

Table 5
Heat of Mixing—Binary Systems

(1) *n*-Octane–(2) ethylbenzene		(1) *n*-octane–(3) Cellosolve		(2) ethylbenzene–(3) Cellosolve	
x_1	ΔH_x^M, kjoules./mole	x_1	ΔH_x^M, kjoules./mole	x_2	ΔH_x^M, kjoules./mole
0.9210	0.2031	0.8663	0.5660	0.9120	0.3508
0.8085	0.4109	0.7684	0.7582	0.7826	0.5715
0.6985	0.5637	0.6521	0.8850	0.6604	0.6140
0.6007	0.6580	0.5297	9.9445	0.5318	0.5610
0.5143	0.6908	0.4235	0.9349	0.3911	0.4472
0.4505	0.7089	0.2387	0.8374	0.2962	0.3510
0.2703	0.6082	0.1616	0.6612	0.2121	0.2502
0.1922	0.4944	0.0956	0.4493	0.1252	0.1484
0.1262	0.3403	0.0391	0.2163	0.0636	0.0610

x_1 = mole fraction *n*-octane.
x_2 = mole fraction ethylbenzene.

Table 6
Experimental and Calculated Heat of Mixing at 25°C. System:

(1) *n*-octane–(2) ethylbenzene–(3) Cellosolve
Heat of Mixing in kilojoules/Mole

x_1	x_2	Exp.	Eq. (14)	Eq. (15)
0.0217	0.0263	0.1534	0.1662	0.1671
0.0593	0.0721	0.3996	0.3610	0.3671
0.2908	0.3536	1.0976	1.0258	1.0695
0.2378	0.2891	1.0036	0.9434	0.9891
0.0472	0.4335	0.6448	0.6435	0.6554
0.1264	0.3975	0.8368	0.8297	0.8432
0.2095	0.3597	0.9731	0.9101	0.9731
0.2884	0.3238	1.0595	0.9786	1.0465
0.3755	0.2841	1.100	1.0409	1.0747
0.4341	0.0698	0.9678	0.9688	0.9878
0.3817	0.1836	1.0138	1.0087	1.0408
0.2878	0.3844	0.9966	1.0204	1.052
0.1704	0.6355	0.8680	0.8603	0.8728
0.1192	0.7449	0.7187	0.6984	0.7040
0.0770	0.8353	0.5231	0.5115	0.5152
0.0308	0.9341	0.2610	0.2307	0.2297

x_1 = mole fraction *n*-octane.
x_2 = mole fraction ethylbenzene.

The system is nonideal and azeotropic in character. The azeotropic conditions were established as follows, in the manner described above:

Total pressure	Temp., °C.	Mole % ethylbenzene	Ref. index
Present work, 755 mm. Hg	127.1	52.3	1.45366
Kieffer and Grabiel, 735 mm. Hg	126.2	52.6	1.4581

n-Octane–ethylbenzene–Cellosolve System

About seventy-four runs were made to describe the vapor-liquid relationships of the ternary system at 760 mm. Hg Wohl's three-suffix Margules equations were used to correlate the ternary data. The values of the binary constants calculated from experimental data are given in Table 7. The calculated values of γ_1, γ_2, and γ_3 along with the experimental data are presented in Table 4. By Equa-

Table 7
Constants for Vapor-liquid Equilibrium and Heat of Mixing Equations

System	Margules equations: Binary	Margules equations: Ternary	Heat-of-mixing equations: Binary	Heat-of-mixing equations: Ternary
1–2	$A_{12} = 0.085$ $A_{21} = 0.085$	—	$A_{0_{1,2}} = 2.8067$ $A_{1_{1,2}} = -0.2864$ $A_{2_{1,2}} = 0.2219$	
1–3	$A_{13} = 0.700$ $A_{31} = 0.715$	—	$A_{0_{1,3}} = 3.7453$ $A_{1_{1,3}} = -0.1490$ $A_{2_{1,3}} = 2.2270$	
2–3	$A_{23} = 0.385$ $A_{32} = 0.455$	—	$A_{0_{2,3}} = 2.1780$ $A_{1_{2,3}} = 1.6497$ $A_{2_{2,3}} = 0.4239$	
1–2–3	—	$C = 0$* $C^* = 0.0275$	—	$C = 2.69$ —

(1) = *n*-Octane.
(2) = Ethylbenzene.
(3) = Cellosolve.
*Assumed for calculations.

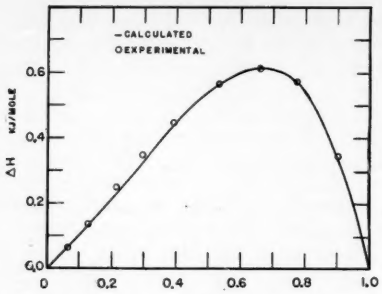

Fig. 7. Heat of mixing at 25°C., ethylbenzene-Cellosolve.

tion (9), on the assumption that $C = 0$ and that for the *n*-octane–ethylbenzene system $A_{12} = A_{21}$,

$$C^* = -0.0275$$

Carlson found the assumption that $C^* = 0$ was satisfactory for many of the systems which he had inspected whose deviations from ideal behavior were either zero or uniformly positive. Severens, Sesonske, Perry, and Pigford (*17*) also supported this view from their experimental results on acetone-methylacetate-methanol and acetone–carbon tetrachloride–methanol systems at 50°C. In the latter system a value of $C^* = -0.16$ was found. A value of $C^* = -0.0275$ from this investigation of the ternary *n*-octane–ethylbenzene–Cellosolve also supports the view. It is difficult to generalize, however, since in the case of the benzene–cyclohexane–methyl Cellosolve system reported by Thoronton and Garner (*19*) the value for C^* was calculated by them (*19*) from the binary to be -1.582. This value is far from zero and contributes greatly to the calculated ternary-activity-coefficient values.

The value or C^* found in this work was small, but it was retained to improve the accuracy of the fit of the data. The average deviations in γ_1, γ_2, and γ_3 respectively are 2.75, 3.79, and 3.18%.

Values of relative volatilities were calculated and smoothed graphically for constant percentage of Cellosolve content. These values were compared with those for the binary system *n*-octane–ethylbenzene reported by Yang and Van Winkle (*23*) and are shown in Figure 4. It is interesting to note that the relative volatility of *n*-octane with respect to ethylbenzene is greatly improved by the presence of cellosolve and this becomes more pronounced as the concentration of the latter increases in the liquid mixture.

There is no evidence of a ternary azeotrope in spite of the azeotropic tendency in the *n*-octane–ethylbenzene binary and of actual azeotropes in the other two binaries. This was confirmed by distilling a mixture of the three components in the column mentioned before and collecting the heart cuts at each constant boiling point. These fractions were analyzed and found to correspond in composition to the binary azeotropes of *n*-octane–Cellosolve and ethylbenzene-Cellosolve systems respectively. Further confirmation was obtained by the analysis of the residual liquids after extraction with distilled water. The analyses showed that the residual liquids were pure *n*-octane and pure ethylbenzene respectively. Hence there is no ternary azeotrope.

Heat of Mixing

The experimental heat-of-mixing data at 25°C. for the three binaries and the ternary systems are given in Tables 5 and 6. The binary data were fitted with Equation (10) and the constants, evaluated by the method of least squares, are listed in Table 7. The fit of the data was examined graphically in Figures 5, 6, and 7 and found to be satisfactory. The correlation of the ternary data was tried with Equations (11), (13), (14), and (15) and the agreement of experimental and calculated values was found to be best where Equation (14) was used. Calculated values from Equations (14) and (15) are shown in Table 6. It was observed that Equations (11) and (13) do not fit the data so well as Equations (14) and (15); however, application of Equation (15) is limited because a knowledge of the ternary data is required for calculation of the constant C.

ACKNOWLEDGMENT

This work was done while P. S. Murti held the Jefferson Chemical Company Fellowship during the years 1953 to 1955, and this opportunity is taken to acknowledge the assistance rendered by the Jefferson Chemical Company. The authors wish to express their appreciation to Surinder P. Vohra for his assistance in the preparation of the graphs.

NOTATION

A, B = Margules constants as expressed by Wohl
A_0, A_1 = constants in heat-of-mixing equation
C = ternary constant in activity-coefficient expressions of Wohl (*21*), also ternary constant in heat-of-mixing equation
C^* = ternary constant in activity-coefficient expressions of Wohl (*22*)
d = density of the liquid, g./ml.
g = interaction constants
$\Delta H_z{}^M$ = heat of mixing in kilojoules/mole of the mixture
P_T = total pressure
P_1 = vapor pressure of component 1
P_c = critical pressure
R = gas constant
T = absolute temperature
V_{11} = molal volume of component 1 in pure liquid state
x = mole fraction in the liquid
y = mole fraction in vapor

Greek Letters

γ = activity coefficient
β = second virial coefficient

Subscripts

1 or 11 = component 1
12 etc. = the mixture of 1 and 2 components
123 = the mixture of the three components 1, 2, and 3
311 = a single molecule of 3 with two molecules of 1

LITERATURE CITED

1. Carlson, C. S., A. E. Schubert, and M. R. Fenske, *Ind. Eng. Chem., Anal. Ed.*, **18**, 109 (1946).
2. Carbide and Carbon Chemicals Corporation, "Solvents-Glycol Ethers," p. 17 (1954).
3. Gilmont, Roger, E. A. Weinman, Franklin Kramer, Eugene Miller, Frank Hashmal and D. F. Othmer, *Ind. Eng. Chem.*, **42**, 120 (1950).
4. Hanson, E. S., *ibid.*, **41**, 96 (1949).
5. Horsley, L. H., and co-workers, "Azeotropic Data," Advances in Chemistry Series, American Chemical Society, Washington (1952).
6. Jones, C. A., E. M. Schoenborn, and A. P. Colburn, *Ind. Eng. Chem.*, **35**, 666 (1943).
7. Kobe, K. A., and R. E. Lynn, Jr., *Chem. Rev.*, **52**, 117 (1953).
8. Kieffer, W. F., and E. E. Grabiel, *Ind. Eng. Chem.*, **43**, 973 (1951).
9. Lecat, Maurice, *Compt. Rend.*, **217**, 733, 882, 1488 (1943).
10. Lyderson, A. L., Rept. 3, Engineering Experiment Station, Univ. Wisconsin (April, 1955).
11. Murti, P. S., Ph.D. dissertation, Univ. of Texas (1956).
12. *Ibid.*
13. Redlich, Otto, and A. T. Kister, *ibid.*, **40**, 341 (1948).
14. Rossini, F. D., *et al.*, *A. P. I. Project* 44, Carnegie Institute of Technology, Pittsburgh, Pennsylvania (1953).
15. Scatchard, George, L. B. Ticknor, J. R. Goates, and E. R. McCartney, *J. Am. Chem. Soc.*, **74**, 3721 (1952).
16. Scatchard, George, S. E. Wood, and J. M. Mochel, *ibid.*, **62**, 712 (1940).
17. Severns, W. H., Jr., A. Sesonske, R. H. Perry, and R. L. Pigford, *A.I.Ch.E. Journal*, **1**, 401 (1955).
18. Streiff, A. J., *et al.*, paper presented before the Div. of Petroleum Chemistry, 110 meeting Am. Chem. Soc., Chicago (1946), referred in *5*.
19. Thoronton, J. D., and F. H. Garner, *J. Applied Chem. (London)*, **1**, suppl. No. 1, s-61 (1951).
20. Weissberger, Arnold, E. S. Proskaner. J. A. Riddick, and E. E. Toops, Jr., ed., "Organic Solvents," Interscience Publishers, Inc., New York (1955).
21. Wohl, Kurt, *Trans. Am. Inst. Chem. Engrs.*, **42**, 215 (1946).
22. ———, *Chem. Eng. Progr.*, **49**, 218 (1953).
23. Yang, C. P., and Matthew Van Winkle, *Ind. Eng. Chem.*, **47**, 293 (1955).

Thermal Resistance of an Eddy

L. G. CLARK and W. W. HAGERTY

University of Delaware, Newark, Delaware

By experimental means a relation is obtained between the thermal resistance of an eddy and its angular momentum. The eddy is stationary, and no extraneous motion is present. The secondary motion which may develop in the annulus between concentric rotating cylinders is used to obtain the eddies. The fluid motion is well defined at all times and at all points of space. Heat is passed through the eddies, and the Nusselt number is obtained, which varies linearly with the angular momentum. Both Nusselt number and angular momentum vary linearly with the peripheral velocity of the inner rotating cylinder, which can be interpreted in terms of a Reynolds number associated with fluid flow perpendicular to a cylinder.

In the field of heat transfer one often speaks of eddies or secondary fluid motion and of the effect of such motion on the heat transfer coefficient of a system. There are many data which show the over-all effect of secondary eddies, but such motion is usually accompanied by other types of flow. There is relatively little, if any, published information bearing on the heat transfer coefficient of a single eddy. It was decided therefore to study the heat transfer characteristics of an eddy of known motion and to compare the heat transferred by the eddy owing to its angular momentum.

The first problem is to obtain an eddy which is free from extraneous motion. This is done by utilizing the secondary motion formed when a fluid is contained in the annulus of two concentric cylinders and the inner one is rotated above some critical speed. Figure 1 is a schematic drawing of the system in which the curved arrow indicates the secondary motion.

The critical angular velocity of the inner cylinder above which the secondary motion appeared was shown by Taylor (*1*) to be

$$\omega_{cr}^{\ 2} = \frac{\nu^2\pi^4(R_1 + R_2)}{2P(R_2 - R_1)^3R_1^{\ 2}}$$

where P = constant depending on the geometry.

At cylinder speeds above this value, fluid particles no longer travel in concentric circles about the axis of rotation but travel in spirals while progressing around the annulus. Figure 2 is a photograph of this secondary motion where the cross-sectional picture is taken as indicated in Figure 3. The secondary motion is of an eddy type where the eddies occur in counterrotating pairs along the annulus. In the system that is presented the length and thickness of the annulus are chosen so that the eddy cells are square. The eddies so formed are stable at speeds substantially above the critical speed. As the speed of the inner cylinder increases, the secondary velocities in the individual eddies increase. It was shown by Hagerty (*2*) and later verified in this work that the general shape of the eddies persists for an appreciable range of higher speeds. The fact that the general form does not change materially simplifies computation of the angular momentum.

In the resulting motion the paths of the fluid particles are clearly defined at all points of the space; therefore no distinction is necessary between the region near the boundary (boundary layer) and the region near the center of the annulus. The heat transfer characteristics of the entire region are compared with the angular momentum of the fluid about an axis tangential to the cylinders.

ANGULAR MOMENTUM

The first step is to measure the angular momentum of the eddies. This is done by the use of motion pictures, as shown in Figure 3, which illustrates the method by which the pictures were taken for different speeds of the inner cylinder. The angular momentum in this case is obtained from the motion relative to an axis perpendicular to the plane of the eddy. This method is equivalent to assuming a two-dimensional or plane motion, which is best approximated if the annulus thickness is small compared with the cylinder radius. Taylor (*1*) showed that at instability the form of the eddies can be represented by the stream function

$$\Psi = f(x)\cos\frac{\pi y}{d} \qquad (1)$$

where y is the coordinate measured parallel to the axis of rotation of the inner cylinder and x is measured in the radial direction (Figure 4).

Then

$$u = -\frac{\partial\Psi}{\partial y}; \qquad v = \frac{\partial\Psi}{\partial x} \qquad (2)$$

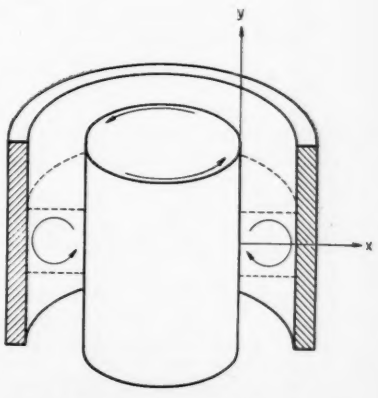

Fig. 1. Idealized representation of system showing secondary eddy motion.

The velocities u and v and the coordinates x and y are defined in Figure 4. If the eddies retain this general shape at speeds above the critical one needs only to determine v at $y = 0$ experimentally to obtain a complete equation for Ψ. If the x axis passes through the center of the eddy, then $v_{y=0} = (\partial\Psi/\partial x)_{y=0} = \partial f/\partial x$ and $u_{y=0} = 0$ and so v need be measured only along the x axis. It was found that the eddies did retain their general form for the range of speeds considered.

Motion pictures are taken at four different speeds above the critical. The values of $v_{y=0}$ are obtained by projecting the pictures on a grid and studying the motion of entrained aluminum filings, frame by frame. The velocity curves are obtained for speeds of 20.0, 26.1, 33.7, and 46.3 rev./min. Figure 5 shows the resulting velocity profile for a speed of 20.0 rev./min.

The values of v from Figure 5 do not satisfy continuity for plane motion, and to allow for the curvature of the cylinders a small correction must be made (see Figure 6) by multiplying each curve by

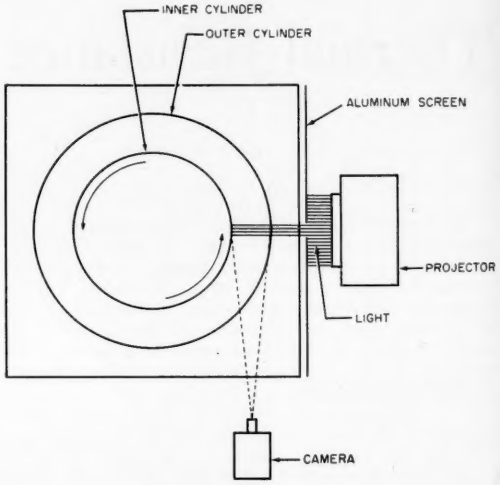

Fig. 3. Arrangement for photographing motion within eddies.

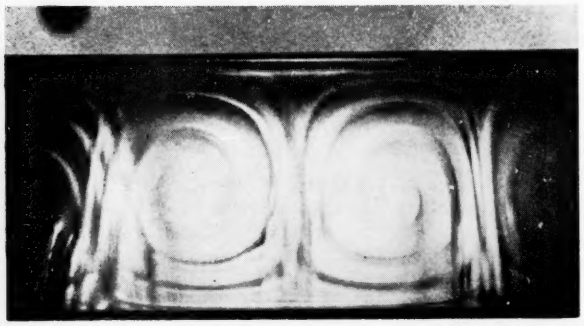

Fig. 2. Cross section of eddies formed between concentric rotating cylinders.

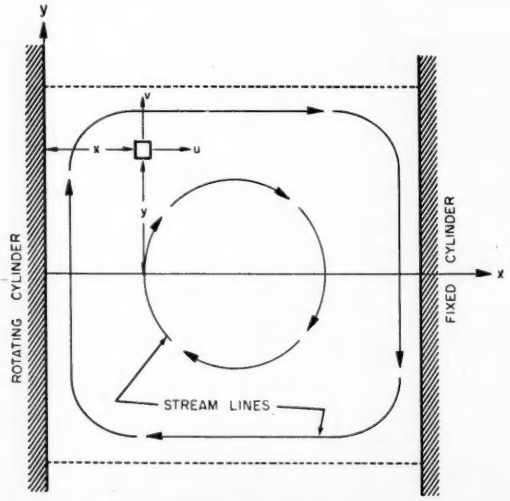

Fig. 4. Coordinates used to describe motion of the eddy.

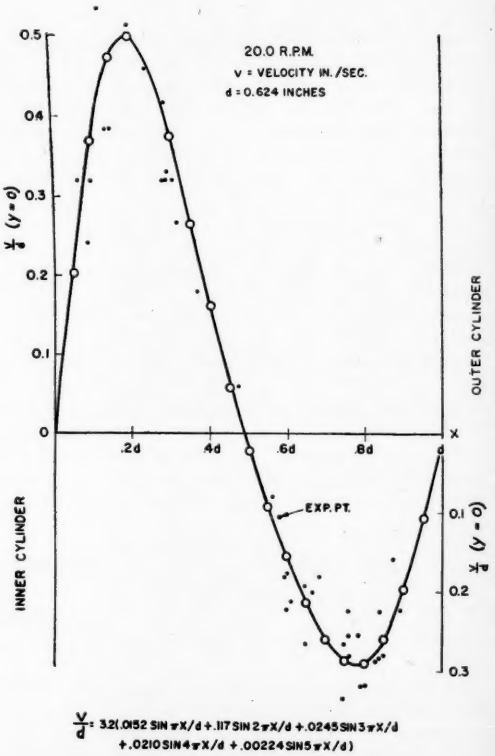

Fig. 5. Typical velocity profile across the section of an eddy.

$[1 + (x_1/R_1)]$ where R_1 is the radius of the inner cylinder.

The resulting corrected velocity curves for the four cylinder speeds are shown in Figure 7. It should be noted that the mass could have been corrected in this way instead of the velocity without producing any effect on the angular momentum. The velocity was changed so as to give better visual comparison with a plane eddy.

The experimental-data curves are now approximated by a harmonic analysis, and values of u and v are obtained. As an example the velocities at a speed of 20.0 rev./min. can be written as

$$u = d \sin(\pi y/d)\,[0.2286 - 0.211 \cos(2\pi x)/d - 0.018 \cos(4\pi x)/d + 0.0004 \cos(6\pi x)/d] \quad (3)$$

$$v = d \cos(\pi y)/d\,[0.44 \sin(2\pi x)/d + 0.072 \sin(4\pi x)/d - 0.0024 \sin(6\pi x)/d]$$

The angular momentum per foot of eddy is written as (see Figure 4) angular momentum

$$= \int_R (uy - vx)\rho\, dxdy \quad (4)$$

where R is the region of one eddy one unit long.

By use of the values from Equations (3), Equation (4) can be written in the form angular momentum $= 2(\rho d^4)/(\pi^2)H$ (1 unit of eddy) (5)

where H is a number depending on the velocity distribution in the eddy and has the unit of time. When the velocities at all speeds are used in Equation (4), Figure 8 then shows the plotted values of the angular-momentum number against n, the speed of the inner cylinder in revolutions per minute. The value of H at $n = 46.3$ may not be accurate owing to difficulties in measurement at this speed. The curve of Figure 8 gives slightly high values because of dynamic dissimilarity between the optical system and the thermal system that is to be used. The proper correction gives the lower dotted line. This correction is based on the assumption that the rate of increase of angular momentum with cylinder speed is the same for a critical speed of 17.5 rev./min. as it is for a critical speed of 14 rev./min. The curve shows the linear relationship between the angular momentum and the cylinder speed for speeds not too far above critical. It is assumed that the heat transfer coefficient varies linearly with the revolutions per minute of the rotating cylinder. If there is an analogy between heat transfer and momentum transfer and if the rate of momentum transfer in this case can be expressed as an angular momentum, then the heat transfer coefficient of the eddies, h_c, and H should vary in the same manner with a change in revolutions per minute.

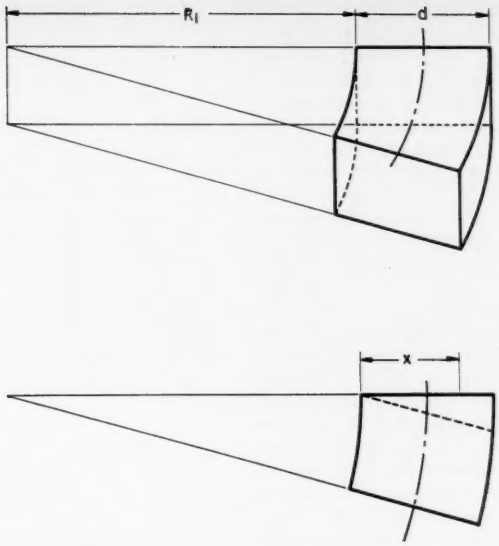

Fig. 6. Effect of curvature on geometry of the system.

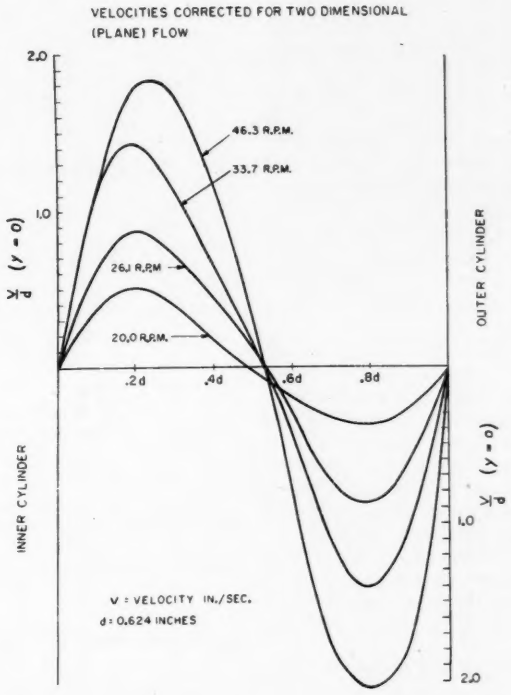

Fig. 7. Velocity distributions as corrected for the effect of curvature of the cylinder walls.

HEAT TRANSFER COEFFICIENT

The next step is to measure the heat transferred across the eddies in the annulus for different rotational speeds of the cylinder and consequently for different speeds of the eddies. These measurements are done in a system which is dynamically and geometrically the same as that used for the motion picture study. The velocity components of the fluid tangential to the cylinders do not affect the heat transferred. Thus if the annulus thickness is small compared

with other dimensions the problem is nearly that of heat transfer through a two-dimensional eddy. In the system described the inner cylinder is heated by an electric heating coil to some given temperature (140° to 150°F.) and the outer cylinder is maintained at a fixed temperature (about 140°F.) by means of a water jacket. By computing the heat loss, measuring the temperatures of the inner cylinder and the bulk water, and measuring the power input to the heating coil, the heat transfer coefficient of the system may be found (*3*). When the thermal resistance of the cylinders, the end corrections, and the cooling water are taken into account, the heat transfer coefficient for the eddies alone may be obtained. This procedure is carried out for speeds of the inner cylinder as high as twice the critical speed. It is found that the heat transferred increased linearly with the speed of the inner cylinder.

In the determination of the heat transfer coefficient the annulus is $\frac{5}{8}$ in. thick, the inner diameter is 4.235 in., and the length is 12 in. It is also noted that the thickness of the annulus is small compared with the other dimensions, and so the secondary motion can be considered as plane motion. The fluid used is Univis J-58 (hydraulic oil), which has the property of a high-viscosity index and a kinematic viscosity of 0.185×10^{-3} sq. ft./sec. for the temperatures considered. With this fluid the critical speed at which eddies form is about 17.5 rev./min. This accounts for the required correction of Figure 8. The fluid temperatures are maintained within $\pm 10°$ of 145°F.

Figure 9 is the plot of the total heat transferred, h_tA, against the rotational speed of the inner cylinder. h_t is the heat transfer coefficient after end effects are eliminated and A is a cylindrical area taken at the mean radius of the annulus. The temperature difference is taken between the inner surface of the inner cylinder and the bulk temperature of the water in the cooling jacket. The lower dotted line represents the h_tA if pure conduction were the only means of heat transfer. The equation

$$h_tA = \frac{20.2(-146.5 + 9.05n)}{-126.3 + 9.04n} \qquad (6)$$

is an approximate equation of the curve for speeds above 17.5 rev./min. The method of obtaining this expression for h_tA will be developed later. The values of h_tA include the effects of the brass cylinders and the cooling water. However, from the equation for speeds above 17.5 rev./min. it is seen that, as the speed n becomes great, h_t approaches the value of 20.2 B.t.u./(hr.)(°F.).

The method of obtaining an equation like (6) is well known, i.e., the "Wilson plot" to find effects of boundaries, etc.

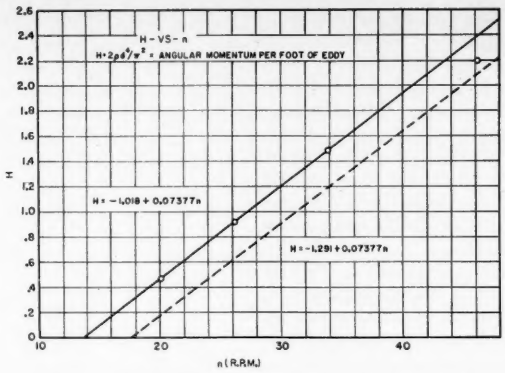

Fig. 8. Angular momentum per foot of eddy vs. rotational speed of inner cylinder.

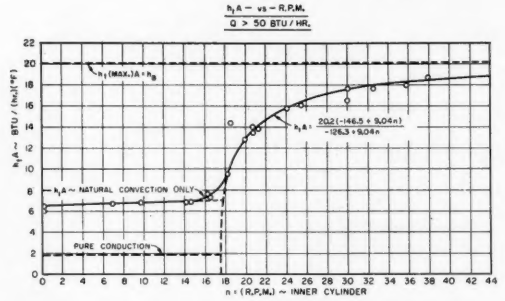

Fig. 9. Total heat transformed vs. rotational speed of the inner cylinder.

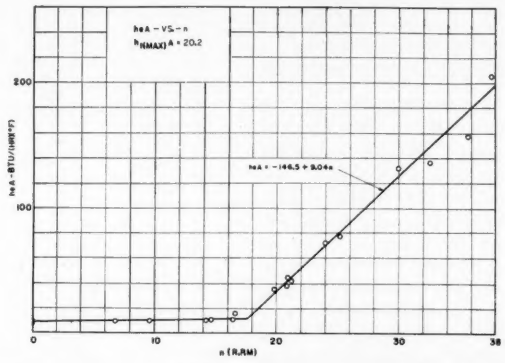

Fig. 10. Heat transfer coefficient for eddies only vs. rotational speed of the inner cylinder.

In the present case, however, the method and reasoning are somewhat different from usual and should be presented. If it is assumed that the thermal resistance of the eddies approaches zero at very high speeds, $h_t\ A_{(max)} = 20.2$ is the heat transfer coefficient of the cylinders and cooling water alone. Defining h_eA as the special heat transfer coefficient of the eddies only ($h_eA = \Delta Q/\Delta T$) gives

$$\frac{1}{h_eA} = \frac{1}{h_tA} - \frac{1}{h_tA_{(max)}} \qquad (7)$$

and h_eA can now be plotted against the revolutions per minute. Figure 10 shows the values of h_eA in terms of the cylinder speed. The equation

$$h_eA = -146.5 + 9.04n \qquad (8)$$

is obtained from Equations (6) and (7).

The method of obtaining the form of Equation (6) can now be shown. If it is assumed that h_e is a linear function of the speed of the inner cylinder n, then it follows that

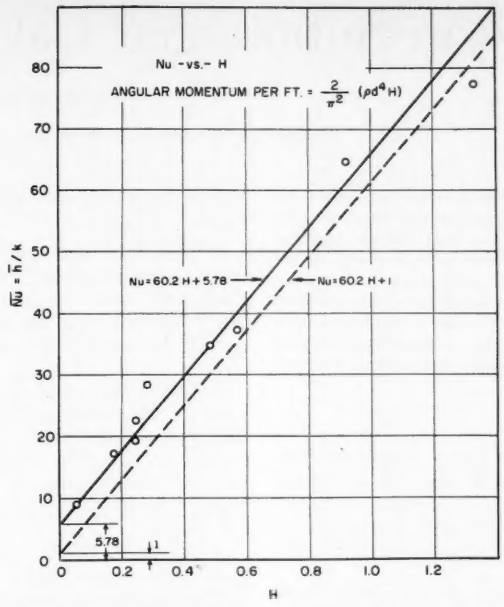

Fig. 11. Heat transfer rate per foot of eddy vs. angular momentum per foot of eddy.

$$h_e A = (a + bn)A \tag{9}$$

$$\frac{1}{h_t A} = \frac{1}{h_t A_{(max)}} + \frac{1}{A(a + bn)} \tag{10}$$

$$h_t = \frac{(a + bn)h_{t(max)}}{a + bn + h_{t(max)}} \tag{11}$$

where a, b, and $h_{t(max)}$ are still undetermined constants. Three experimental points taken from Figure 9 are used to determine these constants, and Equation (6) results. This is also the form of Equation (11).

It is noticed that these equations are of the hyperbolic rather than exponential type, which is usual for the Wilson plot. This is a result of assuming the form of the heat transfer coefficient of the eddies alone to be a linear function of the angular velocity. The reason for assuming $h_e A$ as a linear function of n is evident when one considers the manner in which the angular momentum of the eddy varies with the speed.

Dividing Equation (8) by the product of the number of eddies in the annulus and the mean circumference of the annulus gives a special heat transfer coefficient, $\bar{h}$, the heat transferred per eddy per unit length per degree Fahrenheit, as a function of the revolutions per minute of the inner cylinder.

RELATION BETWEEN ANGULAR MOMENTUM AND HEAT TRANSFER

As a final result one can eliminate the speed and show the relationship between the angular momentum and the heat transfer rate per foot of eddy as in Figure 11. In this plot $\bar{N}_u$ is a special Nusselt number, defined by

$$\bar{N}_u = \frac{\bar{h}}{k} \tag{12}$$

The lower dotted curve in Figure 11 might be expected if there were no natural convection. It would also be the expected lower limit curve for all data. At speeds below critical there is no secondary motion of the eddy type and the special Nusselt number for pure conduction for the equivalent region of one square eddy should be unity if all irregular motions were absent. Thus the curve must pass through $\bar{N}_u = 1$ at $H = 0$. Natural convection makes this condition impossible. The investigation as presented leaves room for experimental error but the error is believed to be less than 8%; this belief is justified in detail by Clark (*3*).

CONCLUSION

In essence the experimental work described has been directed toward a very special problem. For this case the Nusselt number and the angular momentum of an eddy are shown to be linearly related. This result is expected if the analogy between heat transfer by convection and momentum transfer is considered. If it is agreed that the angular momentum of an eddy is a measure of the rate at which fluid moves from one region to another, then it is to be expected that it is an indirect measure of the convective heat transfer coefficient. It is suggested that the angular momentum of an eddy may well be a method of measuring its capacity to transfer heat. However, a stretch of the imagination indicates other possibilities. If turbulence is considered to be a statistical distribution of eddies, which in turn have an effective angular momentum, then possibly there may be a different approach to the study of heat transfer in turbulent flow. A satisfactory mechanistic model to represent turbulence would be required before an investigation in this direction would be fruitful.

The fact that the angular momentum of an eddy was shown to increase linearly with angular velocity (Reynolds number) suggests a different approach to correlating heat transfer data. A detailed discussion of this point will be given in another paper.

Unfortunately heat transfer data could not be obtained for speeds of the inner cylinder greater than about twice the critical, owing to limitations of the recording system used. It is believed that at higher speeds the angular momentum would still maintain a direct proportionality with the heat transferred but that neither would have a linear relation to the angular velocity. Turbulence would certainly change the form of the data. On the other hand, for speeds entirely within the turbulent range there is reason to expect a new linear relation between speed of the inner cylinder and the heat transferred. Further study is to be made on this point.

NOTATION

A	= effective heat transfer area
a, b, P	= constants as defined in text
d	= $(R_2 - R_1)$ annulus thickness
f	= function of the coordinate x
h_t	= total heat transfer coefficient
h_e	= eddy heat transfer coefficient
$\bar{h}$	= special heat transfer coefficient
H	= angular-momentum number
k	= thermal conductivity
n	= cylinder speed, rev./min.
$\bar{N}_u$	= $\bar{h}/k$ special Nusselt number
ΔQ	= heat transfer rate, B.t.u./hr.
R_1, R_2	= inner and outer radius of annulus
ΔT	= temperature difference $(h_e A = Q/T)$
u, v	= velocity components in x and y direction respectively
x, y	= coordinates of annular eddy
ω_{cr}	= critical angular velocity in rad./sec.
ρ	= mass density
ν	= kinematic viscosity
Ψ	= stream function

LITERATURE CITED

1. Taylor, G. I., *Philosophical Transactions.*
2. Hagerty, W. W., Ph.D. thesis, Univ. Mich., Ann Arbor (1946).
3. Clark, L. G. Ph.D. thesis, Univ. Mich., Ann Arbor (1954).

Hydroextraction: Flow in Submerged Cakes

J. ANDERSON STORROW

Levington Research Station, Levington Near Ipswich, England

Flow equations have been proposed for hydroextractor cakes wherein the pores are filled with moving liquid. These equations have been confirmed for the effect of each variable by use of different experimental techniques. The critical wetting rate has provided the most informative steady state, in which the cake is fed with liquid to maintain the inner surface of the liquid at radius r_L coincident with that of the cake at radius r_e. Transient techniques have also been used either with a probe to time the movement of a liquid level between two radii less than r_e, or with a photoelectric detector to observe the coincidence of $r_L = r_e$. The tests have proved the validity of the hydrodynamic assumptions involved in the equations and have provided both precise methods for research and practical methods for industrial purposes.

Analysis of the batch operation of centrifugal hydroextractors is complicated by the succession of hydrodynamic conditions which occur as a cake is built up at low speed, spun at high speed to remove liquor, washed, and spun again to remove adhering solvent. During the cake-building period it may well be that the pores run full of liquid, whereas in the spinning periods it is probable that the majority of cake interstices contain air, the liquid flowing over the bounding surfaces of the cavities. At least two hydrodynamic conditions thus require analysis. The operation of truly continuous hydroextractors should then respond to the application of the relationships derived from these analyses. The batch hydroextractor is governed by relations incorporating the same flow principles, where they are appropriate in the cycle of operation, but requires the solution of the transient equations for the varying centrifugal force during acceleration and deceleration periods of the cycle.

A possible cycle is outlined in Table 1, the pumping force f moving the liquid increasing with increasing rotational speed and the hydrodynamic condition depending on whether the pores run full of liquid F or contain air O. The subdivisions shown are only approximations of the true system in certain periods but they suffice to show the necessity for analyzing specific cases involving selected hydrodynamic conditions, which can then be integrated to provide the whole cycle. The search for the best operating conditions in a particular hydroextraction problem can then be attempted on the basis of the known relationships governing all parts of the cycle. The essential mechanisms requiring understanding are the steady states governing the flow of liquid through (*a*) full pores, e.g., at a moment in operation 1; and (*b*) across the surfaces around open pores, e.g., at a moment in operation 3. These can then be modified for the time functions to cope with movement of the free liquid surface within the cake and with changing centrifugal forces. It is simplest first to study a steady state through which the actual operation passes. A most valuable condition is that of the "critical wetting rate," at which a liquid surface is maintained just at the inner surface of the cake for given cake thickness and hydroextractor speed.

Singularly little endeavor has been applied to the study of the fundamental mechanism of the hydroextraction process, despite its importance in chemical engineering. The researches on the subject conducted by the author and associates concentrated initially (*1, 5, 6, 21*) on problems in which the fundamental mechanism is the flow of liquid through packed beds within a centrifugal field, the interstices between the cake particles being filled with liquid. The flow relationships derived from theoretical considerations were tested for each variable and found satisfactory. They were then applied successfully to the comparison of centrifugation and filtration in both hydroextractor cakes and incompressible porous structures of similar geometrical form. These tests showed that there was no idiosyncrasy in flow in a centrifugal field within the submerged cake. The present review shows how the first fundamental mechanism has been analyzed and applied to the study of cake formation. The relationships can now be applied to the f_1, r_1 problems directly and to the f_1^*, r_1^* problems by appropriate modification for the transient variables with time.

The second major mechanism is concerned with flow through open pores. A report is to be published of work (*18*) aimed at the problems associated with liquid movement and retention within cakes when the void space is not filled with liquid. Knowledge of these two groups of fundamental problems concerning f_2, r_2 and f_2^*, r_2 should allow of considerable progress in the analysis and prediction of the course of complete hydroextraction cycles.

THEORETICAL BASES

The equations suitable for expressing the flow rates are founded on a mechanism requiring a number of limiting assumptions.

1. The effect of the gravitational field is negligible compared with that of the centrifugal field; therefore the liquid always flows through the cake in a plane normal to the axis of rotation of the basket.
2. The interstices at all points in the cake are filled with liquid when $r_L \leq r_e$ (Figure 1, ref. *7*) and the liquid moves in streamline flow through the cake. The latter is probably true for cake materials giving permeabilities of the order of 10^{-7} g./sec.^{2}
3. The liquid flows (radially) outward from the hydroextractor basket, tangential movement being due only to liquid filling the expanding cross section to flow in moving outward.
4. Kinetic energy changes due to changes of the radial component of the space velocity may be neglected, the only significant energy requirement being that to overcome frictional resistance to the liquid movement within the cake.
5. The permeability of the cake may be considered uniform in a preliminary analysis of the system. As will be shown later, it may be necessary to assess permeability distributions for precise analysis in most systems in order to cope with compression or size distributions in cakes and with cloth-cake interface resistance.
6. The highly permeable filter cloth between the cake and the basket wall does not run full of liquid, which means that atmospheric pressure is exerted on the liquid at the outer radius of the cake.

These assumptions were used in the following derivations and the experimental work was designed to test all the variables independently as far as possible. This requirement led to the development of many methods of measuring the effect of certain variables for elaborate cross-checking rather than for industrial use, though certain techniques have proved preferable and can be recommended for specific purposes such as precise research or the testing of operational hydroextractors. It was considered necessary to obtain both the correlation of hydroextractor data with theoretical equations representing the mechanism and an agreement between centrifugation and filtration data. If the hydroextraction equations are sound, they must contain a permeability K_C which is very similar to the filtration permeability K_F. The probability is that they should be the same, but in some cases secondary

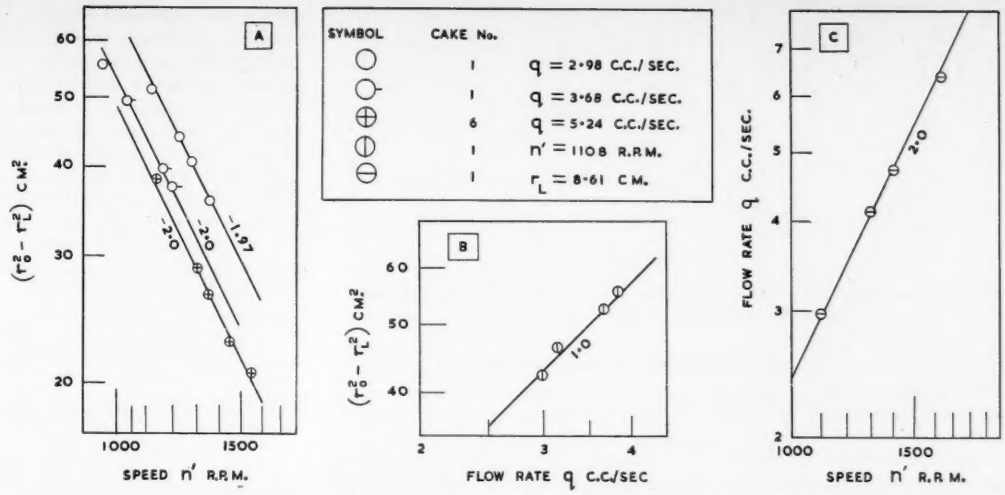

Fig. 1. Tests based on static r_L measurements (Method I), by use of a No. 1 cake of precipitated chalk of thickness 1.55 cm. and a No. 6 cake of cornstarch of thickness 0.98 cm. (*7*).

effects such as the Coriolis acceleration might lead to a flow mechanism significantly different from that in normal filtration (*20*). Apart from such unusual effects, the secondary intention of the work was thus to prove agreement between K_C and K_F to the 1% level. It was considered that once checked with such precision the flow equations could form a sound basis for developed relationships such as the relationship for cake formation. The simple equations developed do not include any effect of compressive stress on cake permeability. Though following the deviation of K_C from K_F in early work extensive studies were made to test the effect of compressive stress in filtration cells and hydroextractor basket (*5*), similar to the studies of Grace (*3*, *4*), the present opinion is that compressive effects have been of minor importance in the work on kieselguhr, metal dust, cornstarch, chalk, and barium sulfate. The early results suggesting compressive effects have been found due to misapplication of critical wetting techniques and lack of attention to cake history. If cake materials are found which show effects of compression on permeability, analytical methods similar to those of Grace should prove valuable.

FLOW EQUATIONS

The fundamental equation providing the key for all developed forms is the steady state equation for flow through the cake when the positions of the liquid surface r_L and the cake thickness $(r_0 - r_c)$ are invariant with time. With relatively low-permeability cakes and thus with relatively slow flow-rate changes, the developed forms such as for cake formation can be found by neglecting acceleration terms and using the steady state equation as the differential form for integration over a range of r_L or r_c.

The assumptions above lead to an energy balance between the pressure development due to the centrifugal field [Equation (1)] and the energy dissipation by friction over an elemental annulus of radius r and thickness δ_r within the cake [Equation (2)] if the liquid is assumed in steady flow without significant energy terms owing to radial acceleration.

$$\delta P_c = \frac{(2\pi n)^2}{g} \cdot r \cdot \delta r \qquad (1)$$

$$\delta P_F = \frac{1}{K_c} \cdot \frac{\mu g}{2\pi X} \cdot \frac{1}{r} \cdot \delta r \qquad (2)$$

The full-pressure differences across the system are $(P_c)_0$ developed from r_L to r_0 and $(P_F)_0$ required to maintain flow from r_c to r_0.

$$(P_c)_0 = \frac{1}{2} \cdot \frac{(2\pi n)^2}{g} \cdot (r_0^2 - r_L^2) \qquad (3)$$

$$(P_F)_0 = \frac{1}{K_c} \cdot \frac{\mu g}{2\pi X} \cdot \ln \frac{r_0}{r_c} \qquad (4)$$

For a balanced system, the values must be equal, $(P_c)_0 = (P_F)_0$, to maintain atmospheric pressure as datum level at the liquid faces at r_L and r_0. Throughout the cake there will be a pressure of $(P_c - P_F)$ above atmospheric pressure as datum at the radius r within the cake, $r_c < r < r_0$, depending on the relationships between the groups in Equations (3) and (4) with r in place of r_0. This is discussed later in terms of the tests on banded cakes.

The steady state leads to the flow-rate equation from the equality $(P_c)_0 = (P_F)_0$ when r_L is not greater than r_c, i.e., with the liquid filling all the cake voids.

$$q = \frac{4\pi^3 n^2 K_c X}{\mu g} \cdot \frac{(r_0^2 - r_L^2)}{\ln r_0/r_c} \qquad (5)$$

A useful experimental technique involves the detection of the critical wetting rate when $r_L = r_c$, the liquid surface coinciding with the inner face of the cake,

$$q_w = \frac{4\pi^3 n_c^2 K_c X}{\mu g} \cdot \frac{(r_0^2 - r_c^2)}{\ln r_0/r_c} \qquad (6)$$

$$= \frac{4\pi^3 n_c^2 K_c X}{\mu g} \cdot (r_0 + r_c) \cdot r_m \qquad (6a)$$

where r_m is the logarithmic mean of r_0 and r_c. The verification of the postulated flow mechanism and related assumptions could be provided by testing Equations (5) and (6) with r_L independent of time, or r_L could be allowed to vary and the resulting time functions applied to the analysis of the experimental data. Both methods were used in order to test the fundamental equations in every conceivable way. Nearly all the tests were carried out on a 9-in.-diam., 4½-in.-depth hydroextractor with a duck-weave cloth behind the cake, though the effect of r_0 was checked by experiments on an 18-in.-diam. hydroextractor.

ANALYTICAL METHODS AND EXPERIMENTAL TECHNIQUES

Method I, Based on r_L Measurements When r_L Is Independent of Time

For the use of Equation (6) in analyzing data, the experimental results must provide flow rate q_w at which $r_c = r_L$ for various speeds n. The early technique (*1*, *2*, *5*), probably similar to that of Smith (*19*), using visual observation of the critical wetting rate, proved dangerously deceptive, and a far superior technique is the use of a photoelectric diffuse-reflection detector (*16*). The light from a lamp L is reflected back to the photocell C (Figure 2, ref. *15*) in increasing intensity as the liquid thickness $(r_c - r_L)$ is reduced. Thus if a cake revolving at a speed n is fed with a constant liquor rate q so that $r_L < r_c$, the photocell output will represent the

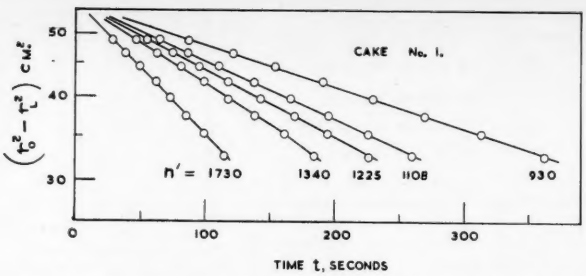

Fig. 2. Tests based on measurement of r_L variations with time (Method II), by use of a No. 1 cake of precipitated chalk (7).

steady state. If n is increased to a new steady value, r_L will change to a new steady state at a larger value of r_L. These positions may be plotted as a graph of photocell output against n. When the liquid film disappears into the cake surface the cell output, a curve nearly linear in n, changes abruptly to a value nearly independent of n. The break point gives a sensitive test of the critical speed n_c at which $q = q_w$ is the critical wetting rate for the cake. This technique is valuable in industrial practice, where the more elaborate probe technique may not be available outside the research laboratory. The logarithmic plot of q_w against n_c for a given cake gives a clear confirmation of the power 2.0 for revolution speed. There are experimental limitations which must be carefully observed in all hydroextractor tests. The cake must be formed under liquor and maintained under liquor throughout all tests. It must first be run at the highest test speed for a short time. Thereafter the results will be reproducible on a q_w, n_c line of gradient 2.0 on a logarithmic plot for all values of n_c (16).

A valuable research technique of high precision is provided by the probe indicator developed by Haruni (6). For any steady state q and n, the position of r_L could easily be measured to 0.01 cm., the probe I being moved vertically and radially by calibrated hand wheels (D and M in Figure 1, ref. 7). With this apparatus the variables in Equation (5) could be examined in various ways for a specific cake and liquid, i.e., for constant r_0, r_c, X, μ, K_c, and for $r_L < r_c$.

From Equation (5) for the steady state flow, for constant r_L, q should vary with n^2. For constant n, the variation of r_L being measured with q, each r_L, q pair being for a steady state, the plot of log $(r_0^2 - r_L^2)$ against log q should be a straight line of gradient 1.0. For constant q, corresponding r_L, n pairs being measured, a plot of log $(r_0^2 - r_L^2)$ against log n should be a straight line of gradient -2.0. The agreement with Equation (5) is shown by the data (7) on Figure 1 and corroborates the form of the equation and the substantial constancy of r_c and K_c, notably with varying compressive stress for the test material.

Method II, from Drainage Times Based on r_L Changing with Time

The technique consists in stopping the feed of liquor to the basket when r_{L_0} is considerably less than r_c and following the changes of r_L with time. Using the probe, the time t is found for r_L to increase from r_{L_0} at $t = 0$ to r_L at $t = t$. If it is assumed that the steady state equation (5) can be used as the differential equation for the rate of change of V_L, the volume of liquor held between r_L and r_c, the variation of r_L with t is given by

$$q = -\frac{dV_L}{dt} = 2\pi X r_L \cdot \frac{dr_L}{dt} \qquad (7)$$

whence with Equation (5)

$$\ln\left[\frac{r_0^2 - r_{L0}^2}{r_0^2 - r_L^2}\right] = \frac{4\pi^2 n^2 K_c}{\mu g \log r_0/r_c} \cdot t \qquad (8)$$

For a selected value of r_{L_0}, a series of tests of r_L against t with constant μ, n, K_c, r_0, r_c should give a straight line of gradient -1 for the plot of log $(r_0^2 - r_L^2)$ against t. Figure 2 shows the agreement with this form for a cake for various hydroextractor speeds.

Method III, Based on Drainage Times for a Specific Volume of Liquid

With the basket running at a constant speed n, with $r_L = r_c$, the feed can be stopped and simultaneously the volume $V_L{}^1$ added to the basket. If this volume of liquid is assumed to accelerate to the appropriate basket speed immediately, functions can be derived from Equation (5) to show the time required for the liquid surface to attain a selected position in terms of the cake volume V_c and the volume of liquid held within the cake radius r_c.

From Equation (5)

$$q = -\frac{dV_L}{dt} = \frac{4\pi^2 n^2 K_c}{\mu g} \cdot \frac{(V_L + V_c)}{\ln r_0/r_c} \qquad (9)$$

$$= \gamma(V_L + V_c) \qquad (10)$$

where γ is a constant for given cake, liquor, and speed. One method consisted of an analysis of the variation of flow rate with liquid volume V_L, which should give for constant γ a straight line for q against V_L with an intercept $q = \gamma \cdot V_c$, when $V_L = 0$ and $r_L = r_c$. The experimental data are compared (9) with a lattice of straight lines of parameter γ, each line having its gradient γ linked with its intercept $\gamma \cdot V_c$ at $V_L = 0$. These rate data are less readily obtained than the time t for the liquid volume to attain V_L from an initial volume $V_L{}^1$ when $t = 0$. In this case the volume $V_L{}^1$ would be added to a critically wetted cake with $r_L = r_c$ and time t found for r_L to attain a selected position,

$$t = \frac{1}{\gamma} \cdot \ln\left[\frac{V_c + V_L{}^1}{V_c + V_L}\right] \qquad (11)$$

or if liquid is allowed to drain to $r_L = r_c$ and $V_L = 0$

$$t^1 = \frac{1}{\gamma} \cdot \ln\left[\frac{V_c + V_L{}^1}{V_c}\right] \qquad (12)$$

An example of such a data series for various $V_L{}^1$ for constant γ and V_c is shown in Figure 3 and also in Figures 2, 3, and 5 of ref. 15. The critical wetting condition can be found by using the photoelectric detector, the output of which will show a clear break point when $r_L = r_c$. Figure 2 (15) shows a photocell fitted to a porous ceramic cylinder used as an incompressible hydroextractor cake; Figure 3 (15) shows a series of critical wetting tests at constant n for various added volumes $V_L{}^1$; the break-point data transferred to Figure 5 (15) indicate the straight-line relationship between ln $(V_c + V_L{}^1)$ and t^1 from Equation (12) with an intercept at ln V_c when $t^1 = 0$. The change of gradient γ with speed n is clear from Figure 5 of ref. 15 and on Figure 4 the data confirm the expected relationship $\gamma \propto n^2$. Even with visual observation, this method can be used to obtain γ and hence K_c for selected conditions on operating plant. The assumption of negligible time for the liquid $V_L{}^1$ to be accelerated to the basket speed is sound for the materials used here but would lead to curvature in these plots for high-permeability cakes giving low t^1 values of the same order as the acceleration time required.

HYDROEXTRACTION AND FILTRATION PERMEABILITIES

The methods described above have been used for testing the fundamental equation in detail (7) and show good agreement for a given cake and liquor. These techniques involve the variation of r_L, q, n, but not the variation of r_0 or μ. By use of centrifuges of different r_0 and liquids of various viscosities, the effect of these variables has been shown to fit Equation (5) and its derived forms. The dependance on the first power of μ confirms the assumption of streamline flow and the negligible effect of radial acceleration kinetic energy terms (7).

The success of these methods means that the assumptions and derived equations are probably correct in that they lead to a complete correlation of hydroextraction data in terms of a permeability K_c for a given cake, the same value being obtained by various methods. The effect of compressive stress appears negligible with the materials used. The proof of the correctness of the equations still lacks agreement between K_c and K_F. Much experimental work has been done on this, leading to detailed analyses of many forms of experiment specifically designed to test this agreement to 1% accuracy (*8* to *15*). The comparison of K_c in a 9-in.-diam. hydroextractor with K_F from samples cut from the cake proved unsatisfactory (*2*, *5*, *6*).

In a cylindrical cell of 1½-in. diam. small cakes of thickness up to about 1½ in. were made which could be tested in both the centrifugal field and the gravitational field (*8*), both K_c and K_F being obtained from the cake without disturbing it. The cell (shown diagrammatically in Figure 8, ref. *8*) was held in a carrier within the hydroextractor and whirled about the center line, a liquid level being maintained at G, while the liquor discharged freely into the atmosphere at the perforated base of the cell. The cell was filled completely with liquid. The cake B held on cloth C had to be protected during formation and testing (*8*) owing to the strong secondary circulation in the space A. For filtration tests the cell was connected to a head tube and K_F obtained from the time for the liquid level to fall from H_1 to H_2:

$$t = \frac{a\mu(r_0 - r_c)}{K_F A} \cdot \ln \frac{H_1}{H_2} \qquad (13)$$

where A is the cross-sectional area of the cake face, and the thickness of the cake is $(r_0 - r_c)$.

In this cell the hydroextraction permeability K_c must be found from a relation similar to Equation (5) but appropriate to the constant cross-sectional area A of the cell.

$$q = \frac{2\pi^2 n^2 A K_c}{\mu g} \cdot \frac{r_0^2}{(r_0 - r_c)} \qquad (14)$$

Tests on the small cell were under centrifugal and gravitational pressure heads similar to those in the large hydroextractor, and the results showed disagreement of 5 to 20% between K_c and K_F. Many tests with this cell and with samples from the hydroextractor cakes of various materials (*8*) showed that though the proof was nearly complete, it could not be attained with the complex experimental conditions and possible cake changes with fine powders for bed material. Tests on incompressible porous ceramic cylinders of dimensions near those of the hydroextractor, of which the figures mentioned above are examples, showed reproducible agreement between K_c and K_F to 5% (*15*) but observable local variations in the permeability of such material probably accounted for the remaining difference. Tests on small sintered metal plugs (Figure 9, ref. *15*) comparable to the small cell work showed the consistent agreement to 1% (*15*), which is regarded as the final proof that the functions proposed are probably correct for the flow mechanism in submerged cakes of incompressible materials.

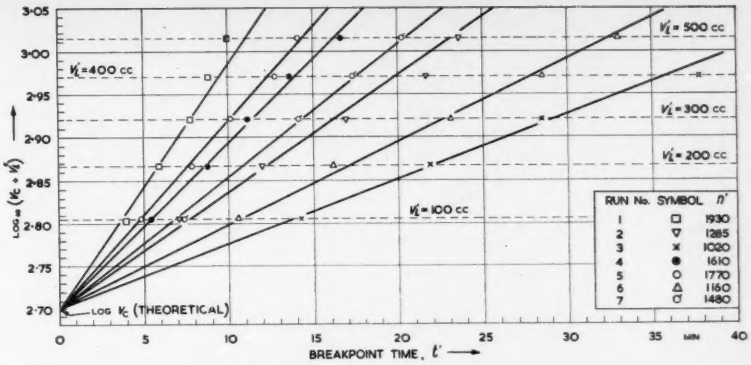

Fig. 3. Break-point data for drainage tests in ceramic cylinders. Cylinder II was of maximum pore size, 2μ and thickness 0.79 cm. (*15*).

PRESSURE AND PERMEABILITY DISTRIBUTIONS IN CAKES

Though the agreement between K_c and K_F from the average permeability functions described above was near enough to show that the proposed mechanism was probably correct, the discrepancies were consistent, and in seeking their cause and greater precision it has been found that significant distributions of permeability may occur within the cake. Analyses of cakes of various thicknesses can be explained reasonably on the basis of relatively small changes in K_c within the cake and a significant resistance at the cloth-cake interface (*10*). This seems clear from the examples shown in Table 2 for cakes of various thicknesses.

The layer permeabilities are found from the analysis of the complete cake permeability K_m in terms of the layer values $K_1, K_2, \cdots K_n$, the inner radius of the n-th layer r_n being r_c, the inner radius for the cake.

$$\tfrac{1}{2}(2\pi n)^2(r_0^2 - r_L^2) = \frac{\mu q g}{2\pi X K_m} \cdot \ln \frac{r_0}{r_c}$$

$$= \frac{\mu q g}{2\pi X}\left[\frac{\ln r_0/r_1}{K_1} + \frac{\ln r_1/r_2}{K_2} + \cdots + \frac{\ln r_{n-1}/r_n}{K_n}\right] \qquad (15)$$

The results show a high resistance in the layer next to the cloth, which can be ascribed to the cloth-cake interface. The cloth tested on its own, when in a dirty condition after use, showed only a flow resistance of about 1% of the cakes.

An interesting study allied to the permeability distribution work is an assessment of the fundamental pressure distribution. The balanced operation in steady state flow requires $(P_c)_0$ to be equal to $(P_F)_0$. Thus it is clear that there are likely to be positions in the cake where the pressure on the liquid is less than atmospheric. The maximum vacuum is probably equivalent to about 100 cm. of water and it is not likely to produce degassing of the liquid, which might cause discontinuities in the pressure distribution along the radial direction. However, it is necessary to test the pressure distribution indirectly so far as possible. By making cakes from layers of differing permeabilities, it is possible (*11*) to test whether the resultant flow rates fit those predicted from the known permeabilities and the assumed pressure distribution of $(P_c - P_F)$.

From detailed analyses of tests with $r_L < r_c$ on various cake thicknesses of a single material in the hydroextractor and in the small centrifuge cell it is possible to assign a value for permeability for any layer of selected material at a particular position when compressed by a particular thickness of material nearer the axis of rotation (*10*, *11*). Figure 5 exemplifies the assessment of such cases in the hydroextractor. The cakes were made from layers of cornstarch and kieselguhr of differing permeabilities (Table 2). The dimensions, permeabilities, and flow rates for specific speeds were known, and thus the P_c distribution is known, rising from $P_c = 0$ at $r_L = 8$ cm. to a maximum $(P_c)_0$ at $r_0 = 10.8$ cm. along the curve Aah. The P_F curve can be calculated as rising almost proportionally to the radial thickness of the cake from zero at r_c to the total value for the particular cake layer; e.g., the P_F requirement for the innermost layer of starch in cake No. 8 is given by ab. The net value of $(P_c - P_F)$ at the inner radius of the kieselguhr layer is given by the ordinate at b. The same flow rate leads to a pressure drop for the outermost starch layer of fg. The equivalent development of P_c through this

layer would be *ef*. Thus excess pressure at the outer layer of the kieselguhr is given by the ordinate at *e*, when *g* is fixed at the atmospheric pressure datum for the outlet at r_0. If the kieselguhr layer runs full, the P_c development is from *b* to *c*. Balanced operation would result if the pressure drop due to friction through the kieselguhr layer is *ce*. Actually in this example it would be *de*. The discrepancy *cd* can be explained ouly by the assumption that the kieselguhr layer did not develop the centrifugal pressure rise *bc* but only *bd*. This means that this layer was not running full of liquid, and it has been confirmed from many tests that this seems the true explanation, a constant pressure region occurring over part of the layer thickness. The case of cake No. 4 with the kieselguhr as the inside layer gives a good agreement. From the experimental *q* and known *K* values, the estimated and actual pressure curves comparable to *bc* and *bd* are very close together, an indication that the kieselguhr layer runs full. Cake No. 3 exemplifies cases in which a high-permeability layer on the outside will not run full. The *q*, *K* data for the inner starch layer running full gives a value of $P_c - P_F$ of zero at the inner layer of the kieselguhr, which means that the atmospheric pressure obtains at the outer radius of the starch layer, the high permeability layer running empty. This type of data from many different cases (*11*) is considered to prove that layers of high permeabilities within a cake will not run full and thus will not develop their maximum centrifugal-pressure contribution and that such layers will not run full on the outside of a cake. This latter case justifies the assumption that the highly permeable cloth layer in a centrifuge cake does not run full and thus does not enter into the resistance functions leading to the flow equations. The conditions demonstrated as leading to these discontinuities in pressure development are absent in uniform cakes of a single material, which affords some indirect proof that the normal cake runs full as originally assumed. It seems unlikely from these tests that the vacuum developed in normal cakes would cause discontinuity in the liquid path sufficient to affect the continuous pressure development according to Equation (1).

EFFECT OF CAKE SHAPE

The formation of cakes differing from the assumed form with constant r_0 and r_c at all positions round the basket and along the vertical height will produce two effects: first, the obvious complication in deducing a flow function leading to the cake-formation function and, second, the problem of proper derivation of the steady state flow equation comparable to Equation (5). The latter problem has been assessed (*12*) by estimating the discrepancy between the flow through a wedge-shaped cake from an Equation (5) based on a mean value of r_c and the true flow from a relaxation solution to the Laplace equations for filtration and centrifugation. These analyses show that in general the simple analysis based on Equation (5) and the mean cake thickness will be satisfactory for most purposes, even with quite large deviations from the theoretical cake form.

The second problem of cake formation has been assessed (*14*) in a manner different from that suggested by Maloney (*17*). It is clear that the method of feeding the slurry to the basket will be all-important. Cake formation by growth all over its inner face is not ensured by the cake being formed underneath a liquor layer or proved by the fact that a cylindrical cake, i.e., one with a vertical inner face, is produced finally. The data in Figures 1 to 5 of reference *14* show the very different type of growth found with slurry fed to the bottom of the basket with a liquor level maintained at a fixed r_L.

The uniform growth of the cake of permeability K_c at all facial positions starting from a layer of inner radius r_0, outer radius r_w, and permeability K_0 would be given by an appropriate integration of the steady state flow-rate equation:

$$q = \frac{\dfrac{4\pi^3 n^2 X(r_w^2 - r_L^2)}{\mu g}}{\left[\dfrac{\ln r_0/r_c}{K_c} + \dfrac{\ln r_w/r_0}{K_0}\right]} \qquad (16)$$

Shortly after the growth starting the K_0 layer ceases to run full if its permeability K_0 is, say, ten times K_c, the term in K_0 becomes inoperative and $(r_w^2 - r_L^2)$ becomes $(r_0^2 - r_L^2)$. For a cake growing on an existing cylindrical layer of the same material K_0 becomes K_c and r_0 disappears from the final bracketed term. This equation is valid for cakes of materials such as starch, chalk, kieselguhr, and barium sulfate, where the sedimentation rate is so high that the liquid layer from r_L to r_0 is effectively clear liquid rather than slurry.

For a slurry volume *V* added from the start of cake formation

$$r_c^2 = r_0^2 - \frac{sV}{\pi X \sigma_p} = r_0^2 - C_1 V \qquad (17)$$

and the relationship between slurry feed rate q_s and liquid drainage rate *q* for a fixed r_L is

$$q = q_s\left(1 - \frac{s}{\sigma}\right) \qquad (18)$$

whence

TABLE 1

OPERATION SEQUENCE IN BATCH HYDROEXTRACTOR

f = centrifugal pumping force
R = flow resistance

	Operation	Speed	Pore flow Initial	Pore flow Final	Hydrodynamic variables
1	Cake formation	Low	*F*	*F*	f_1^*, R_1^*
2*a*	Cake drainage	Increasing	*F*	*F*	f_1^*, R_1
2*b*		High	*F*	*O*	f_1, R_1 to f_2, R_2
2*c*		Decreasing	*O*	*O*	f_2^*, R_2
3	Cake washing	Low	*O* or *F*	*O* or *F*	f_1, R_1 or f_2, R_2
4*a*	Wash water drainage	Increasing	*O* or *F*	*O*	f_1^*, R_1 to f_2^*, R_2
4*b*		High	*O*	*O*	f_2, R_2
4*c*		Decreasing	*O*	*O*	f_2^*, R_2

*The major variable is altering during the period; e.g., as the cake forms, the pumping force f_1 will increase as the liquid bulk in the basket increases and the flow resistance r_1 will increase with cake thickness.

TABLE 2

PERMEABILITY OF LAYERS IN 9-IN. HYDROEXTRACTOR.

Starch

Layer number*	1	2	3	4	5	6	7	8	9
W†, g.	300	400	500	600	700	800	900	1,000	1,100
Layer $K_c \times 10^7$, g./sec.²	2.39	4.07	4.3	4.3	4.05	4.95	4.45	4.55	5.1

Mean K_c for layers 2 to 9 is 4.6×10^{-7} g./sec.²

Kieselguhr

Layer number*	1	2	3	4	5	6
W†, g.	200	300	400	500	600	700
Layer $K_c \times 10^7$, g./sec.²	11.8	51.7	42.07	44.6	47	57

Mean K_c for layers 2 to 6 is 50×10^{-7} g./sec.²

*Layers built in their numerical order.
†W is the total mass of air dried solid in the cake.

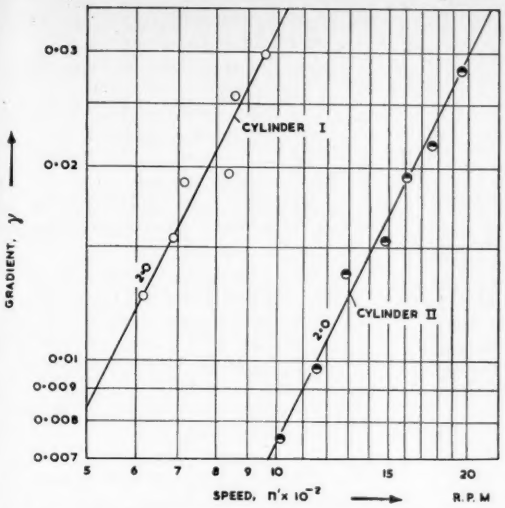

Fig. 4. The dependence of gradient γ on speed of revolution n agrees with the expected power 2.0 from Equation (10) (*15*).

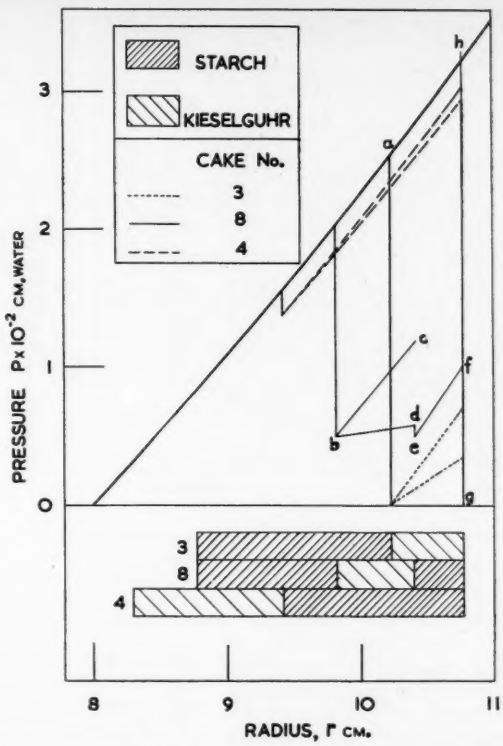

Fig. 5. Pressure distribution with banded cakes in the 9-in.-diam. hydroextractor, with n^1 = 1,080 rev./min. and r_L = 8.0 cm. (*11*).

$$q_s = \frac{CX}{\ln r_0/r_e} \qquad (19)$$

where

$$C = \frac{4\pi^3 n^2 K_c(r_0^2 - r_L^2)}{\mu g\left(1 - \frac{s}{\sigma}\right)}$$

Thus

$$\frac{dV}{dt} = \frac{CX}{\ln\left[\frac{r_0}{(r_0^2 - C_1'V)^{1/2}}\right]} \qquad (20)$$

and integrating from $V = 0$ at $t = 0$ to $V = V$ at $t = t$ with C and C_1 assumed independent of time gives

$$(1 + 2\ln r_0)V + \left(\frac{r_0^2}{C_1} - V\right) \cdot \ln(r_0^2 - C_1V) - \frac{2r_0^2}{C_1}\cdot \ln r_0 = 2CXt \qquad (21)$$

This formation method is that depicted in Figure 1*a*, ref. *14*; however, the cake may form in a very different manner. Figure 3 in ref. *14* shows contour measurements made at stages in a cake's growth and represents many such assessments using the probe and layer-dyeing techniques. It is noteworthy that although dilute slurry fed to the bottom of the cake is spread out along the vertical height X very rapidly, the solid sedimentation must also be very rapid to lead to the forms shown. The limitation caused by r_L is also clear. The formation mechanism seems independent of the presence of cloth only as the original backing, as in Figure 3 of ref. *14* or cloth with a cylindrical cake as in Figure 3*c*.

The extreme case of such growth is shown in Figure 1 (*14*), wherein the cake is pictured as growing vertically along an x axis while confined between the radii r_1 and r_2. For this case

$$\frac{sV}{\sigma_p} = \pi x(r_1^2 - r_2^2) \qquad (22)$$

or $x = C_2V$, where $C_2 = s/\pi\sigma_p(r_1^2 - r_2^2)$ and $r_2 < r_1$. Assuming that the cake is being formed on an existing cylindrical cake of inner radius r_1, outer radius r_0, and permeability K_c results in

$$q_s = \frac{4\pi^3 n^2 K_c(r_0^2 - r_L^2)}{\mu g\left(1 - \frac{s}{\sigma}\right)} \cdot \left[\frac{x}{\ln r_0/r_2} + \frac{X - x}{\ln r_0/r_1}\right] \qquad (23)$$

whence

$$\frac{dV}{dt} = C\left[\frac{C_2V}{\ln r_0/r_2} + \frac{X - C_2V}{\ln r_0/r_1}\right] \qquad (24)$$

$$= R_1V + R_2 \qquad (25)$$

where

$$R_1 = CC_2\left[\frac{1}{\ln r_0/r_2} - \frac{1}{\ln r_0/r_1}\right]$$

$$R_2 = \frac{CX}{\ln r_0/r_1}$$

Integrating from $V = 0$ at $t = 0$ to $V = V$ at $t = t$ and assuming R_1 and R_2 independent of time gives

$$t = \frac{1}{R_1}\cdot \ln\left[1 + \frac{R_1}{R_2}\cdot V\right] \qquad (26)$$

The equation has significance only for $0 < x < X$.

Results for measured starch slurry rates q_s to maintain a constant r_L are shown in Figure 6 and also in Figure 4 of ref. *14*. The permeability of the cake materials, initial cake geometry, and slurry characteristics are all known (ref. *14*, Table I) and one may calculate the curves A, A^1 in Figure 4 (*14*) based on Equation (21) for cylindrical growth and curves B, B^1 based on Equation (26). The experimental data show a good agreement with the vertical growth curves. The set A, B is for growth on an existing cylindrical starch cake and set A^1, B^1 for growth on cloth. To provide a comparison Equations (21) and (26) were based on an initial cake thickness of 1 mm. Further data in Figure 6 show similarly good agreement with Equation (26). It is clear that it cannot be assumed that cakes always grow cylindrically. In each case depending on material and feed method it may be necessary to check cake contours during growth and produce an appropriate equation for a simplified model of the growth mechanism.

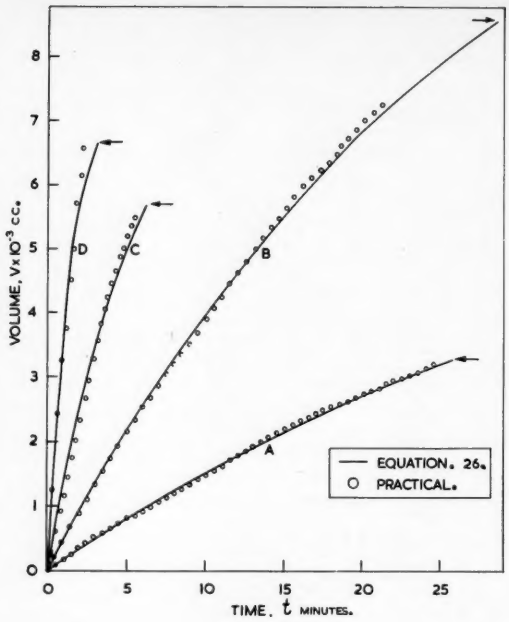

Fig. 6. Agreement between practical results and Equation (26). The arrow indicates the volume of slurry equivalent to the cake volume to fill the basket (*14*).

DISCUSSION

This review has shown that the author's proposals as to flow mechanism and permissible assumptions in submerged cakes were correct. The close agreement between filtration and hydroextraction permeabilities is considered sound proof that the flow in hydroextractor cakes has no major peculiarity. The many analytical and testing methods have also provided various techniques for use at all levels of industrial "accuracy," from those suitable for application to research apparatus to those which can be applied to large-scale operating equipment. It must be emphasized that the work reported here covers only the first problem of centrifugation. The equations so far derived are all dependent on the pressure distributions in a cake wherein the pores run full of liquid. This requires that at all times the cake is submerged, the liquid surface r_L never exceeding r_c and the liquid filling the cake to the outer radius r_0.

There are many problems of liquor flow and liquor retention, the analyses of which require other fundamental relationships. Cake formation methods are used which do not conform to the submerged cake mechanism, e.g., where the cake is formed by spraying a thick slurry or adding a crystal "mush" to the basket. The significant basic relationships are those associated with "whizzing" to remove residual liquor from the cake. Washing the cake may be done with $r_L < r_c$, but often it will consist of spraying water onto the cake at a rate less than the critical wetting rate and the inner surface of the cake will not then run full. The flow problem may then consist of two parts, the "full-flow" state in an outer layer of the cake, and a surface flow over the particles in an inner layer of the cake. The whizzing of cakes will present similar problems of surface flow, in which the significant mean variables include the "effective thickness" of the mobile liquid films on the particle surface and the retained quantities of liquid in the cake interstices, both problems depending on centrifugal field and details of particle arrangement in the cake.

ACKNOWLEDGMENTS

The author is grateful to Professor J. O. Maloney of the University of Kansas for presenting on his behalf the foregoing material as a paper to the A.I.Ch.E. meeting in Louisville in March, 1955. It reports the work of the author and his collaborators in the Chemical Engineering Laboratories, College of Technology, Manchester.

NOTATION

A = cross-sectional area of filter bed, sq. cm.
a = cross-sectional area of falling-head tube, sq. cm.
C, C_1, C_2 = constant groups
g = gravitational acceleration, cm./sec.^{2}
H = hydrostatic head in filtration tests, cm. water
H_1, H_2 = limits of H
h = static head at axial entrance to small spinning cell, cm. water
K = permeability, (g./sec.^{2})
K_F = permeability in filtration tests, g./sec.^{2}
K_c = permeability in centrifugation, g./sec.^{2}
n = speed of revolution, rev./sec.
n^1 = speed of revolution, rev./min.
n_c = speed of revolution at critical wetting condition, rev./sec.
P_c = centrifugal pressure, cm. water
P_F = friction head, cm. water
q = drainage rate through cake, cc./sec.
q_w = drainage rate at critical wetting condition, cc./sec.
q_o = slurry flow rate, cc./sec.
R_1, R_2 = constant groups
r = radius from basket axis, cm.
r_c = radius from basket axis to inner face of cake, cm.
r_L = radius from basket axis to inner face of liquid, cm.
r_0 = radius from basket axis to outer face of cake, cm.
r_w = radius from basket axis to inner face of basket wall, cm.
s = slurry concentration, g. air-dried solid/cc. slurry
t = drainage time, sec.
t^1 = drainage time for $V_L{}^1$, sec.
V = volume of slurry, cc.
V_c = volume of cake = $\pi X(r_0^2 - r_c^2)$ cc.
V_L = volume of liquid = $\pi X(r_c^2 - r_L^2)$, cc.
$V_L{}^1$ = volume of liquid added to basket for drainage test, cc.
W = mass of dry solid in cake, g.
X = depth of hydroextractor basket, cm.
x = height of cake, cm.
μ = viscosity of liquid, poise
γ = $n^2\lambda$
λ = $4\pi^2 K_c/\mu g \ln (r_0/r_c)$
σ = density of air-dried solid, g./cc.
σ_p = packing density of solid in cake, g./cc.

LITERATURE CITED

1. Burak, Nathan, M.Sc.Tech. thesis, Univ. Manchester (1947).
2. Burak, N., and J. A. Storrow, *J. Soc. Chem. Ind.*, **69**, 8 (1950).
3. Grace, H. P., *Chem. Eng. Progr.*, **49**, 303, 367 (1953).
4. *Ibid.*, 427.
5. Gupta, O. P., M.Sc.Tech. thesis, Univ. Manchester (1948).
6. Haruni, M. M., Ph.D. thesis, Univ. Manchester (1952).
7. ———, and J. A. Storrow, *Ind. Eng. Chem.*, **44**, 2751 (1952).
8. *Ibid.*, 2756.
9. *Ibid.*, 2764.
10. ———, *Chem. Eng. Sci.*, **1**, 154 (1952).
11. *Ibid.*, **2**, 108 (1953).
12. *Ibid.*, 164.
13. *Ibid.*, 203.
14. *Ibid.*, **3**, 43 (1954).
15. ———, and K. H. Todhunter, *ibid.*, 87.
16. Inglesent, Harold, and J. A. Storrow, *Ind. Chemist*, **27**, 76 (1951).
17. Maloney, J. O., *Ind. Eng. Chem.*, **38**, 24 (1946).
18. Nenniger, Emile, Ph.D. thesis, Univ. Manchester (1956).
19. Smith, J. C., *Ind. Eng. Chem.* **39**, 474 (1947).
20. Storrow, J. A., and Henry Zychlin, *J. Soc. Chem. Ind.* **69**, 379 (1950).
21. Todhunter, K. H., M.Sc.Tech. thesis, Univ. Manchester (1950).

Presented at A.I.Ch.E. Louisville meeting

Diffusion in a Moving Medium with Time-dependent Boundaries

H. KURT FORSTER

University of California, Los Angeles, California

The problem of diffusion in a moving medium with given motion of the boundaries is considered. The method presented yields the analytical solution to any desired degree of accuracy provided that solutions for certain associated problems of diffusion in a medium at rest with boundaries at rest are known. The method is applied to the analysis of partial and approximate solutions previously presented for the one-dimensional case of a spherical cavity in a liquid with radial boundary motion induced by evaporation.

In melting and freezing and frequently in the propagation of chemical reactions through some material an important group of problems arises in which one substance changes into another with emission or absorption of heat. One essential feature of such problems is the existence of a moving surface of separation between the two phases at which heat is being liberated or absorbed. In melting, freezing, and similar cases the change in specific volume caused by change of phase is negligible and the medium may be considered at rest. The problem in which the motion of the *free* (phase) *boundary* caused by diffusion in a medium *at rest* is to be found is well known as *Stefan's problem*.* In cases of condensation and evaporation (bubbles in boiling and cavitation, rather than evaporation of droplets) an added difficulty arises, because these processes are accompanied by a marked change in specific volume whereby the medium in which the phase change is taking place is set in motion. Thus the problem becomes one of diffusion in a moving medium, which is, in the case of heat diffusion, the problem of heat transfer by simultaneous heat conduction and heat convection. On the other hand, the same circumstance also introduces, for condensation and evaporation, a simplification in Stefan's problem: owing to the large change of volume in evaporation the motion of the phase boundary is determined by the increase of volume of the vapor phase, and the influence of the decrease of volume of liquid by evaporation may, in comparison, be neglected.

In view of the foregoing discussion this paper presents a rather general method which yields, to any desired degree of accuracy, the solution of problems of combined heat conduction and heat convection with *given* motion of the boundaries. The general method will then be used to discuss, analyze, and compare partial and approximate solutions previously presented (*1, 2*) for the special case of a spherical cavity with radial boundary motion induced by evaporation.

DIFFUSION IN A MOVING MEDIUM

In the problem of heat conduction in a moving, incompressible, inviscid fluid with given motion of the boundaries (*3*), $T(\mathbf{r}, t)$ is the temperature and $\mathbf{v}(\mathbf{r}, t)$ the local velocity of the medium, $\mathbf{r}$ being the radius vector (x, y, z); then the differential equation to be solved is

$$a \nabla^2 T - \mathbf{v}(\mathbf{r}, t) \cdot \text{grad } T - \frac{\partial T}{\partial t} = 0 \qquad (1)$$

The motion of the boundary may be given by $\mathbf{r} = \mathbf{r}_0(t)$ as a known function of time, and the boundary conditions which shall be considered in this paper are those of constant temperature or of vanishing heat flux on the moving boundary:

$$T = 0; \quad \text{or} \quad \frac{\partial T}{\partial n} = 0; \quad \text{for: } \mathbf{r} = \mathbf{r}_0(t) \qquad (2)$$

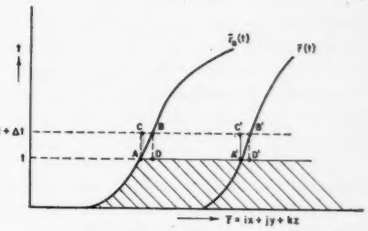

Fig. 1. Continuous and step-by-step boundary motion in the $(\bar{r}, t)$ plane.

As indicated in Equation (1) the velocity $\mathbf{v}$ is in general a function of time and position and the equation thereby becomes one with variable coefficients to be solved for moving boundary conditions. No method for the solution of this general problem exists.

The problem is to find a solution to Equation (1) for boundary conditions given by Equation (2). In the $(\mathbf{r}, t)$ space, which is four dimensional but which may be shown diagrammatically in Figure 1, the domain of integration is a strip bounded by the $\mathbf{r}$ axis and by the curve $\mathbf{r}_0(t)$. The curves $\mathbf{r}_0(t)$ and $\mathbf{r}(t)$ in Figure 1 represent respectively the motion of a fluid particle at the boundary and the motion of a representative fluid particle anywhere in the fluid.

If the motion of the fluid starts at time t_0 with the boundary in position P_0 and proceeds until time t, when the boundary may be at position P_t (see Figure 2), at the intermediate times t_1, t_2, t_3 $\cdots$ the boundary moves through positions P_1, P_2, P_3 $\cdots$, with the liquid moving accordingly in some prescribed manner.

*Some references to Stefan's problem may be found in reference *4*, p. 71.

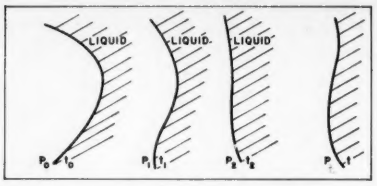

Fig. 2. Motion of the boundary from positions P_0 to P_t; intermediate positions P_1, P_2, etc., are shown.

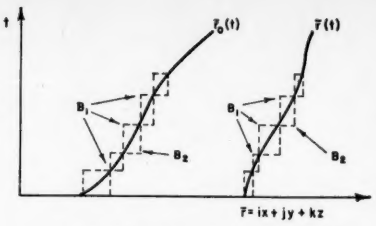

Fig. 3. Path of boundary and of fluid particles in the $(\bar{r}, t)$ plane.

The motion of fluid and boundary is approximated as follows. The boundary remains at P_0 for time $(t_1 - t_0)$; at time t_1 it moves (instantly) to position P_1, where it remains for time $(t_2 - t_1)$; at time t_2 the boundary moves instantly to P_2, where it remains for time $(t_3 - t_2)$, and so on, until position P_t at time t is reached by the boundary, with all fluid particles occupying the position prescribed for them for time t.

It is quite clear that the solution of the heat conduction-convection problem for the step-by-step motion of the fluid particles will converge to the solution of the problem for the given motion of the fluid particles because the given fluid motion is the limiting case of the step-by-step motion for decreasing step size, and for an inviscid fluid the boundary conditions [Equation (2)] can be satisfied throughout the process. The *exact* solution of Equation (1) for the *approximated* fluid motion, however, can be reduced to solutions of the simpler conduction equation

$$a \nabla^2 T - \frac{\partial T}{\partial t} = 0 \qquad (3)$$

Solutions to Equation (3) are well known for most cases of practical interest.

In the diagram for the $(\mathbf{r}, t)$ space (Figure 3) the motion of the fluid boundary described above appears as either one of the boundaries B_1 or B_2 approximating $\mathbf{r}_0(t)$. The space-time path of the general fluid particle is then uniquely determined and approximates $\mathbf{r}(t)$ in a manner similar to the approximation of $\mathbf{r}_0(t)$ by B_1 or B_2. Consequently B_1 or B_2 as used here will include not only the boundary motion but also the motion of the entire fluid as caused by the motion of the boundary B_1 or B_2 respectively.

The details of the calculation may be explained by reference to Figure 1. Between times t and $(t + \Delta t)$ it is assumed that the solution is known for time t; that is, $T(\mathbf{r}, t)$ is known and the solution for time $(t + \Delta t)$, during which the boundary has moved from A to B, is desired. Instead of proceeding from A to B directly, one proceeds from A to C to B, and observes that during the integration from A to C, A' to C', etc., the velocity $\mathbf{v}(\mathbf{r}, t)$ is everywhere zero (because $\mathbf{r}$ remains constant) and Equation (1) goes over into Equation (3), for which the solution may be assumed known. Thus the exact temperature for time $(t + \Delta t)$ for fluid boundary at point C and fluid particles at point C' is obtained; each fluid particle is shifted (instantaneously) from C to B, from C' to B', whereby the redistribution of temperature due to heat convection is achieved, and each fluid particle attains the position it should occupy in accordance with the prescribed motion.

Mathematically these steps are most easily performed by the use of Green's function for Equation (3) (for the domain bounded by AC), which may be denoted by $G(\mathbf{r}, \mathbf{r}', t)$. The temperature $\theta[\mathbf{r}, (t + \Delta t)]$ at the representative point C' is then given in terms of the temperature $T(\mathbf{r}, t)$ by

$$\theta(\mathbf{r}, t + \Delta t) = \int_{\mathbf{r}_0(t)}^{\infty} T(\mathbf{r}') \, G(\mathbf{r}, \mathbf{r}', \Delta t) \, dr' \qquad (4)$$

where dr' is written symbolically for the volume element $(dx'\, dy'\, dz')$ at $\mathbf{r}'$.

The displacement $\Delta\mathbf{r}$ of the fluid particle situated at $\mathbf{r}$ is easily calculated, as the local velocity $\mathbf{v}(\mathbf{r}, t)$ of the fluid is given. Then, as each fluid particle is shifted by $\Delta\mathbf{r}$ (from the representative point C' to the representative point B') the temperature $T(\mathbf{r}, t + \Delta t)$ is given from Equation (4) by $\theta[(\mathbf{r} - \Delta\mathbf{r}), (t + \Delta t)]$ or, explicitly,

$$T(\mathbf{r}, t + \Delta t) = \int_{\mathbf{r}_0(t)}^{\infty} T(\mathbf{r}', t) \cdot G[(\mathbf{r} - \Delta\mathbf{r}), \mathbf{r}', \Delta t] \, dr' \qquad (5)$$

Equation (5) is the exact solution of Equation (1) for the approximating boundary motion A to C to B. Thus, given an initial temperature distribution $T(\mathbf{r}, 0)$, the time interval t may be subdivided into n subintervals and the *exact* solution of Equation (1) is obtained for the strip bounded by B_1 (see Figure 3) by repeated application of Equation (5) to the n subintervals.

For the fluid motion represented by B_2 a related formula may be derived by performing the operations given by Equation (4) and previous to Equation (5) in reverse order, i.e., taking the path (see Figure 1) from A to D to B and from A' to D' to B'.

$T_1^n(\mathbf{r}, t)$ then is the solution of Equation (1) for B_1 and $T_2^n(\mathbf{r}, t)$ that for B_2, both for time t in n intervals. This is not the place to treat questions of convergence mathematically, but the following can be concluded from physical considerations as n tends to infinity: Both T_1 and T_2 tend to the solution of Equation (1) for boundary motion $\mathbf{r}_0(t)$, since both B_1 and B_2 tend to $\mathbf{r}_0(t)$; the difference $(T_1 - T_2)$ tends to zero as n increases; considering that the path $\mathbf{r}(t)$ of every fluid particle is always intermediate between B_1 and B_2, one may assume that for a certain class of fluid motions the temperature of the fluid particle for the given motion is intermediate between T_1^n and T_2^n.

In the foregoing section the problem of diffusion in a moving medium with time-dependent boundaries was reduced to a series of quadratures of known functions, namely, the solutions of a diffusion problem in a medium at rest with boundaries at rest. The method does not involve numerical integrations or procedures; neither does it replace differential equations by difference equations; rather, it yields the final solution as a function of position and time. For instance, if Green's function for diffusion in a moving medium is to be obtained one merely has to insert the temperature distribution of a unit heat source for the initial temperature in Equation (5). Also, by use of Duhamel's theorem very general time dependence of the boundary conditions may be included.

HEAT TRANSFER INTO A SPHERICAL CAVITY WITH RADICAL MOTION

Qualitative Considerations and Application of the Preceding Theory

It is evident from the discussion above that the mathematical expressions for heat conduction-convection problems will in general be quite involved. Fortunately the physical conditions prevailing in vapor-liquid systems permit substantial simplifications in the general formulism. The system of a spherically symmetric vapor bubble in an infinite liquid will be considered in some detail because of its importance in boiling and in cavitation.

To begin with, it must be clearly understood what bearing the transport of liquid has upon the transport of heat toward the bubble wall. In Figure 4 the growing bubble is shown at two successive times, and the influence of liquid convection is seen to arise from two processes:

1. While the bubble grows, the surface area of the bubble increases; to the extent to which heat *conduction* depends on the bubble radius the increase in radius changes the amount of heat conducted to the wall.

2. While the bubble grows, its curva-

ture changes; owing to this change the *relative* position of fluid particles $(ABCD) \rightarrow (A'B'C'D')$ changes and this *relative change* constitutes the convective contribution to the transfer of heat to or from the bubble wall.

It is important to realize that the *absolute* change in position of fluid particles (liquid convection) does not entail the convection of *heat toward* the bubble wall: if the liquid-vapor boundary in Figure 4 is flat (a plane), the *relative* position of fluid particles is not changed by the motion of the boundary and then no convective heat transfer takes place within the liquid or toward the boundary despite considerable convective motion of the liquid. The same is true for the case of a radially moving *spherical* vapor-liquid boundary if the domain under consideration is small compared with the radius. This is evident from the fact that in a region so restricted the flow of liquid is the same as that caused by a moving plane, a circumstance which will prove important and which will be referred to later.

In reference *2* the preceding theory was applied to the present problem. The appropriate Green's function to be used in Equation (5) can be found in Carslaw and Jaeger (*4*). Vapor bubbles, even at slight superheats, grow so fast or, conversely, the time interval under consideration is so short that a *mean value between* T_1^1 and T_2^1 represents the temperature of the phase boundary with sufficient accuracy. This involves the

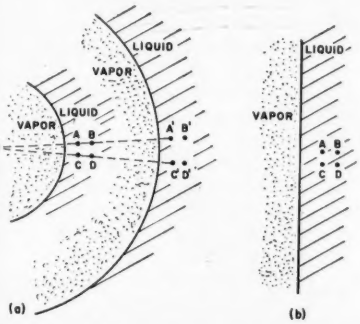

Fig. 4. Relative motion of fluid particles induced by (*a*) radial motion of spherical boundary, (*b*) motion of plane boundary.

calculation of a mean value for $R(\xi)$ for the following expression; it represents the temperature increment at the bubble wall of radius $R(t)$ at time t due to an amount of heat $dQ(x)$ liberated on the bubble of radius $R(x)$ at time x:

$$dT = \frac{dQ(x)}{4\pi\sqrt{\pi a}\,\sqrt{t-x}R^2(\xi)} \cdot\left[1 - \sqrt{\pi}\,\frac{\sqrt{a(t-x)}}{R(\xi)} \cdot \exp\left\{\frac{a(t-x)}{R^2(\xi)}\right\} \cdot \operatorname{erfc}\frac{\sqrt{a(t-x)}}{R(\xi)}\right] \quad (6)$$

where ξ ranges from time x to time t and $R(\xi)$ starts at $R(x)$ and grows to $R(t)$. An appropriate mean value for $R(\xi)$ is calculated in reference *2* to be $R(\xi) = \sqrt{R(x)\cdot R(t)}$, which is the geometric mean of the initial and final radii; Equation (6) then becomes

$$dT = \frac{dQ(x)}{4\pi\sqrt{\pi a}\,\sqrt{t-x}R(x)R(t)} \cdot\left[1 - \sqrt{\pi}\left(\frac{a(t-x)}{R(x)R(t)}\right)^{1/2} \cdot \exp\left\{\frac{a(t-x)}{R(x)R(t)}\right\} \cdot \operatorname{erfc}\left(\frac{a(t-x)}{R(x)R(t)}\right)^{1/2}\right] \quad (7)$$

If greater accuracy is desirable, the time interval must be further subdivided; on the other hand, if Equation (7) is to be used for the calculation of pressure in Rayleigh's equation of bubble dynamics the following circumstance is of importance. Since the time of the process starts at x (and lasts until t), $(t - x)$ starts at zero and therefore the second term in the bracket starts at zero while the factor in front starts at infinity; thus the second term is negligible in the vicinity of the singularity of Equation (7). As time increases, the second term grows, but for the case of a bubble growing by evaporation (even in a slightly superheated liquid) the radius $R(t)$ as well as $\sqrt{t-x}$ increases so fast that the factor in front decreases strongly while the second factor in the bracket increases to about ½. For a vapor bubble growing in water at 103°C., for example, by the time the second term in the bracket has increased to about ½, the radius $R(t)$ has increased by a factor of about 100 and the contribution dT is then less than 1% of its initial value. The second term in the bracket is small when the contribution (dT) is large and the contribution (dT) is small by the time the second term becomes important. For the sake of applications, where Equation (7), integrated, is used in Rayleigh's equation, it is advantageous to accept the small error involved and to neglect the second term in order to make the analysis and integration of Rayleigh's equation feasible without resort to numerical computations from which very little can be learned.

Integration of Equation (7) without the second term yields for the temperature of the bubble wall at time t (*2*) the approximation

$$T(t) = \frac{L\rho_v}{c_L\rho_L(\pi a)^{1/2}} \cdot\int_0^t \frac{R^2(x)\dot{R}(x)\,dx}{R(x)R(t)\sqrt{t-x}} \quad (8)$$

The integrand of Equation (8), it may be noted, is simply the amount of heat liberated (or absorbed) divided by the geometric mean squared of the radius, multiplied by $\sqrt{t-x}$.

Thin-thermal-boundary-layer Theory

A first attempt at the problem of combined heat conduction and convection with moving boundaries was published a few years ago by Plesset and Zwick (*1*), who considered the one-dimensional problem of a radially expanding sphere. They presented a partial solution in the sense that they included in their theory the effect of the surface-area increase of the moving boundary (cf. item 1 above) while inadvertently excluding the effect of heat convection (cf. item 2).

The crucial assumption in Plesset's theory is that the temperature throughout the liquid is constant except in a thin layer of liquid (adjacent to the bubble) which has small thickness compared with $r_0(t)$. Pinney (*5*) pointed out that this assumption implies significant restrictions on the solution but that this question was not discussed by Plesset and Zwick. Inasmuch as controversy arose on this and related matters on several occasions in the last two years (*6, 7*) it will here be analyzed in some detail.

From the point of view of the general theory which was developed in the present paper the implications of the "thin-thermal-boundary-layer" assumption become quite apparent. In Figure 1 this assumption amounts to a restriction of the domain of integration (which extends from $\mathbf{r}_0(t)$ to infinity) to a thin strip to the right of $\mathbf{r}_0(t)$ instead. In terms of the basic equation (5) the thin-thermal-layer assumption implies that the integral is extended from $r_0(t)$ to $(r_0 + h)$ with $h \ll r_0$ instead of from r_0 to infinity; the integral, then, instead of adding up the varying temperature contributions from the entire liquid surrounding the cavity takes in only the variations from the immediate vicinity of the cavity of radius $r_0(t)$. Thereby, of course, *all* effects of convection and conduction in the liquid contained between $(r_0 + h)$ and infinity are eliminated from calculation. In simple words, in a region of assumed constant temperature (i.e., everywhere except in the thin thermal-boundary layer) no effects of convection or conduction exist. In the calculation of the temperature in the boundary layer itself, conduction and convection are included *to the extent to which the latter exists within the thin layer*. However, it must be observed (compare Figure 5) that in consequence of the assumed thinness of the region, explicitly $h \ll r_0(t)$, the calculation is restricted to

only those fluid particles which have negligible relative velocity with respect to the moving boundary ($r_0(t)$) as well as with respect to each other and which therefore do not contribute to heat convection; all other fluid particles which are at greater distance and which do have sizable relative velocities were eliminated previously by the assumption of constancy of temperature at any distance beyond ($r_0 + h$).

As long as h is considered small compared with $r_0(t)$, the region where convection is important is automatically excluded; on the other hand, Plesset's method of successive approximations cannot be extended to include a thickness of liquid equal to or larger than the radius $R(t)$ because, as will be shown, it then diverges.

The method in reference *1* depends critically on the development of

$$r^4 = R^4\left(1 + \frac{3h}{R^3}\right)^{4/3}$$

[stemming from Equation (2*a*), reference *1*] into a power series, in powers of the perturbation parameter (h/R^3),

$$r^4 = R^4\left[1 + 4\,\frac{h}{R^3} + 2\left(\frac{h}{R^3}\right)^2 + \cdots\right]$$

where the terms in the bracket enter successively the 0, 1, 2 $\cdots$ order approximation [cf. sequel to Equation (11) of reference *1*]. However, as is well known, the power series

$$(1 + x)^n = 1 + nx + \frac{n(n-1)}{2}\,x^2 + \cdots$$

for noninteger n and $x \geq 1$ is divergent. The method of successive approximations therefore cannot be extended to include the convective transport of heat to the bubble wall.

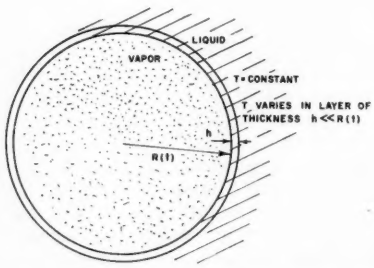

Fig. 5. Temperature conditions under the thin-thermal-boundary-layer assumption.

By means of the thin-boundary-layer theory Plesset and Zwick derive an approximate expression for the temperature at the boundary

$$T(t) = \frac{L\rho_v}{c_L\rho_L(\pi a)^{1/2}} \cdot \int_0^t \frac{R^2(x)\dot{R}(x)\,dx}{\left[\int_x^t R^4(y)\,dy\right]^{1/2}} \qquad (9)$$

which they use throughout their subsequent work. According to their method the differential equation is developed in powers of (h/R^3) and "to the first order h/R^{3}" [cf. reference *1*, Equation (11), Plesset and Zwick],

$$a\,\frac{\partial^2 u}{\partial h^2} - \frac{\partial u}{\partial \tau} = -\frac{4h}{R^3}\,\frac{\partial^2 u}{\partial h^2}$$

This equation, however, which is approximate to the first order in h, is not the one for which Equation (9) is a solution; rather, Equation (9) is the solution of the following equation [cf. reference *1*, Equation (12), Plesset and Zwicki]:

$$a\,\frac{\partial^2 u^0}{\partial h^2} - \frac{\partial u^0}{\partial \tau} = 0$$

which follows from the previous equation only if the thickness h of the boundary layer is no longer assumed small compared with the radius but is set equal to zero. Equation (9) then represents the "zero-order solution" for $h = 0$ and every effect of convection within the fluid has been completely eliminated previous to its calculation. This leaves the effect of surface-area increase due to boundary motion, as the only effect taken into consideration.

Comparison of the Results of the Two Theories

Both Equations (9) and (8) are obviously grossly simplified approximations to an otherwise complex problem. One is therefore led to suspect that the two expressions, despite their entirely different derivation and appearance, must be mathematically very similar, and indeed they are.

The numerator and coefficient of Equations (8) and (9) are identical; therefore one need compare only the denominator of Equation (8)

$$R(x)R(t)\sqrt{t-x} \qquad (10)$$
$$\equiv [\text{geometric mean of } R^2]\cdot\sqrt{t-x}$$

with the denominator in Plesset's Equation (9). Inasmuch as expression (10) was derived by calculating a mean value for R^2, the denominator in Plesset's formulations should also represent a mean value for R^2. If the definition of the root mean square (R.M.S.) of a function $f(y)$ for the interval $x \leq y \leq t$

$$[\text{R.M.S. of } f(y)] = \frac{1}{\sqrt{t-x}}\left[\int_x^t f^2(y)\,dy\right]^{1/2} \qquad (11)$$

is recalled, it is manifest that the denominator of Plesset's Equation (9) is in fact such a mean value, namely

$$\left[\int_x^t R^4(y)\,dy\right]^{1/2} = [\text{R.M.S. of } R^2]\cdot\sqrt{t-x} \qquad (12)$$

Equations (8) and (9) are thereby recognized to differ only in the way in which two closely related mean values are used for R^2 to represent approximately the influence of the continuous radial increase from $R^2(x)$ to $R^2(t)$. Moreover, in the neighborhood of the all-important singularity of the integrand at $x = t$ these mean values are identical. The greater usefulness of Equation (8) lies in its simplicity in application to bubble dynamics. The integral over the square root of another integral in Equation (9) renders Rayleigh's equation (in which either Equation (8) or (9) is tc be used) difficult to analyze.

ACKNOWLEDGMENT

The present study was supported in part by funds from the U. S. Atomic Energy Commission under Contract AT(11-1)-34.

NOTATION

- $\mathbf{r}$ = radius vector ($xi + yj + zk$)
- $\mathbf{r}_0 = \mathbf{r}_0(t)$ = radius vector to the boundary
- $r_0(t)$ = $R(t)$ = radius of spherical cavity
- $\mathbf{v}(\mathbf{r}, t)$ = velocity of a fluid particle
- a = thermal diffusivity
- L = latent heat of vaporization
- $\rho_{v,L}$ = density of vapor or liquid, respectively
- c_L = specific heat of liquid
- T, θ = temperature
- t = time
- x = a time between $t = 0$ and $t = t$ (except as used in $\mathbf{r}$)
- ξ = time integration variable $x \leq \xi \leq t$
- $Q(x)$ = heat liberated at time x
- h = thickness of thermal-boundary layer (cf. reference *1*)
- U, defined by $\partial U/\partial h = T - T_0$; T_0 is the temperature at infinity
- τ = $\int_0^t R^4(t)\,dt$ (cf. reference *1*)

LITERATURE CITED

1. Plesset, M. S., and S. A. Zwick, *J. Appl. Phys.*, **23**, 95 (1952).
2. Forster, H. K., *ibid.*, **25**, 1067 (1954).
3. ———, *Phys. Rev.*, **99**, 660 (1955).
4. Carslaw, H. S., and J. C. Jaeger, "Conduction of Heat in Solids," 1 ed., p. 305, Oxford University Press, London.
5. Pinney, Edmund, *Math. Rev.*, **13**, 751 (1952).
6. Westwater, J. W., in "Advances in Chemical Engineering," Vol. 1., p. 21, Academic Press, New York (1956).
7. *Memo 20-137*, Jet Propulsion Laboratory, Calif. Inst. Technol. (1956).

INDEX TO VOLUME 3

Authors

Subject Index

BOOKS

Viscous Flow Theory: I, Laminar Flow. Shih-I Pai. D. Van Nostrand Company, Inc., New York (1956). 384 pages. $7.75.

The development of aircraft and missiles which travel at velocities in excess of the velocity of sound has necessitated much new research in the hydrodynamics of compressible fluids. For, though it is possible to neglect the compressibility of air at low speeds (about 200 miles an hour), this is not possible at higher speeds. The book under review is concerned with the laminar flow of viscous, compressible fluids with special attention to aerodynamics. Three major topics are discussed: (1) the classical hydrodynamic theory of fluids, including some elementary kinetic theory of gases, (2) generalizations derivable from the theory without explicit solution of the differential equations such as similarity and dimensional analysis and general properties of the Navier-Stokes equation, and (3) boundary-layer theory. The last is by far the largest section, occupying some 216 pages. Considerable detail is given and numerous tables of useful data are included in the text. It is proposed to treat turbulent flow in part II of this work.

This reviewer feels that the major omission from the text is a discussion of the properties of gases at extremely low pressures. Under circumstances prevailing in the upper atmosphere the mean free path of a molecule may easily be of the order of magnitude of the dimensions of the flying object. Under these conditions the relative variation of macroscopic quantities over a mean free path is not negligible. For the limiting case of the Knudsen gas there are striking differences with phenomena under moderate pressures. For instance in Couette flow the force does not depend upon the velocity gradient but rather on the velocity difference, the force depending linearly on the pressure, etc. The transition region between ordinary gas pressures and those for which Knudsen behavior subsists has been the subject of several studies recently. As anticipated, the results differ from those of classical hydrodynamics.

STUART A. RICE

Experimental Physical Chemistry. Farrington Daniels, J. H. Mathews, J. W. Williams, Paul Bender and R. A. Alberty. McGraw-Hill Book Company, Inc., New York (1956). Fifth edition. 482 pages. $6.50.

The latest edition of this well-known text for the physical chemistry laboratory incorporates several new experiments, one entirely new chapter, and the complete rewriting of parts of another. Of primary interest among experimental topics revised or presented for the first time are osmotic pressure, chromatographic adsorption, and differential thermal analysis.

The section on the treatment of experimental data dealing with errors has been rewritten to include several problems on the calculation of error. The rewritten section represents an improvement over previous efforts in that the goal of a relatively clear presentation of the subject of experimental

error to the third-year college student has been accomplished.

An entirely new chapter devoted to the experimental techniques of electronics, high vacuum, and glass manipulation has been added to the book. High-vacuum technology is discussed through consideration of types of vacuum pumps and gauges, the detection of leaks, and the basic theory of viscous, slip, and molecular flow. The section on electronics contains an experiment on the determination of characteristic curves of various vacuum tubes, triode amplification, and rectification.

As the authors point out, space for new experiments can be obtained only by the elimination of those from previous editions which have become part of first- or second-year laboratory courses or which, for various reasons, have become less important to the student of physical chemistry. Such casualties from the previous edition of this book include experiments on photoelectric colorimetry, on partial miscibility, on clock reactions, and on unimolecular films and discussions of dimensions and colorimetry.

The second section of the book, dealing with the apparatus and techniques generally encountered in experimental work, has been left unchanged for the most part other than the section on errors mentioned previously. The few new topics cover principally separate discussions of gamma radiation, high-vacuum distillation, and time measurements.

JOHN B. BUTT

Elements of Gasdynamics. H. W. Liepmann and A. Roshko. John Wiley & Sons, New York (1957). 439 pages. $11.00.

Elements of Gasdynamics is an excellent book. The material covered may be ascertained from the chapter headings, which read: (1) "Concepts from Thermodynamics"; (2) "One Dimensional Gasdynamics"; (3) "One Dimensional Wave Motion"; (4) "Waves in Supersonic Flow"; (5) "Flow in Ducts and Wind Tunnels"; (6) "Methods of Measurement"; (7) "The Equations of Frictionless Flow"; (8) "Small-Perturbation Theory"; (9) "Bodies of Revolution: Slender Body Theory"; (10) "The Similarity Rules of High Speed Flow"; (11) "Transonic Flow"; (12) "The Method of Characteristics"; (13) "Effects of Viscosity and Conductivity"; (14) "Concepts from Gas Kinetics." There are very few criticisms which need to be made. It is unfortunate that the authors chose to use the symbols F and G for the Helmholtz and Gibbs free energy rather than A and G. The use of F for the Helmholtz free energy will cause much confusion since most Americans use F for the Gibbs free energy and the majority of the tables of thermodynamic data adhere to this convention. This reviewer would like to have seen a somewhat more extended discussion of the second law of thermodynamics and of the principles of irreversible thermodynamics, especially since the latter is used in one form or another extensively throughout the text. The treatment of the Clausius-Clapeyron equation is very poor and unconvincing. The usual thermodynamic derivations are superior to the quasimolecular one given by the authors. Also, the treatment of imperfect gases is superficial and the relationship

between thermodynamic properties and gas imperfection incomplete. These criticisms are not meant to imply that the thermodynamics chapter is poor, but rather to indicate some places where improvement is possible. The remainder of the book, especially the sections dealing with the hydrodynamics of compressible fluid flow, is admirably clear.

The final chapter on the kinetic theory of gases is short but complements well the rest of the text. This reviewer was very pleased to see a brief discussion of the properties of Couette flow in the Knudsen region. The development of missiles which fly in regions of the upper atmosphere where the mean free path is of the order of the dimensions of the flying object makes this pressure range of great importance.

Elements of Gasdynamics is to be recommended to all students interested in gasdynamics and its applications. The book will also be of interest to physical chemists, who will find a wide realm of irreversible phenomena which awaits exploration.

STUART A. RICE

The Principles of Chemical Equilibrium. K. G. Denbigh. Cambridge University Press, New York (1957). 491 pages. $9.00.

This is a very good book—well planned and well written. While the major portion of the book is concerned with the applications of thermodynamics to equilibrium, as the title implies, the first part is given over to the fundamental principles of thermodynamics. This fine exposition of the first and second laws and of the various thermodynamic functions is distinguished by its thoroughness and clarity.

The second part, "Reaction and Phase Equilibria," is made up of eight chapters. The subjects treated are the properties and reaction equilibria of gases, the phase rule and phase equilibria of pure substances, and solutions. The treatment of fugacity is very good, and it is a pleasure to report that the term *fugacity coefficient* rather than *activity coefficient* is used for the f/P ratio. The discussion of ideal and nonideal solutions is detailed and lucid. It is unfortunate that the most modern manner of tabular presentation of functions with which standard free energies of formation may be computed is not discussed and that equilibrium ratios (K factors), so useful in hydrocarbon phase equilibria, are not mentioned.

The third part, "Thermodynamics in Relation to the Existence of Molecules," consists of five chapters. Statistical analogues of entropy and free energy, partition functions, the third law, adsorption, and chemical kinetics are discussed. While the last may seem somewhat out of place, it is treated only in its relation to chemical equilibrium. A thermodynamic, as distinct from kinetic, derivation of the Langmuir isotherm is presented. There are a number of problems at the end of each chapter (some from Cambridge University examinations), and answers are given with comments in an appendix. The index is reasonably complete. Professor Denbigh is to be congratulated on this excellent work.

HARDING BLISS

INDEX OF ADVERTISERS

Advertising Offices

New York 36—Lansing T. Dupree, Adv. Mgr.; John M. Gaede, Asst. Adv. Mgr.; Paul A. Jolcuvar, Dist. Mgr.; Donald J. Stroop, Dist. Mgr.; Hale H. Carey, Dist. Mgr.; 25 W. 45th St., Columbus 5-7330.

Chicago 4—Martin J. Crowley, Jr., Dist. Mgr.; Robert Kliesch, Dist. Mgr.; 53 W. Jackson Blvd. Harrison 7-0382.

Cleveland 15—Eugene B. Pritchard, Dist. Mgr., 1836 Euclid Ave., Superior 1-3315.

Pasadena 1—Richard P. McKey, Dist. Mgr., 465 East Union St., Ryan 1-8779.

Dallas 28—Richard E. Hoierman, Dist. Mgr., 2831 El Capitan Drive, Davis 7-3630

Birmingham 9, Ala.—Fred W. Smith, Dist. Mgr., 1201 Forest View Lane—Vesthaven, Tremont 1-5762.

The Future of Arid Lands. Gilbert F. White, editor. American Association for the Advancement of Science, Washington, D. C. (1956). 464 pages. $6.75.

This volume represents the combined efforts of scientists from seventeen countries to evaluate the present-day problems and status of research of the world's arid lands. The arid land area is huge, covering approximately one third of the world's land surface. This area is of vital interest to those concerned with world resource and population problems since misuse of this land can affect adjacent humid lands.

The varied topics concerning the arid lands are conveniently grouped under five main headings: The Broad View, Variability and Predictability of Water Supply, Better Use of Present Resources, Prospects for Additional Water Sources, and Better Adaptations of Plants and Animals to Arid Conditions. This organization greatly facilitates reading since one can more easily select the specialized topic desired. The reader is informed that two impressions were derived from the discussions of these quite varied papers: first, there is a need for an integrated analysis by the various disciplines on a regional basis, e.g., of drainage basins; second, there is a distinct challenge to convert findings of the natural scientists into reality at the level of the farm or ranch.

Nearly every article contains information which will be of interest to the nonspecialist or layman. Shantz, for example, in "History and Problems of Arid Land Development" states that early use of dry lands in the western United States emphasized the maintenance of a dust mulch as a solution to agricultural water problems. Dust mulch provided no more protection to the moisture below than the same amount of hard soil. It was the repeated cultivation connected with dust mulching that eliminated the transpiration losses by weeds and conserved water. Shantz also points out the difficulties associated with practices of loosening the subsoil, deep planting of trees, and the use of nitrate fertilizers in the short-grass country. Koenig in "The Economics of Water Resources" submits the proposition that twentieth-century use of water for irrigation agriculture is not an appropriate use of water since it follows a historical precedent to increase the value of the land. In the United States the water which will support one worker in irrigation agriculture will support about five dozen workers in manufacturing.

Any over-all appraisal of *The Future of Arid Lands* must of necessity mention what the book is not as well as what it is. From the title one might assume that it would include a step-by-step evaluation of all the arid lands of the world. It is however quite selective and contains very little material on the Soviet and Chinese segments of the great Eurasian arid zone.

Each reader will have his own opinion as to what he considers the most important chapters and will find that some are quite specific while others are quite general. Along these lines it might be well to mention that some of the best detailed geographic descriptions of several of the arid countries are contained in this volume. The inclusion of summaries at the end of most chapters as well as extensive bibliographies makes this a valuable reference book.

E. F. Bordne